MODELING AND SIMULATION OF BUBBLES AND PARTICLES

BY

ANDREW JAMES DORGAN

B.S., University of Illinois at Urbana-Champaign, 2001
M.S., University of Illinois at Urbana-Champaign, 2003

DISSERTATION

Submitted in partial fulfillment of the requirements
for the degree of Doctor of Philosophy in Aerospace Engineering
in the Graduate College of the
University of Illinois at Urbana-Champaign, 2009

Urbana, Illinois

Doctoral Committee:

Professor Eric Loth, Chair
Professor Mike Bragg
Professor Ki Lee
Professor Pratap Vanka
Assistant Professor David Saintillan

Abstract

The interaction of particles, drops, and bubbles with a fluid (gas or liquid) is important in a number of engineering problems. The present works seeks to extend the undertanding of these interactions through numerical simulation. To model many of these relevant flows, it is often important to consider finite Reynolds number effects on drag, lift, torque and history force. Thus, the present work develops an equation of motion for spherical particles with a no-slip surface based on theoretical analysis, experimental data and surface-resolved simulations which is appropriate for dispersed multiphase flows. The equation of motion is then extended to account for finite particle size. This extension is critical for particles which will have a size significantly larger than the grid cell size, particularly important for bubbles and low-density particles. The extension to finite particle size is accomplished through spatial-averaging (both volume-based and surface-based) of the continuous flow properties. This averaging is consistent with the Faxen limit for solid spheres at small Reynolds numbers and added mass and fluid stress forces at inviscid limits. Further work is needed for more quantitative assessment of the truncation terms in complex flows.

The new equation of motion is then used to assess the relative importance of each force in the context of two low-density particles (an air bubble and a sand particle) in a boundary layer of water. This relative importance is measured by considering effects on particle concentration, visualization of particle-fluid interactions, diffusion rates, and Lagrangian statistics collected along the particle trajectory. Strong added mass and stress gradient effects are observed for the bubble but these were found to have little effect on a sand particle of equal diameter. Lift was shown to be important for both conditions provided the terminal velocity was aligned with the flow direction. The influence of lift was found to be negligible (in terms of particle concentration predictions) when terminal velocity was oriented in the wall-normal direction. The history force was shown to damp particle diffusion and have some minor impacts on particle concentration. This effect was augmented by using the creeping flow Basset expression and shows that the creeping flow expression should not be used in finite-Reynolds number conditions. The effects due to the

finite-size extensions are also considered as are effects due to spatial reconstruction of the fluid properties. In general, little effect of the finite-size model or choice of spatial interpolation was observed in terms of particle concentration. However, Lagrangian statistics show some interesting sensitivities.

Finally, the new equation of motion was applied to air bubbles and sand particles of several different diameters. Particle-fluid interations observed through flow-visualization, particle concentration, particle-wall interactions, and Lagrangian statistics were all considered. These results were interpreted and compared to heavy-particle results where appropriate. Particle deposition was found to be well-described by the heavy-particle model of Young & Leeming and root-mean-square relative velocities were found to also agree with previous heavy-particle work. A model for the latter is suggested for heavy-particles and found to work similarly well for low-density particles. Non-tracer behavior was observed for bubbles with small Stokes numbers, a result not expected based on heavy-particle expectations. Local clustering of particles was observed in certain fluid structures which may indicate the importance of modeling particle collisions in future studies.

In memory of my paternal grandmother and maternal grandfather,
both of whom were lost while I was conducting this research

Doreen Dorgan

(1926 - 2005)

Charles William Boward

(1928 - 2008)

Acknowledgments

I would like to thank my research advisor, Professor Eric Loth, for his help and guidance in conducting this research and preparing this dissertation. In December of 2003, I left Champaign after completing a Master's Degree (Professor Loth served as my advisor for that degree as well) to take a job with The Boeing Company in St. Louis, Missouri. Since that time Professor Loth has worked with me remotely and has been very understanding of my obligations at work. Somehow, he pushed just hard enough that I am finally finishing this work without totally losing my mind! For his guidance and understanding in all these matters, I am very grateful.

I would also like to thank my family for their encouragement and desire to see me succeed. Hopefully I will get to see more of them now that this endeavor is coming to a close. Thanks also goes to my Boeing colleagues, in particular Dr. Mori Mani and Dr. Andrew Cary, for their understanding during times when I could not be fully dedicated to my job in an effort to finish my degree. Finally, I want to express my thanks to Annie for her encouragement, support, and just generally putting up with me.

Table of Contents

List of Figures

List of Tables

List of Symbols

A	projected area
C_D	drag coefficient
C_f	skin friction coefficient
C_L	lift coefficient
$c_{1,2}$	History force model constants
D/Dt	derivative taken along fluid element path
d/dt	derivative taken along particle path
d	diameter
Δt	computational time-step
ϵ	turbulence dissipation rate and window model ratio of time-scales
$\vec{F}$	force vector
F	force
f	drag law correction factor
Fr	Froude number
$\vec{g}$	gravitational accleration
γ	drift parameter
K	History force kernel
L	computational domain length

m	mass
μ	molecular viscosity
ν	kinematic viscosity
Ω	particle angular velocity
$omega$	fluid vorticity
ψ	density ratio
ρ	density
Re_p	particle Reynolds number
Re_τ	Reynolds number based on u_τ
St_δ	Stokes number based on outer scales
St_Λ	Stokes number based on integral time-scale
St_λ	Stokes number based on Kolmogorov time-scale
St^+	Stokes number based on inner-scales
S	Strouhal number
t	time
τ_c	convective time-scale
τ_d	diffusive time-scale
τ_H	history time-scale
τ_Λ	fluid integral time-scale
τ_p	particle response time-scale
τ_δ	fluid time-scale baed on outer units
τ_f^+	fluid time-scale based on inner units
t_{window}	temporal length of the history force window
u_τ	boundary layer friction velocity

$\vec{V}$	velocity vector
V	velocity magnitude
V_∞	boundary layer freestream edge velocity
$\forall$	volume
x, y, z	streamwise, wall-normal, and spanwise coordinate directions, respectively
$[...]$	Eulerian-averaged quantity
$<...>$	Lagrangian-averaged quantity
$(...)^+$	quantity in inner units
$(...)^*$	non-dimensional quantity
$(...)_{@p}$	fluid property extrapolated to the particle centroid
$(...)_f$	fluid quantity
$(...)_p$	particle/bubble quantity
$(...)_{rel}$	particle to fluid relative quantity
$(...)_{surf}$	surface-averaged quantity
$(...)_{term}$	quantity taken at particle terminal velocity
$(...)_{vol}$	volume-averaged quantity

Chapter 1

Introduction

The term "multiphase" has come to imply the study of fluid dynamics in the presence of multiple phases of matter. Typically these take the form of gaseous, liquid, or solid phases (generically referred to as "particles" herein) immersed in liquid or gaseous fluids. In addition to generically referring to bubbles, droplets, and solid particles as "particles", the present work will also refer to this phase as the "dispersed-phase" or "particulate-phase". The fluid in which the particulate-phase is immersed will by generally referred to as the "continuous-phase". The interaction of the multiple phases results in a challenging problem and is important to many natural processes and engineering systems.

This Chapter discusses the relevance of multiphase flows from an engineering and environmental standpoint and provides a motivation for the present study. A review of previous work is also given. Finally, the Chapter concludes with a statement of the objectives of the present study.

1.1 Motivation

The motion of particles, drops, and bubbles immersed in a fluid is important in many engineering problems. In aerospace, solid particles or droplets are commonly encountered mixed with a gaseous phase. Air breathing propulsion systems can have important multiphase interactions during all phases of the engine cycle. For example, particles can be ingested during near-ground operation which erode the compressor blades. Ingested water droplets may freeze on the compressor and degrade its performance or cause damage to the engine. The characteristics of fuel sprays and fuel-air mixing in the combustor are important to the efficiency of the engine and generation/concentration of soot particles in the exhaust stream. Solid-fuel rocket combustion leads to a complicated multiphase interaction where fuel particles can break free of the burning grain and be transported along the core of the engine where they may combust. If the fuel

particles do not combust, they may cause ablation issues. As a matter of aircraft safety, multiphase interactions are important to the problem of aircraft icing where ice accretion can disrupt the aerodynamic performance of lifting structures.

In environmental science, particles and droplets in the atmosphere can have a substantial impact on weather and environmental safety. Sediment transport in natural bodies of water can play a significant role in the health and maintenance of rivers and coastal areas. For example, silting can dramatically reduce the capacity of rivers and has been cited as one of the reasons for some of the more devastating floods in Asia and elsewhere. Coastal land erosion is another problem that has become more severe in the last few decades since it can lead to substantial losses of animal habitats and affect human population centers. Bubbles are injected in plumes for reservoirs and waste water treatments to increase oxygen content and control pH levels.

Multiphase interactions are also important in the context of friction drag reduction. Carefully placed micro-bubbles or polymers have been shown to substantially reduce viscous drag losses (sometimes by as much as 80%) in pipe flows. The best example of this in engineering practice is the Alaskan oil pipe line which injects polymers into the oil to reduce pumping requirements. Micro-bubbles have been claimed to have similar effects, but the mechanism is less understood. This is an attractive alternative, however, as air micro-bubbles could be generated along the hull of ships to substantially reduce drag without any impact on the environment. This technology has been considered for both military and commercial use and was the focus of a recent DARPA program which funded the initial parts of this work.

In many of the above situations it may be reasonable to assume that the particle phase is "dispersed" such that its motion is driven by interactions with the fluid, not by interactions with other particles. Furthermore, small droplets and bubbles are often spherical due to surface tension. In this context, accurate, robust, and efficient models for the particle-fluid interactions are used to reduce design cost and improve performance and safety of engineering systems. In past years, the use of Computational Fluid Dynamics (CFD) has become common to evaluate and optimize fluid systems as well as guide/supplement experimental investigation. A multiphase interaction can be simulated by coupling a CFD solver and a model for the particulate-phase. Similar to the many different flavors of CFD, many different particle models exist. The choice of model largely depends on a desired level of fidelity, particle concentration level, and computational resource requirements. The highest fidelity approach is the resolved-surface method. In this approach the particle surface

is resolved as part of the CFD solution; identical to standard CFD application work where the surface is represented discretely as a boundary of the solution domain. While this approach provides the highest level of accuracy, it becomes intractable when there are many particles due to grid resolution requirements (not to mention the complexity of moving and updating many overset meshes). Thus, lower-order models are typically sought that define the surface-forces acting on a particle based on samples of the surrounding fluid properties. These models may be implemented in Eulerian or Lagrangian frameworks and may consider the transfer of mass, momentum, and energy between the phases. While the Eulerian approach is good for modeling the motion of many particles and makes phase-coupling (e.g. for momentum transfer) simpler, the Lagrangian approach is chosen herein because we are only concerned with one-way coupling effects. Furthermore, we wish to incorporate wall reflection dynamics which cannot be handled robustly with Eulerian methods. In the Lagrangian approach, an equation of motion is solved for each particle which is tracked and its velocity and position are updated as it passes through the computational domain (and does not necessarily coincide with the solution points of the continuous-phase simulation).

In the present Lagrangian framework, the surface forces acting on the particle are typically decomposed as a combination of several independent forces (e.g. quasi-steady drag force, lift force, forces due to fluid acceleration and the hydrostatic pressure gradient, added mass forces, and unsteady drag forces). The relevance of these various forces is dependent on several factors, the most important of which is the particle-to-fluid density ratio (denoted herein by ψ). For large values of ψ (i.e. particles much denser than the surrounding fluid) the surface forces can be typically limited to drag and lift while for small ψ (e.g. air bubbles in water) other more complex forces become important including added mass, fluid stress, and history forces. Many of these additional forces are not as well understood–especially in the context of finite particle Reynolds numbers. Thus, a better understanding of these forces is needed and is especially important for accurate simulation of low-density particles.

To address the above concerns, the present study seeks to formulate an equation of motion appropriate for finite-sized particles at finite Reynolds numbers. This equation of motion must be efficient such that it can be used to simulate thousands of particles interacting with a fluid. To this end, a survey of existing surface-force descriptions is conducted and a new formulation is proposed which is both accurate and efficient. This new equation of motion is then applied to the simulation of low-density particles in a turbulent boundary layer. The effect of each surface-force is described in the context of its relative effect on particle motion and Lagrangian statistics to identify which

forces are more/less important. Following the force component study, the new equation of motion is then used in its full finite-Reynolds number/finite-size form to investigate the motion of both bubbles and sand particles of various diameters exposed to the turbulent boundary layer. Wall-collision statistics, particle concentration statistics, and Lagrangian metrics collected along the particle trajectory are discussed. To aid in understanding the influence low-density ratio on these statistics, an accompanying study of heavy-particles was conducted with similar flow conditions and a range of inertia parameters.

1.2 Previous studies and unique features of the present work

Before reviewing previous studies some basic particle parameters are introduced to define key physical quantities and dimensionless numbers. These include the Reynolds number, the terminal Reynolds number, and the particle-to-fluid density ratio. Herein, Re_p is referred to as the particle Reynolds number and is based on the magnitude of the particle-to-fluid relative velocity, $Re_{p,term}$ is the particle Reynolds number based on the particle's terminal velocity, and ψ is the density ratio:

$$Re_p \equiv \frac{\|\vec{V}_{rel}\| d_p}{\nu_f}, \quad Re_{p,term} \equiv \frac{V_{term} d_p}{\nu_f}, \quad \psi = \frac{\rho_p}{\rho_f}$$

where ν_f is the fluid kinematic viscosity, ρ_p is the particle density, ρ_f is the fluid density, and $\vec{V}_{rel} \equiv \vec{V}_p - \vec{V}_f$ (where $\vec{V}_p$ is the particle velocity vector and $\vec{V}_f$ is the fluid velocity vector) whose magnitude is equal to V_{term} is quiescent conditions.

1.2.1 Previous descriptions for particle surface-forces

Two particularly important theoretical particle equations of motion are the Maxey-Riley equation [21] for creeping irrotational flow and the Auton-Hunt-Prud'homme equation [22] for inviscid rotational flow. These two equations often serve as baseline equations of motion to which additional effects are incorporated. While these equations will be discussed in detail during the course of formulating the present equation of motion, they are briefly described here for the sake of completeness.

The Maxey-Riley equation assumes a non-rotating, rigid, spherical particle of constant diameter in an unsteady, non-uniform incompressible flow with weak spatial gradients and is limited to

creeping flow conditions with respect to the particle relative velocity. Given these conditions, the effect of linear variation of the flowfield was found to be negligible and therefore no lift force is included by Maxey & Riley. However, the curvature of the velocity field was shown to contribute to the surface forces–this correction, which is typically neglected, gives rise to the higher-order drag corrections often referred to as "Faxen terms". The remaining terms obtained by Maxey-Riley represent added mass forces and effects associated with pressure gradients in the continuous-phase.

The Auton-Hunt-Prud'homme equation considers a very different limit: a sphere moving relative to an inviscid fluid such that there are no drag forces (D'Alembert's paradox). The derivation assumes the particle to be fixed, subjected to a far-field linear shear flow, and that the velocity gradient was weak compared to change in relative velocity across the particle. To extend this to unsteady and straining flows, Auton *et al.*[22] additionally assumed that the temporal velocity variation was weak. The resulting derivation gives rise to surface-forces identified as lift, added mass, and pressure gradient effects associated with the continuous-phase.

Most previous investigations have assumed that the particle diameter is sufficiently small to be treated as a "point". In these cases the representative fluid velocity is taken from the location of the particle centroid (in the absence of the particle) and the approach is referred to as a "point-force" model. As particle size increase, this is no longer an accurate assumption. The work of Bagchi & Balachandar [23] has considered this problem and addressed it through spatial averaging of the fluid velocities observed within some distance of the particle center (herein, referred to as a "distributed-force" model). In general, the spatially-averaged values compared reasonably well with the resolved-surface predictions for particle diameters of 1.5 times the Kolmogorov length-scale (λ) and mean Reynolds numbers of 260. For larger particles with $d_p = 9.6\lambda$ and a mean Re_p of 600, the spatially-averaged method yielded poor correlations to the resolved-surface method but did give the correct level of fluctuations while the point-force approach gave large non-physical oscillations. Similar differences were found by Zeng et al. [24]. A study of a clean bubble conducted by Merle et al. [25] for $d_p = 8\lambda$ and a mean Re_p of 500 found that a point-force model tended to overestimate the resolved-surface force fluctuations somewhat while their spatially-averaged expression with tended to underestimate the fluctuations. While these spatially-averaged approaches seem reasonable, they are not generally theoretically consistent with finite-size effects when considered in the limit of creeping flow. Additionally, there has been no theoretically-based method proposed to handle finite size particles at finite Reynolds numbers. This is an issue because many particles fall into this condition.

1.2.2 Uniqueness of present equation of motion

The present study investigates an equation of motion that is appropriate for finite Reynolds number conditions. This involves connecting the creeping flow expression of Maxey-Riley and the inviscid expression of Auton-Hunt-Prud'homme. The resulting equation of motion contains finite Reynolds number expressions for the drag, lift, fluid acceleration, and history forces. Also, a novel efficient history force model (which can greatly reduce CPU requirements) is constructed and applied in the present research . The lift force model used herein incorporates the effect of equilibrium particle spin and is the first study to include this effect.

In light of the promise of the spatial-averaging models used by other researchers, the present study investigates a more rigorous model to accommodate finite size. This new model is intended alleviate the empiricism associated with the current spatially-averaging techniques. The approach taken by this study is to develop a spatially-averaged technique based on theoretical considerations and ensure consistency with previous analysis at the creeping flow limit.

1.2.3 Previous particle studies

In the presence of turbulence, several additional dimensionless parameters are used to categorize a multiphase interaction. The primary parameters that control particle dynamics in a turbulent boundary layer include the drift parameter, the Stokes number (based on either outer-scale or wall-scales), and the Froude number. Herein, the drift parameter, γ, is defined as the ratio of particle terminal velocity (V_{term}) to the wall friction velocity of the fluid (u_τ), the outer Stokes number (St_δ) is the ratio of the particle response time (τ_p) to a large eddy time-scale ($\tau_\delta \equiv \delta/u_\tau$), the inner Stokes number (St^+) is the ratio of τ_p to a wall time-scale ($\tau_f^+ \equiv \nu_f/u_\tau$), and Fr_δ is an outer Froude number relating convection to gravitation and is based on the boundary layer thickness:

$$\gamma \equiv \frac{V_{term}}{u_\tau}, \quad St_\delta \equiv \frac{\tau_p}{\tau_\delta} = \frac{\tau_p}{(\delta/u_\tau)}, \quad St^+ \equiv \frac{\tau_p}{\tau_f^+} = \frac{\tau_p}{(\nu_f/u_\tau^2)}, \quad St_\Lambda \equiv \frac{\tau_p}{\tau_\Lambda}, \quad Fr_\delta \equiv \frac{u_\tau^2}{g\delta}$$

where δ is the reference boundary layer thickness, and g is the magnitude of gravity vector. The fluid's integral time-scale, τ_Λ (to be defined in Section 2), tends to be bounded by τ_δ and τ_f^+ and is used to formulate a third Stokes number which takes into account particle location.

Heavy particle ($\psi \gg 1$) motion and diffusion in homogeneous isotropic turbulence is a function of both inertial effects (measured by Stokes number) and crossing trajectory effects (measured by γ). For short-times ($t < \tau_p$ and $t < \tau_\Lambda$), the influence of inertial effects can greatly reduce diffusion rates. Once long-times ($t \gg \tau_p$ and $t \gg \tau_\Lambda$) are realized previous experimental and numerical studies have shown that γ (via the "crossing trajectory effect") is the main controlling parameter [26, 27]. In particular, the long-time diffusion rate reduces as approximately γ^{-1} for large drift parameters. Preferential concentration of heavy particles in regions of low-vorticity is well-known and caused by a centrifuge-effect as the particles are tossed from the vortex core. Conversely, bubbles are observed to concentrate in regions of high vorticity as their comparatively low-density allows them to be pulled into the vortex. These effects were first discussed by Wang & Maxey [28].

Particle motion in non-homogeneous turbulent flows is more complicated and can result in preferential concentration which are driven by gradients in the fluid turbulence. Kaftori et. al. [29, 30] experimentally studied the motion of nearly neutrally buoyant particles near the wall in the turbulent boundary layer of a horizontal water flume for a range of St^+ from 0.2 to 18. The studies investigated consider the motion, deposition, concentration, and velocity of the particles in the boundary layer. They found that particle velocities were typically less that of the average fluid velocity observed at a given point off the wall due to preferential concentration of particles in low-speed streaks near the wall. Furthermore, the suggested that the particle dynamics were driven by streamwise funnel vortices in the near-wall region. These wall-structures were shown to be responsible for the entrainment and ejection of particles in the near-wall region as well as being important for particle deposition.

As the method does not rely on empirical turbulence models, direct numerical simulation (DNS) has allowed researchers more fundamental insight into the particle dynamics and deposition for pipe and channel flows, where inhomogeneous effects can be strong close to the wall. For example, McLaughlin [31] used DNS to simulate a channel flow in which a dispersed-phase, consisting of rigid spherical particles, was released with an initially random distribution. The study considered a narrow range of Stokes number ($St^+ = 2 - 6$) and particle densities much greater than the density of the fluid (ψ ranging from 713 to infinite) subject to an equation of motion including Stokesian drag and Saffman lift (and neglecting added mass, history force, and particle weight). McLaughlin noticed that the residence time of the particles in the sublayer was enhanced by the inclusion of the Saffman lift force but had negligible effect outside the boundary layer. McLaughlin also noted that while the average particle Reynolds number was $\ll 1$, particle in the viscous sublayer

experienced higher values on the order of 1 where the Saffman lift is no longer appropriate, thus pointing to the need for finite Reynolds number expressions (which he later suggested in [32]).

In a similar study, Brook et. al. [33] considered a DNS test matrix consisting of St^+ values ranging from 3 to 10 with $\psi = 713$ in a vertical channel flow. This study considered an equation of motion with Stokes drag serving as the only surface-force (Saffman lift and particle weight were neglected) and showed that particle deposition was largely related to particle-fluid interactions within the viscous sublayer; primarily with the structures associated with turbulence production. The free-flight deposition theory of Friedlander & Johnstone [34] was shown to be based on reasonable assumptions about the particle velocity within the viscous sublayer. However, Brooke et al [33] found that depositing particles typically did not experience a free-flight to the wall; rather the deposition was brought about by correlated interactions with the fluid. Thus, the free-flight theory was found to be deficient in describing their observed behavior and indicated the need for a better description of particle deposition.

Young & Leeming [16] considered the inconsistencies between deposition observations and deposition predictions by the free-flight model. They reviewed several studies (involving non-homogeneous turbulence) and created a model which describes particle deposition as a function of particle inertia. They identified three regions of deposition rates and classified these regions as (in order of increasing particle inertia) the diffusional deposition regime, the diffusion-impaction regime, and the inertia moderated regime. The diffusion-impaction regime exhibits a dramatic increase in particle deposition caused by the phenomenon of "turbophoresis" (a convective drift of particles down gradients of mean-square fluctuating velocity, leading to the observed wall-peaking behaviors). Young & Leeming's theory was shown to agree well with heavy-particle experiments and simulations and offers improvements over the free-flight theory (illustrating the importance of turbophoresis).

Marchioli and Soldati [35] observed particle simulations (using DNS for the continuous-phase) for an upward flowing channel in an attempt to understand the mechanisms responsible for increasing the particle concentration in the near-wall region. They considered three different sizes of fly ash particles in air ($\psi \approx 770$) such that their St^+ values ranged from 3.8 to 116.3. Initially, the particles in their simulations were released at randomly determined locations and subjected to a perfectly elastic wall boundary condition. An equation of motion consisting of finite Reynolds number drag, gravity, and McLaughlin's extensions [32] to Saffman's lift formulation was

considered (though the lift effect was deemed negligible due to the flow direction). Their study showed that the initially randomly distributed particle concentration moved toward the wall and that the increased near-wall concentration was due to the increased efficiency of sweeps (over ejections) for the test conditions considered. While the study considered several particle diameters, both St^+ and γ were varied simultaneously to give a constant Froude number (consistent with injecting several sizes of particles into the same flowfield, as typically done in experiments). Their findings suggested that the Stokes number may be the more important parameter for the near-wall dynamics (consistent with the model of [16]).

Dorgan et al [36] studied the motion of heavy particles ($\psi \rightarrow \infty$) injected near the wall ($y^+ = 4$) in a turbulent boundary layer. That study focused on the role of inertia (St_δ ranging from 10^{-4} to 10^0) for a fixed and finite drift parameter ($\gamma = 10^{-2}$). The study considered the effects of Stokes drag combined with a terminal velocity directed away from the wall and an elastic wall collision was specified at $y^+ = 1$. The study examined Lagrangian statistics of particle velocity, particle-to-fluid relative velocity, and particle-to-fluid relative velocity fluctuations and found these to be consistent with analytical models. Evidence of turbophoretic influences were obvious as well as preferential concentration in near-wall low-speed streaks. Comparisons of deposition velocity showed good correlations with both previous experimental and numerical studies as well as with the theory of Young & Leeming [16].

1.2.4 Uniqueness of present heavy-particle investigation

There are several unique differences between the above DNS studies and the present work, though it is an extension of the work of [36]. Firstly, most previous DNS studies were for a channel flow while the present simulations consider a spatially growing boundary layer with a comparatively larger Re_τ of 270. Secondly, most previous simulations were conducted at a constant Froude number. While the present study also considers this configuration, it also examines heavy-particle motion at a constant Stokes number for several values of γ (to separate the inertia and drift parameter effects). The latter condition is not easily replicated experimentally–though Wells & Stock [37] used an electromagnetic field to achieve some aspects of this condition. Thirdly, the present research considers the injection of particles near the wall (at $y^+ = 4$), whereas most previous studies start with particle initially distributed uniformly throughout the computational domain, injected at random points in the domain, or injected at the center-line. Fourthly, the

streamwise recycling of particle injections often used in channel flows is not used herein since the flow, and thus particle concentration, is *spatially developing*. Finally, most of the studies focused on wall-interactions while Lagrangian statistics were also studied in the present investigation.

1.2.5 Previous bubble DNS studies

There are only a few previous DNS bubble simulations, to the author's knowledge, and those have focused on understanding the mechanisms which lead to viscous drag reduction over flat plates and channels when microbubbles are introduced to the flow. One such work is that of Xu, Maxey, and Karniadakis [38] who studied the resulting viscous drag in a channel flow as a function of bubble size and loading. Their study treated the bubble-phase using the force coupling method of Maxey et al. [39] which represents the bubble as a finite force monopole which transmits the influence of the bubble to the fluid as a body force. The resulting particle velocity is extracted from the fluid solution by averaging the fluid velocity over the region which the particle occupies. Thus the bubbles and fluid are considered as one system that embodies the surface-force effects of drag, lift, and added mass. This is a different approach to the Lagrangian particle tracking approach presently considered and is more appropriate for two-way coupling of a moderate number of particles (whereas the present study is interested in one-way coupling a very large number of particles to ensure converged Eulerian and Lagrangian statistics).

The work of Elghobashi's research group has focused in the past on understanding the mechanism of viscous drag reduction on flat plates when micro-bubbles are introduced to the flow [40, 41]. Similar to the present study, their work employs an Eulerian description for continuous-phase and a Lagrangian approach for the bubble-phase. The flow is comprised of a spatially-developing boundary layer of $Re_\theta = 1430$ and is effected by the presence of the particles (necessary to ascertain the drag reduction effects). A surface-force description comprised of Stokes drag, buoyancy, added mass, fluid stress (taken from the equation of motion proposed by [21]), and Auton's inviscid lift formulation [22] was used (but history force was neglected) to simulate the motion of spherical bubbles with a diameter $62\mu m$. Bubble-bubble and bubble-wall collisions were ignored and turbulence statistics as well as viscous drag on the flat plate were monitored. They found that the reduction of viscous drag seems to emanate from the bubbles inducing a non-zero divergence of the fluid velocity.

The most similar work to the present investigation is that of Giusti, Lucci, and Soldati [42]. In that investigation, a direct numerical simulation of the flow equations was coupled with a Lagrangian particle tracking algorithm to study upward and downward flow in a channel with $Re_\tau = 150$. The bubbles were assumed to be spherical and have a diameter of $220\mu m$ (1.65 inner units in diameter). Furthermore, the bubble surface was assumed contaminated such that a no-slip condition on the bubble surface is appropriate. An equation of motion consisting of drag, buoyancy, fluid stress, added mass, Basset history, and lift was considered. Note that finite Reynolds number expressions for the drag and lift forces were considered although the creeping flow history force expression of Basset was employed. The study focused on the influence of the lift force on the bubble concentration and the differences due to upward or downward flow direction. The findings confirmed the expectation that lift drives bubbles towards the wall for an upward flow and away from the wall for a downward flow.

1.2.6 Uniqueness of the present low-density particle investigation

The present study is several regards. It is the first study to examine the influence of various surface forces on particle motion using DNS, especially with respect to accelerating effects such as fluid stress and history force. Both creeping flow and finite Reynolds number expressions are considered and it is shown that the Basset force leads to poor predictions in finite Reynolds number flows. This may be cause for concern in previous studies ([42]) where the Basset force is used in admittedly finite Reynolds number conditions.

Secondly, the present study is the first to examine the effect of density ratio on particle motion using DNS, especially with respect to fluid stress and history force. Note that the Armenio & Fiorotto [43] did consider this effect but in the context of creeping flow (with no lift force or gravitational effects) and for larger density ratios ($2.65 < \psi < 2650$). The present study considers the importance of density ratio using a finite Reynolds number equation of motion which includes the lift force and accounts for the particle weight. Additionally, smaller density ratios are considered in the present study ($\psi = 0.001$ and $\psi = 2$).

Thirdly, this work is the first to present a distributed force model (to account for finite particle size) which is theoretically consistent with the expression of Maxey & Riley [21] in the limit of creeping flow and with the expression of Auton, Hunt, Prud'homme [22] in the limit of inviscid

flows. This distributed force model is applied to the simulation of low-density particles with diameters of 10 inner units or less. Note that the previous works discussed above treat the particles as points and do not account for finite diameter.

Fourthly, this is the first study to develop and use a window-based history force model for finite Reynolds numbers. This new model leads to a substantial savings in computational run-time and can give identical predictions to other finite Reynolds number models when used appropriately. Bounds on the validity of the model are created and good performance is shown in a turbulent DNS flowfield.

Finally, the present study is the first to use an equilibrium spin lift model for finite Reynolds numbers. While often neglected, the contribution of particle spin to the lift force can be important. The model proposed by Loth [44] is employed herein and is valid over a much wider range of flow conditions and considerably more accurate than models previously proposed.

1.3 Objectives of the present study

The present study considers multiphase interactions in the context of a spatially-evolving turbulent boundary layer with a particulate-phase that has a rigid, no-slip, spherical surface. The objectives of the present study are four-fold:

1. Construct and implement an appropriate model for finite-Reynolds number and finite-sized particle dynamics.
2. Conduct heavy-particle simulations using a simplified equation of motion and investigate the particle dispersion and wall interaction phenomena.
3. Determine, through simulation, the relative importance of the surface forces and discretization techniques for low-density particles.
4. Apply the new model to several low-density particle conditions and interpret and compare the results to the heavy-particle observations.

The first objective is typically straightforward for heavy-particle ($\psi \gg 1$) simulations as one may only need to consider the effect of quasi-steady drag (and possibly lift depending on the problem of

interest). For low-density particle simulations, one must generally consider all surface-forces as they can be of the same order as (or sometimes larger than) quasi-steady drag. The lift force is perhaps the most difficult to model. Many models exist in the literature and are shown to have limited applicability. The present work uses the form proposed by [44] which shows much greater robustness compared to other models. The unsteady drag or "history" force typically gives rise to computational concerns as its evaluation involves an integral over the particle's entire lifetime. A new, efficient, approach is described herein and shown to greatly reduce the required run-time associated with history force models. The extension to account for finite particle size is accomplished through theoretical analysis (where possible) and a discrete formulation is proposed which is consistent with the Faxen terms at creeping flow conditions. The formulation of the equation of motion is the topic of the first three sections of Chapter 3.

The second portion of Chapter 3 considers the discrete representation of the particle equation of motion. Evaluating the surface-forces requires derivatives of the continuous-phase velocity as well as inter-cell interpolation of the continuous-phase properties. Approaches for obtaining these terms are discussed and the results of Chapter 5 will quantify the effect of using these different techniques. The finite-size aspect of the new model also requires evaluation of surface and volume integrals. The chosen discrete forms are shown to be fourth-order accurate in space compared to current models which are generally only first-order correct. Computational resource requirements are also considered with the hope of guiding future studies which may benefit from reduced-fidelity modeling (where appropriate) resulting in substantial CPU-time savings.

Chapter 4 presents heavy-particle results obtained using a simplified equation of motion where only Stokes drag and the body force are included. This reduced formulation results in a de-coupled set of partial differential equations for the three Cartesian directions and simplifies interpretation of the results. This study displays interesting physics and led to the creation of theoretical models to describe the observed behavior.

Chapter 5 presents a study of the relative importance of the various surface forces. This investigation considers an air bubble in water and a sand particle in water and applies several equations of motion to determine the effect of the forces on output quantities of interest (e.g. concentration profiles and Lagrangian statistics). The first equation of motion considers only the quasi-steady drag force. Subsequent equations add additional surface-forces terminating with an equation including quasi-steady drag, added mass, stress gradient, lift, and history surface-forces.

The intent of this study is to identify which forces are most important to the prediction of particle motion.

Chapter 6 presents an application of the proposed equation of motion to several low-density conditions of finite Reynolds number and finite size. The results of this study show that while many of the trends observed for the heavy-particles hold true at lower density-ratios, some new effects emerge that are not intuitive based on heavy-particle expectations. Surprisingly, the theoretical models developed in the context of heavy-particles to describe relative velocity behavior and particle deposition are shown to agree well with the low-density results.

Chapter 2

Continuous-phase simulation

2.1 Governing equations

The continuous-phase for the present study is assumed to be an Newtonian fluid with mean-free path much smaller than the size of the particulate phase. Thus, the governing equations are derived from statements of conservation of mass and linear momentum assuming the fluid can be represented as a continuum. Specializing the continuity equation for an incompressible fluid (incompressible meaning that the fluid's density is not a function of the pressure applied to the fluid), one obtains a constraint on the velocity field which requires it to be divergence-free, i.e.

$$\nabla \cdot \vec{V}_f = 0 \tag{2.1}$$

where $\vec{V}_f$ is the fluid velocity vector. Conservation of momentum is embodied by the well-known Navier-Stokes equations, which can be expressed as

$$\frac{\partial \vec{V}_f}{\partial t} + \vec{V}_f \cdot \nabla \vec{V}_f = -\frac{1}{\rho_f} \nabla p + \nu \nabla^2 \vec{V}_f + \vec{F} \tag{2.2}$$

where t represents time, ρ_f is the fluid density, p is pressure, ν is the fluid's kinematic viscosity, and $\vec{F}$ represents any additional external forces exerted on the fluid (e.g. body forces appearing when the fluid is subjected to gravitational or electromagnetic field and the forces exerted on the fluid by a set of particles immersed in it). For the present study, $\vec{F}$ is chosen to be zero such that it is assumed the continuous-phase is *unaffected* by the presence of the dispersed-phase. This choice is made as the present study seeks to understand the complexities of surface-force influence on particle motion without the additional complication of coupling the particle momentum back to the fluid. A more detailed discussion of this assumption is given at the beginning of Chapter 3.

2.2 Numerical technique

The solution of the governing equations is obtained by direct numerical simulation (DNS) in which the turbulent scales, down to the Kolmogorov scale, are fully resolved (i.e. no modeling of the turbulent features is required). This DNS code was developed some years ago (see [45, 46]) and has since passed through the hands of several researchers, including P.K. Yeung who provided his version in FORTRAN and restart files for the Reynolds number used in this study. Presently, the DNS code simulates an incompressible, three-dimensional, spatially developing turbulent boundary layer with zero streamwise pressure gradient. Note that Spalart & Watmuff [46] devised a way to include a pressure gradient but those terms are not used herein. The solution domain is semi-infinite over a flat, smooth surface with $0 \leq x \leq L_x$, $0 \leq y < \infty$, and $0 \leq z \leq L$, where x, y, and z represent the streamwise, spanwise, and transverse (or wall-normal) directions, respectively. The streamwise and spanwise directions are treated as periodic and Λ_x, Λ_z represent the length of one period in the streamwise and spanwise directions, respectively. Obviously, the streamwise direction is physically non-periodic and some numerical tricks (described later) are required to make it behave as such. The domain is discretized by 256 nodes in the stream direction, 96 in the span direction, and 55 in the transverse direction for a total of 1,351,680 nodes in the three-dimensional mesh.

The simulation uses a pseudo-spectral method (the ground-work of which was laid by Orszag & Patterson [47] and Rogallo [48]) with Fourier decomposition in the spanwise and streamwise directions while Jacobi polynomials are used in the wall-normal direction [45]. The solution is periodic in the spanwise direction and readily admits the application of a Fourier basis. However, the spatially-evolving aspect of a boundary layer (manifested as a every increasing boundary layer thickness in the streamwise extent) does not present a periodic problem in the streamwise direction. A novel approach was used by [49] whereby a "fringe" velocity is added to the fluid solution near the physical ends of the streamwise domain and forces that direction to appear periodic. Effectively, this fringe velocity subtracts out a portion of the vertical velocity in order to thin the boundary layer and remove the effect of spatial growth across the domain, thus allowing the outflow conditions to be recycled to the inflow [46] and providing a periodic problem. The wall-normal direction is inherently inhomogeneous and thus is expanded as a set of Jacobi polynomials. By using fast transform algorithms, the pseudo-spectral method can efficiently transfer the relevant variables between physical-space (where the non-linear terms can be

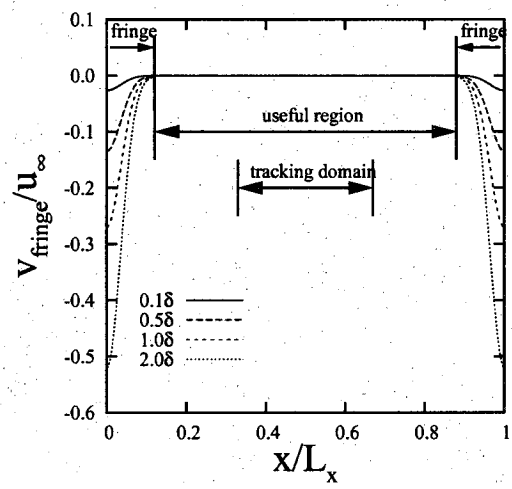

Figure 2.1: Fringe velocities and extent of statistically useful region.

efficiently evaluated) and wave-space (where differentiation is efficient) and provides a solution algorithm with superior accuracy.

The process of forcing the streamwise direction to fit the periodic boundary condition comes at a cost: a section of the domain (i.e. the "fringe") is left unusable as the DNS code is no longer solving the Navier-Stokes equations in these regions (due to the addition of the fringe velocity). Spalart & Watmuff [46] discuss and evaluate the implications of the fringe on the remainder of the flowfield (i.e. the "useful region") and note that there were no unacceptable effects. The the fringe velocity is defined by

$$v_{fringe} = -Sy[1 - \exp(-y/y_1)]G(x) \tag{2.3}$$

$$G(x) = \exp\left(-\left[\frac{x}{x_1}\right]^2\right) + \exp\left(-\left[\frac{x - \Lambda_x}{x_1}\right]^2\right) \tag{2.4}$$

where the function $G(x)$ controls the streamwise extent of the fringe and x_1, y_1, and S are constants which can be modified to control the fringe and inflow thickness of the boundary layer [46]. The fringe velocities used in the current study are shown in Figure 2.1 for several y-locations over the entire streamwise extent and the "fringe" and "useful" regions are indicated. For this choice of fringe values, the fringe occupies 12.5% of each end of the domain such that $3L_x/40 < x < 37L_x/40$ can be considered the statistically useful region.

The present study defines a subset of the useful region for the purpose of injecting and tracking

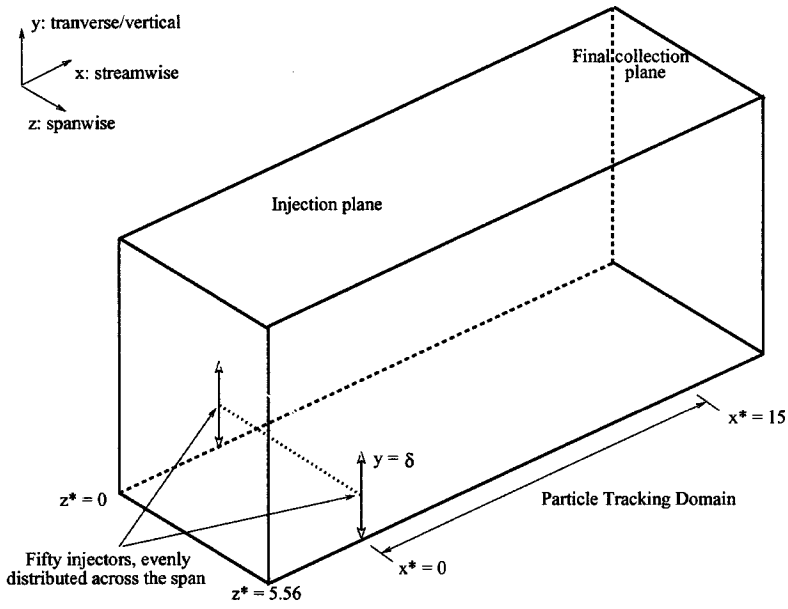

Figure 2.2: Illustration of the particle tracking domain.

particles. This sub-domain is indicated on Figure 2.1 to illustrate its position relative to the fringe. Furthermore, Figure 2.2 presents a cartoon of the three-dimensional particle tracking domain and describes it in terms of the below non-dimensional coordinates:

$$\begin{aligned} x^* &= (x - L_x/3)/\delta \\ y^* &= y/\delta \\ z^* &= z/\delta \end{aligned} \tag{2.5}$$

where δ is the mean boundary layer thickness at $x^* = 0$.

The equations are advanced in time through a low-storage, three-stage, hybrid implicit-explicit scheme for second-order accuracy in time [45]. For each time-step, the DNS code computes a value for Δt based on a user-specified CFL number. This process is designed to generate large, but stable, time-steps and is entirely suitable for the continuous-phase simulation. However, it was found that stable integration of low-inertia particle trajectories typically required a time-step which was smaller. For simplicity, it is desirable to use the same time-step in both the continuous and dispersed-phase integrations. As such, a maximum time-step was set to a constant value of

$0.286\tau_f^+$, where τ_f^+ is an inner-layer time-scale defined by

$$\tau_f^+ \equiv \frac{\nu}{u_\tau^2} \tag{2.6}$$

but smaller values were allowed such that the continuous-phase solution always remained at or below the specified CFL number. The undefined symbol in Equation 2.6, u_τ, represents boundary layer friction velocity ($\equiv V_\infty\sqrt{C_f/2}$, where V_∞ is the freestream edge velocity of the boundary layer and C_f is the local skin friction coefficient) respectively. In practice, the maximum time-step of $0.286\tau_f^+$ was used for the majority of time-steps and smaller values were rarely encountered.

Eulerian time-averaged/spanwise-averaged statistics of selected fluid properties are shown in Figures 2.3-2.4. The Eulerian-averaged properties in these figures are denoted by $[\ldots]$ and represent averaging over a period of the spanwise domain and a time of about $10\tau_\delta$ for each transverse nodal location at $x = L_x/3$, where

$$\tau_\delta \equiv \frac{\delta}{u_\tau} \tag{2.7}$$

is a time-scale associated with the motion of the largest eddies in the boundary layer. Figure 2.3 shows the streamwise velocity in the boundary layer (in inner units) as compared to the conventional high-Reynolds number curve fits for the linear and log-layers. Herein, the conventional definition for the inner units is employed such that

$$u^+ \equiv \frac{u}{u_\tau} \tag{2.8}$$

$$y^+ \equiv \frac{yu_\tau}{\nu} \tag{2.9}$$

where we observe that the non-dimensional inner length-scale, y^+, is a Reynolds number based on distance from the wall and u_τ. In Figure 2.3 it can be observed that the edge of the boundary layer is at $y^+ = 270$ which serves as the serves as our reference Reynolds number for the fluid simulation, i.e. $Re_\tau = 270$, where

$$Re_\tau \equiv y^+|_{y=\delta} = \frac{\delta u_\tau}{\nu} \tag{2.10}$$

Figures 2.4a and 2.4b show the turbulent kinetic energy and dissipation rate as a function of y^+ and illustrate the expected behavior including a peak kinetic energy at about $y^+ = 10$ and nearly uniform dissipation close to the wall followed by a rapid decrease in the (nearly inviscid) outer

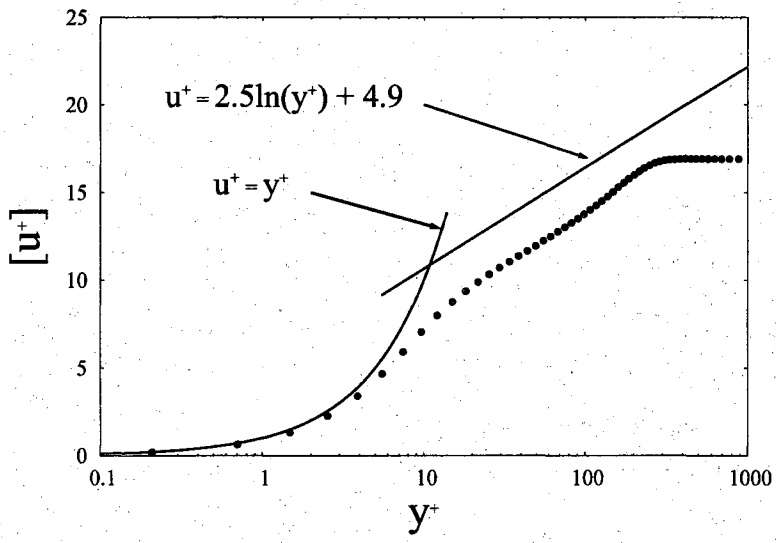

Figure 2.3: Mean velocity profile at $\Lambda_x/3$.

layer. Note that the kinetic energy and dissipation rate are defined as

$$k = \frac{1}{2}\left([u'u'] + [v'v'] + [w'w']\right) \tag{2.11}$$

$$\epsilon = 2\nu\,[S_{ij}S_{ij}] \tag{2.12}$$

where S_{ij} is the strain rate tensor and the components which form k are the diagonal entries of the Reynolds stress tensor. These diagonal components are shown in Figure 2.5 where it should be noted that $[u'u']$ is the largest component followed by $[w'w']$ while $[v'v']$ is the smallest. These results are qualitatively consistent with results of [49] which shows results from a DNS of a turbulent boundary layer at a different Reynolds number.

The evolution of the mean boundary layer thickness is shown in Figure 2.6 as a function of streamwise position (and confined to the vicinity of the particle tracking domain). While there are subtle wiggles in the mean boundary layer thickness (which would disappear with further temporal averaging) the growth of the boundary layer is consistent with canonical turbulent boundary layer correlations, e.g.

$$\delta = \frac{0.16x}{(Re_x)^{1/7}} \tag{2.13}$$

Since the boundary layer thickness is non-zero at the $x = 0$ (due to the re-cycling of the flowfield from the outflow) an offset was added to x-coordinate to generate the curve shown in Figure 2.6.

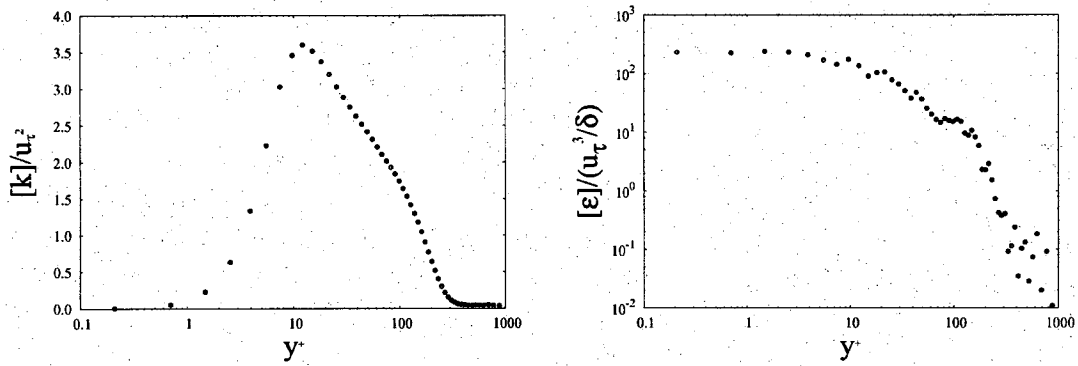

a) Turbulent kinetic energy b) Rate of dissipation

Figure 2.4: Turbulence properties at $\Lambda_x/3$

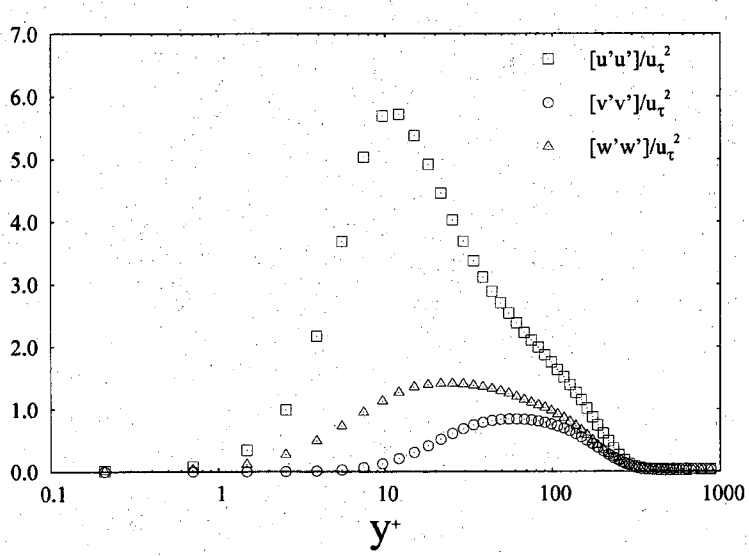

Figure 2.5: Mean Reynolds stresses observed at $\Lambda_x/3$

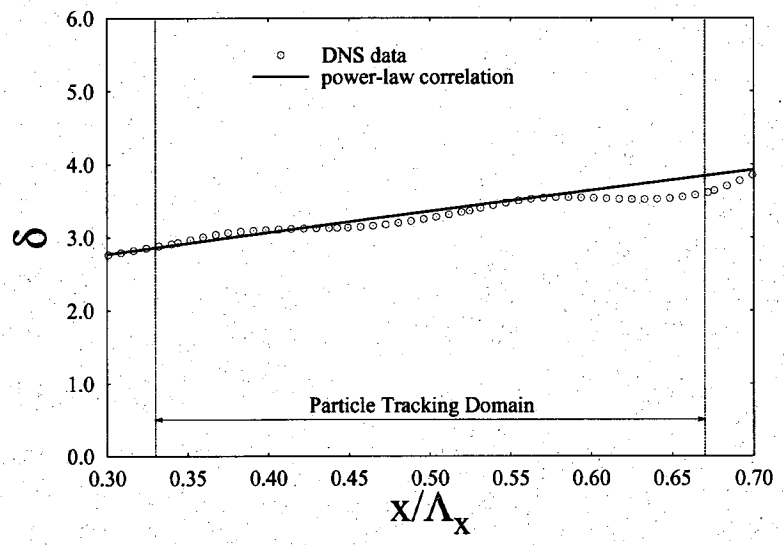

Figure 2.6: Mean boundary layer thickness across the particle tracking domain.

Finally, we consider the integral Lagrangian time-scale of the fluid as a function of vertical position for the streamwise location $\Lambda_x/3$. The integral time-scale for the streamwise velocity component ($\tau_{\Lambda,u}$) is defined by the decorrelation of the streamwise velocity fluctuations, $u_f^{'}$,

$$\tau_{\Lambda,u}(y) = \int_0^\infty \frac{\left\langle u_f^{'}(y,t) u_f^{'}(y,t+\tau) \right\rangle}{\left\langle u_f^{'}(y,t)^2 \right\rangle} d\tau \tag{2.14}$$

where

$$u_f^{'}(x,y,z,t) \equiv u_f(x,y,z,t) - [u_f(x,y)] \tag{2.15}$$

and where $\langle ... \rangle$ denotes a Lagrangian average taken. Several DNS runs were conducted to find the above Lagrangian decorrelation for a fluid tracer injected at various transverse locations. In addition to the streamwise integral time-scale, $\tau_{\Lambda,v}$ and $\tau_{\Lambda,w}$ were obtained for the transverse and spanwise directions, respectively, and all three are shown in Figure 2.7 . To define a single representative integral time-scale for the fluid, these three time-scales were averaged together (shown as the solid line in Figure 2.7) following the approach of [50]. This average time-scale (denoted τ_Λ) will be shown later to be of importance in predicting the relative importance of inertial effects concerning particles and bubbles.

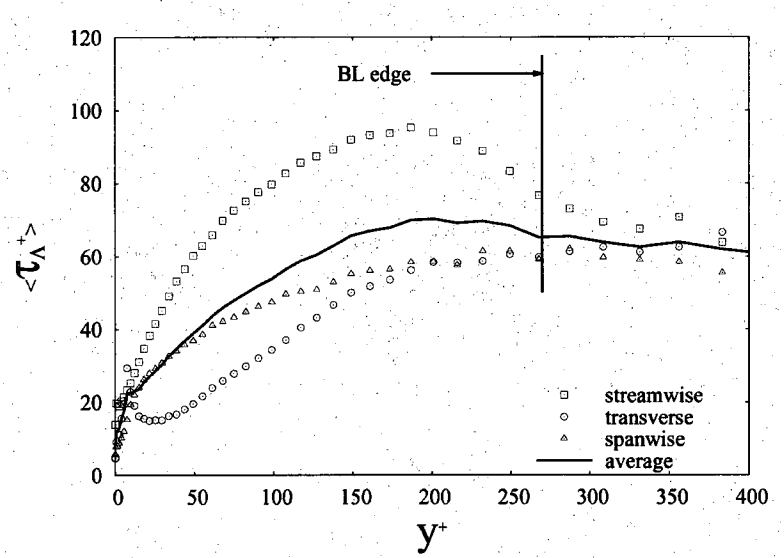

Figure 2.7: Integral Lagrangian time-scales observed at $\Lambda_x/3$

Chapter 3

Particulate-phase simulation

Multiphase interactions are sometimes categorized based on particle mass/volume fraction. Small volume fractions result in isolated particles which are driven by the motion of the undisturbed flow. Not surprisingly, as the concentration of particles increases, the physics of the interaction become more complicated such that the influence of the particle's presence begins to have a significant effect on the continuous-phase. Further increase in particle concentration leads to the importance of particle-particle interactions. These regimes may be grouped into four phase-coupling categories:

- "one-way": particle-phase motion affected by the continuous-phase; particles have negligible influence on continuous-phase
- "two-way": particle-phase also affects the continuous-phase through fluid coupling
- "three-way": flow disturbances caused by particles affect the motion of nearby particles
- "four-way": contact collisions also influence the overall particle motion

The first three regimes include only fluid dynamic interactions, whereas the fourth regime includes particle collisions. These regimes occur in many practical multiphase flows. An example of one-way coupling is the drag of a particle, which is caused by fluid dynamic forces acting on the particle's surface. An example of two-way coupling is the upward momentum of a liquid induced by a bubble rising in a plume. Three-way coupling is important when a particle is drafting behind another particle. Small rain drops colliding and coalescing to form larger rain drops is an example of four-way coupling. Particle collisions may also become important in regions of locally high particle concentration which can arise through preferential concentration, a bias associated with particles existing in particular flow structures. This does not fit the assumption stated above which claims four-way coupling is important for high volume fractions. Later results will give evidence that this may be important for low-density particles in a boundary layer where the overall volume

fraction is small but local high concentrations are observed. So long as fluid dynamic forces dominate the particle movement, these are all considered dispersed flow regimes (in contrast to "dense" flows where particle-particle interactions are the dominant physics).

The modeling complexity associated with the coupling regimes increases as more effects are included. For efficiency's sake, one would like to employ the simplest appropriate model for a given multiphase interaction. In the context of momentum coupling, Crowe et al. [51] defines a "momentum coupling parameter" as the ratio of the drag force induced by the particulate-phase to the bulk momentum flux of the continuous-phase,

$$\Pi = \frac{F_D}{M_f} \tag{3.1}$$

where Π is the momentum coupling parameter, F_D is the drag force acting on the particles, and M_f is the flux of fluid momentum through the domain. As $\Pi \to 0$, the effect of two-way coupling is unimportant. Crowe et al. [51] shows that this expression can be recast in terms of a particle Stokes number (a ratio of the time-scale associated with momentum transfer between the phases to a time-scale appropriate to the momentum flux through the domain) as

$$\Pi = \frac{C}{1+St} \tag{3.2}$$

where C is a measure of the concentration of particles in the fluid and the Stokes number is defined as

$$St = \frac{\tau_p U}{L} \tag{3.3}$$

and where U is a relevant fluid velocity scale, L is a characteristic dimension of the domain, and τ_p is the particle "response-time" which is left to be defined in the following sections. Based on Eq. 3.2 we see that low concentrations or large Stokes numbers lead to small values of Π indicating that the effects of two-way coupling can be neglected.

While the present simulation considers generally small Stokes numbers, it is assumed that the instantaneous particle concentration is sufficiently small such that a one-way coupled approach is appropriate. While this places some limits on the physical analog to the present numerical study, it is largely unimportant in the context of simulation. The present study chooses to inject a given number of particles over a fixed set of time. In some cases this can lead to excessively high local concentrations. Experimentally, this could be resolved by injecting the particles over a longer

period of time such that the concentrations remained dilute (i.e. $C \rightarrow 0$). To match the experiment numerically would require extending an already expensive simulation. However, if one assumes the particle field to be dilute and neglects two-way coupling, the numerical simulation may be conducted over any segment of time provided the results are statistically stationary. This approach is taken this study to reduce the total simulation time.

In the below sections, the particle equation of motion appropriate for dilute concentrations of particles is discussed where particular attention is paid to the effects of finite particle size and finite particle Reynolds number. A discussion of numerical techniques employed in solving the particle equation of motion is given in the final section.

3.1 Surface force decomposition

The dynamic motion of a particle is described by equating the product of mass and acceleration with the sum of the external forces acting on the particle, e.g.

$$m_p \frac{d\vec{V}_p}{dt} = \vec{F}_{surf} + \vec{F}_g \tag{3.4}$$

where m_p is the particle mass, $\vec{V}_p$ is the three-dimensional particle velocity, $\vec{F}_{surf}$ is the net force induced by pressure and shear stresses imposed by the continuous phase on the particle surface, and $\vec{F}_g$ is the particle body force induced by the gravitational field. For a particle of homogeneous density, the mass and body force can be written in terms of the particle volume, $\forall_p$, such that $m_p = \rho_p \forall_p$ and $\vec{F}_g = \rho_p \forall_p \vec{g}$ where ρ_p is the particle density and $\vec{g}$ is the gravity vector. While these expressions are simple to employ in a multiphase calculation, $\vec{F}_{surf}$ has been the subject of much research and must be handled carefully to properly model a multiphase interaction.

One possible approach for obtaining $\vec{F}_{surf}$ in multiphase calculations is to explicitly model the physical problem and immerse the particle (with its true size and shape) in the continuous-phase flowfield. In this way, the flowfield around the particle is resolved as part of the continuous-phase simulation and the net pressure and shear stresses can be directly computed and applied in the particle's equation of motion. This technique may be referred to as a "resolved-surface simulation" and is identical to the process that is applied when predicting loads on a wing or aircraft using computational fluid dynamics. The resolved-surface simulation has the advantage of tightly

coupling the particle and continuum motion, as well as the interplay of momentum transfer. However, it is only feasible when a small number of particles are to be modeled. This is due to the computational requirements associated with the grid resolution needed to resolve each particle's boundary layer and wake. Additionally, using the resolved surface simulation for a many particle study introduces great complexity in the continuous-phase solver with the introduction of many overset meshes which may interact. Therefore, in simulating a large number of particles, a decomposition approach is typically employed to generate $\vec{F}_{surf}$ which attempts to model the surface force based on fluid properties in the vicinity of the particle's location. This approach in usually referred to as the "point-force" approximation.

In its conventional construction, the point-force approximation assumes the particle is sufficiently small compared to the local length scale of the fluid structures such that it is reasonable to use the continuous-phase properties at a single point in space (corresponding to particle center of mass) to describe the force on the particle. In particular, $\vec{F}_{surf}$ can be represented as a linear combination of specific independent forces such that,

$$\vec{F}_{surf} = \vec{F}_D + \vec{F}_L + \vec{F}_{AM} + \vec{F}_{SG} + \vec{F}_H \tag{3.5}$$

where $\vec{F}_D$ is the quasi-steady-state drag force, $\vec{F}_L$ is the lift force generated by rotation of the particle and fluid shear, $\vec{F}_{AM}$ is the so-called added, or virtual, mass force which accounts for the work required to change the momentum of the surrounding fluid as the particle accelerates, $\vec{F}_{SG}$ is the fluid stress gradient force which accounts for forces that would exist in the absence of the particle due to acceleration of the continuum and the hydrostatic pressure gradient, and finally, $\vec{F}_H$ is the unsteady-drag force or "history" force which accounts for the temporal development of the viscous region in the vicinity of the particle. While the quasi-steady drag is typically the dominant surface force for particles with large density ratio (i.e. large ψ where $\psi = \rho_p/\rho_f$ and where ρ_f is the fluid density) this is not the case for moderate to low-density ratio particles where all of the forces are generally important. It should be noted that this linear decomposition of the forces is assumed to be valid but is not necessarily robust (when compared to resolved-surface simulations) as there can be non-linear interactions between the various force. However, these interactions are not well understood and typically small enough to be neglected for many conditions which is assumed to be the case in the present study.

The description of $\vec{F}_{surf}$ as a summation of distinct forces is generally empirical except for some

limiting cases which permit a fully theoretical solution for a spherical particle. These solutions are often related to the continuous-phase properties extrapolated to the particle centroid ($\vec{x}_p$), in the absence of the particle's influence; an assumption appropriate when particle length-scales are much smaller than flow gradient length-scales. In this situation, the particle Reynolds number can be defined as

$$Re_p = \frac{d_p \|\vec{V}_{rel}\|}{\nu} \tag{3.6}$$

$$\vec{V}_{rel} = \vec{V}_p - \vec{V}_{f,@p} \tag{3.7}$$

where d_p is the particle diameter which is related to its volume by $d_p = \sqrt[3]{6\forall_p/\pi}$. Additionally, $\vec{V}_f$ represents the fluid velocity and the subscript $_{@p}$ implies the fluid velocity is at $\vec{x} = \vec{x}_p$. There are many such analytical solutions (starting from the seminal work of Stokes in 1851 [52]) which generally assume *a)*inviscid flow conditions ($\nu = 0$) or *b)*creeping flow conditions ($Re_p \to 0$).

Two particularly important theoretical particle equations of motion are the Maxey-Riley (MR) equation for creeping irrotational flow and the Auton-Hunt-Prud'homme (AHP) equation for inviscid rotational flow. These two equations often serve as baseline equations of motion to which additional effects are incorporated.

3.1.1 Maxey-Riley (MR) point-force expression

The Maxey-Riley equation [21] assumes a non-rotating, rigid, spherical particle of constant diameter in an unsteady, non-uniform incompressible flow with weak spatial gradients and is

limited to $Re_p \ll 1$. The resulting derivation yields a decomposition of surfaces forces given by:

$$\vec{F}_D = -3\pi\mu d_p \vec{W} \tag{3.8}$$

$$\vec{F}_{SG} = \rho_f \forall_p \left(\frac{D\vec{V}_{f,@p}}{Dt} - \vec{g} \right) \tag{3.9}$$

$$\vec{F}_{AM} = -\rho_f \forall_p C_M \frac{d}{dt} \left(\vec{V}_{rel} - \frac{d_p^2}{40} \nabla^2 \vec{V}_{f,@p} \right) \tag{3.10}$$

$$\vec{F_H} = -3\pi\mu d_p \left[\int_0^t K(\tau) \frac{d\vec{W}}{d\tau} d\tau + K(0)\vec{W}(0) \right] \tag{3.11}$$

$$\vec{W} = \vec{V}_{rel} - \frac{d_p^2}{24} \nabla^2 \vec{V}_{f,@p} \tag{3.12}$$

$$K = \left[\frac{d_p^2}{4\pi\nu(t-\tau)} \right]^{1/2} \tag{3.13}$$

where μ is the fluid's molecular viscosity and is related to the kinematic viscosity by $\mu \equiv \rho_f \nu$. The original Maxey-Riley derivation assumed $\vec{W}$ is zero at $t = 0$, but the contribution for finite $\vec{W}(0)$ has been included here based on later work by Maxey [53]. At creeping conditions, the effect of linear variation of the flowfield was found to be negligible (hence no lift force due to fluid shear) but curvature of the velocity field does contribute to the surface forces. The corrections associated with this curvature (the ∇^2 terms) are often called Faxen terms, since Faxen [54] was first to obtain such contributions.

3.1.2 Auton-Hunt-Prud'homme (AHP) point-force expression

Auton [55] and Auton *et al.*[22] considered a much different limit for the continuous-phase: a sphere moving relative to an inviscid fluid such that $\vec{F}_D = \vec{F}_H = \vec{0}$. These studies assumed that the particle was fixed, subjected to a far-field linear shear flow, and that the spatial velocity gradient was weak compared to change in relative velocity across the particle. To extend this to unsteady and straining flows, Auton *et al.*[22] additionally assumed that the temporal velocity variation was weak.

Auton's derivation leads to the following surface forces

$$\vec{F}_{SG} = \rho_f \forall_p \left(\frac{D\vec{V}_{f,@p}}{Dt} - \vec{g} \right) \tag{3.14}$$

$$\vec{F}_{AM} = \frac{\rho_f \forall_p}{2} \left(\frac{D\vec{V}_{f,@p}}{Dt} - \frac{d\vec{V}_p}{dt} \right) \tag{3.15}$$

$$\vec{F}_L = \frac{1}{2} \rho_f \forall_p C_L \left(\vec{V}_{rel} \times \vec{\omega}_{shear} \right) \tag{3.16}$$

where $\vec{\omega}_{shear} = \vec{V}_{rel}/d_p$. Note the different derivatives in Eq. 3.15: D/Dt denotes derivatives taken along the fluid path, and d/dt denotes a derivative along the particle path.

It is interesting to compare the AHP equation to the Maxey-Riley equation. We first note that the fluid stress is the same in both cases, so that one may expect it to be generally applicable for spherical particles. The added mass terms are slightly different between Eq. 3.10 and 3.15, though Maxey [53] noted that the differences are negligible. For finite Re_p conditions with spherical particles, there have been several experimental and numerical studies [56, 57, 13, 58, 59, 60, 61] which have investigated the added mass force. These studies all showed that that the AHP expression for the added mass force is remarkably reasonable for a wide variety of Re_p values for both solid and fluid particles. They also demonstrated that the empirical (and often used) form proposed by Odar & Hamilton [62] is incorrect, due to their incorrect interpretation of the history forces.

3.2 Surface forces for particles at arbitrary Reynolds numbers

In this section, surface forces appropriate for the simulation of particles at arbitrary Reynolds number are developed and discussed. The intent of this section is to "bridge the gap" between the Maxey-Riley equation for creeping flow conditions and the Auton-Hunt-Prud'homme equation for inviscid conditions. As noted in the discussion above, the added mass and fluid stress forces given by Eqs. 3.14 & 3.15 are generally accepted for a wide range of Reynolds numbers within the point-force limitations [13, 61]. The quasi-steady drag force can also be given with a commonly accepted form and is discussed in Section 3.2.1. Expressions for the torque-free lift and history force at finite Reynolds numbers are also put forth in Sections 3.2.3 and 3.2.2. While the

quasi-steady drag and lift sections provides reviews of existing approaches, the history force section details a method and contributions created as part of this study. Note that a spherical no-slip surface is assumed which is reasonable for solid particles and contaminated bubbles so long as the combination of Reynolds number and Weber number is moderate [44].

3.2.1 Quasi-steady drag force

The quasi-steady drag force ($\vec{F_D}$ in Eq. 3.5) arises from the pressure and viscous stresses applied to the particle surface when the particle is subjected to a constant, spatially uniform fluid velocity. The drag force resists relative velocity and is therefore defined to act in the direction opposite of the particle relative velocity, e.g.

$$\vec{F_D} = -\frac{1}{2}\rho_f \|\vec{V}_{rel}\| \vec{V}_{rel} A_p C_D \tag{3.17}$$

where A_p is the projected area of the particle with value $\pi d_p^2/4$ for a sphere, and C_D is the particle drag coefficient which is a function of particle Reynolds number. Stokes [52] derived the analytical solution for the flowfield around an isolated sphere in an unbounded domain for the case creeping flow ($Re_p \ll 1$) in which the non-linear inertial terms of the Navier-Stokes equations are negligible. In this regime the flow over the sphere's surface is fully attached and laminar as shown in Fig. 3.1a and the drag coefficient is given by

$$C_D = \frac{24}{Re_p} \tag{3.18}$$

Neglecting the effects of flowfield non-uniformity, this is the same form used in the Maxey-Riley equation (Eq. 3.8). Since this is a result of Stokes's solution for flow around a sphere it is sometimes referred to as the "Stokesian drag law". While this form is strictly valid for $Re_p \ll 1$, it tends to agree fairly well with experimental observations up to $Re_p \sim 8$.

For intermediate particle Reynolds numbers ($0.1 < Re_p < 1,000$), the flowfield in the rear of the particle undergoes several transitions: from an attached laminar wake (Fig. 3.1a), to a separated but still laminar wake (Fig. 3.1b), to an unsteady wake. In these Reynolds number regimes and beyond, there is no analytical solution available from which one can extract the sphere's drag. In

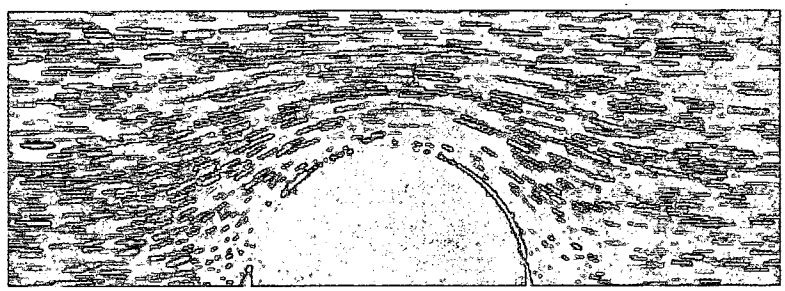

a) creeping flow at $Re_p = 0.1$ where flow is symmetric from top to bottom with no flow separation

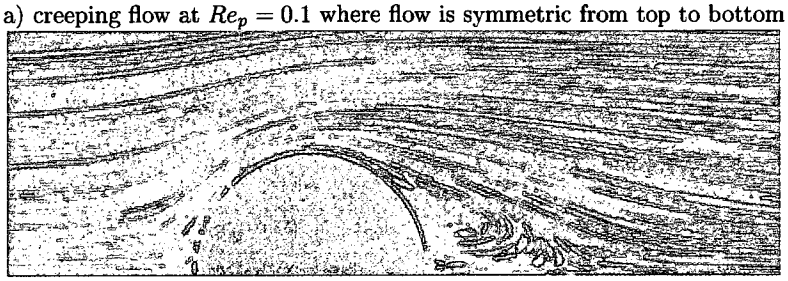

b) flow at $Re_p = 56.5$ where separation yields a steady symmetric laminar wake

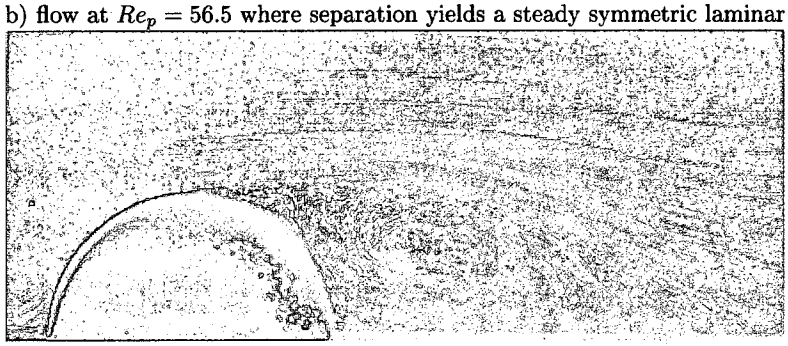

c) time-averaged flow field at $Re_p = 15,000$ (laminar boundary-layer, turbulent wake)

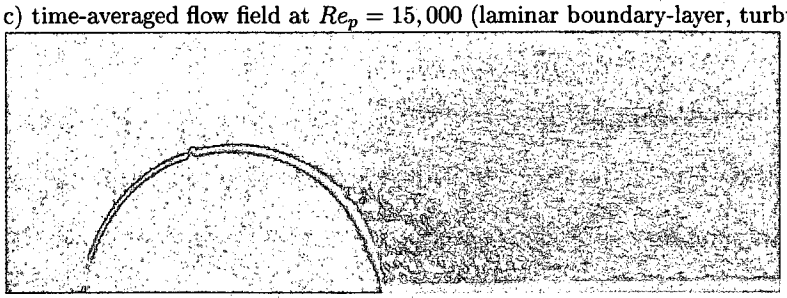

d) time-averaged flow at $Re_p = 30,000$ with a trip wire to induce a turbulent boundary layer

Figure 3.1: Flow about a sphere for several Reynolds number regimes [1]

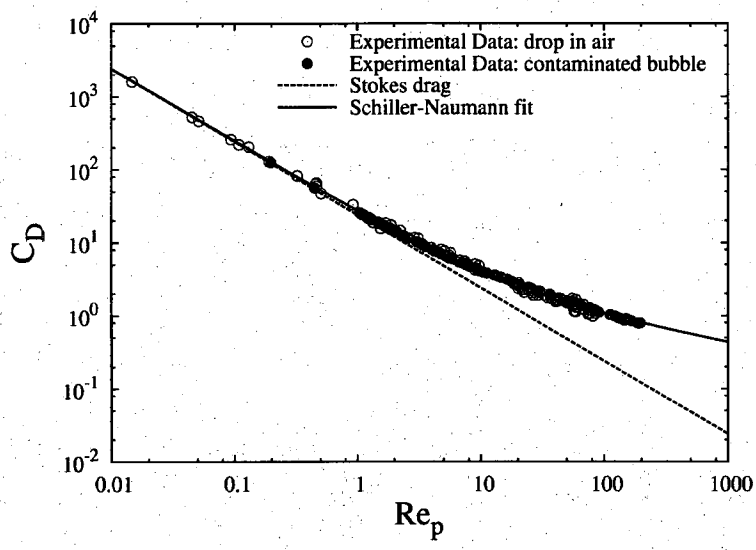

Figure 3.2: Experimental results of drag coefficient of spherical particles including drops in gas [2] and contaminated bubbles [3, 4] with comparison to rigid-sphere fit of [5].

these cases it is common to write the drag coefficient as

$$C_D = \frac{24}{Re_p} f \tag{3.19}$$

where f is a correction factor to account for finite Reynolds number drag effects. There are a number of reasonable expressions for f such as

$$f = 1.0 + 0.15 Re_p^{0.687} \tag{3.20}$$

which was suggested by [5]. This reverts to Eq. 3.8 in the limit of $Re_p \ll 1$ and uniform flow. Note that no Faxen-type correction has been proposed to the author's knowledge for finite Re_p point-force expressions.

3.2.2 History force

The history force accounts for the unsteady component of the drag force which is generated by the temporal development of the viscous region in the vicinity of the particle. As such the force decays in time provided the particle reaches a constant velocity (e.g. terminal velocity in a quiescent

fluid). The basic form of the history force for a uniform flow is given by

$$\vec{F_H} = 3\pi\mu_f d_p \int_{-\infty}^{t} K(t-\tau)\frac{d\vec{V}_{rel}}{d\tau}d\tau \tag{3.21}$$

which is the same as given by [21]. In the limit of creeping flow, the kernel, K, is given by Basset [63]

$$K_{Basset}(t-\tau) = \left[\frac{4\pi\nu(t-\tau)}{d_p^2}\right]^{-1/2} \tag{3.22}$$

where it is noted that the kernel decays like $t^{-1/2}$. For finite Re_p, the long-time behavior of the history force kernel is not fully understood but is generally accepted to be a function of Reynolds number. Mei and Adrian [64] used results from resolved-surface simulations conducted by [60] and an asymptotic analysis to investigate the history force at finite convective conditions for small amplitude (10%) fluctuations of the mean flow (no flow reversal). They determined that the limiting behavior yields a short-time period decay rate proportional to $t^{-1/2}$ (as given by the creeping flow expression, K_{Basset}) while the long-time decay rate is much faster and proportional to t^{-2} (as illustrated in Figure 3.3). They further suggested an interpolation between the short and long-time limits to obtain a model reasonable for the history force kernel for Re_p values up to 100 (see Figure 3 of [64] and associated discussion) as

$$K(t-\tau) = \left(\left[\frac{4\pi\nu(t-\tau)}{d_p^2}\right]^{1/2c_1} + \left[\frac{\pi(t-\tau)^2}{f_H\tau_d}Re_p^3\right]^{1/c_1}\right)^{-c_1} \tag{3.23}$$

where τ_d is a diffusive time-scale and f_H is a function of Reynolds number,

$$\tau_d = \frac{d_p^2}{\nu} \tag{3.24}$$

$$f_H = (0.75 + c_2 Re_p)^3 \tag{3.25}$$

The specific constants used for the Mei & Adrian kernel (K_{Mei}) were obtained by matching their oscillating flow simulations which yielded $c_1 = 2$ and $c_2 = 0.105$.

It was later shown that the t^{-2} behavior was not universally valid. For example, Lovalenti and Brady [65] observed exponential decay rates of the kernel for long-times while Mei [66] found that the long-time decay rate for an impulsively started flow could be described as algebraic decay faster than t^{-2} or as "slow-exponential" decay. Lawrence and Mei [67] show that the appropriate long-time decay rate for a particle falling from rest to terminal velocity $t^{-1/2}$, but found different

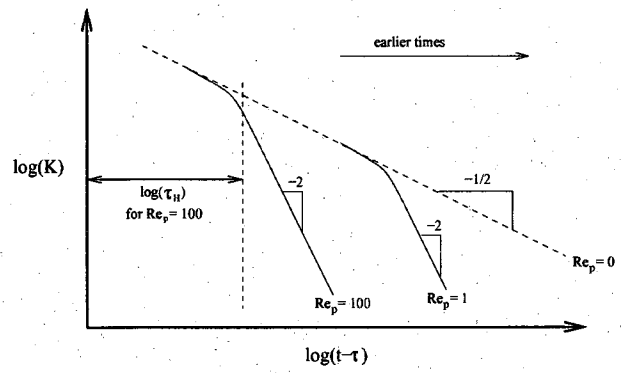

Figure 3.3: Schematic of history kernel as a function time, where short-times give creeping flow response but long-times result in faster decays. The window model limit of integration is shown for $Re_p = 100$.

behavior for a particle suddenly coming to rest or undergoing flow reversal where the decay rate is t^{-1}. Similar findings were reported by Lovalenti and Brady [65] who examined the history force analytically and noted that the transition from short-time decay rate of $t^{-1/2}$ to a more rapid decay depends on whether the particle was being accelerated or decelerated. Kim et al. [57] developed a more detailed semi-empirical formulation (including six constants determined by calibration with resolved-surface simulations) with the goal of increased robustness using a more detailed combination of the $t^{-1/2}$ and t^{-2} dependence. The Kim et al. model for weak accelerations is given by Eq. 3.23 where their values of the constants are $c_1 = 2.5$ and $c_2 = 0.126$ based on their own resolved-surface simulations (and will be referred to as K_{Kim}). As such, there is some disagreement on how best to model the transition from short-time behavior to long-time behavior with the effects of finite Reynolds number in terms of the values of c_1 and c_2. However, the form of Eq. 3.23 is deemed reasonable for simple flows so long as the particle does not ingest its own wake due to an abrupt stop, rapid deceleration, or direction reversal. As such, the present work seeks to evaluate improved choices for c_1 and c_2 by comparing the model to experimental data. Additionally, an approach is sought to alleviate the significant computational overhead associated with evaluating the integral in Eq. 3.21.

The desire to evaluate and potential choices for c_1 and c_2 arose due to the range of values available in the literature and because there has not been a comprehensive comparison with all available quantitative experiments in this matter. The second objective of reducing the computational overhead associated with evaluating the history force integral was motivated by the significant (and sometimes prohibitive) computational cost of including that term for a many-particle

simulation. The memory requirements needed to store the full history of particle information and the CPU requirements needed to compute the kernel at a large number of integration points can become problematic for many multiphase flows. For example, storing the three-dimensional relative velocity for 100,000 particles (consistent with [36]) for 1000 time-steps using 4-byte real values would require 1.2 GB of memory. To establish a more efficient method for computing the history force integral (that would reduce the CPU hours and memory requirement), a "window model" was developed. This was inspired by the experiments of Mordant & Pinton [6] who noted that the history force at finite Re_p was well-represented by the creeping flow expressions for short time periods (consistent with the resolved-surface simulations of Chang & Maxey [68, 69]), but that the history force became negligible after a finite time interval. This is consistent with similar experiments by Moorman [70] and the nature of Eq. 3.23. This suggests that the finite Re_p history force can be represented by the creeping flow history force "clipped" at some finite time which may be achieved by replacing the lower limit of integration with $t - t_{window}$, where t_{window} is obtained by assuming the relevant acceleration is approximately constants and by equating the integral with that which would have been obtained by Eq. 3.23.

3.2.2.1 Calibration of c_1 and c_2

This section discusses the optimization of the constants c_1 and c_2 of Eq. 3.23 based on experimental data. In particular, the falling particle data given by Moorman [70] is considered for the calibration. Herein, a "falling particle" is one released from rest and allowed to accelerate to terminal velocity under the influence of gravity. A number of these falling particle data sets were examined and compared to the predictions given by the K_{Mei} and K_{Kim} history force kernels. Three typical data sets (which have density ratio of 3.9 and terminal Reynolds numbers ranging from 28.2 to 166, where the terminal Reynolds number $Re_{p,term} \equiv d_p V_{term}/\nu$ and V_{term} is the magnitude of the terminal relative velocity) are showing in Figure 3.4 along with predictions made using the various coefficient sets for the history force kernels as well as a prediction made using no history force. The experimental data correspond to, in order of increasing Reynolds number, Run #22, #21, and #19 as given in Table 3.1. While K_{Mei} and K_{Kim} give much better predictions than the K_{Basset}, they tend to slightly over-predict the velocities (i.e. under-predict the history force) associated with the Moorman data. This minor deficiency can be generally improved for the Moorman data by using $c_1 = 2.5$ and $c_2 = 0.2$ (labeled "present kernel" in Figure 3.4). These values were also found to be quite robust for the falling particle data of [6].

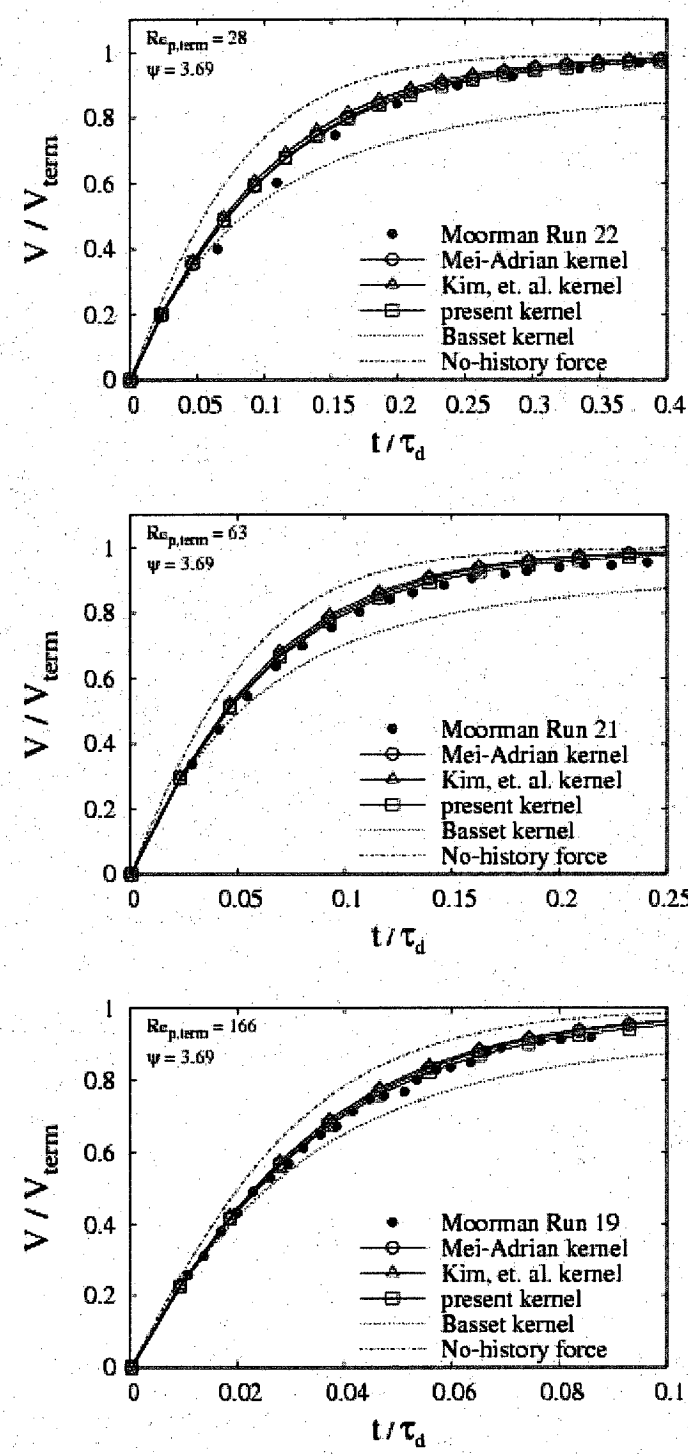

Figure 3.4: Comparison of the various history force kernels with falling particle experiments of constant density ratio and various terminal Reynolds numbers.

Table 3.1: Experimental data sets considered in the history force study

Run #	$Re_{p,term}$	ψ	$t_{window}/(\tau_p/f)$
Moorman			
9	55	9.32	0.11
10	31	9.15	0.10
11	15	9.15	0.09
12	9	9.15	0.10
17	600	3.51	1.16
18	301	3.51	0.71
19	166	3.69	0.46
21	63	3.69	0.28
22	28	3.69	0.22
26	45	2.47	0.35
27	29	2.47	0.31
28	15	2.47	0.30
32	853	1.65	2.85
33	319	1.22	1.71
34	231	1.41	1.24
35	136	1.72	0.77
36	48	1.27	0.60
37	15	1.17	0.53
Mordant & Pinton			
1	43	2.57	0.33
4	260	7.73	0.31
Odar			
9	11.5	0.911	1.16
18	30	0.911	2.13
29	6.5	1.77	1.85
38	17	1.77	2.80
50	20	0.589	1.03
56	36	0.589	1.59
65	30	0.442	1.04
68	39	0.442	1.27

(a) Moorman data [70], (b) Mordant & Pinton data [6], and (c) Odar data [7].

3.2.2.2 Development of the window model

In general, evaluating the history force kernels discussed above requires integration over a temporal range of $\tau = -\infty$ to $\tau = t$ regardless of Reynolds number. The concept behind the window model is simple–we wish to prescribe a finite integration window such that the history force only requires integration over a temporal range of $\tau = t - t_{window}$ to $\tau = t$ over which the Basset kernel K_{Basset} is used. If such a window can be specified, only the particle history for a time length of t_{window} would need to be stored and integrated for each particle.

The primary assumption for the window model is that the particle acceleration is constant (or nearly so) over the recent relevant time, i.e. the window duration. In this case, the history force can be correctly retained by equating the proposed modified integral to the integral using the desired finite Reynolds number kernel, i.e.

$$\int_{t-\tau_H\tau_d}^{t} K_{Basset}(t-\tau)d\tau = \int_0^t K(t-\tau)d\tau \tag{3.26}$$

The objective is to solve for the non-dimensional "history time", τ_H which is equivalent to t_{window}/τ_d, appearing in the lower limit of the first integral. Equating the two integrals for $t \to \infty$ allows τ_H to be specified for a particular Re_p and τ_d, i.e.

$$\tau_H = \lim_{t\to\infty} \pi \left[\int_0^t K(t-\tau)d\tau\right]^2 \tag{3.27}$$

Another option would have been to normalize t_{window} by the convective time-scale $\tau_c = d_p/V_{rel}$ which is more important at high Re_p (whereas τ_d is more important at low-Re_p). However, both time-scales will be incorporated since we will take $\tau_H = f(K(Re_p))$ and since $Re_p \equiv \tau_d/\tau_c$. Thus, the proposed lower limit of integration for the new history force model is given by

$$t - t_{window} = \min(0, t - \tau_H) \tag{3.28}$$

Therefore, the total integration time will initially grow but eventually reaches a point where only a portion of the particle history will be considered.

The function τ_H can be obtained by integrating the kernel of Eq. 3.23 for a given Re_p and choice of c_1 and c_2. As shown in Figure 3.5, the integrations of K_{Mei}, K_{Kim}, and the present history force kernel (shown as symbols) can be accurately represented by the following three curve fits

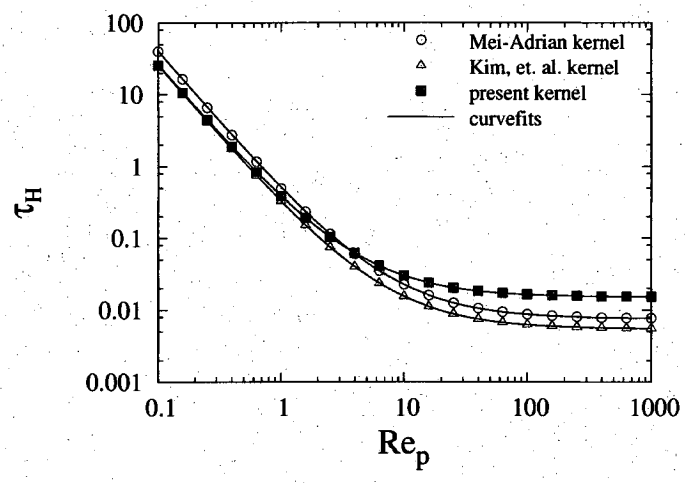

Figure 3.5: History force transition time-scale for several finite Reynolds number kernels.

(shown as lines):

$$\tau_{H,Mei} = \left(\frac{0.632}{Re_p} + 0.087\right)^2 \tag{3.29}$$

$$\tau_{H,Kim} = \left(\frac{0.502}{Re_p} + 0.074\right)^2 \tag{3.30}$$

$$\tau_{H,present} = \left(\frac{0.502}{Re_p} + 0.123\right)^2 \tag{3.31}$$

Note that the present τ_H is more similar to the Kim et al. model at low-Re_p but is closer to (yet greater than) the Mei & Adrian model at large Reynolds numbers.

As previously mentioned, the window model is only valid if the changes in acceleration over t_{window} are sufficiently small once the long-time behavior is realized. (Note that for short-times, changes in acceleration are modeled appropriately as the window model reverts to the Basset kernel for the case of $t_{window} > t$.) As such, we define ϵ to be the ratio of the change in acceleration over the window to the change in acceleration over the particle's trajectory, i.e.

$$\epsilon = \frac{J_{window} t_{window}}{J_{traj} \tau_{traj}} \tag{3.32}$$

where J is the derivative of acceleration (i.e. the "jerk") and τ_{traj} is a time-scale relevant to the changes in relative velocity the particle will experience. For negligible changes in acceleration over the window period we require $\epsilon \ll 1$. If we assume that the ratio of the two jerks is of order unity

(which was verified for most of the falling particle cases) we can write

$$\epsilon \approx \frac{t_{window}}{\tau_{traj}} \tag{3.33}$$

For falling particles we will choose $\tau_{traj} = \tau_p / f$, where τ_p is the "particle response time-scale" defined as

$$\tau_p \equiv \frac{(\psi + C_M)\, d_p^2}{18\nu} \tag{3.34}$$

and where f is the drag correction factor discussed in Section 3.2.1 and C_M is the added mass coefficient as shown in Eq. 3.10. For oscillating particles (like those investigated by [7]) we will choose $\tau_{traj} = \tau_f / 2$, where τ_f is the period of the particle oscillation (for the relative velocity). In these cases, ϵ can be roughly approximated as

$$\epsilon \approx \frac{18\tau_H}{\psi + C_M} f \qquad falling\, particle \tag{3.35}$$

$$\epsilon \approx 4\tau_H Re_{p,rms} S \qquad oscillating\, particle \tag{3.36}$$

For the falling particle case, the Re_p used for τ_H and f is based on the terminal velocity for simplicity. For the oscillating particle case, $Re_{p,rms}$ is based on $V_{rel,rms}$ (the root-mean-square of the relative velocity history) while S is the Strouhal number defined as

$$S \equiv \frac{d_p}{2\tau_f V'_{rel,rms}} \tag{3.37}$$

where $V'_{rel,rms}$ is the root-mean-square of the relative velocity fluctuations about the mean, i.e.

$$V_{rel,rms} = \sqrt{\overline{V_{rel}^2}} \tag{3.38}$$

$$V'_{rel,rms} = \sqrt{\overline{\left(V_{rel} - \overline{V_{rel}}\right)^2}} \tag{3.39}$$

where the over-bar denotes a time-average. The results will show that the above rough approximation to ϵ are a good indicator for the window model limits of applicability.

3.2.2.3 Computational expense

The key advantage of the window model compared to conventional history force expressions is its relatively small storage and its comparatively few number of required integration points; both of

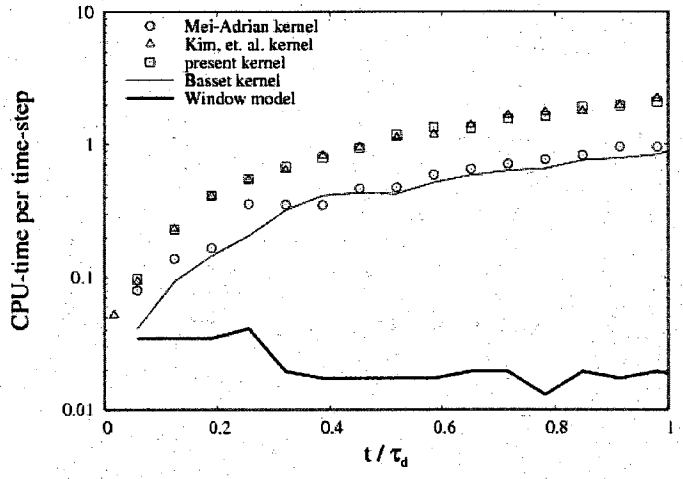

Figure 3.6: Normalized CPU-time per time-step for the various history force expression applied to Moorman Run 27.

which result from a finite lower limit of integration. A comparison of the computational cost per time-step was performed for a falling particle simulation and the results are presented in Figure 3.6. For this particular case, a savings of nearly two-orders of magnitude is seen for the integration times nearing one τ_d compared to K_{Basset} and K_{Mei}. Thus, in cases where the window model formulation remains valid (i.e. sufficiently small ϵ) the savings in CPU-time for a many-particle simulation is quite substantial. An interesting point is that K_{Kim} and the present kernel require approximately twice the CPU-time as compared to K_{Mei}. This is due to the value of c_1 for these kernels (in both cases $c_1 = 2.5$) which leads to floating point exponentiation which must be done is software routines. This is in contrast to K_{Mei} whose square-root operation can be done at the hardware level at much greater speed.

3.2.2.4 Comparison of predictions with experimental data

In this section, predictions obtained using the window model with Eq. 3.31 are compared with experimental data. To assess robustness and accuracy of the window model for the falling particle data set of Moorman [70], a variation of particle Reynolds number (for a fixed density ratio) is first considered followed by a variation of density ratio (for a fixed Reynolds number). The falling particle section is concluded by comparing both the window model and present kernel to data from [6]. Similar comparisons are made in the following paragraphs for some cases of oscillating particle data of Odar [7]. Table 3.1 summarizes the conditions for these cases and for the cases presented in

Appendix A, which includes all of the other experimental cases for which sufficient quantitative data was available (some cases had too few data points or uncertainties in the initial conditions and so were not included). The predictions in Appendix A support all the general statements made for the example cases discussed here and are shown in order of increasing ϵ to illustrate the deterioration of the model as that parameter increases.

The ability of the window model was first assessed by predicting the velocity of a particle with density ratio 3.69 and three different terminal Reynolds numbers (varying from 166 to 28.2). This is shown in Figure 3.7 where the present model is compared to experimental data given by [70], as well as predictions made using K_{Basset} and predictions without the history force. The model gives good agreement with the data and with the kernel predictions given in Figure 3.4. Next, a variation in density ratio in the Moorman data is similarly compared in Figure 3.8. The importance of the history force is seen to increase as density ratio decreases as the window model again performs well compared to the experimental data.

Two selected cases of the falling particle experiments of Mordant & Pinton [6] are shown in Figure 3.9. Both the window model and the present kernel perform reasonably well for the case of $Re_{p,term}$ values of 43 and 260 given there is some experimental uncertainty (ca. $1-2\%$) in the velocity measurements. Notably, the window model gives the same results as the present kernel and both provide better predictions of the experimental data than that based on K_{Basset} or no history force at all.

The oscillating particle experiments of Odar [7] are considered to illustrate performance on a second flowfield. Odar forced a particle to oscillate in a vat of fluid and recorded the total hydrodynamic force observed during steady-state oscillation. In Figure 3.10, Odar's measured hydrodynamic surface force, F_{hydro}, (normalized by the quasi-steady drag based on the rms relative velocity) is compared with numerical predictions as a function of dimensionless time. Note that Figure 3.10a and b have different Reynolds numbers but the same Strouhal number, while

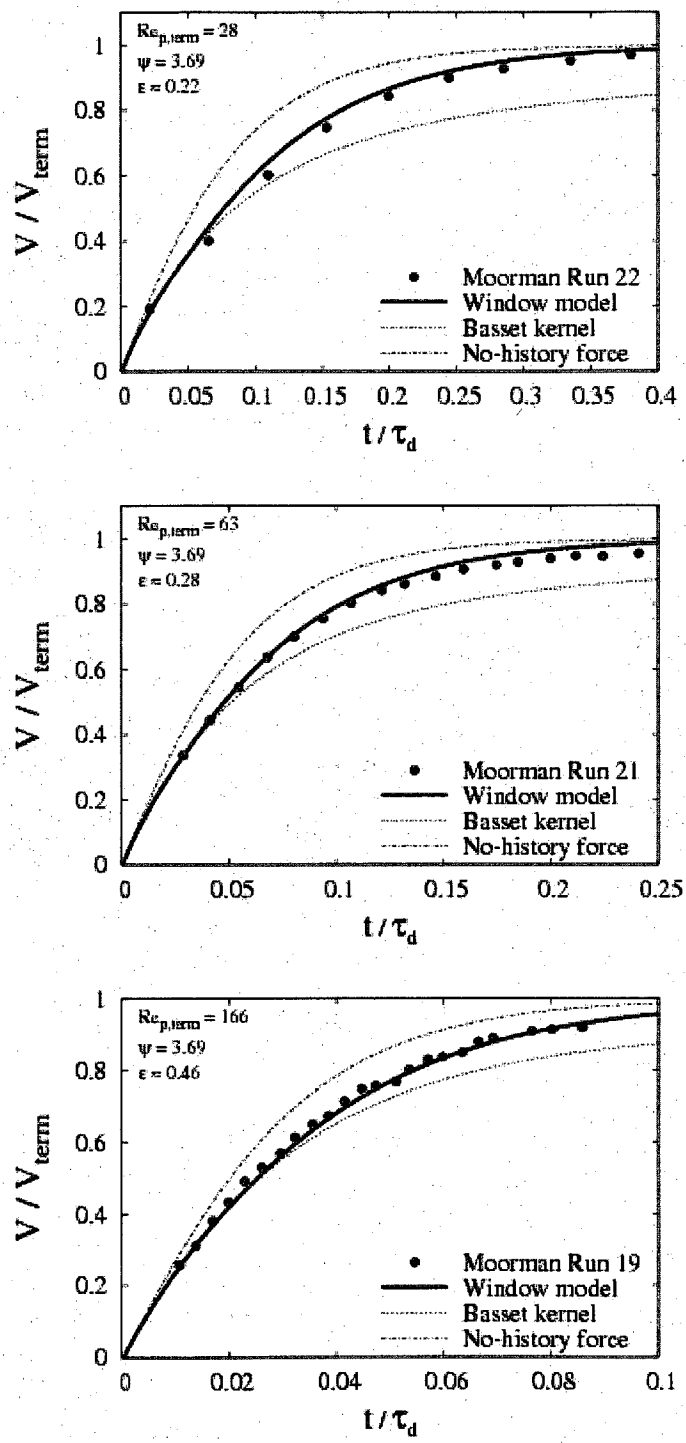

Figure 3.7: Comparison of the window model with falling particle experiments of constant density ratio and various terminal Reynolds numbers.

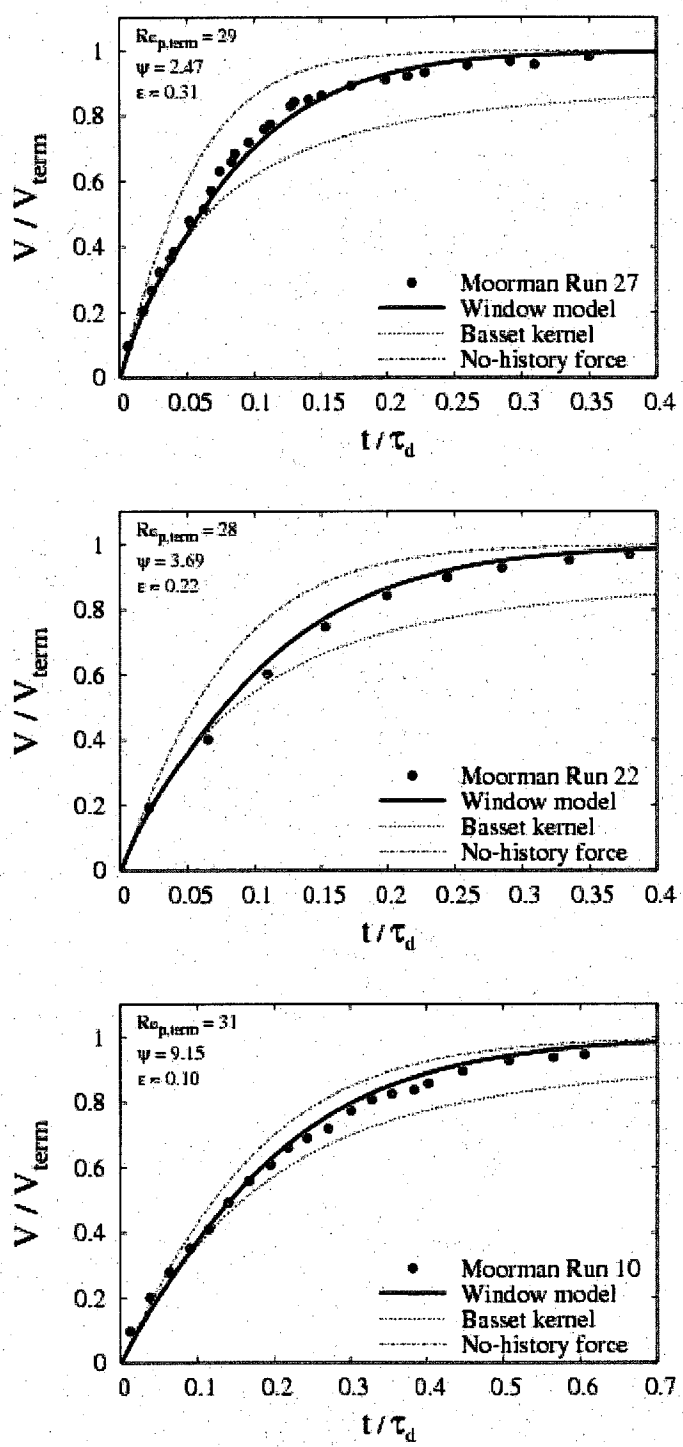

Figure 3.8: Comparison of the window model with falling particle experiments with approximately constant Reynolds number and varying density ratio.

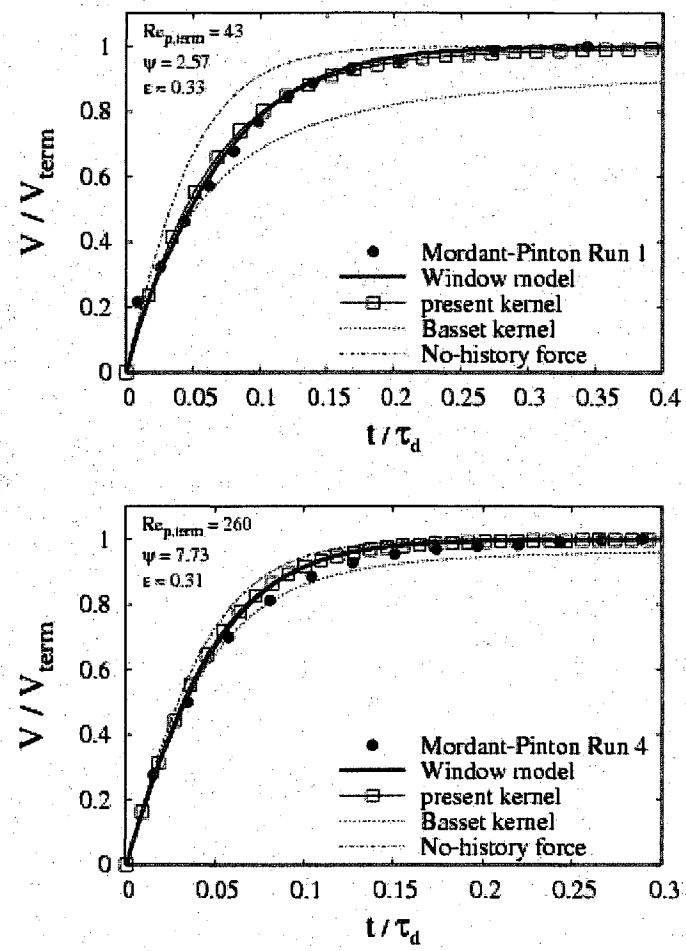

Figure 3.9: The present model compared with experiments of [6].

Figure 3.10b and c have different Strouhal numbers but the same Reynolds number. Finally, Figure 3.10d is for the highest Strouhal number (1.77) considered by Odar. As previously discussed, the long-time decay rate (t^{-2}) assumed by the kernel of the form given in Eq. 3.23 may not be appropriate, regardless of the values of c_1 and c_2. This is because the particle stops and reverses direction leading to wake ingestion which can alter the long-time decay rate to exponential or even t^{-1} if these events occur abruptly. However, the predictions made by the Mei & Adrian and present kernels are reasonable indicating that this effect is generally not large for the present conditions (S of order unity or less), especially considering that the unsteady drag shown here may be a small portion of the total drag. It is likely that the errant decay rate would become more evident for the higher Strouhal number cases ($S \gg 1$) where the reversal of relative velocity is more violent.

Figure 3.10 also shows predictions made using the window model version of the present kernel. Here we note that the predictions are substantially different than those made by the present kernel and can even be worse than the predictions made using the Basset kernel. Additionally, a non-physical change in slope is seen around the upper and lower peaks where the slope changes too quickly compared to the data. These problems are generally related to the range of applicability of the window model as discussed below.

The data shown in Figures 3.7-3.9 and the cases in Appendix A indicate good agreement between the window model and experimental data until ϵ becomes somewhat greater than unity. This is qualitatively consistent with our expectations and illustrates the model's limitations. However, the simple definitions of ϵ employed herein involve quantities that are generally known *a priori* such that the applicability of the window model may be assessed prior to simulating the particle's trajectory. In the presence of turbulence this is less obvious but a correlation will be discussed later which estimates $V'_{rel,rms}$ and $Re_{p,rms}$ in turbulence such that ϵ can be approximated.

3.2.3 Lift force

The lift force is one of the more difficult forces to properly model as there are a number of physical phenomena that lead to the generation of lift; the two primary mechanisms being vorticity in the continuous-phase and rotation of the particle. A special case that combines these two effects is that of "free-rotation" where there is zero torque on the particle, a result achieved when the particle attains an equilibrium spin rate related to the imposed shear. For particles with sufficiently small

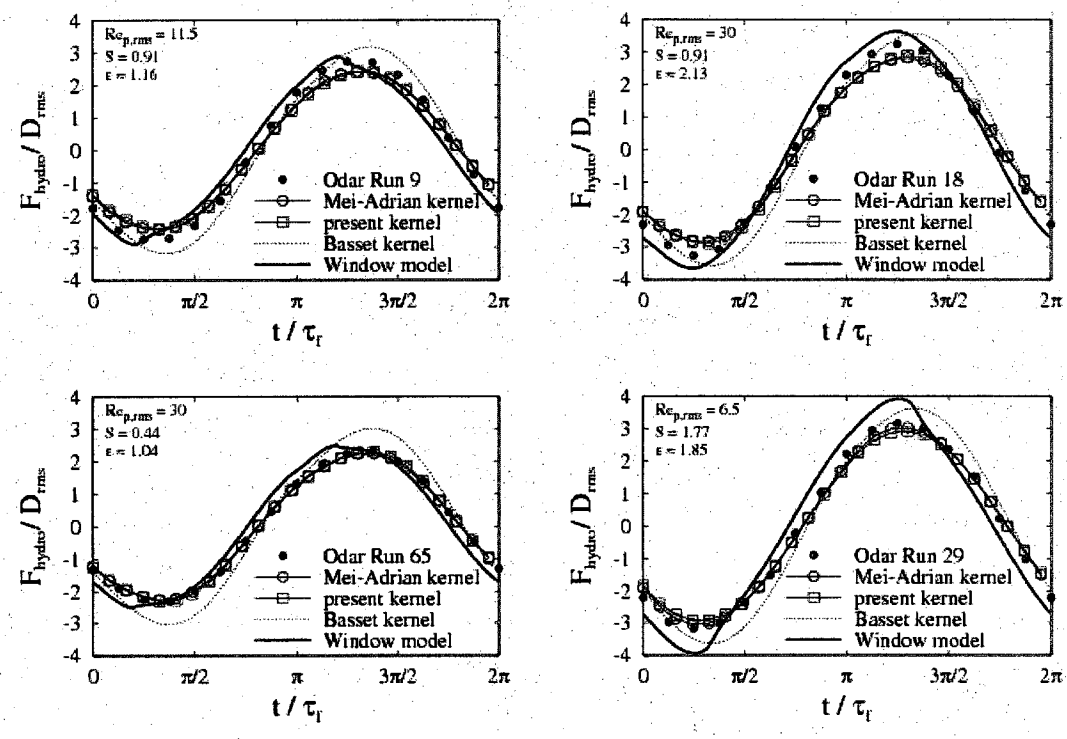

Figure 3.10: Comparison of the present model with oscillating particle experiments of [7].

inertia (e.g. gas bubbles in a liquid), the equilibrium spin rate is quickly realized such that one may often treat the particle as being in *constant equilibrium*. In all these cases, the magnitude of the vorticity or the spin rate is typically expressed in terms of ω^* and Ω_p^*, which are proportional to the velocity gradient across the particle normalized by the particle's relative velocity, e.g.

$$\omega^* = \frac{\|\vec{\omega}\| d_p}{\|\vec{V_{rel}}\|} \tag{3.40}$$

$$\Omega_p^* = \frac{\|\vec{\Omega}_p\| d_p}{\|\vec{V_{rel}}\|} \tag{3.41}$$

where $\vec{\omega}$ is the fluid vorticity and $\vec{\Omega}_p$ is the particle angular velocity. The magnitude of the lift force is typically expressed as a "lift-coefficient" non-dimensionalized in the same manner as Eq. 3.17:

$$C_L = \frac{\|\vec{F_L}\|}{\frac{\pi}{8}\rho_f \vec{V_{rel}} \cdot \vec{V_{rel}} d_p^2} \tag{3.42}$$

The direction of the lift is defined to be perpendicular to $\vec{V}_{rel}$ and a positive C_L is taken in the direction of $\vec{\omega} \times \vec{V}_{rel}$ for vorticity-induced lift and in the direction of $\vec{\Omega}_p \times \vec{V}_{rel}$ for particle-spin induced lift.

The different types of lift are often associated with the founding theories for each. For continuous-phase vorticity induced lift, there are three types: "Saffman lift" which is based on particles at $Re_p \ll 1$ subjected to a linear-shear flow [71], "Heron lift" which is based on particles at low-Re_p subjected to a vortex with solid-body rotation [72], and "Auton lift" which was presented as part of the AHP equation. In most flows, particles experience more of a "shearing" behavior than a "vortex" behavior. This behavior was confirmed for the present investigation by a conducting a direct numerical simulation of particles in a turbulent boundary layer. The magnitude of Saffman and Heron lifts were computed and compared and it was observed that the former was many times larger than the latter.

3.2.3.1 Shear-induced lift

The Saffman lift is based on the assumption of a particle exposed to creeping flow and a linear-shear velocity profile. In this situation a lift force is generated on the particle due to the difference in pressure exerted by the fluid on opposite sides of the particle (owing the different fluid velocities resulting from the velocity shear). Saffman's matched asymptotic expansion for the lift

force is restricted to creeping flow conditions where

$$Re_p \ll Re_\omega^{1/2} \tag{3.43}$$

$$Re_\omega \equiv \frac{\|\vec{\omega}\| d_p^2}{\nu} \ll 1 \tag{3.44}$$

Further assuming $Re_p \ll Re_\omega^{1/2}$ gives, to leading-order,

$$F_{L,Saff} = 1.615 \mu \|\vec{V}_{rel}\| d_p^2 \sqrt{\frac{\|\vec{\omega}\|}{\nu}} \tag{3.45}$$

Note that Saffman lift can be written in lift-coefficient form as

$$C_{L,Saff} \equiv \frac{12.92}{\pi} \sqrt{\frac{\omega^*}{Re_p}} \tag{3.46}$$

Saffman noted that two higher-order terms also arise but that these are generally negligible in comparison, particularly for a freely-rotating particle at low-Re_p [15]. McLaughlin [32], extended Saffman's result to eliminate the restriction of $Re_p \ll Re_\omega^{1/2}$. This function was approximated by Mei [73] as

$$\begin{aligned} J^* \equiv \frac{C_{L,\omega}}{C_{L,Saff}} \simeq \; & 0.3 \left\{ 1 + \tanh \left[\frac{5}{2} \left(\log_{10} \sqrt{\frac{\omega^*}{Re_p}} + 0.191 \right) \right] \right\} \\ & * \left\{ \frac{2}{3} + \tanh \left[6 \sqrt{\frac{\omega^*}{Re_p}} - 1.92 \right] \right\} \end{aligned} \tag{3.47}$$

This expression was derived for small Reynolds numbers but Loth [44] found that this lift force is reasonable for $Re_p < 50$ and $\omega^* < 0.8$ and is shown compared to the data of Cherakut et al [8] in Figure 3.11.

3.2.3.2 Lift induced by particle rotation

For small but finite Re_p, Rubinov & Keller [74] derived the analytic solution for spin-induced lift in the limit of small spin rates ($\Omega_p^* \ll 1$) for a solid sphere. Their analysis considers a velocity field which is a linear combination of the Oseen solution and that due to a rotating sphere in an otherwise stagnant fluid. Their expression can be generalized as:

$$\vec{F}_{L,\Omega_p} = \frac{\pi}{8} d_p^3 \rho_f \left(\vec{\Omega}_p \times \vec{V_{rel}} \right) C_{L,\Omega}^* \tag{3.48}$$

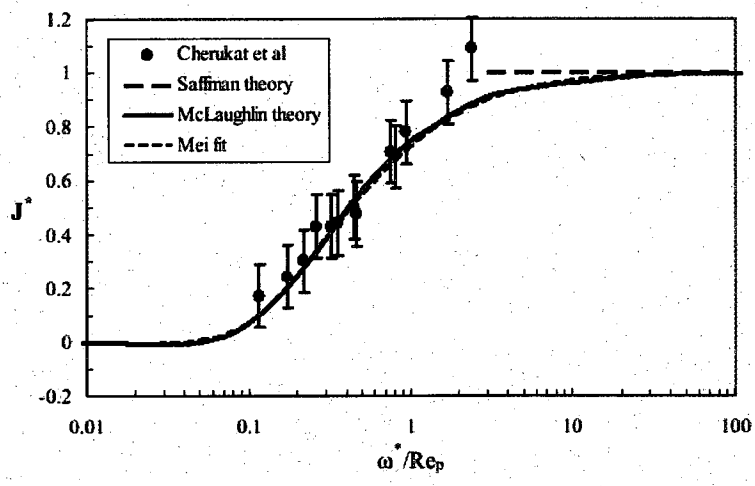

Figure 3.11: Shear-induced lift theories assuming $Re_p \ll 1$ compared to data at $0.1 < Re_p < 1.0$ from [8].

where $C^*_{L,\Omega} = 1$ for $Re_p \ll 1$. To include finite rotation rate and finite Reynolds number effects, an empirical correction is constructed by Loth [44] based on theory, experiments, and resolved-surface simulations (RSS) as

$$C^*_{L,\Omega} = 1 - \left\{0.675 + 0.15\left(1 + \tanh\left[0.28\left(\Omega^*_p - 2\right)\right]\right)\right\} \tanh\left[0.18 Re_p^{1/2}\right] \tag{3.49}$$

This reverts to the theoretical value for $Re_p \ll 1$ and approximately to the Tanaka [75] fit for high Re_p as shown in Figure 3.12. This model is more robust than previous models which assume the lift coefficient is simply a constant, e.g. $C^*_{L,\Omega} = 0.4$ [9] or $C^*_{L,\Omega} = 0.55$ [12].

3.2.3.3 Combined shear-induced and rotation-induced lift

To represent both the contribution of fluid vorticity and particle rotation to the particle lift force, one can consider summing the rotational and shear induced lift coefficients. Saffman [71] showed this to hold true for the theoretical particle spin lift of Rubinov & Keller combined with the first-order shear-induced lift assuming creeping flow conditions and $\Omega^*_p \ll 1$. In this case, the combined lift coefficient (assuming spin and shear are both perpendicular to the relative velocity

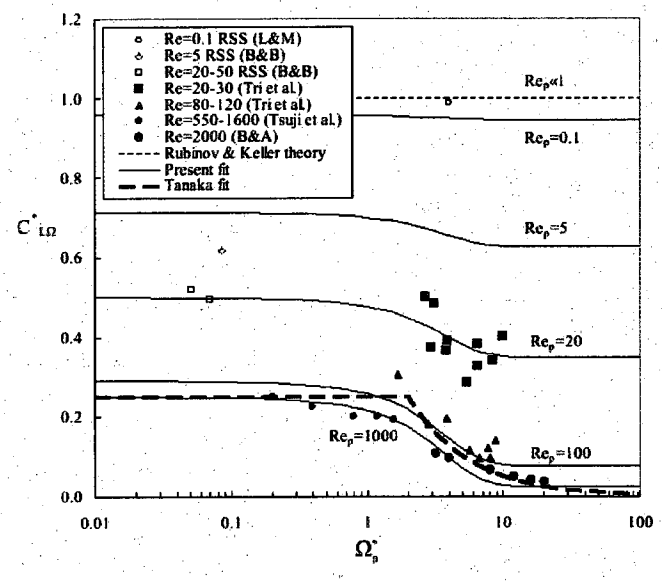

Figure 3.12: Spin lift force coefficient compared with small and intermediate Reynolds number ($Re_p < 2000$) compared to data of Tri et al. [9], Tsuji et al. [10], Barkla & Auchterlonie [11] (B&A), and resolved surface simulations (RSS) of Bagchi & Balachandar [12] (B&B) and Legendre & Magnaudet [13] (L&M).

and yield a positive lift) is given by:

$$C_L = \frac{12.92}{\pi}\sqrt{\frac{\omega^*}{Re_p}} + \Omega_p^* \tag{3.50}$$

Bagchi & Balachandar [12] and others proposed that this simple linear combination could also be extended to Reynolds numbers, shear rates, and spin rates that were no longer much less than unity, i.e. the lift for combined fluid shear and particle spin can be given as

$$\vec{F}_L\left(\omega \neq 0, \Omega \neq 0\right) \approx \vec{F}_{L,\omega}\left(\omega \neq 0, \Omega_p = 0\right) + \vec{F}_{L,\Omega}\left(\omega = 0, \Omega_p \neq 0\right) \tag{3.51}$$

This assumption was found to be reasonable based on RSS results for ω^* and Ω_p^* values as high as 0.4 and Re_p values as high as 100 [12] and an example is given in Figure 3.13.

To employ spin-induced lift for a free particle, one must keep track of the instantaneous spin rate. Using a point-force approximation to the angular momentum of the particle, one can relate the particle rotation to surface torque (τ) and angular moment of inertia about the centroid (I_p) along

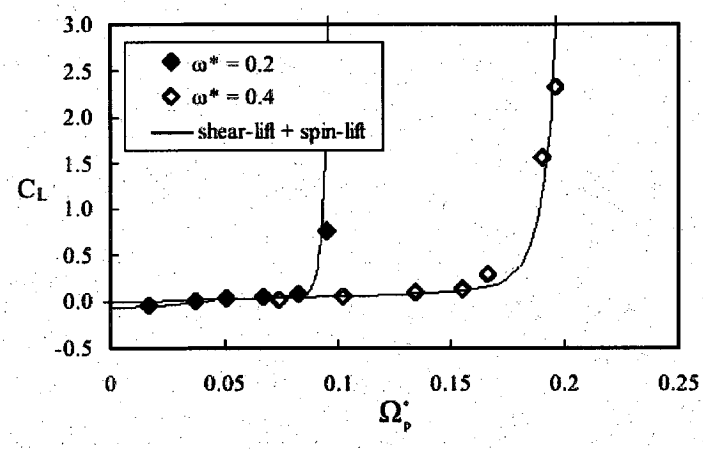

Figure 3.13: Lift force coefficient for particles under both spin and shear based on data of [12] for $1 < Re_p < 100$.

the particle path. The rotational equation of motion specifies that the rate of change of angular momentum is equal to the sum of torques acting on the particle:

$$\frac{d\left(I_p\Omega_p\right)}{dt} = \tau_{surf} + \tau_{coll} \tag{3.52}$$

The collisional torque (τ_{coll}) includes the effects of other particles or walls coming into contact with the particle while the surface torque (τ_{surf}) is the sum of moments associated with the surrounding fluid stress on the particle surface. For a sphere in quiescent flow with only fluid dynamic torque (τ_{surf}), the unsteady creeping flow angular momentum equation was obtained by Basset [63] but will not be repeated here. Basset's expression is similar to the translational equation of motion such that the angular momentum is resisted by the fluid viscosity and includes an unsteady history torque component. However, hydrostatic and pressure distributions do not contribute to torque as they operate perpendicular to the particle surface. Another surface torque expression was derived by Happel & Brenner [76] by assuming weak acceleration but allowing for a finite fluid vorticity, yielding

$$\vec{\tau}_{surf} = -\pi\mu d_p^3\left(\vec{\Omega}_p - \frac{\vec{\omega}_f}{2}\right) = -\pi\mu d_p^3\vec{\Omega}_{p,rel} \tag{3.53}$$

Since $\tau_{surf} = 0$ corresponds to spin-equilibrium, this yields $\Omega_{p,rel} = 0$ at creeping flow, i.e.

$$\vec{\Omega}^*_{p,eq} = \frac{\vec{\omega}^*}{2} \tag{3.54}$$

which simply implies that the rotation of the particle is equal to the rotation rate of the fluid.

Using Eq. 3.53, the angular equation of motion can be written as

$$\frac{d\vec{\Omega}_p}{dt} = -\frac{\vec{\Omega}_{p,rel}}{\tau_\Omega} \tag{3.55}$$

where τ_Ω is the angular momentum time-scale of the particle as is defined as

$$\tau_\Omega \equiv \frac{I_p \|\vec{\Omega}_{p,rel}\|}{\|\vec{\tau}_{surf}\|} = \frac{\rho_p d_p^2}{60\mu} \tag{3.56}$$

If $\tau_p \gg \tau_\Omega$, it is reasonable (from a modeling standpoint) to assume that the particle will always be in spin-equilibrium. This is especially true in the case low density particles ($\rho_p \ll \rho_f$) because there is *no added mass effect* associated with the torque. As such the angular response becomes nearly instantaneous, so that a bubble (contaminated or clean) can be assumed to always be in spin equilibrium for almost any Stokes number. This is convenient as one can avoid solving the angular equation of motion by employing the assumption of constant equilibrium.

To extend Happel & Brenner's expression to finite Re_p and finite Re_ω values, an empirical model (shown in Fig. 3.14) can be developed based on experimental data and resolved-surface simulations as

$$\Omega^*_{p,eq} = \frac{\omega^*}{2}\left(1 - 0.0075Re_\omega\right)\left(1 - 0.062Re_p^{1/2} - 0.001Re_p\right) \tag{3.57}$$

This expression differs from that of [44] which used a different non-dimensionalization and had an error in the subscript. This new expression is superior to the fit by [77] which is also shown in Figure 3.14.

Noting that Eq. 3.57 does a reasonable job predicting the equilibrium spin rate for a range of conditions, it can be used along with the McLaughlin lift (Eq. 3.47) to define a lift coefficient appropriate for spherical particles which are solid or have a contaminated fluid interface at finite Reynolds numbers and are constantly in rotational equilibrium. To summarize, the lift of such

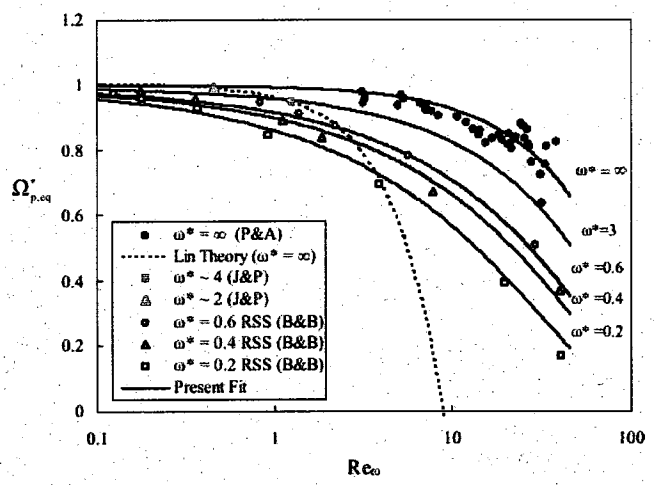

Figure 3.14: Equilibrium particle rotation rates based on data from Jeffrey & Pearson [14] and Poe & Acrivos [15] as well as resolved surface simulations (RSS) from Bagchi & Balachandar [12]. The curve fits demonstrate accuracy of the respective models.

spin-equilibrium particles at finite Reynolds numbers of up to $Re_p = 50$ can be given as

$$C_L = J^* \frac{12.92}{\pi} \sqrt{\frac{\omega^*}{Re_p}} + \Omega^*_{p,eq} C^*_{L,\Omega} \tag{3.58}$$

3.3 Equation of motion for finite-sized particles

The above point-force expressions in Section 3.2 assumes weak spatial variations on the order of the particle scale. This lack of Faxen-type corrections for finite Reynolds numbers is consistent with almost all multiphase simulations for which the particle surface has not been resolved. In fact, such finite-size corrections are typically avoided even in creeping flow conditions because few, if any, studies have investigated the impact of discretization on representing such corrections. The point-force assumption in turbulent flow formally requires $d_p \ll \lambda$ [78], where λ is the Kolmogorov length-scale. For example, consider a particle in a turbulent flow where one can show that for a Stokesian drag law, the particle diameter normalized by λ is proportional to Kolmogorov Stokes number (St_λ),

$$\left(\frac{d_p}{\lambda}\right)^2 = \frac{18}{\psi + C_M} St_\lambda \tag{3.59}$$

where $\psi = \rho_p/\rho_f$ and

$$\lambda = \left(\frac{\nu_f^3}{\epsilon}\right)^{1/4} \qquad \text{and} \qquad St_\lambda = \frac{(\psi + C_M)\, d_p^2}{18\nu} \left(\frac{\epsilon}{\nu}\right)^{1/2} \tag{3.60}$$

and where $\nu_f = \mu_f/\rho_f$. The above relation for a glass particle in a gas with $\psi = 1800$ suggests $St_\lambda \ll 100$ is appropriate for a conventional point-force approximation. However, an air bubble in water requires $St_\lambda \ll 1/36$ to satisfy this condition. Such a small Stokes number is effectively negligible in most cases. As such, an interesting bubble (i.e. one with appreciable inertia) will not, regardless of flow conditions, satisfy the point-force requirements and one is forced to seek a better technique.

The spatially-averaged method is based on an Eulerian representation of the continuous-phase flow and a Lagrangian description of the particle trajectories and velocities. Previous versions of this approach have employed a simple volume-average for the continuous-phase velocity within a filter-radius. In particular, a Heaviside weighting function ($\mathcal{H}$) can be specified as non-zero when the distance from the particle centroid (r) is within the filter-radius so that the continuous-phase velocity from all the nodes within this filter-radius are averaged:

$$\mathcal{H}(\vec{x}_j, \vec{x}_p) = \begin{cases} 1 & r \le a_z r_p \\ 0 & otherwise \end{cases} \tag{3.61}$$

$$\vec{V}_{f,avg} = \frac{\sum_{j=1}^{N_z} \vec{V}_f(\vec{x}_j)\, \mathcal{H}(\vec{x}_j, \vec{x}_p)}{\sum_{j=1}^{N_z} \mathcal{H}(\vec{x}_j, \vec{x}_p)} \tag{3.62}$$

where a_z is the non-dimensional filter radius. The relative particle velocity for drag and lift forces can then be obtained as $\vec{V}_{rel,avg} = \vec{V}_p - \vec{V}_{f,avg}$. Bagchi & Balachandar [23] investigated this weighting function with a_z values of 1.2 and 10 for a fixed solid particle in a turbulent flowfield. The spatially-averaged force results were compared to both resolved-surface force predictions and point-force predictions. In general, the spatially-averaged method compared reasonably well with the resolved-surface predictions for $d_p = 1.5\lambda$ with mean Re_p of 260. For larger particles with $d_p = 9.6\lambda$ with a mean Re_p of 600, the spatially-averaged method yielded poor correlations but at least gave the correct level of fluctuations, whereas the point-force gave large non-physical oscillations. Similar differences were found by Zeng et al. [24] in a turbulent boundary layer for $d_p = 14.3\lambda$ and a Re_p of about 300 for various a_z values. The Zeng et al. study also noted that effects of turbulence intensity, d^+, Re_p were significant but secondary to the effects of d_p/λ. A

study of a clean bubble conducted by Merle et al. [25] for $d_p = 8\lambda$ with a mean Re_p of 500 found that a point-force model tended to overestimate the resolved-surface force fluctuations somewhat while a spatially-averaged expression with $a_z = 1$ tended to underestimate the fluctuations. Thus, previous spatial-averaging models show some promise but are largely empirical in design and have only been examined in the context of high Reynolds number particles. Another option, proposed herein, is to develop a spatially-averaged technique based on theoretical considerations.

In the following, a distributed-force technique based on spatial-averaging is discussed. This new approach takes into account variations in the continuous-phase properties over the particle volume such that the length-scale (and corresponding Stokes number) restriction can be relaxed. This technique is developed for both low-Reynolds number and inviscid theoretical limits, followed by a generalized semi-empirical expression and discrete representations for computational implementation. This new approach is generally fourth-order accurate with respect to particle diameter such that much larger particles can be modeled than allowed by conventional point-force approaches.

3.3.1 Surface force in non-uniform flow at low Reynolds numbers

The quasi-steady drag force for general particle shapes was considered for a non-uniform continuous-phase velocity field by Brenner [79]. He used the reciprocal theorem to express the drag force at small Reynolds numbers in terms of the average continuous-phase velocity on the particle surface ($\vec{V}_{f,surf}$):

$$\vec{F}_D = -3\pi\mu d_p \frac{1}{A_p} \oiint_{A_p} \left(\vec{V}_p - \vec{V}_f\right) d(A_p) = -3\pi\mu d_p \left(\vec{V}_p - \vec{V}_{f,surf}\right) \tag{3.63}$$

where A_p is the particle surface and has a value of πd_p^2 for a spherical particle. It can be shown that the particle torque can be similarly related to the surface-averaged vorticity at small Reynolds numbers. Thus, the spin-equilibrium of Eq. 3.57 should also be based on surface averages of vorticity and continuous-phase velocity. For a spherical particle surface, a Taylor series can be used to replace the surface average of a quantity q with its value and its even-numbered derivatives evaluated at the particle center [80] as

$$\oiint_{A_p} q dA_p = A_p \left[q_{@p} + \frac{d_p^2}{24} \left(\nabla^2 q\right)_{@p} + \frac{d_p^4}{1920} \left(\nabla^4 q\right)_{@p} + ... \right] \tag{3.64}$$

For Stokes flow, $\nabla^4 V_f \equiv 0$ so that the drag force can then be expressed in terms of the conventional Faxen corrections given by the MR equation of motion (Eq. 3.8):

$$\begin{aligned} \vec{F}_D &= -3\pi\mu_f d_p \left(\vec{V}_p - \vec{V}_{f,surf}\right) = -3\pi\mu_f d_p \left[\vec{V}_p - \vec{V}_{f,@p} - \frac{d_p^2}{24}\left(\nabla^2\vec{V}_f\right)_{@p}\right] \\ &= -3\pi\mu_f d_p \left[\vec{V}_{rel} - \frac{d_p^2}{24}\left(\nabla^2\vec{V}_f\right)_{@p}\right] \end{aligned} \tag{3.65}$$

Note that the history force of MR includes a similar Faxen correction (Eq. 3.11) also consistent with $\vec{V}_{f,surf}$. In summary, the low Reynolds number drag and surface torque in a non-uniform flow arise from a surface average of the continuous-phase velocity and vorticity.

The reciprocal theorem was also used by Lovalenti & Brady [65] to extend the surface forces to incorporate conditions of small but finite Reynolds numbers (for which the Oseen correction is valid and for which Saffman lift is valid). They showed that the above Faxen corrections are still appropriate for a solid particle but that the correction should be reduced for a fluid particle with finite viscosity as:

$$\vec{F}_D = -3\mu_f d_p \left[\left(\frac{3\mu_p + 2\mu_f}{3\mu_p + 3\mu_f}\right)\left(\vec{V}_p - \vec{V}_{f,@p}\right) - \frac{d_p^2}{24}\left(\frac{3\mu_p}{3\mu_p + 2\mu_f}\right)\left(\nabla^2\vec{V}_f\right)_{@p}\right] \tag{3.66}$$

where μ_p is the particle viscosity. The right-hand-side in the limit of a clean bubble with negligible viscosity in uniform flow is consistent with the Hadamard-Rybczynski solution, i.e. $-2\mu_f d_p(\vec{V}_P - \vec{V}_{f,@p})$. As such, the drag force of a clean bubble should employ a centroid-based fluid velocity and not a surface-average, which is qualitatively consistent with the results of Merle *et al.*[25].

For small but finite Reynolds numbers, Lovalenti & Brady [65] considered unsteady conditions and showed that the fluid stress and added mass force for a solid sphere can be written in terms of volume-based averages of the fluid accelerations:

$$\vec{F}_{SG} = \rho_f \iiint_{\forall_p} \left(\frac{D\vec{V}_f}{Dt} - \vec{g}\right) d\forall_p = \rho_f \forall_p \left[\left(\frac{D\vec{V}_f}{Dt}\right)_{vol} - \vec{g}\right] \tag{3.67}$$

$$\begin{aligned} \vec{F}_{AM} &= -C_M \rho_f \iiint_{\forall_p} \frac{d\left(\vec{V}_p - \vec{V}_f\right)}{dt} d\forall_p = -C_M \rho_f \forall_p \left[\frac{d\vec{V}_p}{dt} - \left(\frac{d\vec{V}_f}{dt}\right)_{vol}\right] \\ &\approx -C_M \rho_f \forall_p \left[\frac{d\vec{V}_p}{dt} - \left(\frac{D\vec{V}_f}{Dt}\right)_{vol}\right] \end{aligned} \tag{3.68}$$

The approximation of the particle Lagrangian time-derivative as the continuous-phase Lagrangian time-derivative is appropriate in the limit of small Reynolds numbers [53]. As such, the fluid stress and added mass forces for a solid particle in a non-uniform flow arise directly from a volume average. As with the drag force, adjustments are required for an uncontaminated fluid particle with finite viscosity [65].

By applying two additional assumptions, the above volume-averaged result for added mass can be simplified to yield conventional the Faxen correction. The first of these assumptions is to swap the differentiation and the spatial-averaging as follows:

$$\left(\frac{D\vec{V}_f}{Dt}\right)_{vol} = \left(\frac{\partial \vec{V}_f}{\partial t}\right)_{vol} + \left[\vec{V}_f \cdot \nabla \vec{V}_f\right]_{vol} \approx \frac{\partial \vec{V}_{vol}}{\partial t} + \vec{V}_{f,vol} \cdot \nabla \vec{V}_{f,vol} \approx \frac{D\vec{V}_{f,vol}}{Dt} \tag{3.69}$$

This is often a reasonable approximation because the fluid-acceleration gradients are typically weak since they are higher-order than the fluid-velocity gradients. Next, a Taylor series can be used to replace the volume average of a quantity q in terms of properties at the centroid if the particle is spherical:

$$\iiint_{\forall_p} q d\forall_p = \forall_p \left[q_{@p} + \frac{d^2}{40} \left(\nabla^2 q\right)_{@p} + \frac{d^4}{4480} \left(\nabla^4 q\right)_{@p} + ... \right] \tag{3.70}$$

Making the second assumption of creeping flow which yields Faxen corrections for the fluid stress and added mass forces:

$$\vec{F}_{SG} = \rho_f \forall_p \frac{D}{Dt} \left[\vec{V}_{f,@p} + \frac{d^2}{40} \left(\nabla^2 \vec{V}_f\right)_{@p} \right] - \rho_f \forall_p \vec{g} \tag{3.71}$$

$$\vec{F}_{AM} = -C_M \rho_f \forall_p \frac{d}{dt} \left[\vec{V}_p - \vec{V}_{f,@p} - \frac{d^2}{40} \left(\nabla^2 \vec{V}_f\right)_{@p} \right] \tag{3.72}$$

This added-mass correction is equal to that of MR (Eq. 3.10) but the correction for the fluid-stress force was not included by MR (Eq. 3.9) since they assumed that the fluid stress was approximately constant in the vicinity of the sphere (which is a generally reasonable assumption). Thus, the conventional Faxen corrections are consistent with, but actually less accurate than, the volume-average expressions of Eqs. 3.67 & 3.68 for finite Reynolds numbers.

The lift in a non-uniform flow at small Reynolds numbers was discussed by Saffman [71], who found a solution for a linear shear field. He also discussed the potential extension to Poiseuille flow with non-uniform shear but found the problem to be "intractable". Because of this, no Faxen-type

corrections have been previously derived for lift. However, the Saffman lift derivation is based on a surface integral of the square root of the vorticity, so that the lift force for small but finite Reynolds numbers can be written as

$$\vec{F}_{L,Saff} = 1.615\rho_f d_p^2 \sqrt{\frac{\nu_f}{\omega_{shear,surf}}} \left(\vec{\omega}_{shear,surf} \times \left(\vec{V}_p - \vec{V}_{f,surf}\right)\right) + \mathcal{O}\left(d_p^3 \frac{\nabla\omega_{shear,surf}}{\sqrt{\omega_{shear,surf}}}, d_p^4 \frac{\nabla^2\omega_{shear,surf}}{\sqrt{\omega_{shear,surf}}}\right) \tag{3.73}$$

The third-order truncation term may be expected to be small owing to symmetry (as found for other surface and volume forces) as is the fourth-order truncation term since $\nabla^2\omega \equiv 0$ for Stokes flow. However, a better understanding of these truncation terms probably requires numerical experiments in flows with varying vorticity.

3.3.2 Surface force in non-uniform inviscid flow

The AHP expressions for surface-force include fluid-stress, added-mass and lift forces. Recall the fluid-stress force is simply the continuous-phase stresses on the particle surface in the absence of the particle disturbances. This can be transformed to a volume integral based by employing Gauss's theorem. As such, the inviscid fluid-stress force is equal to the low Reynolds number volume-averaged form of Eq. 3.67. This is not surprising force since this derivation is independent of particle Reynolds number.

The added mass for a quadratically varying shear flow is difficult to assess as there is no closed-form inviscid solution for a solid sphere. However, one may reasonably argue that it should be the same as that in Eq. 3.68, where the creeping flow result for a solid particle in a non-uniform flow arises directly from a volume average. This is because the added mass force for both uniform flow and linear shear is the same at both creeping flow and inviscid flow and is independent of particle Reynolds number for intermediate conditions.

The only other remaining inviscid force to consider is the Auton lift force. For constant vorticity, the inviscid lift is the same for pure rotational flow as it is for linear shear flow (which includes strain). If the flow does not have any strain so that it is in pure rotation, the vorticity does not affect the zero-penetration surface boundary conditions and so can vary radially. Neglecting the time derivatives, assuming weak gradients in the vorticity, and employing the linearization for

surface pressure of [22] allows the lift force to be expressed as:

$$\vec{F}_L = \frac{1}{2}\rho_f \forall_p \left[\vec{\omega}_{vortex,surf} \times \left(\vec{V}_p - \vec{V}_{f,surf}\right)\right] \tag{3.74}$$

Since the inviscid lift derivation is not straightforward for shear flow with non-uniform vorticity as discussed above, truncation terms are needed to generalize the lift force:

$$\vec{F}_L = \frac{1}{2}\rho_f \forall_p \left[\vec{\omega}_{surf} \times \left(\vec{V}_p - \vec{V}_{f,surf}\right)\right] + \mathcal{O}\left(d_p^3 \frac{\nabla\omega_{surf}}{\sqrt{\omega_{surf}}},\ d_p^4 \frac{\nabla^4\omega_{surf}}{\sqrt{\omega_{surf}}}\right) \tag{3.75}$$

Quantitative assessment for the truncation terms in the above expression may require numerical experiments in such flows. However, the impact of vorticity gradients may be weak based on the results of Merle et. al. [25].

3.3.3 Generalized particle surface force in non-uniform flow

Based on the above, a semi-empirical expression for a spherical particle which is solid or a contaminated fluid at finite Reynolds number and non-uniform unsteady flows can be constructed:

$$\begin{aligned}
\vec{F}_{surf} \;=\; & -3\pi d_p \mu_f \left(\vec{V}_p - \vec{V}_{f,surf}\right)\left(1 + 0.15 Re_{p,surf}^{0.687}\right) \\
& + \rho_f \forall_p \left[(1 + C_M)\left(\frac{D\vec{V}_f}{Dt}\right)_{vol} - C_M \frac{d\vec{V}_p}{dt}\right] \\
& + \vec{F}_L\left(\vec{V}_{f,surf},\, \vec{\omega}_{surf}\right) \\
& - 3\pi d_p \mu_f \left[\int_0^t K\left(t-\tau,\, Re_{p,surf}\right) \frac{d\left(\vec{V}_p - \vec{V}_{f,surf}\right)}{d\tau} d\tau\right] \\
& - \rho_f \forall_p \vec{g}
\end{aligned} \tag{3.76}$$

This form is limited to Re_p of 50 or less and spin-equilibrium if one employs the empirical corrections for the history force and lift force discussed in Sections 3.2.2 and 3.2.3 but the relative velocity in the Reynolds number should be replaced with a surface-average. However, it should be noted that the non-uniform effects have only been strictly derived for limits of small Reynolds number and inviscid conditions for certain sets of these forces. Similar corrections can be applied to the particle energy ODE with heat and mass transfer since [81] shows that it employs a Laplacian correction for the continuous-phase temperature analogous to the Faxen correction for the momentum transfer. As such, a "Michaelides correction" for surface heat transfer can be

represented by employing a surface-averaged fluid temperature while the unhindered thermal stress can be described in terms of a volume-averaged fluid temperature.

3.3.4 Discrete surface- and volume-averages

For the discrete form of the surface and volume-averages, it is straightforward to use sampling at particular locations. The surface-average can employ six sampling points to capture the gradients in all three directions. If the surface sampling points are denoted by (x_s, y_s, z_s), they can be set based on left/right, top/bottom and front/back, i.e. $x_s = x_p \pm r_p$, $y_s = y_p \pm r_p$, and $z_s = z_p \pm r_p$. The surface-averaged velocity is then

$$\vec{V}_{f,surf} = \frac{1}{A_p} \iint_{A_p} \vec{V}_f dA_p \approx \frac{1}{6} \sum_{i=1}^{6} \vec{V}_{f,s} \equiv \vec{V}_{f,surf,\Sigma} \tag{3.77}$$

A similar six-point approach for the surface-averaged vorticity can be used for lift. To show that this sampling gives a reasonable surface-average description, consider an unhindered flowfield with a polynomial variation in horizontal shear and a uniform vertical velocity:

$$\vec{V}_f = u_{f,@p} \left[1 + \frac{y}{l_1} + \left(\frac{y}{l_2}\right)^2 + \left(\frac{y}{l_3}\right)^3 + \left(\frac{y}{l_4}\right)^4 + \left(\frac{y}{l_5}\right)^5 \right] \hat{\imath} + v_{f,@p} \hat{\jmath} \tag{3.78}$$

In this expression l_1, l_2, etc. are length-scale constants which are inversely proportional to the velocity derivatives which are first-order, second-order, etc. Substitution into Eq. 3.77 yields:

$$\vec{V}_{f,surf,\Sigma} = \vec{V}_{f,@p} + \frac{d_p^2}{24} \left(\nabla^2 \vec{V}_f\right)_{@p} + \frac{d^4}{1152} \left(\nabla^4 \vec{V}_f\right)_{@p} \tag{3.79}$$

For Stokes flow with $\nabla^4 \vec{V}_f \equiv 0$, the discrete distributed-force method is identical to the exact solution and the Faxen correction even if the sampling points on the sphere are rotated. In contrast, the conventional point-force (using only $\vec{V}_{f,@p}$) yields a second-order error which increases with the particle diameter and flow gradient as shown in Figure 3.15. For non-Stokesian flows with a finite $\nabla^4 \vec{V}_f$, the discrete average (Eq. 3.79) is fourth-order accurate in diameter compared to both the exact solution (Eq. 3.64) and the Faxen correction (Eq. 3.63) and substantially more accurate than a conventional point-force (Figure 3.15b).

For the volume-averaged fluid acceleration, it is convenient and computationally efficient to use the same six surface sampling points along with an additional sampling point at the particle centroid

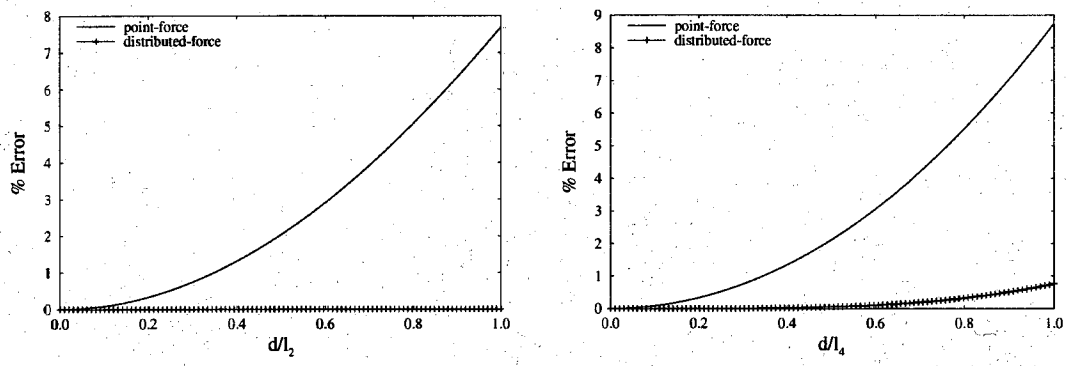

a) quadratic variation b) quartic variation

Figure 3.15: Surface-averaged horizontal force error for point-force and distributed-force approaches for a stationary particle subjected to polynomial shear flows of quadratic and quartic variation.

$(\vec{x}_p)$. This combination can be optimized using a fourth-order accurate Simpson's rule for spherical integration to approximate the volume average:

$$\left(\frac{D\vec{V}_f}{Dt}\right)_{vol} = \frac{1}{\forall_p}\iiint_{\forall_p}\left(\frac{D\vec{V}_f}{Dt}\right)d\forall_p \approx \frac{3}{5}\left[\frac{1}{6}\sum_{i=1}^{6}\left(\frac{D\vec{V}_f}{Dt}\right)_{s,i}\right] + \frac{2}{5}\left(\frac{D\vec{V}_f}{Dt}\right)_{@p} = \left(\frac{D\vec{V}_f}{Dt}\right)_{vol,\Sigma} \tag{3.80}$$

Application of this discrete approximation to the steady velocity field of Eq. 3.78, for which

$$\left(\frac{D\vec{V}_f}{Dt}\right) = v_{f,@p}\frac{\partial u}{\partial y}\hat{i} \tag{3.81}$$

yields:

$$\left(\frac{D\vec{V}_f}{Dt}\right)_{vol,\Sigma} = \left(\frac{D\vec{V}_f}{Dt}\right)_{@p} + \frac{d_p^2}{40}\left[\nabla^2\left(\frac{D\vec{V}_f}{Dt}\right)\right]_{@p} + \frac{d^4}{1920}\left[\nabla^4\left(\frac{D\vec{V}_f}{Dt}\right)\right]_{@p} \tag{3.82}$$

Again, the discrete sampling method and the Faxen correction (Eq. 3.67) are exact for Stokes flow conditions and (based on Eq. 3.70) are fourth-order accurate with respect to particle diameter for non-Stokesian flows. Comparisons are made in Figure 3.16 of the point-force and distributed force error compared to the analytical solution for both the complete velocity field described by Eq. 3.78 and truncated velocity field which neglects the 4^{th} and 5^{th}-order terms. Figure 3.16 shows that the distributed force formulation is exact for the cubic variation (as expected) while the point-force expression admits $\sim 4.5\%$ error at $d/l_3 = 1$. The distributed force admits errors on the higher-order variation but is still $\sim 5x$ more accurate than the point-force formulation at $d/l_5 = 1$.

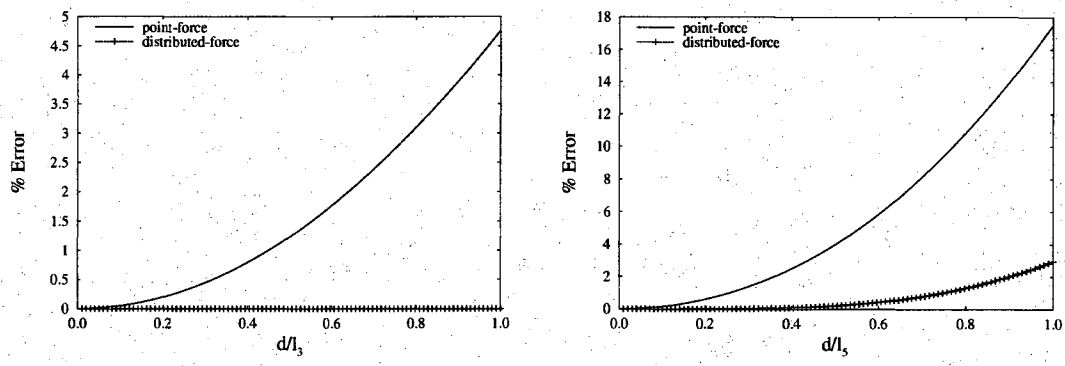

a) cubic variation b) quintic variation

Figure 3.16: Volume-averaged error for point-force and distributed-force formulations for a stationary particle subjected to a polynomial shear flow velocity variation that is: a) cubic and b) quintic.

3.3.5 Sinusoidal shear flow

To investigate the discrete distributed-force approach in the context of a flowfield more relevant to turbulence, a sinusoidal shear layer is considered whose spatial variation is characterized by a length scale and a velocity amplitude:

$$\vec{V}_f = u_l \sin\left(\frac{2\pi y}{l}\right)\hat{\imath} + v_{y@p}\hat{\jmath} \tag{3.83}$$

The horizontal velocities for the point-force, exact and discrete surface-averages are given by:

$$u_{@p} = u_l \sin\left(\frac{2\pi y_p}{l}\right) \tag{3.84}$$

$$u_{surf} = u_l \sin\left(\frac{2\pi y_p}{l}\right)\left[1 - \frac{(\pi d_p)^2}{6} + \frac{(\pi d_p)^4}{320}\right] \tag{3.85}$$

$$u_{surf,\Sigma} = u_l \sin\left(\frac{2\pi y_p}{l}\right)\left[1 - \frac{(\pi d_p)^2}{6} + \frac{(\pi d_p)^4}{72}\right] \tag{3.86}$$

Again, the point-force method is second-order accurate in particle diameter and the discrete method is fourth-order accurate (a result which can also be shown to be true for a volume average). A spatially-integrated velocity difference from the exact solution may be obtained by considering all particle positions in the sine wave (equivalent to the particle moving at a constant vertical speed through one wavelength). The error in the point-force expression for a

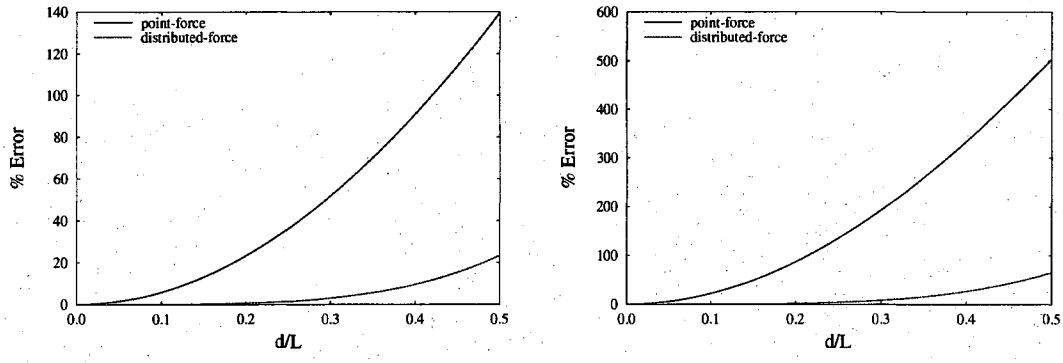

a) surface-average b) volume-average

Figure 3.17: Horizontal force errors for point-force and distributed-force representations for a particle subjected to a sinusoidal shear flow based on: a) surface-average and b) volume-average.

surface-averaged horizontal force (e.g., drag force) can be expressed as:

$$\text{error} = [u_{surf} - u_{@p}]_{rms} = \left[\frac{1}{2\pi l}\int_0^{2\pi l} [u_{surf} - u_{@p}]^2 \, dy_p\right]^{1/2} \tag{3.87}$$

The integrated errors are shown in Figure 3.17a, for which an increase in particle diameter with respect to the wavelength results in a substantial increase for the point-force approach. For the distributed-force approach, the errors are generally an order of magnitude smaller. A similar result is found volume-averaged forces of added mass and fluid-stress (based on the volume-averaged fluid acceleration) as shown in Figure 3.17b.

Based on the above analysis, some comments may be made on possible implications for turbulent flow conditions. Consider a particle falling at a speed approximately equal to its terminal velocity which approximately follows Stokes drag law. Assume that the flow is composed of a range of wavelengths (l) where each is associated with a velocity fluctuation amplitude (u_l) all superimposed upon a mean velocity ($\bar{u}$). The errors in the drag point-force method for a given wavelength will be small if the turbulence is weak ($u_l \ll \bar{u}$) or if the particle is small ($d_p \ll l$). For finite particle sizes with $d_p < l$, the relative drag force error is of order $(u_l d_p)/(\bar{u}l)^2$. Since the turbulence intensity in the inertial sub-range varies only weakly with wavelength, $u_l \sim (\epsilon l)^{1/3}$, the largest errors will occur as $d_p \to l$. However, once the particles become larger ($d_p > l$), the wavelengths become sub-scale and so that variations across the particle only increase weakly, i.e. with $l^{1/3}$. As such, the point-force errors can be primarily related to wavelengths on the order of the particle size. In turbulence, this indicates that the errors will scale with $u'_{rms}/(u'_{rms} + \bar{u})$ for

particle sizes larger than the Kolmogorov scale ($d_p > \lambda$) where u'_{rms} is the turbulence intensity and is proportional to u_l. This result is qualitatively consistent with resolved-surface simulations of [82] for $d = 2\lambda$ and $Re_p \sim 5 - 20$ who noted that the point-force errors (primarily related to drag) were as large as 30% and scaled with turbulence intensity. The trends shown in Figure 3.17 indicate that the errors for the distributed force may be an order of magnitude smaller than that for the point-force, but investigation with resolved-surface simulations and/or experiments are needed before this can be confirmed for turbulent flow or even simple polynomial or sinusoidal shear flows. Furthermore, the proposed distributed force expressions are developed based on theoretical limits for idealized conditions of a single spherical particle and may only be approximate for lift and do not include effects of fluid strain [83].

3.4 EOM summary and non-dimensionalization

In this section, the form of the Lagrangian particle equation of motion is summarized. Recalling the general form of the particle equation of motion given by Eq. 3.4, along with the surface and body forces previously discussed, one can write the equation of motion for a spherical particle as

$$\begin{aligned}
\rho_p \forall_p \frac{d\vec{V}_p}{dt} &= -3\pi\rho_f \nu d_p f \vec{V}_{rel} \\
&\quad + \frac{\pi}{8}\rho_p \left(\vec{V}_{rel}\cdot\vec{V}_{rel}\right) d_p^2 \vec{C}_L \\
&\quad + C_M \rho_f \forall_p \left[\left(\frac{D\vec{V}_f}{Dt}\right)_{vol} - \frac{d\vec{V}_p}{dt}\right] \\
&\quad + \rho_f \forall_p \left(\frac{D\vec{V}_f}{Dt}\right)_{vol} - \rho_f \forall_p \vec{g} \\
&\quad - 3\pi\rho_f \nu d_p \int_{t-t_{window}}^{t} K_{Basset}(t-\tau)\frac{d\vec{V}_{rel}}{d\tau} d\tau \\
&\quad + \rho_p \forall_p \vec{g}
\end{aligned} \tag{3.88}$$

where the first term on the right-hand-side is the quasi-steady drag force and f represents the Schiller-Naumann finite Reynolds number correction, the second is the lift force, the group of terms on the third line is the added mass which is followed on the next line by the fluid stress gradient force, the fifth line gives the unsteady drag (or history force), and the final line is the body force, or weight, of the particle. In the above expression, the form of $\vec{V}_{rel}$, $\vec{C}_L$, K, and the meaning of and $(...)_{vol}$ will be summarized later. A more convenient form of the equation of

motion can be obtained through algebraic manipulation, outlined below.

Dividing each term in Eq. 3.88 by $\rho_p \forall_p$ and introducing the density ratio, ψ, one can write

$$\begin{aligned}\frac{d\vec{V}_p}{dt} &= -\frac{3\pi\nu d_p}{\psi\forall_p} f\vec{V}_{rel} + \frac{\pi\left(\vec{V}_{rel}\cdot\vec{V}_{rel}\right)d_p^2}{8\psi\forall_p}\vec{C}_L + \frac{C_M}{\psi}\left[\left(\frac{D\vec{V}_f}{Dt}\right)_{vol} - \frac{d\vec{V}_p}{dt}\right] + \frac{1}{\psi}\left(\frac{D\vec{V}_f}{Dt}\right)_{vol} \\ &\quad -\frac{3\pi\nu d_p}{\psi\forall_p}\int_{t-t_{window}}^{t} K_{Basset}(t-\tau)\frac{d\vec{V}_{rel}}{d\tau}d\tau + \frac{1}{\psi}(\psi-1)\vec{g} \end{aligned} \tag{3.89}$$

where the buoyancy component of the fluid stress term has been combined with the body force. Noting that the added mass contains the particle acceleration the next step involves moving that term to the left-hand-side, combining the fluid derivatives, and multiplying each term by the density ratio, e.g.

$$\begin{aligned}(\psi+C_M)\frac{d\vec{V}_p}{dt} &= -\frac{3\pi\nu d_p}{\forall_p} f\vec{V}_{rel} + \frac{\pi\left(\vec{V}_{rel}\cdot\vec{V}_{rel}\right)d_p^2}{8\forall_p}\vec{C}_L + (1+C_M)\left(\frac{D\vec{V}_f}{Dt}\right)_{vol} \\ &\quad -\frac{3\pi\nu d_p}{\forall_p}\int_{t-t_{window}}^{t} K_{Basset}(t-\tau)\frac{d\vec{V}_{rel}}{d\tau}d\tau + (\psi-1)\vec{g} \end{aligned} \tag{3.90}$$

Using the definition of the spherical particle volume, $\forall_p \equiv d_p^3\pi/6$, and dividing each term by the coefficient on the left-hand-side, one obtains

$$\begin{aligned}\frac{d\vec{V}_p}{dt} &= -\frac{18\nu}{(\psi+C_M)d_P^2} f\vec{V}_{rel} + \frac{3\left(\vec{V}_{rel}\cdot\vec{V}_{rel}\right)}{4(\psi+C_M)d_p}\vec{C}_L + \frac{1+C_M}{\psi+C_M}\left(\frac{D\vec{V}_f}{Dt}\right)_{vol} \\ &\quad -\frac{18\nu}{(\psi+C_M)d_P^2}\int_{t-t_{window}}^{t} K_{Basset}(t-\tau)\frac{d\vec{V}_{rel}}{d\tau}d\tau + \frac{\psi-1}{\psi+C_M}\vec{g} \end{aligned} \tag{3.91}$$

At this point the "particle response time" or "particle relaxation time" scale may be introduced to give

$$\begin{aligned}\frac{d\vec{V}_p}{dt} &= -\frac{f\vec{V}_{rel}}{\tau_p} + \frac{Re_p\|\vec{V}_{rel}\|}{24\tau_p}\vec{C}_L + \frac{1+C_M}{\psi+C_M}\left(\frac{D\vec{V}_f}{Dt}\right)_{vol} \\ &\quad -\frac{1}{\tau_p}\int_{t-t_{window}}^{t} K_{Basset}(t-\tau)\frac{d\vec{V}_{rel}}{d\tau}d\tau + \frac{\psi-1}{\psi+C_M}\vec{g} \end{aligned} \tag{3.92}$$

where the particle response time, τ_p, is given by Eq. 3.34.

The above equation can be used to give an expression for the terminal velocity of a spherical particle in a quiescent fluid. At terminal velocity, the left-hand-side will be zero such that the equation of motion reduces to the drag force balancing the particle body force. Carrying out this

analysis one can show that the terminal velocity is given by

$$\vec{V}_{term} = \left(\frac{\psi - 1}{\psi + C_M}\right)\frac{\tau_p \vec{g}}{f} \tag{3.93}$$

which for the case of a small particle Reynolds number (i.e. one for which Stokes drag law is appropriate) $f = 1$ such that the Stokesian terminal velocity is given by

$$\vec{V}_{term,Stokes} = \left(\frac{\psi - 1}{\psi + C_M}\right)\tau_p \vec{g} \tag{3.94}$$

Using this result the body force can be re-written compactly as

$$\frac{\psi - 1}{\psi + C_M}\vec{g} = \frac{\vec{V}_{term,Stokes}}{\tau_p} \tag{3.95}$$

As a final manipulation of the particle equation of motion we introduce reference quantities which lead to a non-dimensional form. Herein the reference velocity and time-scales will be u_τ (the friction velocity) and τ_p (the particle response time), respectively, such that

$$\vec{V}^* = \frac{\vec{V}}{u_\tau} \tag{3.96}$$

$$t^* = \frac{t}{\tau_p} \tag{3.97}$$

where the superscript * denotes a non-dimensional quantity. Using these reference quantities in Eq. 3.92 the equation of motion may be recast in non-dimensional form as

$$\begin{aligned}\frac{d\vec{V}_p^*}{dt} &= -f\vec{V}_{rel}^* + \frac{Re_p\|\vec{V}_{rel}^*\|}{24}\vec{C}_L + \frac{1 + C_M}{\psi + C_M}\left(\frac{D\vec{V}_f^*}{Dt^*}\right)_{vol} \\ &\quad - \int_{t^* - t^*_{window}}^{t^*} K_{Basset}\left(t - \tau\right)\frac{d\vec{V}_{rel}^*}{d\tau^*}d\tau^* + \gamma_{Stokes}\frac{\left(\psi - 1\right)\vec{g}}{\|\left(\psi - 1\right)\vec{g}\|}\end{aligned} \tag{3.98}$$

where γ_{Stokes} can be thought of as an approximate drift parameter defined as

$$\gamma_{Stokes} \equiv \frac{\|\vec{V}_{term,Stokes}\|}{u_\tau} \tag{3.99}$$

which is similar to the standard drift parameter

$$\gamma \equiv \frac{\|\vec{V}_{term}\|}{u_\tau} \tag{3.100}$$

To complete Eq. 3.98 we now summarize the relative velocity, lift coefficient, history kernel, and the surface and volume averaged fluid velocity derivatives (where the "*" notation has been dropped for convenience)

$$\vec{V}_{rel} = \vec{V}_p - \vec{V}_{f,surf} \tag{3.101}$$

$$f = 1.0 + 0.15 Re_p^{0.687} \tag{3.102}$$

$$\vec{C}_L = C_{L,McL} \frac{\vec{\omega} \times \vec{V}_{rel}}{\|\vec{\omega} \times \vec{V}_{rel}\|} + C^*_{L,\Omega} \frac{\vec{\Omega} \times \vec{V}_{rel}}{\|\vec{\Omega} \times \vec{V}_{rel}\|} \tag{3.103}$$

$$C_{L,McL} = J^* C_{L,Saff} = J^* \frac{12.92}{\pi} \sqrt{\frac{\omega^*}{Re_p}} \tag{3.104}$$

$$\begin{aligned} J^* \simeq\ & 0.3 \left\{ 1 + \tanh \left[\frac{5}{2} \left(\log_{10} \sqrt{\frac{\omega^*}{Re_p}} + 0.191 \right) \right] \right\} \\ & * \left\{ \frac{2}{3} + \tanh \left[6 \sqrt{\frac{\omega^*}{Re_p}} - 1.92 \right] \right\} \end{aligned} \tag{3.105}$$

$$C^*_{L,\Omega} = 1 - \left\{ 0.675 + 0.15 \left(1 + \tanh \left[0.28 \left(\Omega^*_{p,eq} - 2 \right) \right] \right) \right\} \tanh \left[0.18 Re_p^{1/2} \right] \tag{3.106}$$

$$\Omega^*_{p,eq} = \frac{\omega^*}{2} \left(1 - 0.0075 Re_\omega \right) \left(1 - 0.062 Re_p^{1/2} - 0.001 Re_p \right) \tag{3.107}$$

$$\omega^* = \frac{\|\vec{\omega}_{surf}\| d_p}{\|\vec{V}_{rel}\|} \tag{3.108}$$

$$\Omega^* = \frac{\Omega_p d_p}{\|\vec{V}_{rel}\|} \tag{3.109}$$

$$Re_p = \frac{d_p V_{rel}}{\nu} \tag{3.110}$$

$$Re_\omega = \frac{\|\vec{\omega}\|_{surf} d_p^2}{\nu} \tag{3.111}$$

$$K_{Basset} = \left[\frac{4\pi(t-\tau)}{d_p^2} \right]^{-1/2} \tag{3.112}$$

$$t - t_{window} = \min \left(0, t - \tau_H \tau_d \right) \tag{3.113}$$

$$\tau_H = \left(\frac{0.502}{Re_p} + 0.123 \right)^2 \tag{3.114}$$

$$(...)_{surf} = \frac{1}{6} \left[(...)_{(x_p \pm r_p, y_p, z_p)} + (...)_{(x_p, y_p \pm r_p, z_p)} + (...)_{(x_p, y_p, z_p \pm r_p)} \right] \tag{3.115}$$

$$(...)_{vol} = \frac{2}{5} (...)_{(x_p, y_p, z_p)} + \frac{3}{5} (...)_{surf} \tag{3.116}$$

3.5 Numerical solution of the equation of motion

This section describes the numerics associated solving the particle equation of motion coupled to the DNS field. The first section discusses the procedure for temporally advancing the particle position–this is heart of the Lagrangian tracking method used in this research. A second section covers methods for interpolating the continuous-phase properties (generally considered to reside at the nodes of the computational grid) to inter-cell locations which are required by the particle equation of motion. Several techniques are discussed and the effect they have on the outcome of the simulation will be discussed in Section 5.2.

3.5.1 Temporal integration

The equation of motion (Eq. 3.98) is numerically advanced using an exponential-Lagrangian scheme implemented in a predictor-corrector for second-order accuracy in time. The exponential-Lagrangian scheme was presented by Barton [84] for a heavy particle under the influence of Stokes drag. Herein additional forces are considered such that the general from of equation of the equation of motion can be given by

$$\frac{d\vec{V}_p}{dt} + \frac{1}{\tau_p}\vec{V}_p = \vec{G}(t) \tag{3.117}$$

where $\vec{G}(t)$ is a general function of time chosen such that the above equation matches Eq. 3.98. i.e.

$$\begin{aligned}\vec{G}(t) \;=\; & \frac{\vec{V}_f}{\tau_p} f + \frac{\vec{V}_p}{\tau_p}(1-f) + \frac{Re_p \|\vec{V}_{rel}\|}{24\tau_p}\vec{C}_L + \frac{1+C_M}{\psi + C_M}\left(\frac{D\vec{V}_f}{Dt}\right)_{vol} \\ & -\frac{1}{\tau_p}\int_{-\infty}^{t} K(t-\tau)\frac{d\vec{V}_{rel}}{d\tau}d\tau + \gamma_{Stokes}\frac{(\psi-1)\vec{g}}{\|(\psi-1)\vec{g}\|}\end{aligned} \tag{3.118}$$

The analytical solution of the above equation between times t_1 and t_2 is given by

$$e^{t_2/\tau_p}\vec{V}_p(t_2) - e^{t_1/\tau_p}\vec{V}_p(t_1) = \int_{t_1}^{t_2} e^{t/\tau_p}\vec{G}(\tau)\,d\tau \tag{3.119}$$

If we assume that $\vec{G}$ is approximately constant over the interval $[t_1, t_2]$, we can simplify the expression to

$$\vec{V}_p(t_2) = e^{-\Delta t/\tau_p}\vec{V}_p(t_1) + \tau_p\left(1 - e^{-\Delta t/\tau_p}\right)\vec{G}(\bar{t}) \tag{3.120}$$

where $\Delta t = t_2 - t_1$ is the "time-step" and $\bar{t} \in [t_1, t_2]$ has yet to be given a specific value but controls the character of the numerical solution. Equation 3.120 is the Exponential-Lagrangian scheme written for a generic, non-homogeneous, separable, differential equation and is unconditionally stable if $\vec{G}$ is simply a constant. This is the same form obtained by Bocksell [50]. If $\bar{t} = t_1$ then Eq. 3.120 is called an *explicit* scheme and if $\bar{t} = t_2$ the Eq. 3.120 is called an *implicit* scheme. If $\vec{G}$ is sufficiently constant over the interval than the choice of t_i is largely irrelevant. However, in most application $\vec{G}$ will be strongly varying in time and the choice t_i will affect the accuracy and stability of the numerical solution.

The key advantage of using Eq. 3.120 over simpler finite difference representations is that the exponential-Lagrangian scheme provides superior accuracy in the presence of large time-steps ($\Delta t > \tau_p$). Recalling the Maclaurin series for the exponential function

$$e^{-x} = \sum_{n=0}^{\infty} \frac{(-x)^n}{n!} = 1 - x + \frac{x^2}{2} - \frac{x^3}{6} + ... \tag{3.121}$$

and substituting into Eq. 3.120 we obtain

$$\vec{V}_p(t_2) = \left(1 - \Delta t^* + \frac{\Delta t^{*2}}{2} - \frac{\Delta t^{*3}}{6} + ...\right)\vec{V}_p(t_1) + \tau_p\left(\Delta t^* - \frac{\Delta t^{*2}}{2} + \frac{\Delta t^{*3}}{6} - ...\right)\vec{G}(t_i) \tag{3.122}$$

where $\Delta t^* = \Delta t/\tau_p$. In the limit of vanishingly small Δt^{*2} the above equation reduces to the implicit or explicit Euler schemes (depending on the choice of t_i). However, when Δt^{*2} is appreciable the exponential-Lagrangian scheme will remain stable and accurate where the Euler methods will suffer from inaccuracies (and instabilities in the explicit case). Thus, using the exponential-Lagrangian scheme can alleviate the prohibitively small Δt restriction for low inertia particles.

Equation 3.120 provides an update which is exact if $\vec{G}$ is constant but is only first-order accurate if $\vec{G}$ varies with time. To obtain higher-order prediction, the scheme can be implemented as a multistep method as discussed by [50]. The derivation follows that of the common multistep methods referred to as the Adams-Bashforth (explicit) and Adams-Moulton (implicit) schemes. These methods provide higher-accuracy integration by retaining information from previous time-steps and using that information as collocation points for an interpolating polynomial and

Table 3.2: Exponential-Lagrangian multistep methods

Order of accuracy	c_0	c_1	G_0	G_1
$O(\Delta t)$ Explicit	1	N/A	$G(t)$	N/A
$O(\Delta t^2)$ Explicit	$3/2$	$-1/2$	$G(t)$	$G(t-\Delta t)$
$O(\Delta t)$ Implicit	1	N/A	$G(t+\Delta t)$	N/A
$O(\Delta t^2)$ Implicit	$1/2$	$1/2$	$G(t+\Delta t)$	$G(t)$

have the general form of

$$\vec{V}_p\left(t+\Delta t\right) = e^{-\Delta t/\tau_p}\vec{V}_p\left(t\right) + \tau_p\left(1-e^{-\Delta t/\tau_p}\right)\left(c_0\vec{G}_0 + c_1\vec{G}_1 + ...\right) \tag{3.123}$$

where "c_i" represents a set of constants and "$\vec{G}_i$" is the right-hand-side evaluated at different times. The constants for a particular order or accuracy are determined in the same fashion as for the Adams-Bashforth-Moulton methods.

Table 3.2 gives the results obtained by [50] for first and second-order accurate implicit and explicit schemes for the exponential Lagrangian. These schemes turn out to have the same coefficients as the standard Adams-Bashforth-Moulton schemes for the presented orders of accuracy but unlike the standard schemes, the present method cannot be extended beyond second-order [50]. However, we choose the present schemes in favor of the conventional methods due to its enhanced stability for low-inertia drag-dominated particles. The appropriate convergence rate for the first and second-order schemes is illustrated in Figure 3.18, however, the present DNS work uses only the second-order methods.

As for standard multistep methods, the truncation error at a given order of accuracy will be less for the implicit scheme than for its explicit counterpart. This combined with the additionally stability implied by an implicit scheme drives us to seek an implementation that can take advantage of the more accurate method. Since the implicit method requires $\vec{V}_p(t+\Delta t)$ (through $\vec{G}(t+\Delta t)$) on both the left and right-hand-sides we must have some approximation of the solution at the next time to use the implicit algorithm. In the context of multistep methods, this approximation is typically obtained by using one of the explicit schemes to *predict* the solution at the next time-step. Then the implicit scheme can be used to *correct* the predicted solution and obtain a higher fidelity update. This is the essence of a *predictor-corrector* scheme which is sometimes referred to as PECE (predict-evaluate-correct-evaluate). The present approach uses an equivalent interrupted version that allows simple implementation within the DNS code and

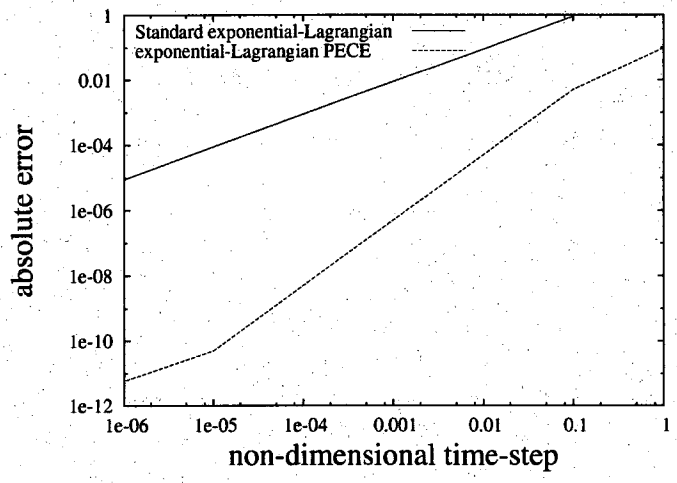

Figure 3.18: Convergence of the first and second-order accurate exponential-Lagrangian schemes.

prevents storing the fluid solution at multiple time instances. The present approach is sketched in Figure 3.19 where the interrupted nature of the algorithm makes it appear in reverse order, i.e. ECEP. While implemented in generic fashion, the present study used two iterations of the corrector phase; a compromise between efficiency and accuracy.

The interrupted predictor-corrector algorithm was implemented to accommodate the terms on the right-hand-side of Eq. 3.98 that are functions of fluid quantities while allowing the original DNS code to serve as the main program and the particle tracking as a callable feature. Thus at the top of Figure 3.19 we have a fluid velocity field and its derivatives at a given point in time. This fluid solution serves as the "$t + \Delta t$" field for the previous particle time-step and as the "t" field for the current time-step. Thus, the algorithm completes (corrects) the previous time-step and initializes (predicts) the particle field for the next time-step before returning to update the fluid solution for the next time-step.

The fluid solution computed at the beginning of Figure 3.19 is comprised of the spectrally-accurate velocity and vorticity at each grid node. The substantial derivative of the fluid velocity is also required to evaluate the right-hand-side. Expanding the substantial derivative leads to an approach for obtaining the quantity at the grid nodes (where the streamwise velocity is used for the sake of illustration):

$$\frac{Du_f}{Dt} = \frac{\partial u_f}{\partial t} + \vec{V}_f \cdot \nabla u_f \tag{3.124}$$

The spatial derivatives are obtained in wave-space such that gradient at the nodes is obtained with

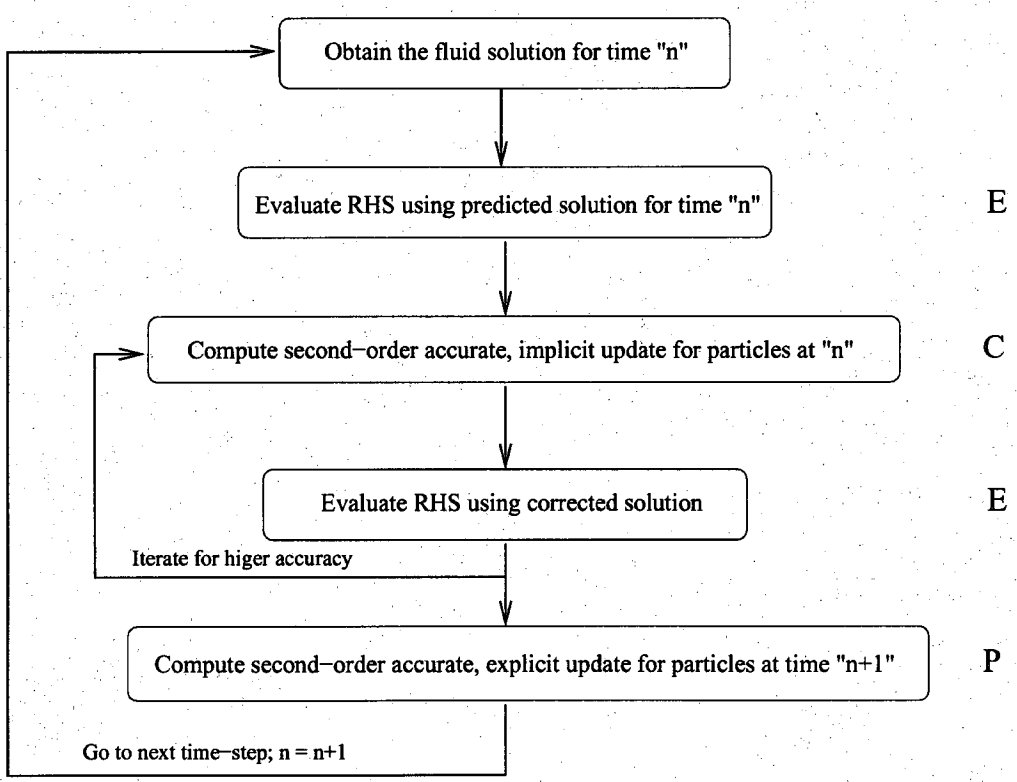

Figure 3.19: Illustration of predictor-corrector scheme.

the same accuracy as the velocity field. The temporal derivative is simply evaluated using a three-point backwards difference of the velocity field from previous time-steps. The three-point stencil gives second-order accurate approximation which is consistent with the temporal discretization of the particle equation of motion and can be shown to have the following form (accounting for a variable time-step):

$$\left(\frac{\partial u_f}{\partial t}\right)^n \approx \frac{u^n\left(\left(\Delta t_1+\Delta t_2\right)^2-\Delta t_1^2\right)-u^{n-1}\left(\Delta t_1+\Delta t_2\right)^2+u^{n-2}\Delta t_1^2}{\Delta t_1\left(\Delta t_1+\Delta t_2\right)^2-\Delta t_1^2\left(\Delta t_1+\Delta t_2\right)} \tag{3.125}$$

where

$$\Delta t_1 = t^n - t^{n-1} \tag{3.126}$$

$$\Delta t_2 = t^{n-1} - t^{n-2} \tag{3.127}$$

and where the superscript "n" denotes the current time-level.

3.5.2 Spatial interpolation of fluid quantities

In general, the particle positions will not coincide with the nodes of the continuous-phase mesh. Therefore, inter-cell reconstruction of the solution is required to obtain the fluid properties in the vicinity of the particle. This becomes especially important with very high accuracy representations of the flowfield as the variables can be rapidly and non-linearly changing across each cell. For the case of a spectral representation, one option is to evaluate the global basis functions at each particle position, e.g.

$$u\left(x,y,z,t\right) = \sum_{k_x,k_y,k_z} \hat{u}\left(k_x,k_y,k_z,t\right) * e^{ik_x x} * J\left(k_y,y\right) * e^{ik_z z} \tag{3.128}$$

where J represents the coefficients of the Jacobi polynomial $\hat{u}$ represents the transformed velocity (in Fourier and Jacobi space), and $k_{x,y,z}$ represents the modes solved for in the continuous-phase method. Given the solution in transformed-space, we could employ Equation 3.128 to obtain the physical-space velocity at any desired point within the computation domain. While this is accurate and consistent with the continuous-phase methodology (Chapter 2), it is computationally impractical when considering a large number of particles as the sum in Equation 3.128 should be taken over *all* computed modes. As such the present study seeks a different approach.

A tempting approach which is simple and quick to evaluate is to use tri-linear interpolation within the cell that contains the physical-space point of interest. This algorithm first identifies the cell containing the point and then forms a three-dimensional linear basis function from the eight nodes that define the cell (other comparable algorithms could be constructed for non-hexahedral cells). However, this approach will truncate higher-order variation that is available in the fluid solution given the high degree of accuracy provided by the pseudo-spectral solution algorithm. As such, a more accurate approach should be considered.

A general approach to polynomial interpolation is provided by writing the interpolant in Lagrange form. This approach will provide a variable degree of accuracy and is formulated from the data at the surrounding N nodes thus limiting the degrees of freedom to a manageable quantity but allowing for higher-order variation of the fluid properties. The resulting polynomial can then be evaluated at the desired location to obtain an approximation to the solution at that point. Squires and Eaton [85] studied Lagrangian turbulence statistics in isotropic turbulence using a Lagrange basis interpolant. That study was conducted with third-order accurate Lagrange polynomials and the authors noted that higher (than third-order) accuracy interpolants were not found to significantly modify the results.

For a 1–D grid in the x-direction, the data can be represented as:

$$u(x) = \sum_{m=1}^{N} u_m l_m(x) \tag{3.129}$$

$$l_m(x) = \prod_{i=1, i\neq m}^{N} \frac{x_p - x_i}{x_m - x_i} \tag{3.130}$$

where u is the fluid properties at the nodes, x is the position of the nodes, and x_p is the position we wish to interpolate. For an orthogonal three-dimensional grid where the spacing in a given direction is not a function of the other two directions, the interpolant is given by the product of the three 1-D interpolants, e.g.

$$u(x,y,z) = \sum_{i=1}^{N}\sum_{j=1}^{N}\sum_{k=1}^{N} u_{ijk} l_{ijk}(x,y,z) \tag{3.131}$$

$$l_{lmn}(x) = \prod_{l=1, l\neq i}^{N} \frac{x_p - x_l}{x_i - x_l} \prod_{m=1, m\neq j}^{N} \frac{y_p - y_m}{y_m - y_j} \prod_{n=1, n\neq k}^{N} \frac{z_p - z_n}{z_n - z_k} \tag{3.132}$$

General structured grid topologies will not satisfy these constraints in physical space. However,

they are always met when the grid is mapped to the typical uniform and orthogonal computational space. Other approaches are suggested by Marchioli, Armenio, and Soldati [86] for curvilinear grids. For the present study, the flat plate grid satisfies all requirements of the three-dimensional interpolant in physical space so no transformation is required. The general framework of this approach can be reduced to the tri-linear basis function described in the preceding paragraph by selecting $N = 2$, but can also be extended to higher-accuracy using a larger value of N. The present study will consider both $N = 2$ and $N = 4$ and the impact associated with the different schemes will be discussed in Section 5.2. The reduced-order variant ($N = 2$) is used for the heavy particle study discussed in Chapter 4 for second-order spatial accuracy. The case of $N = 4$ results in fourth-order spatial accuracy and will be used for the majority of the results generated in the low-density studies presented in Chapters 5 and 6.

The final piece of the interpolation algorithm is to define the set of nodes in the vicinity of the particle on which the interpolant is based. Herein, the more complicated case of $N = 4$ is discussed but it should be noted that the $N = 2$ algorithm uses a similar approach, albeit with less nodes. The process is illustrated in Figure 3.20 in two-dimensions for a point-force algorithm which requires fluid information at the particle center. First, a search algorithm identifies the lower-left node of the cell containing the particle. Then the stencil is designed by selecting this node, one node in the decreasing coordinate direction, and two nodes in the increasing coordinate direction. With this information, the interpolant may finally be constructed. Note that special treatment must be given when the particle is contained in the first cell off the wall. In this case the stencil still uses four points in all directions but is biased rather than centered.

For the case of finite-sized particles (Section 3.3) the evaluation of volume and surface-averaged quantities is required and are obtained through spatial samples on the surface and inside of the particle. These values are obtained using the same approach described above with one modification–the search algorithm now looks for the cell which contains the surface or volume point in question (rather than the cell which contains the particle center of mass). This modified approach is illustrated in Figure3.21.

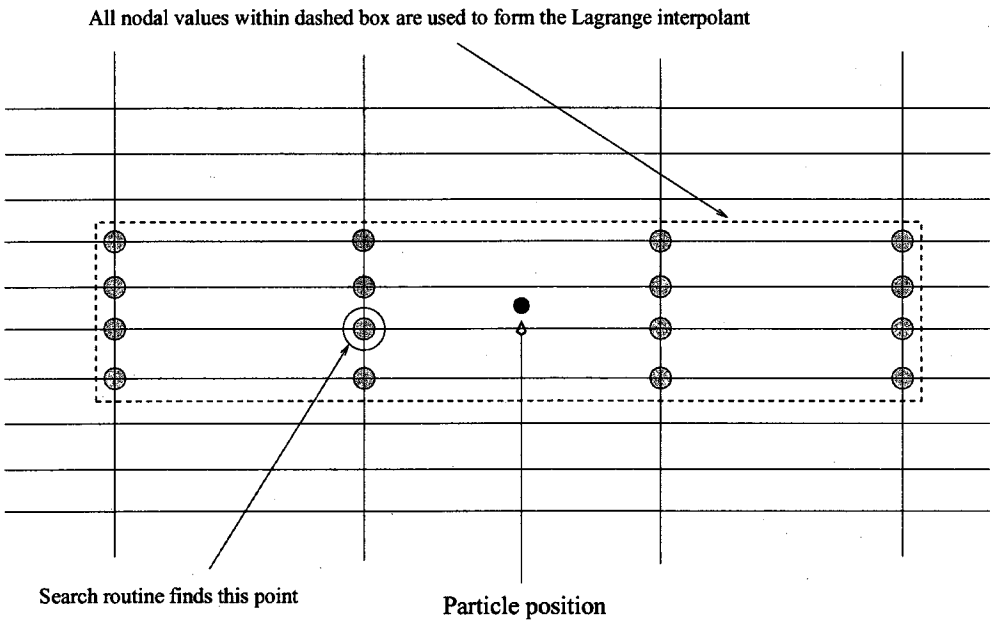

Figure 3.20: Construction of the Lagrange basis.

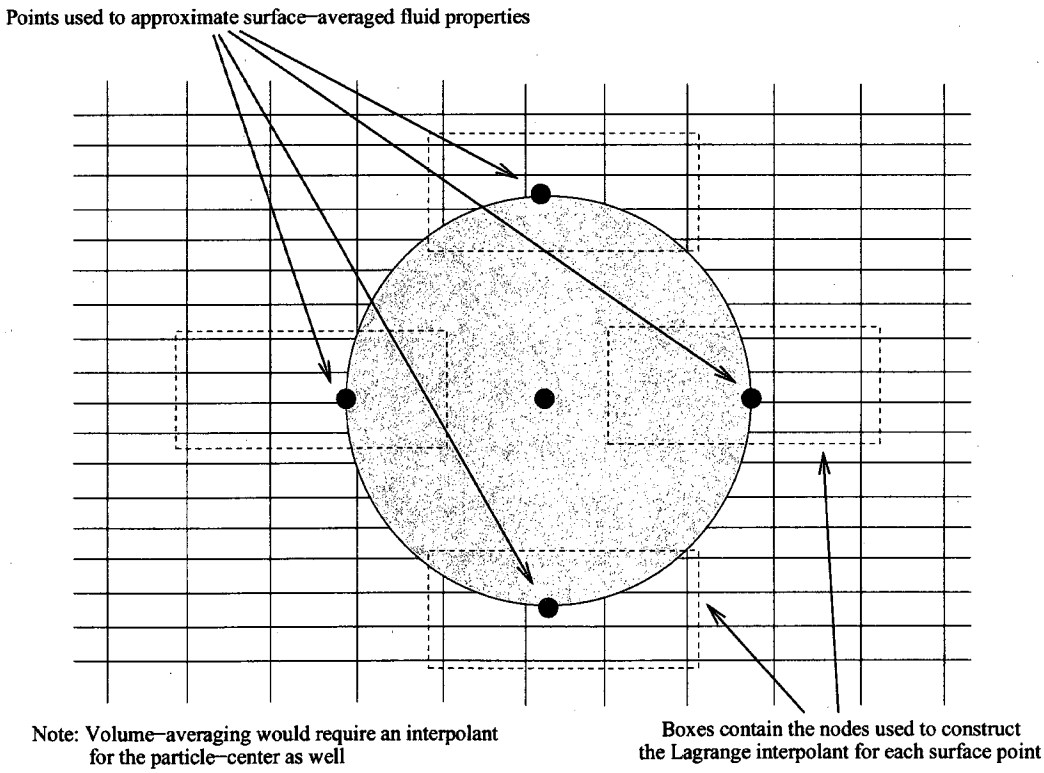

Figure 3.21: Construction of Lagrange basis for surface quantities for a particle larger than the local grid spacing.

Chapter 4

Heavy particles injected near the wall

This chapter is concerned with the motion of "heavy particles" (which are herein defined as particles with $\rho_p \gg \rho_f$) released in the turbulent boundary layer very-near the wall (with terminal velocity directed away from the wall) for which an equation of motion consisting of drag and body force alone is appropriate. Additionally, the particle is assumed arbitrary small such that the point-force approximation remains valid and a Stokesian drag law is also used. The objective of this research was to study particle diffusion, reflection, and mean velocity in the context of two parametric studies: one investigated the effect of the drift parameter (the ratio of particle terminal velocity to fluid friction velocity) for a fixed and finite particle inertia, and the second varied the drift parameter and particle inertia by the same amount (i.e. for a constant Froude number). A range of drift parameters from 10^{-4} to 10^{0} were considered for both cases. The particles were injected into the simulations at a height of four wall units for several evenly distributed points across the span and a perfectly elastic wall collision condition was imposed at one wall unit.

Statistics collected along the particle trajectories demonstrated a transition in particle movement from one that is dominated by diffusion to one that is dominated by gravity. For small and intermediate sized particles (i.e. ones with outer Stokes numbers and drift parameters much less than unity) transverse diffusion away from the wall-dominated particle motion. However, preferential concentration is seen near the wall for intermediate-sized particle due to inhomogeneous turbulence effects (turbophoresis), consistent with previous channel flow studies. Particle-wall collision statistics indicated that impact velocities tended to increase with increasing terminal velocity for small and moderate inertias, after which initial conditions become important. Finally, high relative velocity fluctuations (compared to terminal velocity) were found as particle inertia increased, and were well-described with a quasi-one-dimensional fluctuation model.

4.1 Heavy-particle equation of motion

The Lagrangian equation of motion for a heavy, rigid, spherical particle is a special case of the general EOM presented in Eq. 3.88 and is given by

$$\frac{d\vec{V}_p}{dt} = -\frac{18\rho_f \nu_f}{\rho_p d_p^2}\vec{V}_{rel} + \vec{g} = -\frac{\vec{V}_{rel}}{\tau_p} + \vec{g} \tag{4.1}$$

where we recall that d_p is the particle diameter, and ρ_p and ρ_f are particle and fluid densities, respectively. To arrive at this expression, ρ_p was assumed to be much greater than ρ_f such that the added mass and stress gradient forces are negligible. Furthermore, the lift force is neglected due to the choice of gravity direction (lift will typically be strong when the terminal velocity is aligned with the flow direction). Consistent with many other previous studies, the history force is also neglected. The first term on the right-hand-side of Eq. 4.1 represents the Stokesian drag force and the second term is due to the buoyancy force with $\vec{g}$ representing the gravity vector. A Stokesian drag law (i.e. a linear drag law) has been employed for this study to avoid as it decouples the equation of motion into three independent components and makes interpretation of the results simpler. This choice has been made in many other previous studies and is reasonable provided the particle Reynolds number remains small. These assumptions were employed to focus the study on drag, inertia, and gravitational effects.

The particle trajectories are computed by numerically integrating the particle equation of motion. The integration is performed using the exponential-Lagrangian technique described in Section 3.5 where

$$g(t) = \frac{u_f}{\tau_p} + \vec{g} \tag{4.2}$$

Spatial interpolation for the heavy particle study was conducted via tri-linear interpolation and the point-force approximation was employed (details on these techniques given in Section 3.5.2)

4.2 Heavy-particle test conditions

The baseline test condition for the particle/turbulent boundary layer interaction was chosen as $St_\delta = 10^{-2}$ and $\gamma = 10^{-2}$. This is consistent with a $24\mu m$ diameter solid sphere with a density of $1000\,kg/m^3$ in a flow of air with $\delta = 22$cm and $u_\tau = 1.47$m/s ($Re_\tau \approx 22{,}000$). In this case, the

Table 4.1: Heavy particle test conditions for a) constant Stokes number study and b) constant Froude number study

γ	St_δ	$\langle St_\Lambda \rangle$	St^+	τ_{dom}/τ_Λ	τ_{dom}/τ_p
(a)					
1×10^{-4}	1×10^{-2}	9.74×10^{-2}	2.7	21.0	216
1×10^{-3}	1×10^{-2}	9.46×10^{-2}	2.7	19.7	208
1×10^{-2}	1×10^{-2}	8.33×10^{-2}	2.7	14.6	176
1×10^{-1}	1×10^{-2}	6.66×10^{-2}	2.7	9.2	138
1×10^{0}	1×10^{-2}	4.74×10^{-2}	2.7	4.9	103
(b)					
1×10^{-4}	1×10^{-4}	8.3×10^{-4}	2.7×10^{-2}	14.8	17695
1×10^{-3}	1×10^{-3}	8.3×10^{-3}	2.7×10^{-1}	14.6	1757
1×10^{-2}	1×10^{-2}	8.3×10^{-2}	2.7×10^{0}	14.6	176
3.16×10^{-2}	3.16×10^{-2}	2.6×10^{-1}	8.4×10^{0}	14.4	55
1×10^{-1}	1×10^{-1}	7.9×10^{-1}	2.7×10^{1}	12.6	16
3.16×10^{-1}	3.16×10^{-1}	2.0×10^{0}	8.4×10^{1}	9.3	5
1×10^{0}	1×10^{0}	4.5×10^{0}	2.7×10^{2}	7.4	2

particle radius is equal to one wall unit, and elastic reflection with the wall occurs when the transverse location of the particle centroid (y_p^+) equals one.

The test conditions for the constant inertia study are centered on the baseline condition and used a range of five drift parameters varying from 10^{-4} to 10^0, all for the baseline St_δ of 10^{-2} ($St^+ = 2.7$). This St_δ value ensures that the inertial effects are small (i.e. the particle is able to effectively respond to the majority of the fluid structures in the boundary layer but does not simply behave as a passive tracer in the near-wall region). Since Stokes number is held constant, the exclusive effect of varying the drift parameter can be isolated. The test conditions for the constant Fr_δ study include seven different cases all with $Fr_\delta = St_\delta/\gamma = 1$, through a range of γ from 10^{-4} to 10^0. In both studies, the baseline test condition described above represents the center of the γ range as viewed on a logarithmic scale (Table 4.1) where the wall Stokes number, St^+, is seen to be much larger than the outer Stokes number, St_δ, which is more representative of the local Stokes number, $St_\Lambda \equiv \tau_p/\tau_\Lambda$ (recall that τ_Λ is the integral fluid time-scale presented in Figure 2.7).

The particles were injected with the sum of the mean fluid velocity and the particle terminal velocity, i.e. with $u_p = [u_f]$ (approximately $4u_\tau$), $v_p = [v_f] + V_{term}$, and $w_p = [w_f] = 0$ (where u, v,

and w represent the streamwise, vertical, and spanwise velocity components, respectively, and where $(...)_p$ and $(...)_f$ distinguish particle velocities from fluid velocities). This choice of injection (as opposed to injecting at the *instantaneous* fluid velocity plus the terminal velocity) ensured that the particles with the largest Stokes numbers would not possess unrealistically large initial velocity variations that are generally inconsistent with their long response times. In order to prevent wall collisions from acting as the dominant diffusion phenomena for the larger particles, the particle's terminal velocity is directed away from the wall. A perfectly elastic wall collision at $y^+ = 1$ was imposed as a reflection condition (consistent with the baseline physical particle dimensions) so that the particles would move downstream in a reasonable time period regardless of the Stokes number.

The particles were injected at uniform spanwise locations at $y^+ = 4$ and $x = \Lambda_x/3$ and tracked through a distance of 15 boundary layer thicknesses downstream (see Figure 2.2). Fifty particles were injected every other time-step (i.e. at every $0.57\tau_f^+$) for a period of 4000 time-steps ($4.38\tau_\delta$) such that a total of 100,000 particles were injected (large enough sample size for converged statistical results). The streamwise injection location corresponds to $Re_\delta = 4500$ and $Re_\tau \approx 270$.

4.3 Heavy-particle results

4.3.1 Flow-visualization

In order to identify how the particles interact with the carrier phase, several instantaneous snapshots of the simulation were obtained for the various conditions considered. In the following figures, the particle positions are mapped onto the streamwise velocity field for a given spanwise location. The fluid solution corresponds to $z^* = 2.78$ (the center of the span) and the particles (shown as black dots) are located in a range surrounding the fluid plane from $2.60 \leq z^* \leq 2.95$. This limited spanwise range for particle positions was chosen to be large enough to include a significant number of particle for the visualization, but at the same time remain sufficiently small to insure that the selected fluid plane is a good representation of the fluid solution in the neighborhood of the actual particle location. Figure 4.1 gives visualizations of the constant Stokes number simulation for the particle conditions $\gamma = 10^{-4}$, 10^{-1}, and 10^0 with $St_\delta = 10^{-2}$. Figure 4.2 shows the visualizations of the constant Froude number study for the $\gamma = 10^{-4}$, 10^{-1}, 0.316, and 10^0 cases with $Fr_\delta = 1$. Note comparisons between the two studies for the same γ (e.g. 10^{-4}, 10^{-1}, 10^0) would indicate differences due to the Stokes number.

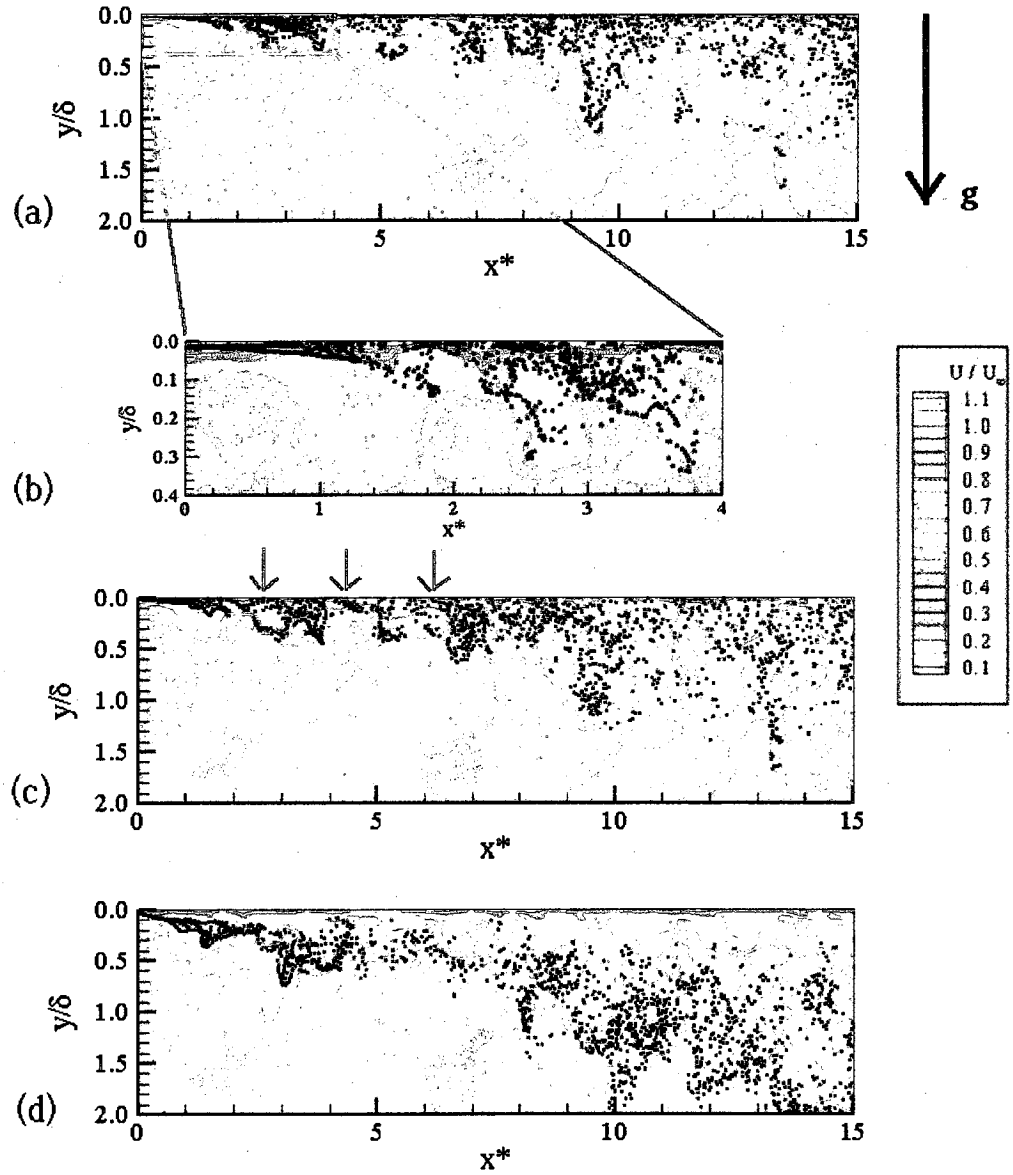

Figure 4.1: Instantaneous streamwise distribution (color range) with particle locations (shown as black dots) with constant $St_\delta = 10^{-2}$ for (a) $\gamma = 10^{-4}$, (b) $\gamma = 10^{-4}$ but with magnified view of the red box seen in (a), (c) $\gamma = 10^{-1}$ (red arrows indicate wall sweeps), and (d) $\gamma = 10^{0}$.

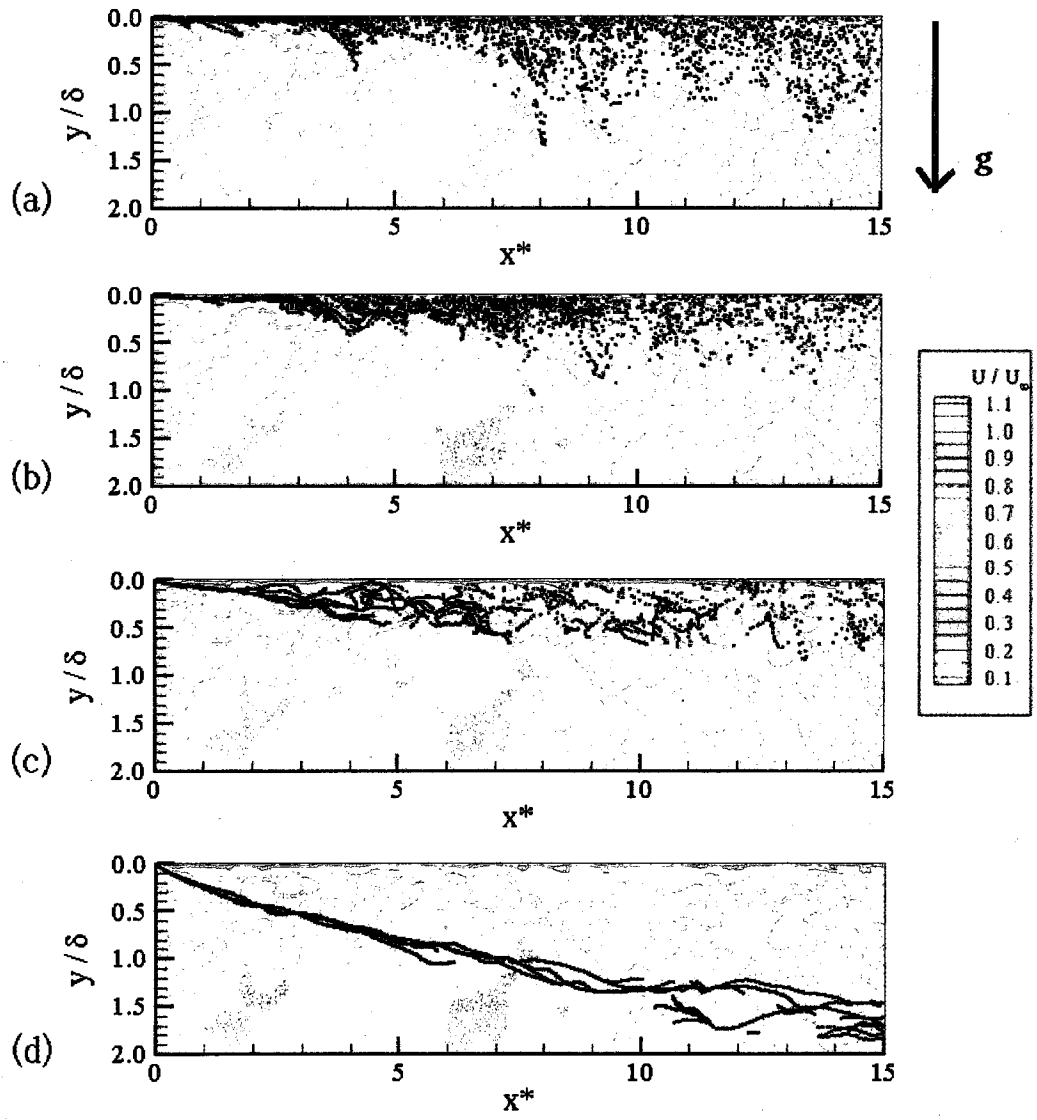

Figure 4.2: Instantaneous streamwise distribution (color range) with particle locations (shown as black dots) with constant $Fr_\delta = 10^{-2}$ for (a) $\gamma = 10^{-4}$, (b) $\gamma = 10^{-1}$, (c) $\gamma = 3.16 \times 10^{-1}$, and (d) $\gamma = 10^{0}$.

First, the constant Stokes number study shown in Figure 4.1 will be discussed. In looking at the close-up picture for the $\gamma = 10^{-4}$ case (Figure 4.1b), it is noted that the particle ejections tend to correspond to boundary layer ejections from the near-wall region, i.e. low-speed fluid thrusting into the outer region of the boundary layer. This preferential concentration is expected as boundary layer ejections should be the primary mechanism for moving particles rapidly away from the wall. As the particle move farther downstream (and away from the wall) the correlation between the fluid structures and the particle location tends to be reduced but is still significant (Figure 4.1a). In addition to this mechanism for particle movement, sustained near-wall concentration is also evident in the low-speed regions close to the wall. This particle condition has sufficient inertia ($St^+ = 2.7$) to experience preferential concentration in the near-wall region through the process of turbophoresis. As noted by Marchioli and Soldati [35], the mechanism responsible for high near-wall concentrations of inertial particle is the superior effectiveness of wall-sweep structures moving particle to the wall as opposed to boundary layer ejections removing particles from the near-wall region.

The $\gamma = 10^{-1}$ (Figure 4.1c) case shows effects of the increased terminal velocity. The level of near-wall concentration is reduced as the particles are more effectively pulled from the near-wall structures (i.e. the terminal velocity is strong enough to overcome the effects of turbophoresis). Far downstream ($x^* > 10$) the particles tend to be in the outer-region of the boundary layer and show less correlation with low-speed fluid pockets ejected from the wall than noted for the $\gamma = 10^{-4}$ case. This is attributed to the increased crossing-trajectory effect whereby particles cut through eddies instead of remaining trapped inside them. An interesting phenomenon shown in Figure 4.1c are tongues of high speed fluid (wall sweep structures) forcing particles back to the wall at x^* location of approximately 2.5, 4.5, 6.5 (see red arrows). Figure 4.1d gives the snapshot of the $\gamma = 10^0$ simulation. The particles are seen to immediately leave the transverse injection location and enter the outer region of the boundary layer due to the particle's higher terminal velocity. However, the cloud disperses as much as is seen in the lower drift parameter case due to the constant Stokes number condition.

As mentioned above, the constant Froude number results are shown in Figure 4.2 for four selected test conditions. Figure 4.2a shows a visualization taken from the $St_\delta = \gamma = 10^{-4}$ case ($St^+ = 0.027$)–the nearly tracer particle case. After the particles move from the injection location where the concentration is necessarily compact, it is noted that the particles are more uniformly distributed across a portion of the boundary layer than in Figure 4.1b (i.e. less correlation is

noticed between particle location and fluid structure than in the case shown in Figure 4.1a where $St^+ = 2.7$). This is attributed to their tendency to exhibit fluid tracer diffusion characteristics since turbophoresis and preferential concentration effects are negligible due to a lack of particle inertia ([28, 16]).

In Figure 4.2b ($\gamma = 10^{-1}$ and $St_\delta = 10^{-1}$) the particles maintain a stronger near-wall concentration despite their increase in terminal velocity. As the particles in this test case have a St^+ of 27 they are difficult to remove from the near-wall structures (i.e. γ is not sufficiently large to pull the particles from the near-wall structures). This is consistent with the fact that the large particle ejections (e.g. $x^* = 3.5$) correspond to previous large fluid ejections from the boundary layer. In comparing the $\gamma = 10^{-1}$ cases of Figures 4.1c and 4.2b, it is obvious that the higher Stokes number in the latter case yields much less diffusion, which is attributed to the increased inertia.

Figures 4.2c and 4.2d show the $St_\delta = \gamma = 0.316$ and $St_\delta = \gamma = 1.0$ cases, respectively, where the increased particle inertia and crossing trajectory effect are quite evident in that the correlation with flow structures is reduced. For each case, all the particles tend to leave the injection location on a similar trajectory (especially for $\gamma = St_\delta = 1$) for a significant distance. After some downstream location, several trajectories can be identified but the particles fail to become strongly diffused. In the $\gamma = 1$ case, it can be seen that the particles do not initiate significant diffusion until near the mean boundary layer edge. In comparing Figures 4.1d and 4.2d, it is seen that both cases yield the same net transverse rise velocity for the particle cloud, but the condition in Figure 4.2d shows much less mean diffusion that that of Figure 4.1d. This is a consequence of the particle, 100 times greater inertia for the present case shown in Figure 4.2d. In general, the $St_\delta = 1$ particles primarily convect downstream while moving away from the wall at their terminal velocity (mostly ignoring the turbulence as they pass).

4.3.2 Particle concentration distribution

Figure 4.3 shows the transverse particle distribution profile for both the constant inertia ($St^+ = 2.7$) study and the constant Froude number ($Fr_\delta = 1$) study at 15 boundary layer thicknesses downstream of injection. In this figure, C, represents the concentration of particles in a transverse bin (obtained through net flux statistics) and C_0 is the bulk concentration (equal to the average concentration over all bins containing particles). The y^+ values shown for $\gamma = 10^{-4}$ locate

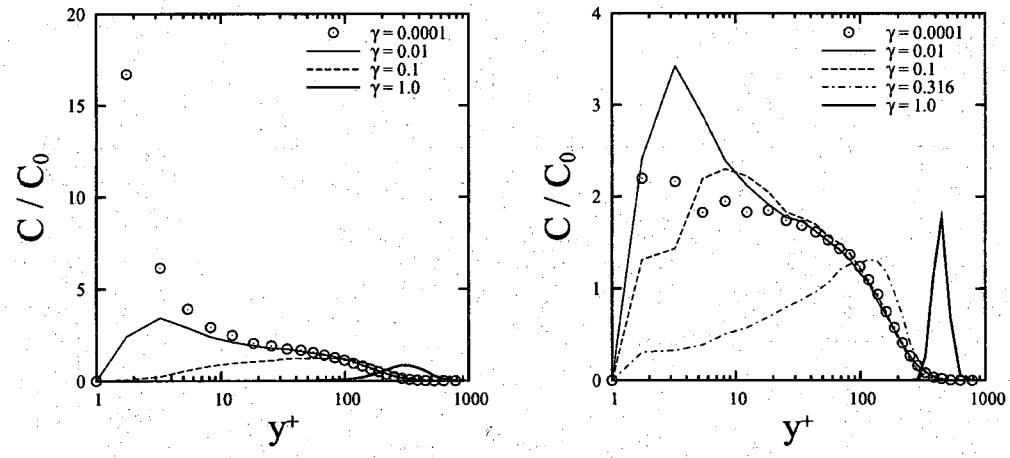

(a) $St_\delta = 10^{-2}$ (b) $Fr_\delta = 1.0$

Figure 4.3: Normalized concentration profiles at $x^* = 15$ for both parameter studies.

the center of each of the 26 transverse bins. Note that the $\gamma = 10^{-3}$ case is omitted in this figure (and others) as it was reasonably represented by the $\gamma = 10^{-4}$ case, i.e. the drift parameter effects were found to be generally negligible for $\gamma < 10^{-3}$ [87].

The St^+ for all of the cases shown in Figure 4.3a is of order one, implying that they should possess inertial tendencies in the near-wall region (i.e. the particle's response time is too large to allow it to effectively react to the short time-scale turbulent fluctuations in the near-wall fluid). Young and Leeming [16], as well as Marchioli and Soldati [35] noted that this condition leads to particles becoming trapped in the near-wall region through the turbophoresis effect. The turbophoresis phenomenon is caused by gradients in the fluid turbulence and acts to carry particle away from the peak turbulence location. As such, particles released at $y^+ = 4$ will be in a region where transverse velocity fluctuations increase away from the wall (Figure 2.4) and will therefore be moved toward the wall if terminal velocity effects are negligible. This "trapping" feature is evident in the distribution profile as a large near-wall peak is seen at $y^+ = 2$ for the smallest γ condition at $x^* = 15$. Additionally, the 10^{-1} case yields a leg that tends to flatten out smoothly in the outer regions of the boundary layer where St_δ is the governing parameter and where the particle should behave as a passive scalar since $St_\delta \ll 1$.

Increasing the drift parameter essentially increases the strength of the terminal velocity (directed away from the wall) and pulls the particles away from the near-wall structures of the turbulence. As such, the effect of turbophoresis (a near-wall, inertial phenomenon) competes with the strength

of the terminal velocity in determining the particle cloud's transverse movement. For example, the $\gamma = 10^{-2}$ case has a peak concentration at $y^+ \approx 3$ shifted towards the wall due to turbophoresis. However, as γ increases, the terminal velocity is sufficiently large that many of the particle are pulled to the outer regions of the boundary layer where they are capable of diffusing like fluid tracers since the effective Stokes number, $\langle St_\Lambda \rangle$, is of the order of St_δ (and not St^+) in this region. The largest γ case ($\gamma = 1$) has the lowest peak concentration and appears to be the most diffused as the width of the distribution profile is considerably larger than that of the other cases. This is most likely due to its immediate withdrawal from the near-wall region and its abrupt exposure to the larger turbulent scales in the outer regions of the boundary layer.

Figure 4.3b shows the particle distribution profile for selected cases with $Fr_\delta = 1$ at $x^* = 15$. As the drift parameter (and Stokes number) increase, the particles generally move away from the wall and have smaller peak concentrations (for both streamwise locations). It should be noted that the smallest particles for the constants Fr_δ study ($St_\delta = \gamma = 10^{-4}$) tend to behave as passive tracers (since their St^+ is much less than unity) and simply move with the fluid–this was not the case for the constant Stokes number study results for $\gamma = 10^{-4}$. Examining the results for $\gamma = 10^{-4}$ shown in Figure 4.3a ($St^+ = 2.7$) and Figure 4.3b ($St^+ = 0.027$), it is seen that the near-wall concentration in the former case is predominately a result of the inertial effect. This qualitatively supports the postulate by Young and Leeming [16] that turbophoresis is a function of St^+, and not γ for turbulent wall-bounded shear flows.

The larger cases ($\gamma = 10^{-1}$, 0.316, and 1) have a reduced concentration in the near-wall region when compared to the smallest two cases shown in this figure, and is attributed to their relative magnitudes of terminal velocity. The increase in the drift parameter pulls the particles from the near-wall region and prevents inertial effects such as turbophoresis from pushing them to the wall. The influence of γ on the largest particle condition is very obvious as the distribution profile peaks in the neighborhood of $y^+ = 400$ (approximately 1.5δ) at $x^* = 15$. The sharper peak, as compared to particle of lesser γ, indicates a reduction in diffusion caused by the increase in the crossing trajectory effect. Additionally, this reduced diffusion (as compared to the $\gamma = 1$ case of Figure 4.3a) is a result of the high inertia of the particle ($St_\delta = 1$), which causes the initial short-term diffusion rates to be significantly reduced (as noted in Section 1.2).

Figure 4.4a shows the transverse location of the peak concentration at $x^* = 15$ for the entire range of γ for both the constant Stokes number and constant Froude number simulations when subjected

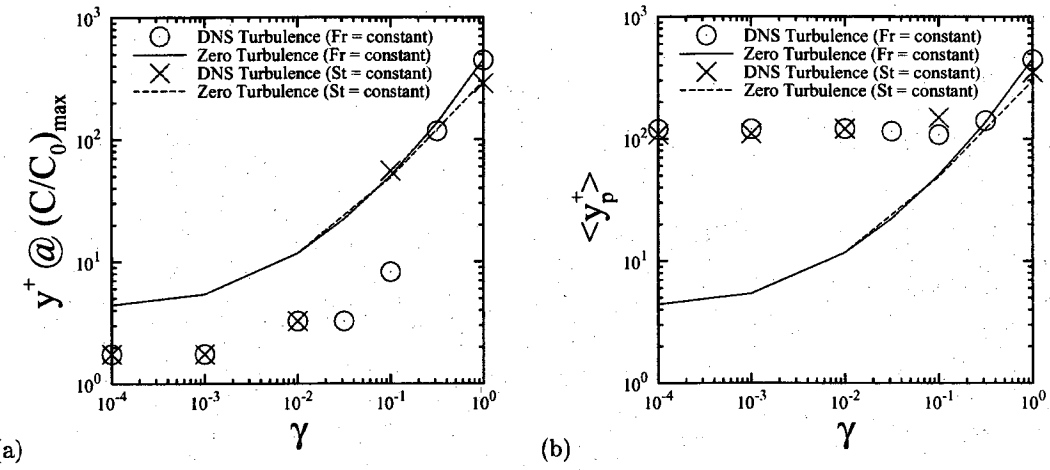

Figure 4.4: Location of (a) maximum particle concentration and (b) mean particle trajectory at $x^* = 15$.

to the turbulence of the DNS solution. Additionally, a "zero-turbulence" curve is given for both cases. This zero-turbulence data was collected by integrating the particle EOM using only the mean flowfield of the DNS solution, i.e. using only $\left[\vec{V}_f\right]$ and neglecting the fluctuating $\vec{V}_f'$. As such, all particles in the zero-turbulence field followed identical trajectories and yielded a Dirac delta function for the concentration profile. In general, the peak concentration locations for the zero-turbulence simulations are primarily a function of the drift parameter, where an increase in terminal velocity leads to an increase in mean transverse path location. Note that after moving 15δ downstream, the particle locations in the zero-turbulence case for $\gamma = 10^{-4}$ are still very near the transverse injection location of $y^+ = 4$, since the move by the influence of $[v_f]$ and V_{term} alone, both of which are quite small for this condition.

Now let us consider the DNS trends where the particle trajectories include the effects of turbulence. In general, the peak location increases with increasing γ (as in the zero-turbulence case). However, the smallest γ values have peak locations very near the wall (e.g. $y^+ = 2$) indicating the influence of the wall boundary condition for the initial concentration evolution (recall Figure 4.3). The smallest three γ values (10^{-4}, 10^{-3}, 10^{-2}) for both the constant Froude number ($Fr_\delta = 1$) and constant inertia ($St_\delta = 10^{-2}$) studies have the same peak concentration locations at $x^* = 15$ suggesting that changes in Stokes number at this level are negligible in terms of peak concentration location (though St^+ did have a large effect on peak concentration *magnitude* and overall distribution shape as noted in comparing Figures 4.3a and b).

The $\gamma = 10^{-1}$ case shows the largest difference due to Stokes number variation. The smaller Stokes number case ($St^+ = 2.7$) joins the corresponding zero-turbulence curve while the larger Stokes number case ($St^+ = 27$) remains well below its respective zero-turbulence level. This is attributed to a reduction in diffusion caused by the increased inertia of the latter case. As γ is increased to 1.0, the particles are pulled from the near-wall region and the DNS data points coincide with the zero-turbulence curves indicating that the mean particle transverse flux in these cases is dominated by the terminal velocity.

Figure 4.4b shows the location of the mean transverse particle trajectory location at $x^* = 15$ for the entire range of γ for both studies. Note that the data shown for the zero-turbulence curves is identical to that presented in Figure 4.4a due to the absence of turbulent diffusion. Figure 4.4b indicates that turbulent diffusion causes the mean particle trajectory to lie on or above that predicted by the zero-turbulence simulation. This is in contrast to the *peak concentration* shown in Figure 4.4a, where the DNS data fell on or below that predicted by the zero-turbulence simulation. For a small drift parameter and small Stokes number, the mean transverse location (and thus mean transverse velocity) is approximately constant. This is caused by the diffusion of fluid particles away from the near-wall region and is a byproduct of the injection location, e.g. particles would diffuse equally away from the injection location if the particles were instead released a distance away from the reflection plane. For large γ values, the terminal velocity begins to dominate the movement away from the wall such that the DNS and zero-turbulence mean trajectories become similar.

4.3.3 Particle diffusion rates

Figure 4.5 shows the spanwise mean-square deviation of the particle's position relative to the injection location. Figure 4.5a gives the data for four drift parameters of the constant Stokes number study while Figure 4.5b shows the data for five drift parameters of the constant Froude number study. As there is no component of terminal velocity acting in the spanwise direction (i.e. $[z_p - z_0] = 0$) these plots can be directly related to turbulent diffusion. In general, the spanwise diffusion increases with time for Figure 4.5a and b. However, in Figure 4.5a (constant Stokes number) the diffusion *increased* with γ while in Figure 4.5b (constant Froude number) the diffusion *decreased* with increasing γ.

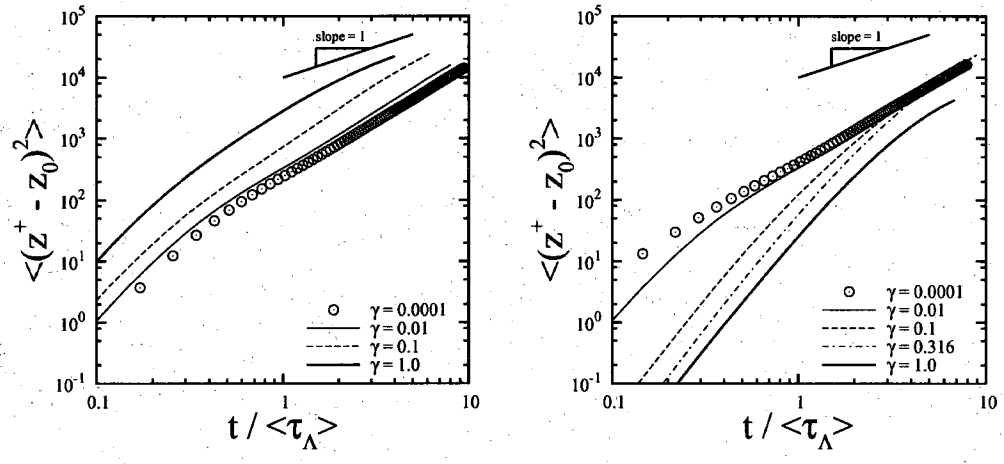

(a) $St_\delta = 10^{-2}$ (b) $Fr_\delta = 1$

Figure 4.5: Spanwise diffusion for both parametric studies.

To understand this result, it is instructive to first consider the case of $\gamma = 1$ and $St_\delta = 10^{-2}$ of Figure 4.5a. Unlike the other cases, this particle set will not be significantly affected by near-wall turbophoresis as few of the particle continue to reside in $y^+ < 70$ (see Figure 4.3a). In addition, the particle Stokes number is sufficiently small with respect to the eddies in the outer region that it may be considered to have long-time diffusion as $t/\langle \tau_\Lambda \rangle$ approaches 10. Furthermore, the outer region is approximately homogeneous and isotropic. As such, one should expect the mean-square diffusion to approach a linear variation with time as discussed by Hinze [88], which is reflected in the Figure 4.5a results. As γ is reduced (for $St_\delta = 10^{-2}$, $St^+ = 2.7$) the mean diffusion is reduced since the particles are less likely to reside in the outer region of the boundary layer where τ_Λ is greatest. Thus, the inhomogeneity and anisotropy of the near-wall region significantly modifies the spread rate of the overall particle cloud.

For Figure 4.5b, the tracer particles ($\gamma = St_\delta = 10^{-4}$) tend to transition from roughly quadratic diffusion at short-times to nearly linear diffusion at long-times, as expected. However, the increase in γ is associated with an increase in Stokes number. As such, the reduction in the short-time particle diffusion can be expected, owing to the increased inertia and reduced responsiveness of the particles. In fact, the initial diffusion rate for $\gamma = 0.01$ is nearly quartic. This suggests that the crossing trajectory effect significantly modifies the particle cloud spread rate. For $\gamma = St_\delta = 1$, one can expect that the particle diffusion is generally due to homogeneous, isotropic turbulence once the particle have exited the inner region of the boundary layer, as $t/\langle \tau_\Lambda \rangle$ approaches 10. However, at these times, τ_p is an order of magnitude greater that τ_Λ (see Table 4.1b) such that one could

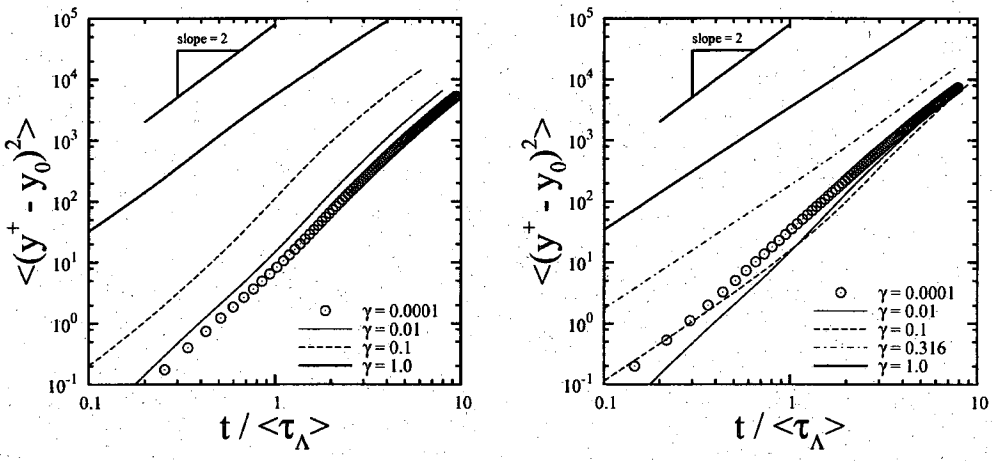

(a) $St_\delta = 10^{-2}$ (b) $Fr_\delta = 1$

Figure 4.6: Transverse mean-square deviation from the injection location for both parametric studies.

expect large inertial effects [88]. Thus, short-time diffusion behavior can be expected, consistent with the observed quadratic diffusion rate. Indeed, the mean-square spread tends to obey the classic, short-time quadratic dependence on time as shown in Figure 4.5b.

Figure 4.6 displays the data from both studies for the transverse mean-square deviation from the injection location for the same cases previously discussed with respect to Figure 4.5. In Figure 4.6a, little difference is noticed between the 10^{-1} case and the 10^{-2} case. This results is interesting in that it indicates that the slope of mean transverse deviation for all the particles is approximately the same for $\gamma < 10^{-2}$ (and $St_\delta = 10^{-2}$), even though the profiles in the near-wall region showed substantial differences (see Figure 4.3a). Thus, examining mean transverse deviation alone obscures the substantial local near-wall turbophoresis effects. Additionally, the largest γ value gives the greatest transverse deviation for the constant Stokes number study and approximately a quadratic slope. This is simply a consequence of the dominance of terminal velocity in carrying particles away from the injection location, i.e. this increase primarily results from $[y_p - y_0] \approx t * V_{term}$.

Figure 4.6b gives the transverse mean-square deviation (from the injection location) results for five of the cases considered in the constant Fr_δ study. Interestingly, the $\gamma = 10^{-2}$ and 10^{-1} cases show an overall mean deviation which is somewhat less than the tracer case of $\gamma = 10^{-4}$. This is attributed to the larger particle inertia for these cases and leads to a reduced diffusion rate at short-times. Further increase in the γ results in a mean-square value greater than that of the 10^{-1} case simply due to the increased y^+ location caused by terminal velocity (as also noted in Figure

4.6a).

4.3.4 Particle-wall impact velocities

Figures 4.7a and b show the horizontal and vertical bounce velocities for both studies normalized by u_τ. These data were collected in a bin stretching from $x^* = 8$ to $x^* = 15$ such that the effect of the initial condition on this statistic will be minimized. In this figure, the absence of a data point implies that no particle in the simulation made contact with the reflection plane imposed at $y^+ = 1$ (e.g. no reflections at either of the $\gamma = 1$ cases). Similar to the results of Uijttewall and Oliemans [89], the magnitude of the particle's horizontal and vertical impact velocities were found to generally scale with u_τ. The streamwise and vertical bounce velocities increase with γ up to a value of 10^{-1} which is consistent with the increasing capture distance necessary for wall collisions as V_{term} increases (especially at high inertias). Beyond $\gamma = 10^{-1}$ for $Fr_\delta = 1$, Figure 4.7 shows that tangential impact velocities increased but vertical impact velocities decreased since these particles cannot respond as quickly to wall-trapping velocities (velocities directed towards the wall). Interestingly, the streamwise and transverse bounce velocities are constant and nearly identical in both studies for $\gamma \leq 10^{-3}$ indicating that the bounce velocities are not dependent on terminal velocity or Stokes number for these conditions. This is consistent with other test conditions shown in [90].

Figure 4.7c displays the ratio of the bounce velocities and is related to the angle that the particle contacts the reflection plane. For $\gamma \leq 0.0316$ the results are virtually identical between the two studies. At $\gamma \leq 10^{-3}$, the particles are nearly passive scalars with respect to crossing the $y^+ = 1$ reflection plane and yield small angles due to the low ratio of $v'_{f,rms}/u'_{f,rms}$ near this plane. At higher γ values, the increased vertical velocity directed toward the wall needed to overcome the higher V_{term} values, caused steeper angles when the particles impact the reflection plane, though the angles remain small (the impact angles range from 0.3° to 4.4°). Once γ and Stokes number are both large ($\langle St_\Lambda \rangle$ greater than unity), there is a reduction in the angle caused by reduced transverse particle velocity fluctuations at high inertias (as previously noted).

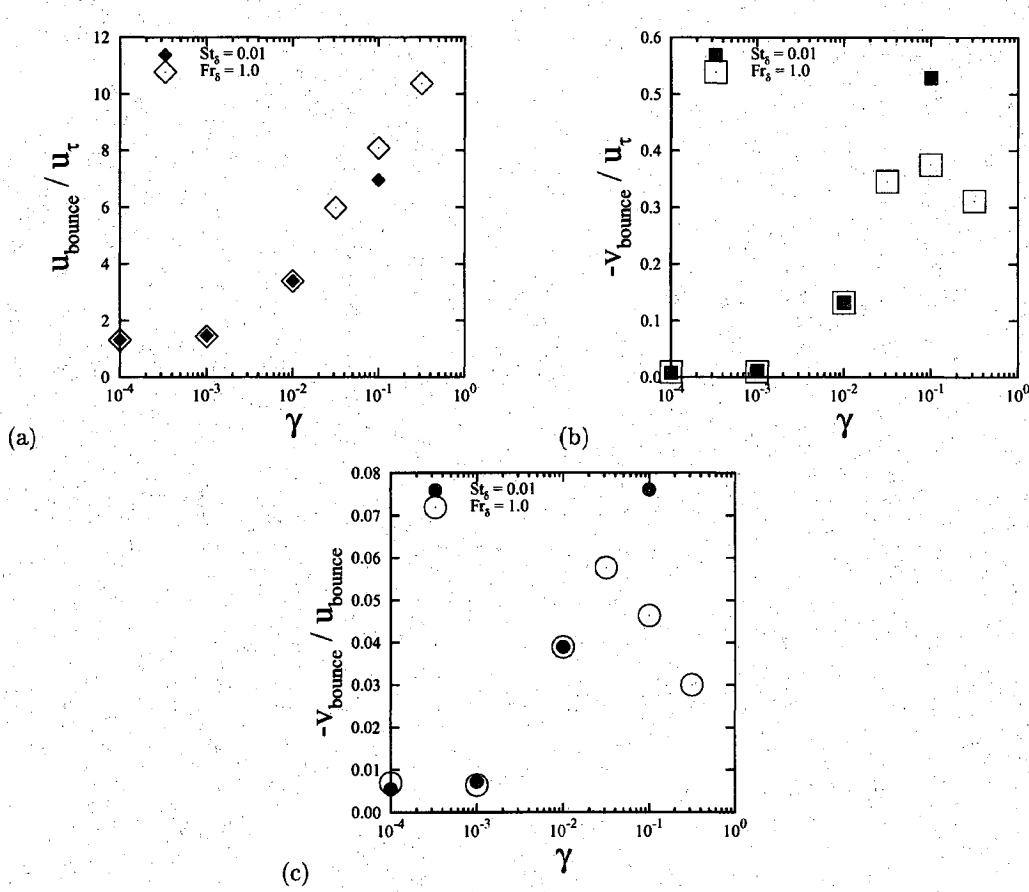

Figure 4.7: Bounce velocity statistics: (a) horizontal component, (b) vertical component, and (c) the ratio of components.

4.3.5 Velocities along the particle trajectory

Figure 4.8a shows the vertical particle velocity collected in the DNS flow as well as the vertical particle velocity collected in the zero-turbulence flow, both normalized by V_{term}. These statistics are Lagrangian averages taken over all particle trajectories within the particle tracking domain of Figure 2.2, and thus represents the average velocity of the particle cloud as it moves downstream. In considering the zero-turbulence results, it is helpful to recall that these simulations simply involved integrating the particle equation of motion in the mean flowfield (neglecting all influence of turbulent fluctuations). As such, in the cases with $\gamma \geq 10^{-2}$, $\langle v_p \rangle / V_{term}$ is approximately equal to one since $V_{term} \gg [v_f]$. However, for $\gamma = 10^{-3}$, $[v_f]$ at the injection point is approximately $V_{term}/3$, such that the combination of $[v_f]$ and V_{term} should (and does) result in a particle transverse velocity of approximately $4/3\, V_{term}$. In the DNS flow (fluid velocity fluctuations present), $\langle v_p \rangle$ is approximately 200 times larger than the terminal velocity for the smallest γ value shown on the plot. This indicates the dominance of turbulent diffusion at moving particles away from the wall when vertical velocities decrease and approach the zero-turbulence curve where the two coincide at the largest γ values, since gravitational effects dominate the mean particle velocity.

Figure 4.8b and c show the Lagrangian vertical relative velocity for the constant Stokes number and constant Froude number studies, respectively. If the particles were released in a homogeneous, isotropic turbulent field and no particle reflection condition was imposed at the wall, one would expect the Lagrangian vertical relative velocity to equal the terminal velocity of the particle, i.e. $\langle v_{rel} \rangle = V_{term}$, after transients have decayed. Note that a linear (Stokesian) drag law and Lagrangian averaging eliminates the bias due to preferential concentration [28, 27]. Notable departures from this behavior are seen in the present study and are found to be related to the transient effects as discussed in the following.

Recall that the particles are injected with the sum of the average Eulerian fluid velocity and the particle's terminal velocity (Section 4.2) and as such, they are not in equilibrium (on average) if there is a mean drift in the transverse fluid velocity observed along the particle path. This phenomenon can be qualitatively demonstrated by constructing an analytical model for particle response to simple sinusoidal fluid velocities. In particular, two sinusoidal fluid velocity profiles 180° out of phase are applied with an initial particle velocity of V_{term} yielding the result [90]:

$$\frac{\langle v_{rel} \rangle}{V_{term}} = 1 - \frac{k v'_{f,rms}}{b V_{term}} \int_0^{b\tau_f} \mathrm{e}^{-t/\tau_p} \tag{4.3}$$

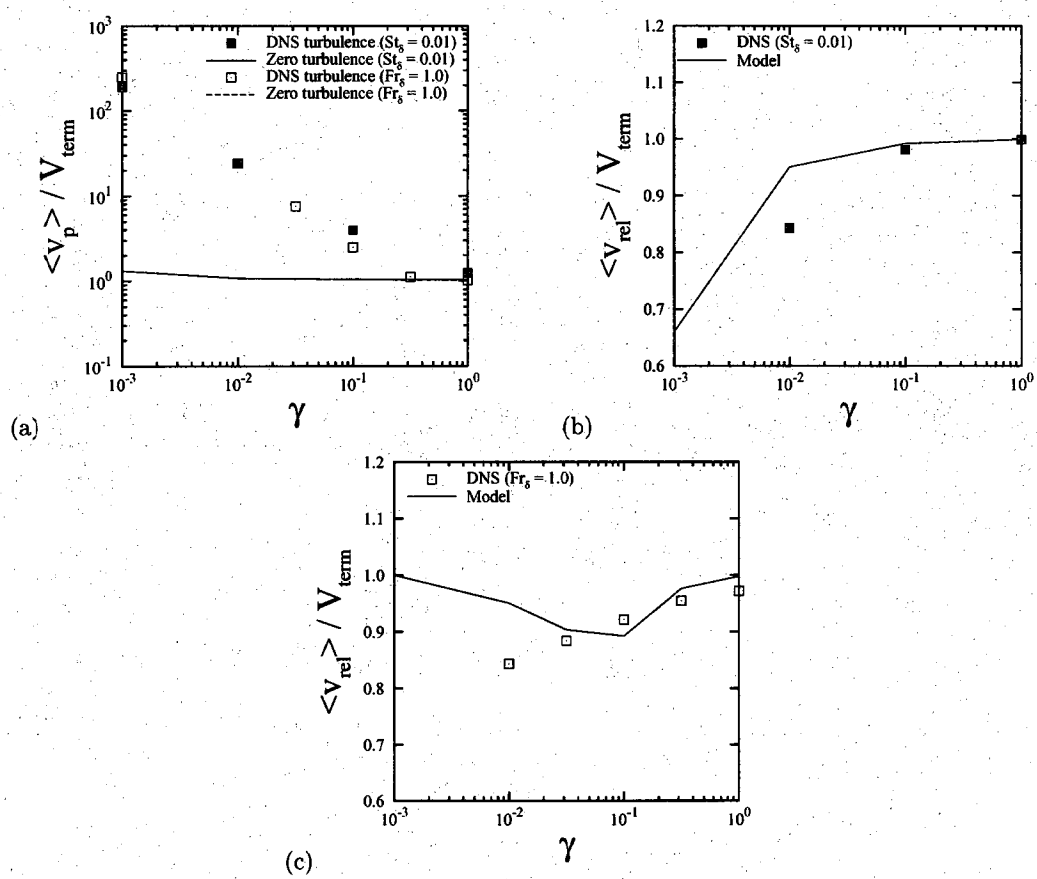

Figure 4.8: Lagrangian mean of transverse velocity normalized by the terminal particle velocity: (a) particle velocity, (b) relative velocity for constant Stokes number and (c) relative velocity at constant Froude number.

In the above expression, "b" is chosen to be an integer and k is a constant used to account for the Lagrangian mean drift in the fluid velocity as seen by the particle. Choosing $b\tau_f$ to be consistent with the integrations times in Table 4.1 and taking k as the values given by the data of the DNS fluid velocity statistics (presented in [90]) will result in a $\langle v_{rel} \rangle$ which deviates from V_{term}. Application of this model to the constant Stokes number study (where k is approximately constant) predicts that $\langle v_{rel} \rangle / V_{term}$ should approach $-\infty$ as γ becomes much less than one, whereas $\langle v_{rel} \rangle / V_{term}$ should approach unity as γ increases. This is qualitatively consistent with the DNS data (Figure 4.8b). For the constant Froude number study, $\langle v_{rel} \rangle / V_{term}$ is approximately predicted as unity for very high γ and very low γ, but a lower $\langle v_{rel} \rangle$ for γ on the order of 10^{-1} due to the combination of transient effects and the mean drift in the Lagrangian fluid velocity.

To complement the mean relative velocity statistics, the fluctuations of the relative velocity were also considered. The rms of the relative transverse velocity fluctuations with respect to the Lagrangian mean can be defined as

$$v_{rel,rms} = \left\{ \left\langle (v_{rel} - \langle v_{rel} \rangle)^2 \right\rangle \right\}^{1/2} \tag{4.4}$$

Figure 4.9a shows these fluctuation magnitudes normalized by the Eulerian fluctuation value collected along the particle along trajectories, $\left\langle \left[v'_{f,rms} \right] \right\rangle$. These results indicate that the fluctuations are approximately constant for the constant Stokes number case but increase for the constant Froude number case. Similar trends were found for the streamwise relative velocity fluctuations, as well as statistics from other DNS cases from [90, 87]. This indicates that the variations are primarily a consequence of changing inertia (St_Λ). For small inertia cases, the the relative velocity fluctuations are negligible compared to the turbulence intensity and are of the order of V_{term} (as expected). As the particle inertia becomes large ($St_\Lambda > 1$) the particles tend towards a moving Eulerian trajectory such that the fluid turbulent fluctuations will dominate the relative velocity, i.e. $V_{rel,rms} \rightarrow V'_{f,rms}$ for $St_\Lambda \gg 1$. Evidence of this behavior was also given in the channel flow studies of van Haarlem et al. [91] and Narayanan et al. [92].

To predict these trends, a simple model was constructed based on the analytical response of the particle's relative velocity subjected to a sinusoidal fluid velocity with zero mean. Dorgan [90] shows that the relative velocity fluctuations in this case have the following form:

$$\frac{v_{rel,rms}}{v'_{f,rms}} = \frac{u_{rel,rms}}{u'_{f,rms}} = \left\{ \left(\frac{\beta St_\Lambda}{1+\beta^2 St_\Lambda^2} \right)^2 + \left(\frac{1}{1+\beta^2 St_\Lambda^2} - 1 \right)^2 \right\}^{1/2} = \frac{\beta St_\Lambda}{(1+\beta^2 St_\Lambda^2)^{1/2}} \tag{4.5}$$

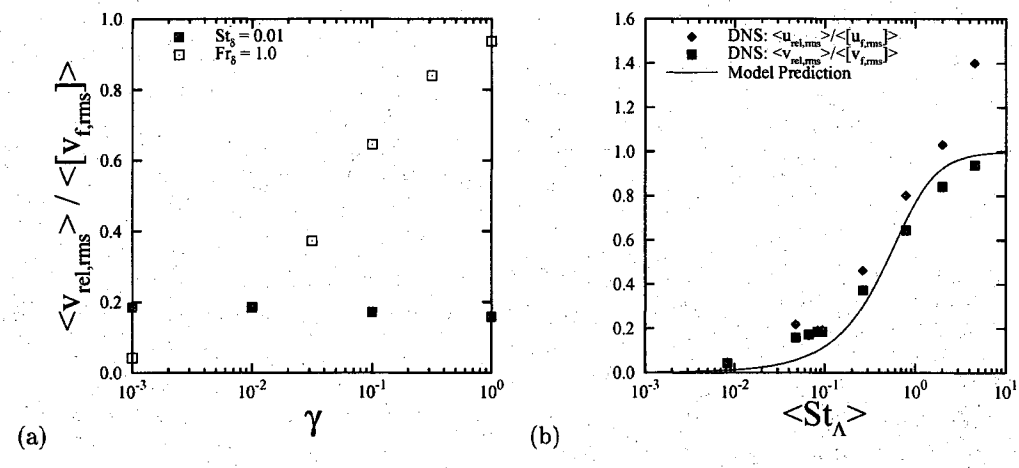

Figure 4.9: (a) Relative velocity fluctuation amplitude normalized by the rms of the Eulerian fluctuations along the particle trajectory for the transverse DNS data. (b) A comparison of the DNS data with a theoretical prediction.

where $\beta = \cos^{-1}(1/e)$. The theoretical predictions are compared with streamwise and transverse velocity results in Figure 4.9b indicating reasonable qualitative agreement, despite the inhomogeneous complex nature of the DNS flow.

Finally, the particle Reynolds number is considered as it is of importance when considering the validity of the linear drag-law assumption. As such, Figure 4.10 gives the Reynolds number based on both V_{term} and based on the magnitude of the relative velocity averaged along the particle path where

$$\langle |Re_p| \rangle = \frac{\left\langle \|\vec{V}_{rel}\| \right\rangle d_p}{\nu_f} \tag{4.6}$$

$$\left\langle \|\vec{V}_{rel}\| \right\rangle = \left\langle \left(u_{rel}^2 + v_{rel}^2 + w_{rel}^2\right)^{1/2} \right\rangle \tag{4.7}$$

As a result of its definition, $Re_{p,term}$ will increase with drift parameter for the present test conditions as demonstrated by the solid lines in Figure 4.10. The constant inertia case (Figure 4.10a) yields a slope of unity since the fluid viscosity and the particle diameter were held constant while the terminal velocity increases linearly with γ (due to changes in gravity). However, the constant Froude number case has a slope of 1.5 (Figure 4.10b) since the particle diameter is also increasing as V_{term} increases.

The results of Figure 4.10a indicate that Re_p is approximately constant with respect to changes in γ for a given Stokes number (in stark disagreement with the terminal velocity result). This is due

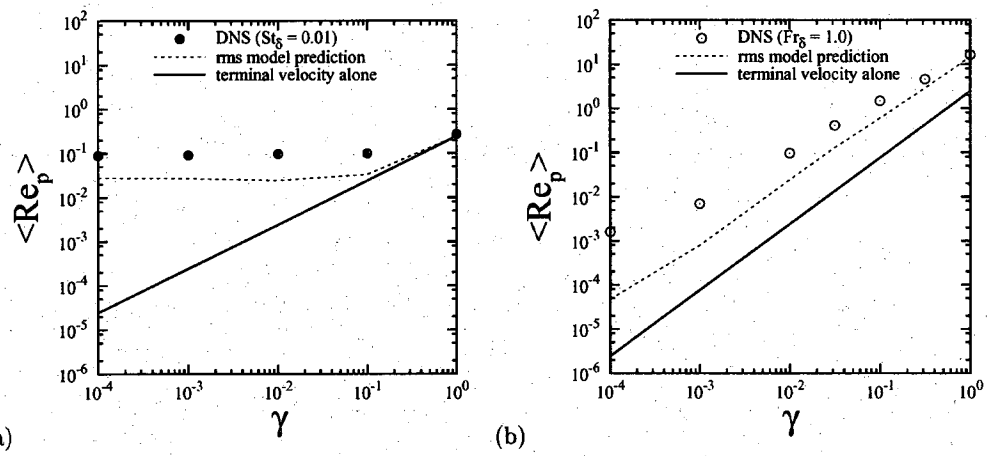

Figure 4.10: Particle Reynolds number based on $\left\langle \|\vec{V}_{rel}\| \right\rangle$ for (a) the constant Stokes number study and (b) the constant Froude number study.

to the strong contributions made by the turbulent fluctuations for particle conditions with large ratios of Stokes number to drift parameter (i.e. large Froude numbers). In such cases, the gravitational effects should be expected to be of secondary importance and as such, the Reynolds number based on the terminal velocity is a poor indicator for $\gamma \ll 1$ in these flows. For the constant Froude number results shown in Figure 4.10b, it is seen that the DNS particle Reynolds number increases with γ and has approximately the same slope as the $Re_{p,term}$ curve, although it is shifted upwards due to the presence of the finite rms of the relative velocity experienced by the particle in the DNS flow.

To explain these trends, a simple theoretical model was constructed based on the results from the zero-turbulence data combined with Eq. 4.5, such that

$$\|\vec{V}_{rel}\|^2 = \|\vec{V}_{rel,zero-turbulence}\|^2 + \vec{V}^2_{rel,rms} \tag{4.8}$$

As shown in Figure 4.10, this simple approximation gives a reasonable representation of the results for both the constant Stokes number and constant Froude number simulations, despite the inhomogeneous, anisotropic nature of the flow.

4.4 Heavy particle summary

Simulations have been conducted in a turbulent boundary layer ($Re_\tau = 270$) for a range of particle drift parameters ($10^{-4} \leq \gamma \leq 10^{0}$) with a fixed inertia ($St_\delta = 10^{-2}$) and then with a variable inertia ($Fr_\delta = 1$). Flow visualization indicated that for nearly fluid tracer conditions (γ and $St^+ \ll 1$), particle ejections from the near-wall region initially correlated strongly with boundary layer ejections of the carrier phase. For higher terminal velocities directed away from the wall, the correlation was reduced due to the crossing trajectory effect. Additionally, increases in the Stokes number resulted in substantially reduced diffusion and an increase in γ generally results in lower near-wall concentration of particles as the higher terminal velocity tends to remove particles from this region. The concentration profiles near the wall were also affected by changes in the Stokes number since turbophoresis force particles towards the wall when St^+ was of order unity or greater.

Examination of the spanwise mean statistics showed increased diffusion for increases in γ for constant Stokes number, but decreased diffusion for increasing γ for constant Froude number. These results were attributed to turbophoresis, inertia, and wall interaction effects such that canonical homogeneous, long-time diffusion rates were never fully realized. Similar behavior was noted for the transverse diffusion except that terminal velocity dominated at large γ values.

With respect to particle-wall collisions, the drift parameter was found to be the dominant parameter in determining the impact velocity for $St^+ > 3$ with the present flow conditions where increasing γ yielded increasing velocities. This was attributed to the increasing capture distance necessary for collision with the reflection plane even though the terminal velocity was directed away from the wall. However, at larger Stokes numbers, the inertia and injection conditions were found to be influential.

With respect to Lagrangian-average velocities, a close coupling was noted between transverse particle velocities and turbulent diffusion for small drift parameters, whereas the terminal velocity dominated the movement as the drift parameter approached unity. In addition, the high inertia particles were seen to experience large relative streamwise velocity fluctuations on the order of the Eulerian fluctuations, whereas the small inertia particles had comparatively lower fluctuations (as the trajectories were more coupled to the fluid unsteadiness). Similarly, particle Reynolds numbers based on the average of the relative velocity magnitude, $\left\langle \|\vec{V}_{rel}\| \right\rangle$, indicated a transition from being dominated by turbulent diffusion at small drift parameters and small Stokes numbers, to

being dominated by the particle's terminal velocity at large drift parameters. The relative velocity fluctuations and the average Reynolds number were reasonably predicted by considering a simple sinusoidal model for the fluctuations in the relative velocity.

Chapter 5

Bubbles and sand particles: EOM effects

The simulation of particle motion in a liquid is of particular interest to many engineering applications. Unlike the heavy particles discussed in Chapter 4, the increased density of the surrounding phase can lead to the importance of other surface forces beyond drag for the acceptable prediction of particle trajectories. In particular, air bubbles or sand particles immersed in water have many other surface forces which are less well-understood but become important for the particle equation of motion. Often these forces are important in near-wall regions where turbulence can cause bubbles or sand to be diffused, lifted and/or sedimented. As such, a study of the relative importance of the various forces on particle motion (and the corresponding computational overhead) in a turbulent boundary layer would be valuable to guide future studies.

The present study considers the case of low-density particles in dilute concentrations in a low-Reynolds number, spatially-developing, turbulent boundary layer obtained through a DNS of the incompressible Navier-Stokes equations (see Chapter 2). The DNS approach eliminates issues associated with turbulence modeling. The particles are injected near the wall at a distance consistent with the physical diameter of the particle being modeled. The Lagrangian tracking technique described in Sections 3.4 and 3.5 is used to solve the particle equation of motion and advance individual particles through the boundary layer flowfield.

The framework of the distributed-force equation of motion for finite-sized particle will be used to consider surface force description which involve quasi-steady drag alone to one which also includes lift, added mass, stress gradient, and history forces. Several history force models are considered from the low-Reynolds number Basset force to the high-Reynolds number expression of Mei & Adrian [64]. The efficient "window-model" history force calculation is also considered and shown to significantly reduce the overall computational effort of including the history force. The results obtained from different equations of motion (e.g. with and without history force) are compared in terms of particle concentration at several streamwise locations. In addition, Lagrangian relative

velocity and diffusion statistics are considered demonstrating the relative importance of the forces on particle diffusion and mean trajectories.

A second study compares the predictions of the distributed equation of motion using Lagrange interpolants to simpler formulations which use tri-linear interpolation and a point-force description. The full equation of motion (Eq. 3.88) will be employed to ascertain these differences and show that in terms of concentration profiles the methods differ only slightly.

5.1 Force study

This section considers the effects of inclusion of various surfaces forces. In all cases, the equation of motion uses the distributed surface force formulation and employs a Lagrange basis to represent the inter-cell fluid property variation. Two particle conditions are considered in this section and physically correspond to (see Table 5.1) an air bubble (1a) and sand particle (2a) in a boundary layer of water ($\nu = 10^{-6}m^2/s$) with $Re_\tau = 270$, $\delta = 4.5$mm, and freestream velocity of $1m/s$. These flow conditions were chosen to match the non-dimensional parameters of the DNS flow while representing a physical test condition with relevance to many multiphase flows. Both particle conditions have identical diameters ($164\mu m$) and nearly-identical terminal velocities (and thus identical drift parameters) but different Stokes numbers owing to the different inertias. Note that the terminal velocities are equal since

$$V_{term} = \frac{|\psi - 1| d_p^2}{18\nu f} g \tag{5.1}$$

(Eq. 3.93 re-written with substitution of τ_p) and $|\psi - 1| \approx 1$ for both of these conditions (and d_p, ν, and g are matched as well). The particles were released into the DNS flow at the position where their centroid was one diameter away from the wall (i.e. at $y^+ = 9.8$) with a velocity equal to $\vec{V}_{term} + [\vec{V}_f]$, consistent with the heavy particle study presented in Chapter 4. An elastic collision (which is reasonable for small solid spheres and bubbles) was specified at $y^+ = 4.9$ (i.e. one r_p^+) such that the particle velocity was reflected when the particle centroid reached this y-location.

For both particle condition 1a and 2a described above, a total of ten different equations of motion were considered and are described in Table 5.2. The simplest EOM is FS-1 which considers Stokes drag and buoyancy and matches the same terminal velocity of the finite Reynolds number case.

Table 5.1: Summary of particle conditions for low-density EOM study. Note that the Stokes numbers include added mass effects (per the definition of τ_p in equation 3.34).

Particle condition	ψ	d_p [μm]	r_p^+	St_δ	St^+	γ	$Re_{p,term}$
1a	0.00126	164	4.9	0.0081	2.18	0.197	1.94
2a	2.0	164	4.9	0.040	10.9	0.198	1.94

This represents a linear drag condition often used for theoretical diffusion theories. The next, FS-2, trades the Stokes drag for the finite Reynolds number form of Eq. 3.20.

From FS-2 to FS-4 the finite Reynolds number drag is retained and the added-mass, stress gradient, and lift forces are additionally considered. FS-5 includes the history force where several variants are considered and denoted by the trailing letters of the force study tag. The various history force models include the creeping flow expression of Basset (FS-5-B), the finite Reynolds number kernel of Mei & Adrian [64] (FS-5-MA), and the finite Reynolds number kernel of Dorgan & Loth [93] (FS-5-DL) as well as its window model formulation (FS-5-W) which is described in detail in Section 3.2.2). All of these conditions (FS-1 through FS-5) consider a buoyancy force that is directed away from the wall to be consistent with the conditions presented in Chapter 4. However, this choice of buoyancy will tend to minimize the effects of the lift force in terms of vertical concentration since the mean lift force will point in the direction of $\omega_z \times \vec{V}_{term}$ (which is $+x$ when buoyancy is directed in $+y$). Thus, two additional cases (FS-6 and FS-7) are considered to show the effects of the lift force on particle concentration when the mean lift direction is in $\pm y$ (as would be the case for flow along a vertical wall). These two cases are identical to FS-5-W accept that the gravity vector has been modified. A final case (FS-8) is also included which is identical to FS-6 but without the lift force.

5.1.1 Flow-visualization

Section 4.3.1 presented and discussed the particle-fluid interactions in the context of several instantaneous snapshots of the simulation. Here, a similar presentation is made where both horizontal and vertical cuts are examined. The horizontal plane shown in Figure 5.1 corresponds to a transverse location of $y^+ = 15$ where instantaneous streamwise velocity is indicated by color contours and the black dots correspond to particle locations in the vicinity of the plane ($12 \leq y_p^+ \leq 18$). While more coherent low-speed streaks are shown in the streamwise velocity by [90] at a lower location ($y^+ = 9.96$), evidence of these structures are still present in the current

Table 5.2: Summary of EOM's considered in the force studies.

Force study tag	steady-drag	buoyancy	added-mass	stress-gradient	lift	history
FS-1	Stokes	$+y$	no	no	no	no
FS-2	Schiller-Naumann	$+y$	no	no	no	no
FS-3	Schiller-Naumann	$+y$	yes	yes	no	no
FS-4	Schiller-Naumann	$+y$	yes	yes	yes	no
FS-5-B	Schiller-Naumann	$+y$	yes	yes	yes	Basset
FS-5-MA	Schiller-Naumann	$+y$	yes	yes	yes	Mei-Adrian
FS-5-DL	Schiller-Naumann	$+y$	yes	yes	yes	Dorgan-Loth
FS-5-W	Schiller-Naumann	$+y$	yes	yes	yes	Window
FS-6-W	Schiller-Naumann	$+x$	yes	yes	yes	Window
FS-7-W	Schiller-Naumann	$-x$	yes	yes	yes	Window
FS-8-W	Schiller-Naumann	$+x$	yes	yes	no	Window

illustration which is taken at higher y-location due to the farther off-wall injection location required for these finite-sized particles. Figure 5.2 shows a similar pictures for a vertical cut (at $z^* = 2.78$; the center of the span) with the particle locations collected from $2.60 \leq z^* \leq 2.95$. In both figures, the top row of images corresponds to condition 1a while the bottom row is condition 2a. Additionally, the left column snapshots were taken from the FS-2 simulation while the right column was taken from FS-5-W. Both conditions were found to have far fewer particles downstream of $x^* = 5$ than upstream of that location due to diffusion of the particle cloud into the remainder of the boundary layer. Thus, only the upstream area is shown.

The sand particles show a higher concentration on the horizontal plane indicating a larger near-wall concentration. This result will be confirmed in subsequent sections when considering other statistics and is attributed to the higher inertia associated with the sand particle case. Some evidence of this feature can also be seen in the vertical cuts, where there are more sand particles in close proximity to the wall than observed in the bubbles condition. In both cases, the initial migration of the particles away from the wall seems to correspond to the ejection of low speed fluid from the near-wall region (consistent with observations made in Section 4.3.1) as shown in Figure 5.2 in the vicinity of $x^* = 1$.

Larger differences are observed when comparing the different equation of motions (comparing the left and right columns). The full equation of motion (FS-5-W) is seen to improve the correlation of particles existing in low-speed streaks as well as increasing the number of particles remaining close

to the wall (Figure 5.1). Figure 5.2 shows that the FS-5-W EOM produces stronger correlation with the low-speed ejection events and results in "clumps" of particles being formed in the fluid structure at $x^* = 2.5$. This stronger correlation with turbulent structures may be attributed to the reduced relative acceleration of the particle brought on by including the history force (whereas quasi-steady drag, FS-2, reduces only the relative velocity). The formation of particle clumps may be cause to include collision modeling even when the particle loading is assumed to be dilute by standard criteria. Rani, Winkler, and Vanka [94] have proposed a binary collision model which could be used to include this effect. However, these effects are neglected herein so that focus can be placed on the proper form and sensitivity of the surface forces since these have not been previously examined in a turbulent flow with low density particles.

5.1.2 Particle concentration distribution

This section discusses the effect of various surface forces on wall-normal particle concentration profiles at several streamwise locations. The EOM's with terminal velocity directed away from the wall (FS-1 to FS-5) are considered first. In a second study, the direction of V_{term} is rotated to point upstream and downstream (FS-6 and FS-7, respectively) and these results are compared to the previous results. The intent of this second study is to show the importance of the lift force is directly related to orientation of V_{term} with respect to the freestream velocity.

In both cases, the particle concentration is defined by constructing discrete "bins" from the DNS data. These bins were chosen to give good near-wall resolution as well as contain statistically meaningful numbers of particles in the outer regions of the boundary layer. These properties were enforced by fixing the first two bins to have a width of r_p^+ (for the baseline condition) followed by third bin-width being set to d_p^+. For the remaining bins, a bin-stretching function was defined (based on hyperbolic tangent) to grow the width to a maximum size of 30 inner-units at $y^+ > 100$. This bin-width distribution is shown in Figure 5.3 and differs from that used in the heavy-particle study due to the increased injection/reflection locations.

The particle concentration in each bin (C_i) was computed as

$$C_i = \frac{1}{t_{collect}} \frac{N_i}{\bar{u}_{p,i} \Delta y_i} \tag{5.2}$$

where N_i is the number of particles passing through bin i, $\bar{u}_{p,i}$ is the average streamwise particle

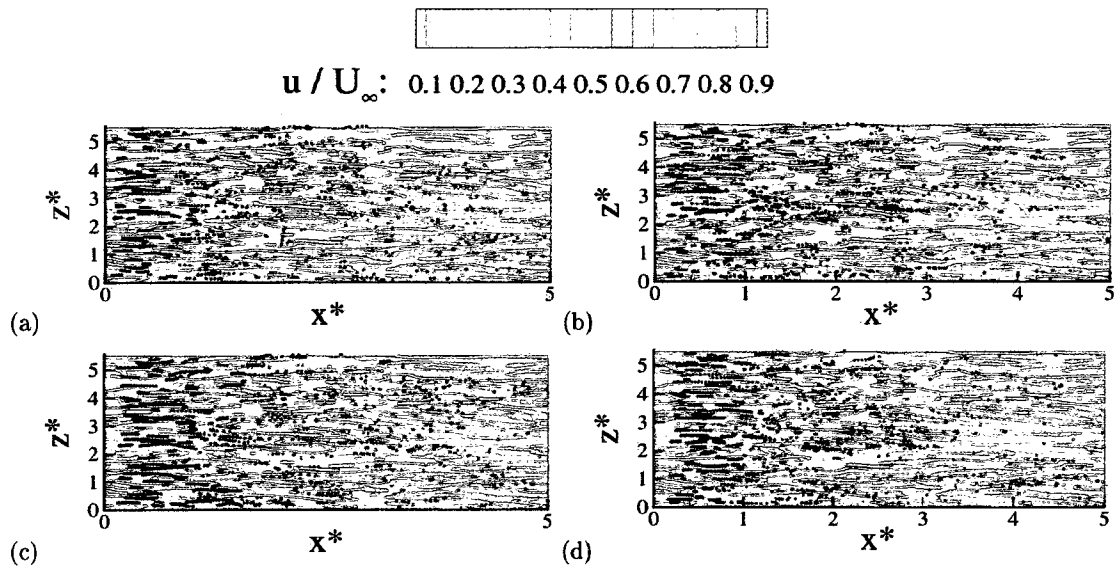

Figure 5.1: Horizontal plane at $y^+ = 15$ with instantaneous u-velocity contours and particle locations (shown as black dots) for conditions 1a (top row) and 2a (bottom row) with FS-2 (left column) and FS-5-W (right column).

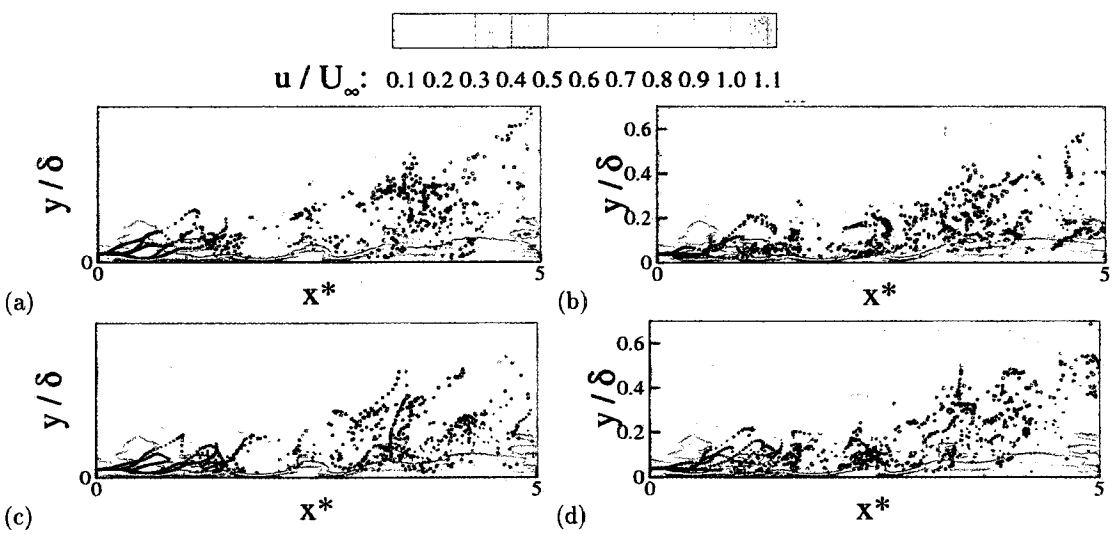

Figure 5.2: Vertical plane at $z^* = 2.78$ with instantaneous u-velocity contours and particle locations (shown as black dots) for conditions 1a (top row) and 2a (bottom row) with FS-2 (left column) and FS-5-W (right column).

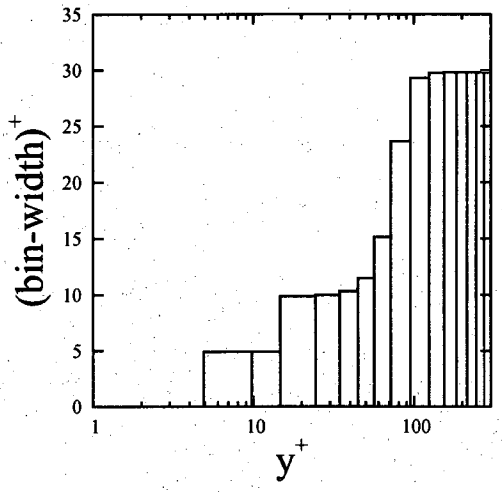

Figure 5.3: Bin-locations and widths for concentration calculations.

velocity associated with particle passing through bin i, Δy is the bin-width of bin i, and $t_{collect}$ is the time over which particles were collected. This bin concentration is then normalized by the average particle concentration taken over the entire boundary layer,

$$C_0 = \frac{1}{t_{collect}} \frac{N}{\bar{u}_{p,\delta}\delta} \tag{5.3}$$

where N is the total number of particles, $\bar{u}_{p,\delta}$ is the average streamwise particle velocity associated with particles passing through the streamwise location of interest and δ is the mean boundary layer thickness. Therefore, the normalized concentration shown in the plots discussed in this section is given by

$$\frac{C_i}{C_0} = \frac{N_i \bar{u}_{p,\delta}\delta}{N \bar{u}_{p,i} \Delta y_i} \tag{5.4}$$

such that $C/C_0 = 1$ corresponds to particles being evenly distributed over a vertical distance equal to the mean boundary layer thickness.

5.1.2.1 Concentration distribution for wall-normal terminal velocity

Figure 5.4 shows the transverse particle distribution profile for the bubble condition "1a" at a streamwise location 2δ downstream of the injection location. At this upstream location, little difference is seen in the concentration profile between the FS-1 and FS-2 indicating that the effects of finite Reynolds number drag is small. The addition of the fluid acceleration terms and the lift

force tend to sharpen the concentration profile (indicating less diffusion of the particle cloud) but the peak location is the same as in FS-2.The mechanisms responsible for reduced diffusion in the presence of the fluid acceleration terms is not understood at this time. Future studies may wish to independently consider the contributions from added mass and fluid stress separately. The fact that lift further reduces diffusion may be a result of lift moving bubbles into eddy cores (where they will not diffuse as rapidly) as discussed by Spelt & Biesheuvel [20] and others.

Figure 5.4b shows the transverse distribution prediction of FS-4 to the EOM's including history force for condition 1a. Here it is seen that the Basset force dominates the concentration prediction and is attributed to its infinite memory of past events (all the way back to the initial state) appropriate in creeping flow conditions. For the present conditions which involve a finite (though not large) Reynolds number, the Basset kernel is a poor choice for modeling the history force and is seen to dramatically contaminate the predictions. This is concerning given previous studies (e.g. [42]) have used the Basset force in finite Reynolds number conditions and the findings may be contaminated. The finite Reynolds number history force models are shown to generate a slightly higher near-wall concentration of particles compared to the equation neglecting history force (FS-4). The history force effectively strengthens the quasi-steady drag so it is not surprising that the inclusion of this force pushes the distribution back towards that of FS-2. It is also worth noting that the predictions made with the finite Reynolds number history force kernels are seen to nearly collapse to a single curve indicating that the specific choice of coefficients (see discussion in Section 3.2.2) may not be particularly critical in turbulent flows. Thus, the model of Mei & Adrian is preferred as it is cheaper to evaluate than the Dorgan & Loth kernel (given that square root operations are required in contrast to floating point exponentiation).

An important result to note in Figure 5.4b is the successful application of the window model for this case (the first time this has been demonstrated for a turbulent flowfield). The window model is seen to compare well with the other finite Reynolds number kernels but at a fraction of the CPU cost (to be shown later). As discussed in Section 3.2.2, this agreement is expected provided the change in relative acceleration over the "window" is small. Following Eq. 3.33, one may estimate ϵ for this case as

$$\epsilon = \frac{\tau_H}{\tau_{traj}} \approx \frac{\tau_H}{\tau_\Lambda} \tag{5.5}$$

where τ_Λ is the average integral fluid time-scale observed along the particle path. Using the τ_H expression given as Eq. 3.31, and taking the necessary data from the DNS results, an *a posteriori*

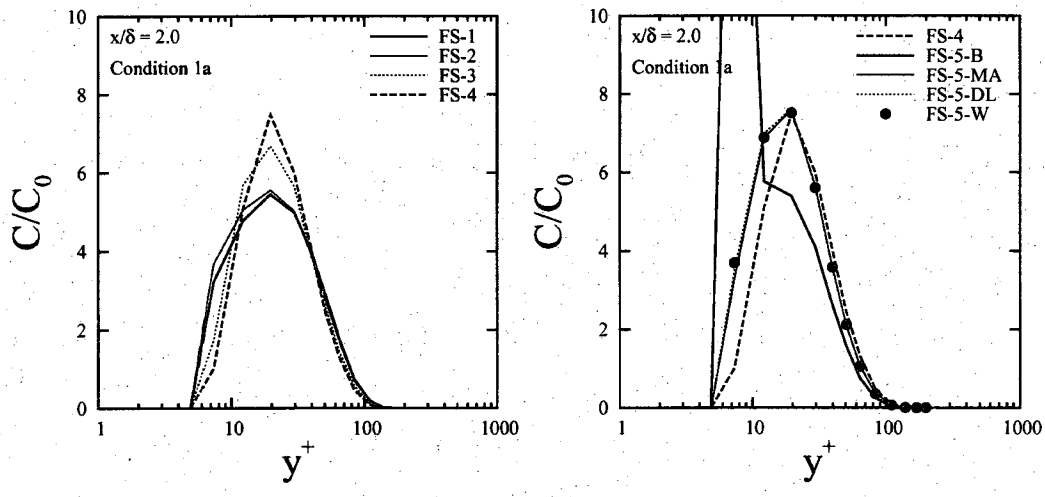

Figure 5.4: Particle concentration comparison for condition 1a force study at $x = 2\delta$.

estimate can be formed to give $\epsilon \approx 0.09 \ll 1$ for this case. Thus, it is reasonable to expect the window model to give accurate predictions of the history force. Note that using the integral time-scale assumes that the particle remains trapped in an eddy over the course of the eddy-lifetime. This would not be appropriate for particle's with large γ as the particle will cut through eddies rather than being trapped inside of them. In these case, one should employ an eddy-traversal time scale [27].

Figure 5.5 shows similar distribution profiles for a further downstream location of $x = 8\delta$. The left figure shows similar trends compared to the distribution at $x = 2\delta$ where the effect of finite Reynolds number quasi-steady drag is small and the fluid acceleration terms are seen to sharpen the profile and prevent sustained near-wall concentration. Again, the effect of the lift force is small, as expected for this condition. Looking at the comparison between FS-4 and the history force EOM's, it is again obvious that the Basset kernel prediction is an outlier and that the remaining history force kernels give very similar results. Unlike the distribution profiles at 2δ, negligible difference is seen between FS-4 and the finite Reynolds number history force variants. This indicates that the finite Reynolds number history force is becoming negligible as the particles move downstream and that the particle are seeking an equilibrium state in which the relative particle acceleration is small.

Figure 5.9 shows the distribution profiles at the end of the particle tracking domain ($x = 15\delta$) for condition 1a. Similar to the upstream locations, the strongest effect is observed for FS-3 where the

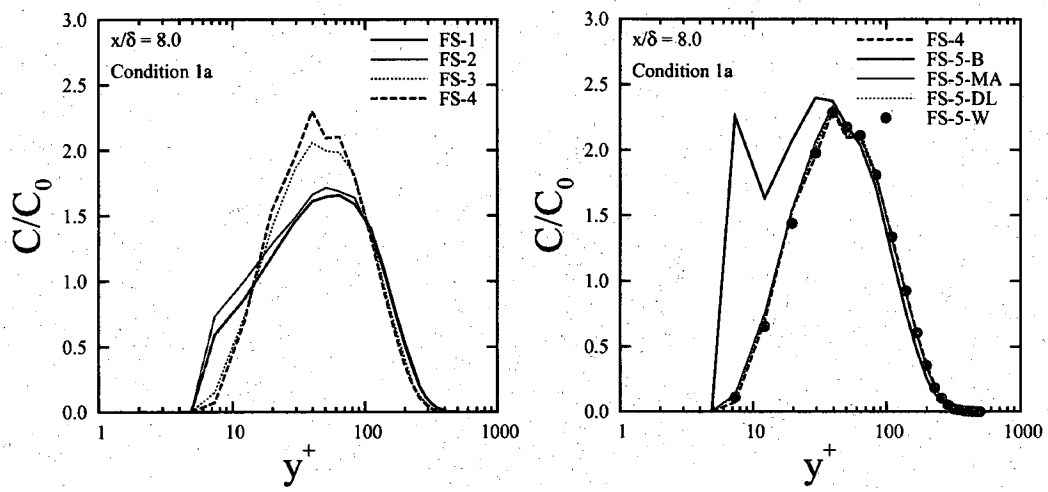

Figure 5.5: Particle concentration comparison for condition 1a force study at $x = 8\delta$.

particle concentration remains less diffused than that predicted with drag alone. FS-1 and FS-2 are seen to maintain a sizable near-wall concentration around the injection location of $y^+ = 9.8$. In Figure 5.9b, it can be seen that the Basset kernel is beginning to approach the predictions made with the finite Reynolds number kernels. Given that little difference is seen between FS-4 and the finite Reynolds number history force predictions, we again conclude that the integrated impact of the history force must be small by this location due to the particles being in some state of acceleration equilibrium. This is also consistent with the Basset force becoming weaker as time goes on. The collapse of FS-4 and FS-5 for long-times is an interesting result in that if one is only interested in predicting long-time particle distributions the history force can likely be neglected in boundary layer flows with similar conditions.

Figures 5.7 through 5.9 present transverse distribution profiles for the sand particle (condition 2a). In Figure 5.7 it is once again seen that there is only a small difference in the concentration predictions of FS-1 and FS-2 indicating that the effects of finite Reynolds number quasi-steady drag are small for this case. In contrast to the condition 1a results, the sand particle shows less effect of added mass and fluid acceleration (compare Figures 5.4 and 5.7, curves FS-2 and FS-3). This is attributed to the increased density ratio associated with condition 2a since these force scale with $1/\psi$, see Eq. 3.98, and thus become less important as density ratio increases.

The effect of lift force (compare FS-3 to FS-4) is seen to be small for this relative velocity condition, similar to what was observed for condition 1a. Addition of the finite Reynolds number

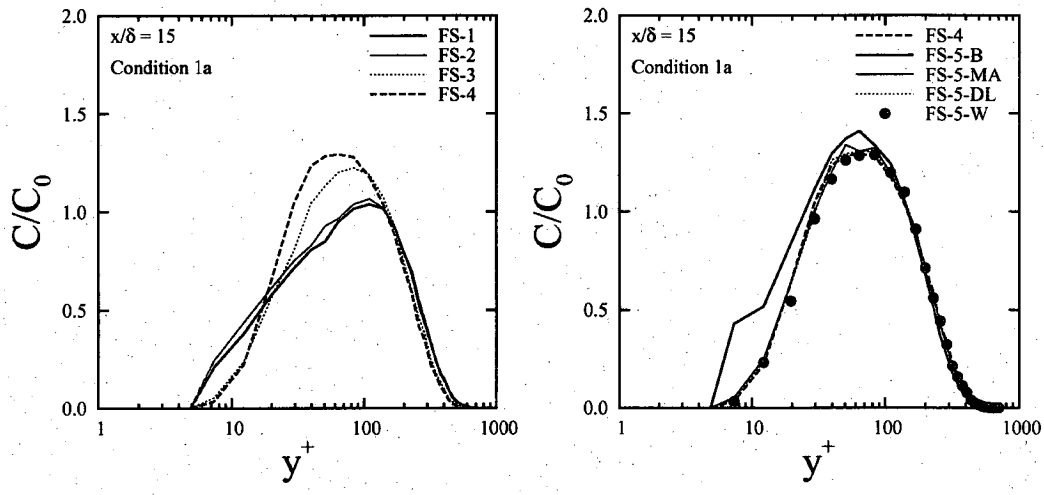

Figure 5.6: Particle concentration comparison for condition 1a force study at $x = 15\delta$.

history force (Figure 5.7b) tends to sharpen the concentration profile and push it towards the drag-only result of FS-2. As discussed above, this is an expected result as the history force amplifies the quasi-steady drag and accounts for the unsteady contributions to the drag force. The Basset kernel is again seen to dominate the other forces for short-times and give erroneous predictions. The window model performs well except for the first bin location where the finite Reynolds number history force has been over-predicted. This is attributed to a large amount of relative jerk in this region which leads to the history force transition time, τ_H, being over-predicted.

Figure 5.8 shows the distribution profiles for condition 2a at $x = 8\delta$. Like the upstream location at 2δ, less difference is seen among the curves compared to the condition 1a results (Figure 5.5). Interestingly, the inclusion of lift (FS-4) appears to move the particles slightly further from the wall and prevented the sustained concentration inside $y^+ = 10$. Figure 5.8b shows little impact of including finite Reynolds number history force outside of an increased near-wall concentration in the first bin off the wall. As such, significant differences associated with history effects may be expected primarily in wall statistics. The Basset kernel is seen to again over-predict the unsteady drag force at this x-location while the window model performs quite well. The window model errors observed at the upstream location of 2δ have largely disappeared by this location and the prediction agrees well with the Mei & Adrian and Dorgan & Loth kernel predictions.

Concluding the discussion of transverse particle concentration, Figure 5.9 shows the distribution of particles at the end of the particle tracking domain 15δ downstream of the injection location.

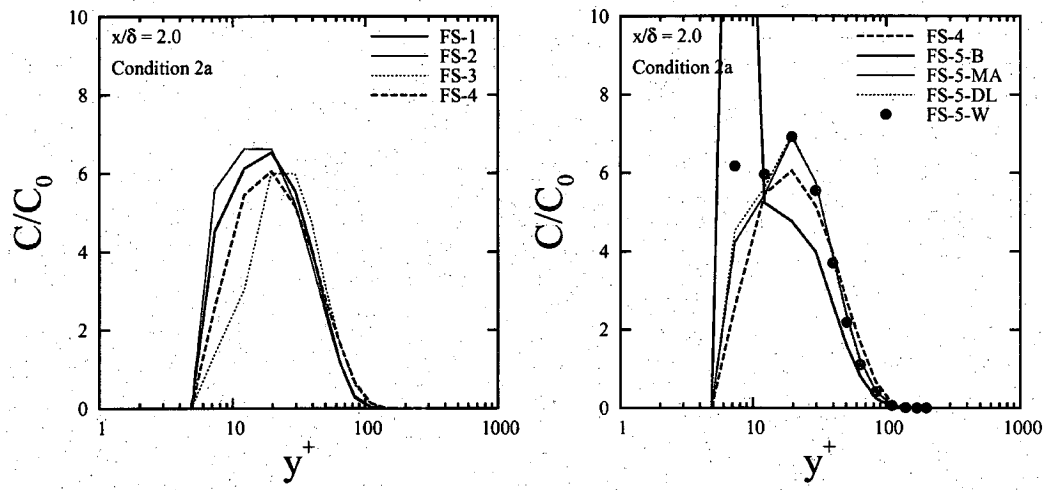

Figure 5.7: Particle concentration comparison for condition 2a force study at $x = 2\delta$.

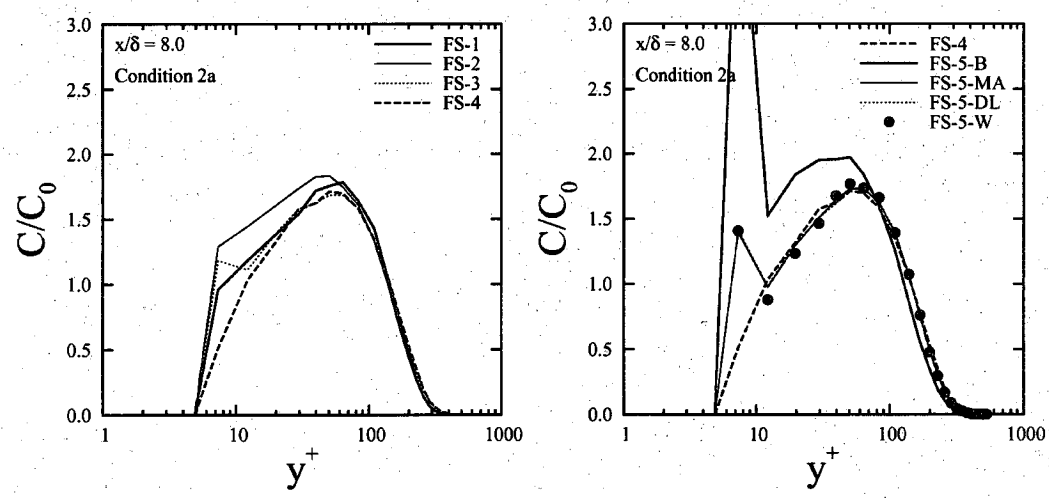

Figure 5.8: Particle concentration comparison for condition 2a force study at $x = 8\delta$.

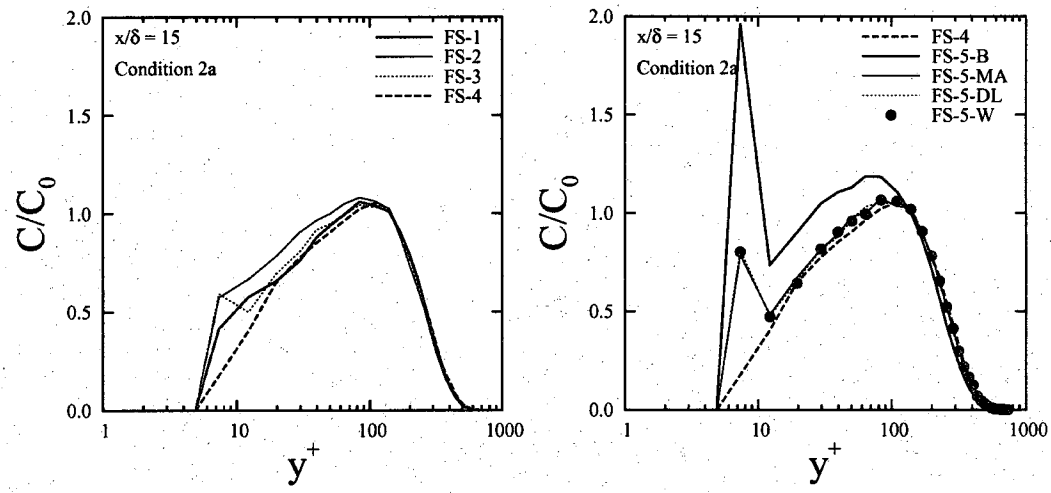

Figure 5.9: Particle concentration comparison for condition 2a force study at $x = 15\delta$.

Similar to the results shown for $x = 8\delta$, FS-1, 2, 3, and 5 all show a sustained near-wall concentration of particles while FS-4 does not. This removal of particles from the near-wall region in the FS-4 results may be related to fluctuations in the lift force. These fluctuations are related to fluctuations in the vorticity (which scales with turbulent dissipation rate [95]) which are strong for $y^+ < 10$ (Figure 2.4b). Note that this is not the case for velocity fluctuations which are small in the near-wall region (Figure 2.5) and thus cause little transverse perturbation.Outside of this near-wall region, all EOM's are shown to produce similar results except for FS-5-B where the Basset kernel is again seen to produce very high near-wall concentrations. The finite Reynolds number history force kernels, including the window model, collapse to the same curve and also gives a finite near-wall concentration. Thus, the wall-peaking effect that lift eliminated is bought back by history force, indicating that the latter tends to dominate.

5.1.2.2 Concentration distribution with streamwise terminal velocity

While the above figures show little effect of the lift force, there can be other configurations (e.g. a flow along a vertical wall) where the lift force can be quite important. The next several figures consider these effects by rotating the gravity vector to induce stronger lift forces in the wall-normal (y) direction. These figures employ conditions FS-6-W and FS-7-W (described in Table 5.2) and are presented in terms of "lift direction". For example, Figure 5.10a shows results generated using particle condition 1a at $x = 2\delta$ where the first curve, FS-5-W, has the buoyancy vector oriented in

$+y$ and thus generates an expected lift force in the $+x$ direction. Thus, the migration of particles to higher y^+ values for this case is largely due buoyancy. The case of a rotated gravity vector in the $+x$ direction (so that mean lift is in the $-y$ direction) is shown in Figure 5.10a. This leads to strong wall concentrations as observed by experiments with similar conditions (Felton & Loth [96, 97]).

The third curve, FS-7-W, chooses buoyancy directed in the $-x$ direction such that the mean lift force should drive particles in the $+y$ direction and away from the wall. Comparing the $L = \pm y$ curves, one can clearly see that FS-7-W results in a distribution profile that is significantly pushed out from the wall compared to FS-6-W. Additionally, the FS-7-W particles have migrated nearly the same distance away from the wall as the FS-5-W condition. The final curve, FS-8-W, shows a prediction with no lift force and falls in between the FS-6-W and FS-7-W curves. Note that both FS-6-W and FS-7-W conditions were ran with no-lift and were found to give very similar distribution profiles such that only one case (FS-8-W) is shown here. Compared to the zero-lift case, the case with buoyancy away from the wall (FS-5-W) and the case with mean lift away from the wall (FS-7-W) both result in a substantial shift in profile, with the lift effect being somewhat weaker. This result is consistent with the "measured" ratio of lift-to-buoyancy of about 0.5. Further downstream locations will confirm that the terminal velocity of FS-5-W is indeed slightly stronger than the lift force of condition FS-7-W.

Figure 5.10b shows the same comparison for the sand particle (condition 2a). The same trends can be observed for this figure where it is seen that the FS-6-W produced the largest near-wall concentration and peak migration of particles away from the wall is similar for FS-5-W and FS-7-W. In both Figures 5.10a and 5.10, a factor of approximately 3 is seen in maximum concentration level depending on the direction of buoyancy. Thus, lift can be seen to be a quite important force in turbulent diffusion for low density particles.

Figure 5.11 shows the same conditions but at a streamwise location about halfway through the particle tracking domain. Similar but more pronounced effects of lift are noted at this location where the $L = -y$ cases shows the strongest near-wall concentration followed by the no-lift prediction with noticeable lower values. The distributions observed at the end of the tracking domain are shown in Figure 5.12. Similar trends are observed at this location as well but we note that the sand particle has retained a much higher near-wall concentration of particles compare to the bubble. This is likely a combination of the lift force driving particles to the wall and

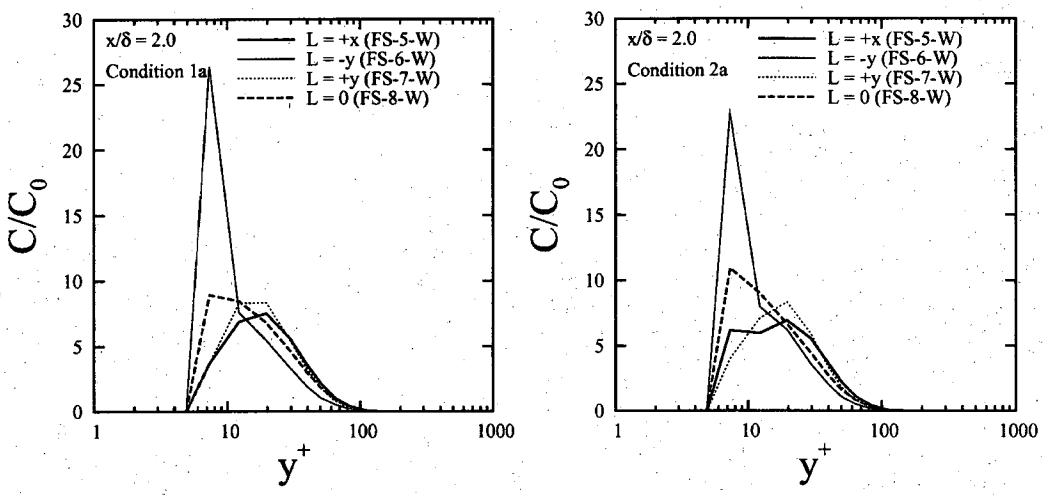

Figure 5.10: Effect of gravity direction for (a) condition 1a and (b) condition 2a at $x = 2\delta$.

turbophoresis (as discussed in Section 4.3.2) encouraging a drift of particles below $y^+ = 10$ towards the wall; the latter may be attributed to the sizable inertia associated with the sand particle condition.

5.1.3 Particle diffusion rates

Figures 5.13 and 5.14 show the spanwise mean-square deviation of the particle's position relative to the injection location. Since there is no component of terminal velocity acting in the spanwise direction, these plots can be directly related to turbulent diffusion. In general, the spanwise diffusion increases with time and shows little difference due to equation of motion with the exception of the FS-5-B where the Basset kernel is seen to significantly reduce diffusion. This is consistent with sharp peaks that were observed in the distribution profiles for this condition in Section 5.1.2. Figure 5.13b shows a slight reduction in diffusion rate when the finite Reynolds number history force is included and this is consistent with the damping effects the drag force should have on particle motion. Note that the window model has again performed well and predicted identical results compared to the standard finite Reynolds number kernels.

Figure 5.14a shows even less changes in the diffusion rate than the small variations observed for the bubble condition. This is consistent with the reduced sensitivity of this condition to the choice of equation of motion which was observed and discussed in terms of distribution profile in the

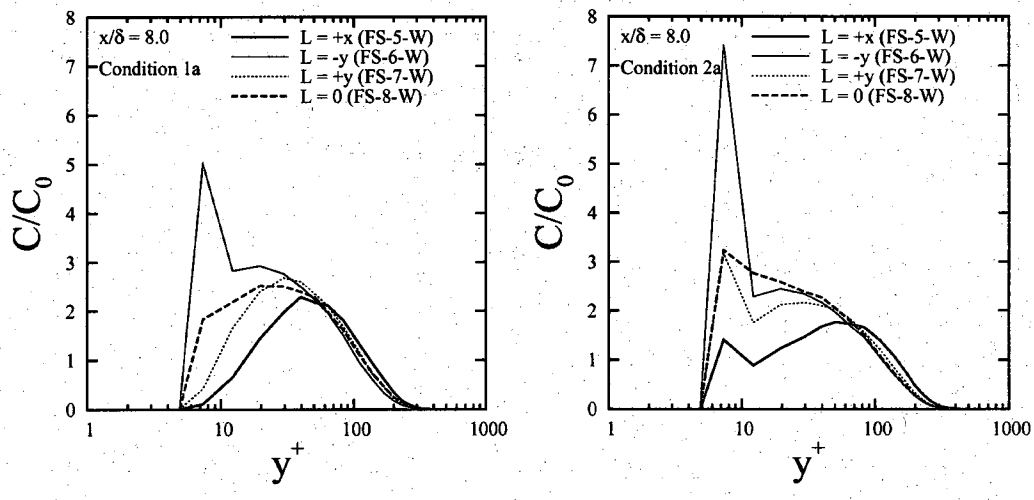

Figure 5.11: Effect of gravity direction for (a) condition 1a and (b) condition 2a at $x = 8\delta$.

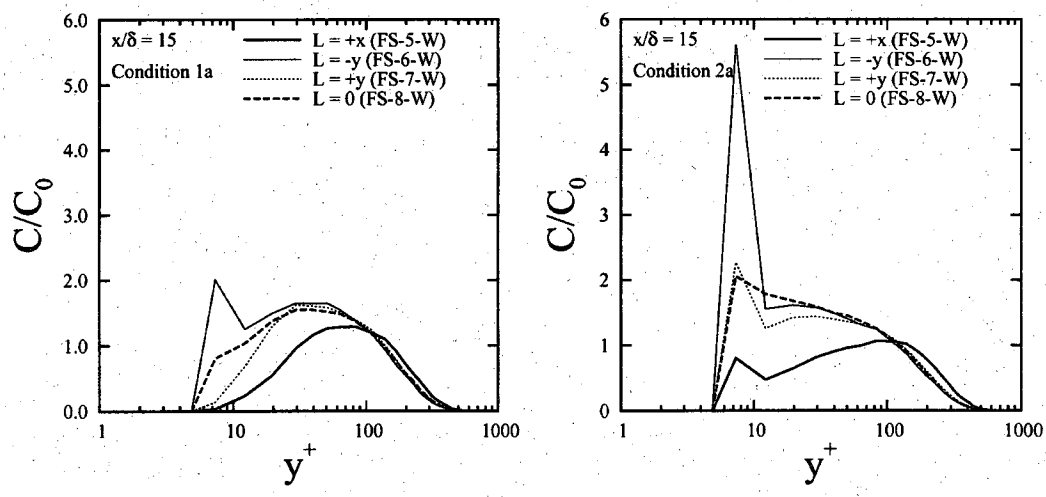

Figure 5.12: Effect of gravity direction for (a) condition 1a and (b) condition 2a at $x = 15\delta$.

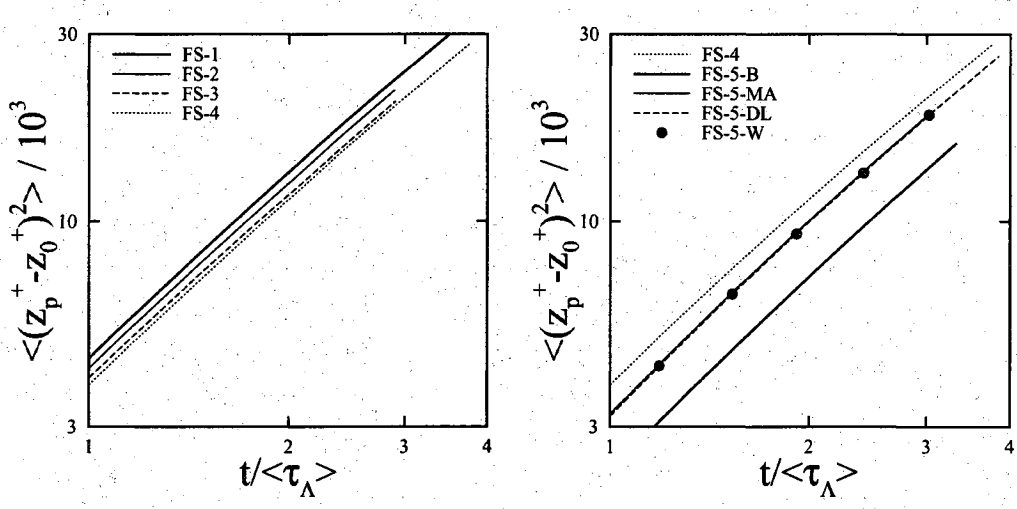

Figure 5.13: z^2-diffusion for condition 1a.

preceding section. In Figure 5.14b a reduced diffusion rate is observed when the history force is included.

Figures 5.15 and 5.16 shows the transverse mean-square deviation from the injection location which includes the mean particle drift induced by terminal velocity. Figure 5.15 shows the predictions for bubble condition, 1a. Here the trends that were observed in the transverse distribution profiles can clearly be identified as well. For example, Figure 5.15a shows that FS-1 and FS-2 drift farther from the injection location than does FS-3 and FS-4. Thus, lift can lead to slight anti-diffusion; perhaps because diffusion events due to drag force incur weak lift forces in the opposite direction. This was observed in terms of concentration profile as FS-1 and FS-2 having a broader profile with a lower peak compared to FS-3 and FS-4. As expected, 5.15b shows that the history force reduces diffusion with the Basset kernel again playing the outlier. Figure 5.16 shows the predictions for the sand particle, 2a, where similar observation can be made comparing the results to the distribution profiles presented in Section 5.1.2.

5.1.4 Velocities along the particle trajectory

This section compares particle statistics measured along the particle trajectories as a function of choice of equation of motion. The first statistic considered in the rms particle velocity about the mean as shown in Figure 5.17 where the results have been normalized by the mean particle

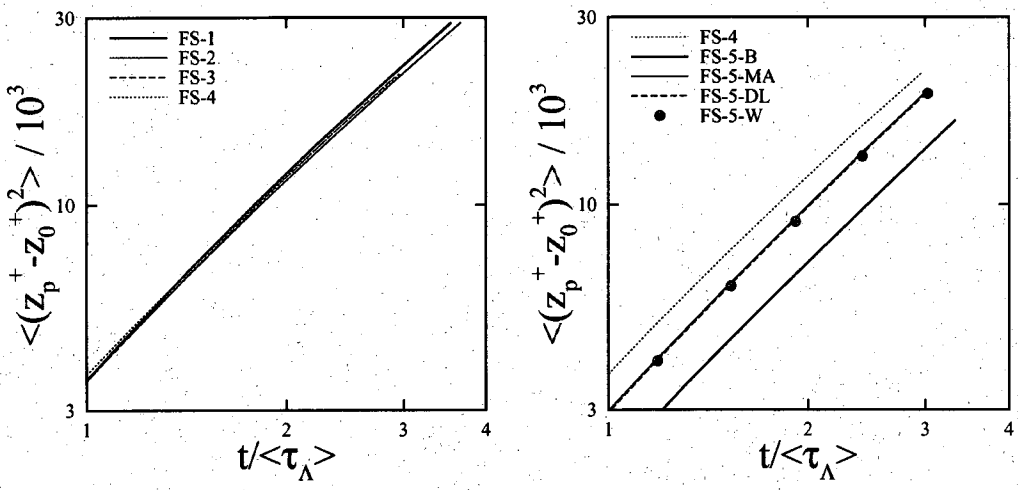

Figure 5.14: z^2-diffusion for condition 2a.

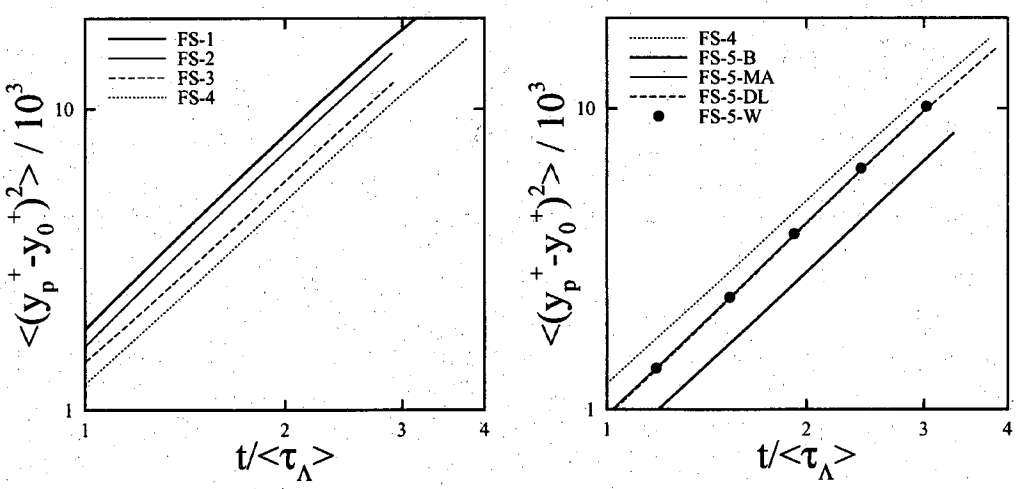

Figure 5.15: y^2-diffusion for condition 1a.

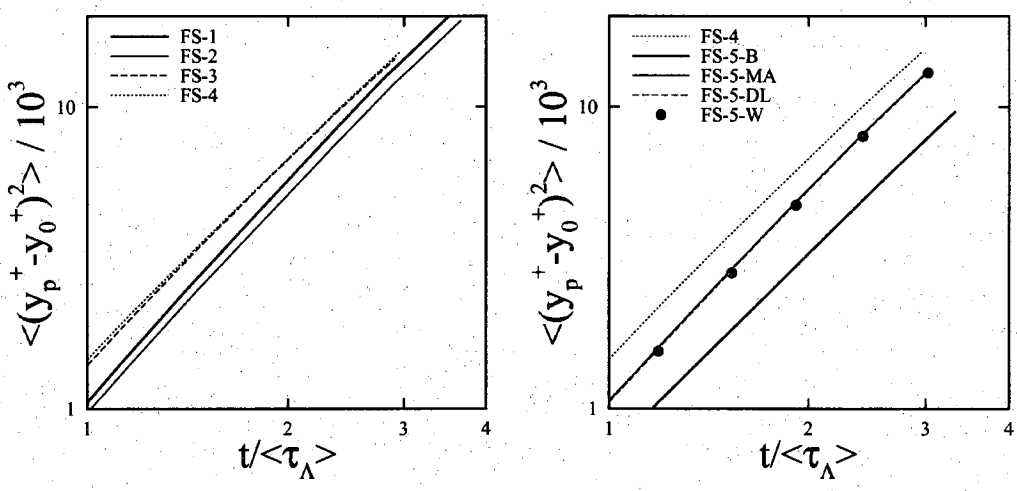

Figure 5.16: y^2-diffusion for condition 2a.

velocity. Recall that the rms about the Lagrangian mean is given by

$$V'_{p,rms} \equiv \left\{ \left\langle (V_p - \langle V_p \rangle)^2 \right\rangle \right\}^{1/2} \tag{5.6}$$

While this form appears to require the Lagrangian mean *a priori*, a simple rearrangement gives a more convenient form:

$$V'_{p,rms} = \left\{ \langle V_p^2 \rangle - \langle V_p \rangle^2 \right\}^{1/2} \tag{5.7}$$

such that one can collect both the mean and mean-square over the course of a simulation and be able to compute the rms as a post-processing step.

Figure 5.17 shows that the rms deviations from the mean are higher for the EOM's including history force. This is likely a result of the particle experiencing a larger drag force due to the inclusion of the history force term. Again it is noted that the Basset kernel produces a result which is an outlier compared to the remaining data. Interestingly, the FS-4 has the lowest rms velocity of all EOM's for both particle conditions attributed to an anti-diffusive property of the lift force. Considering all appropriate EOM's for these conditions (excluding FS-1 and FS-5-B) the variation in rms particle velocity is relatively small and on the order of a few percent of the mean velocity. It is also noteworthy that the history force generally increases $V'_{p,rms}$ and thus should be included to model this aspect accurately. Additionally, note that the history force actually increases the rms particle velocity whereas it was seen to reduce mean diffusion.

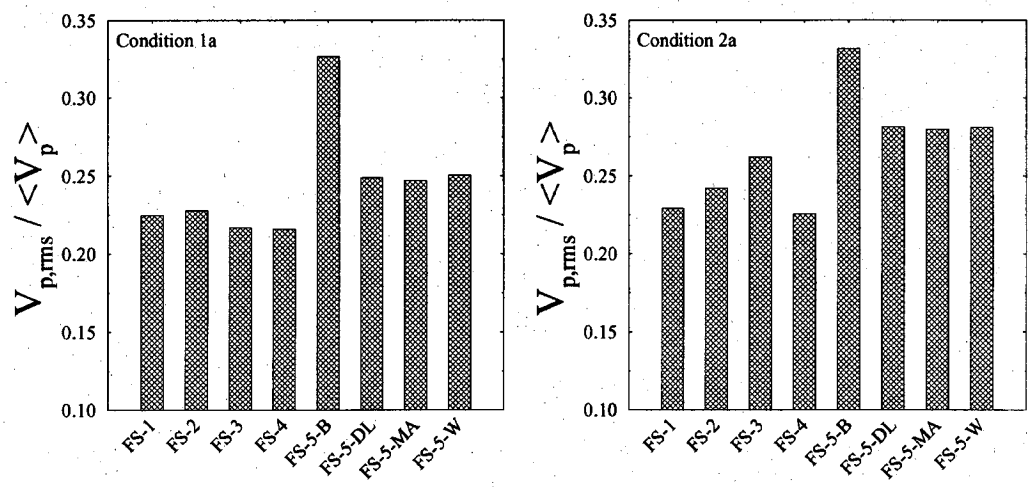

Figure 5.17: Particle rms velocity predictions for (a) condition 1a and (b) condition 2a.

Secondly, the mean Reynolds number is considered for all of the equations of motion in Figure 5.18. Both particle conditions experience roughly the same Reynolds number for FS-1 and FS-2 EOM's with the sand particle of Figure 5.18b showing more variation due to the stronger finite Reynolds number effects at this higher Stokes number. For the bubble condition, Figure 5.19a, the addition of fluid acceleration forces results in an increased Reynolds number while the sand particle, Figure 5.19b, shows the opposite trend. This is a result of the magnitude of the coefficient in front of the fluid acceleration term. For bubbles, this coefficient has a value of 3 such that (neglecting the other forces) the particle would experience accelerations that were 3 times greater than the fluid acceleration, a phenomenon which is also discussed by Hinze [88]. This over-correction (taken from a drag force standpoint) in the particle velocity will induce a mean total relative velocity which is higher than that predicted by FS-2 as seen in Figure 5.18a. Now consider the sand particle: the coefficient in this case is 0.6 such that the particle is required to accelerate at 60% of the fluid acceleration (again neglecting other forces). Thus, the fluid acceleration for the sand particle "helps" the drag force in that the particle will attenuate quicker to changes in the fluid velocity and on average experience a lower relative velocity (and thus lower Reynolds number) compared to the drag alone case as seen in Figure 5.18b. These consequences of the fluid acceleration term are interesting in that the sand particle showed little sensitivity to that term when considering transverse distribution and diffusion rate. Comparing FS-3 to the FS-5-W both cases are observed to experience lower Reynolds numbers when the finite Reynolds number history force is included. Interestingly, both particle conditions experience much similar mean Reynolds numbers when the

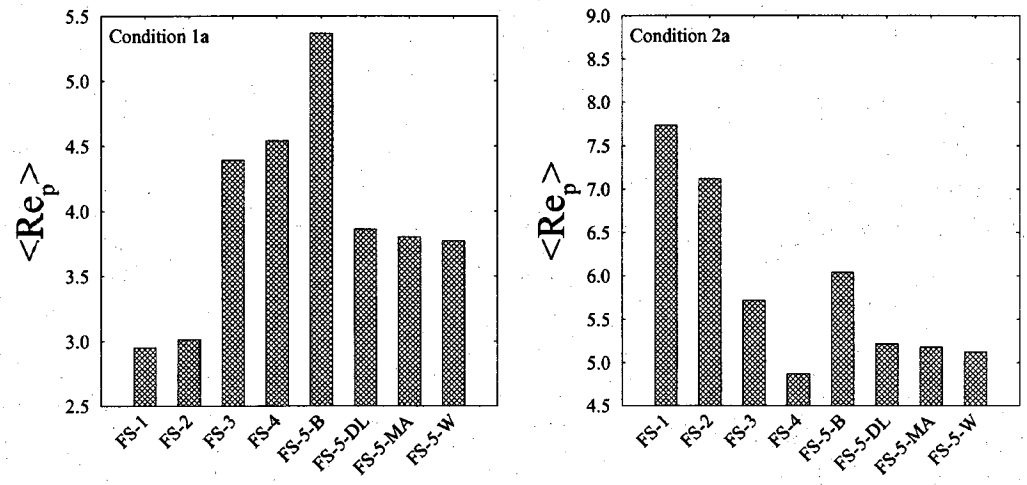

Figure 5.18: Mean particle Reynolds numbers for (a) condition 1a and (b) condition 2a.

full EOM is used (compared to the factor of ~ 3.5 when drag alone was considered).

Next, the vertical relative velocity is considered for all of the equations of motion in Figure 5.19. Here the vertical relative velocity is normalized by the particle's terminal velocity such that the statistic should be unity in the case of undisturbed flow. Additionally, one would expect this statistic to be near-unity for the FS-1 EOM since the Stokes drag law results in a decoupled EOM whereby the relative velocities in one coordinate direction does not affect the others. This is trend seen for both conditions 1a and 2a for FS-1. Trading the Stokes drag for a finite Reynolds number formulation is seen to drop the vertical relative velocity for both conditions. This is due to the non-linearity of the finite Reynolds number form where the non-zero relative velocity components in the streamwise and spanwise directions affect the vertical component of the drag force. This results in a reduced mean vertical relative velocity as long as the other components remain non-zero. For the bubble condition, Figure 5.19a, the addition of fluid acceleration forces results in a decrease in relative vertical velocity while the sand particle, Figure 5.19b, shows the opposite trend. This is attributed to the magnitude of the fluid acceleration coefficient as discussed above for the mean Reynolds number but rather than causing an increase in relative velocity for the bubble condition we see that the vertical component has been reduced. This is an effect of the non-linear finite Reynolds number drag where the relative velocity vector has increased in magnitude, but the vertical component has been reduced. This says that the streamwise and spanwise fluid fluctuations (and the fluid acceleration components in those directions) are larger than the wall-normal component which would be expected for the present near-wall injection

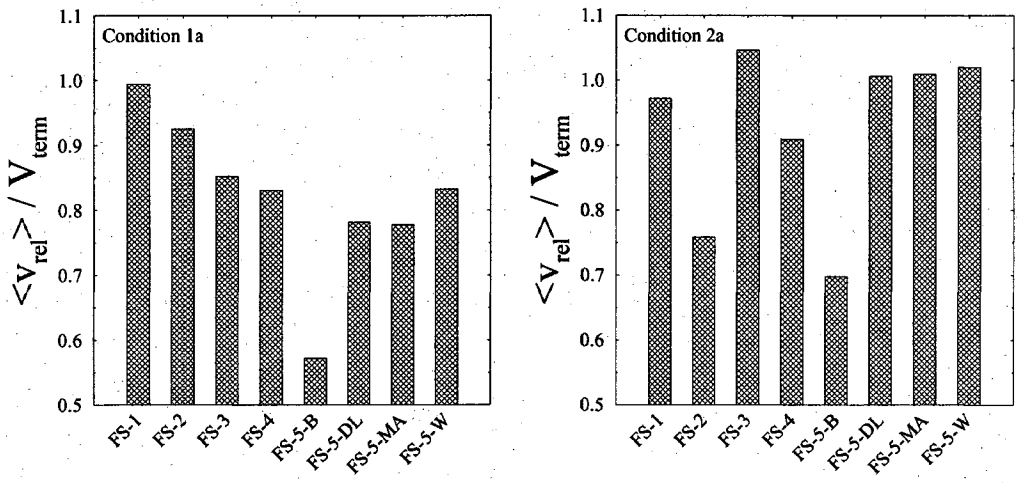

Figure 5.19: Particle relative velocity in the wall-normal direction normalized by V_{term} for (a) condition 1a and (b) condition 2a.

location. The opposite is true for the sand particle where the vertical relative velocity is increased and is evidence of the particle being in better equilibrium with the fluid consistent with the fluid acceleration force helping the drag force to keep the particle caught up with the fluid. Comparing the FS-5-W results between the two particle conditions it is seen that relative vertical velocity is near V_{term} for the sand particle case while the bubble condition sees only $0.85V_{term}$. This result is again attributed to the fluid acceleration forces whereby the bubble is less in equilibrium due to over-acceleration. Without being in equilibrium, the particle can experience relative velocities much different than V_{term}.

Finally, the rms deviation of Reynolds number from the Lagrangian mean is considered and the results are shown in Figure 5.20. Similar to the definition used for the rms particle velocity, the rms Reynolds number is defined as

$$Re_{p,rms} = \frac{V'_{rel,rms} d_p}{\nu} \tag{5.8}$$

$$V'_{rel,rms} = \left\{ \langle V_{rel}^2 \rangle - \langle V_{rel} \rangle^2 \right\}^{1/2} \tag{5.9}$$

and can be compared to the mean values shown in Figure 5.18 to assess the level of fluctuations observed along the particle paths. For both the bubble and the sand particle, Figure 5.20 shows that FS-1 admits noticeably more oscillation in the relative velocity than FS-2. This is expected given that the mean Reynolds numbers for these cases are too large for the Stokes drag law to be

appropriate. As the Reynolds number increases, Stokes drag law predicts a drag coefficient which is too small and allows comparatively larger relative velocity excursions, detected here in the rms Reynolds number. A significant increase in rms Reynolds number is observed for the bubble condition when the fluid acceleration forces are included (FS-3). This is again consistent with the expected behavior of the fluid acceleration for bubble conditions where fluid unsteadiness is amplified by a factor of 3 through the coefficient of the fluid acceleration term. The opposite is true for the sand particle, consistent the the fluid acceleration term acting to reduce the particle to fluid relative velocity when $\psi > 1$. In both cases, the history force is seen to dampen the unsteady behavior of the relative velocity. Interestingly, the rms Reynolds number for both conditions (considering FS-5-W) is roughly 80% of the mean Reynolds number (see Figure 5.18) such that considering the mean alone would be inappropriate for estimating effects such as heat transfer.

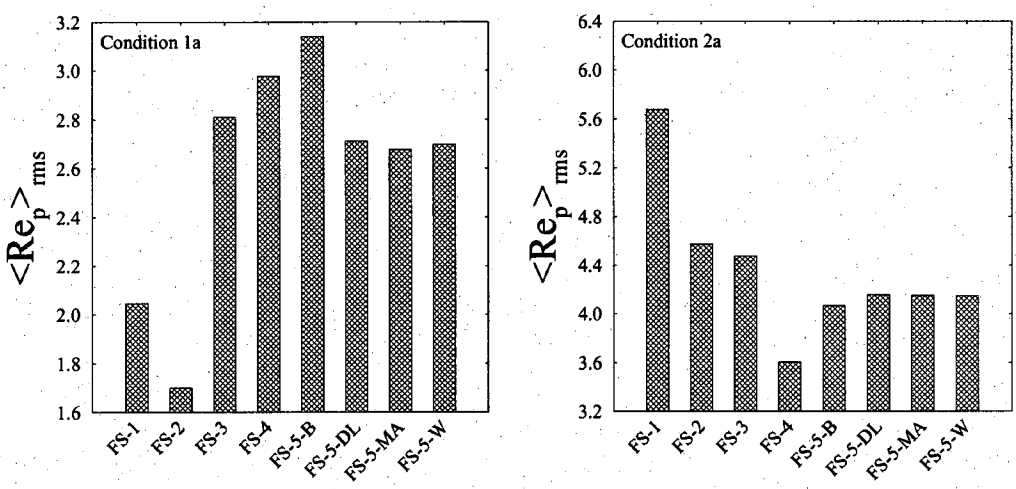

Figure 5.20: RMS particle Reynolds numbers for (a) condition 1a and (b) condition 2a.

5.1.5 Computing resource requirements

In recent years the availability of vast amounts of memory (RAM) has dramatically increased while the cost has fallen. While the DNS code used in the present research has been run in past studies on supercomputers like the Blue Horizon machine at the San Diego Supercomputing Center, today it can be run on basic desktop machines. However, when the history force is added to the equation of motion, the memory requirement can increase drastically and scales with the number of particles to be considered. The present implementation stores the required data for the history force

calculation in a linked-list data structured (one link for each particle) such that the list can be grown or reduced with ease. The base memory requirement for each link is 20 bytes which includes allocatable arrays which are grown (in chunks corresponding to 1000 time-steps of data) to hold the particle relative velocity history. Therefore, the relative velocity arrays soon dominate the memory associated with other parts of the linked-list (20B) and the overhead of this storage structure is insignificant comparatively. All three relative velocity components must be stored such that the memory requirement is 12 bytes for each time-step (using single precision, 4 byte real values). If we assume the average particle experiences 1000 time-steps on its journey through the particle tracking domain, and a total of 100,000 particles were to be tracked, the use of static arrays would require 1.2 GB of memory. However, the use of static arrays would have to allow for additional time-steps to be sure that program did not run out of space to store new history data. The present dynamic approach employed via a linked-list avoids these problems and can additionally deallocate memory associated with particles that have left the tracking domain and was observed to cut the memory requirement by more than a factor of 2 for the present simulations. Other approaches for mitigating the memory usage, such as retaining only a portion of relative velocity history over which the kernel is sizable, was not considered. This may prove to be necessary for studies which involve recycling of the particle field (typically done for channel flow studies) as the particles exist in the tracking domain for an arbitrary number of time-steps and thus an arbitrarily large amount of history information would be stored given the current approach.

Aside from memory, another important measure of computational hardware requirements is the run-time associated with a particular model. Figure 5.21 shows the CPU-time required for each of the equations of motion normalized by the CPU-time associated with FS-2 (considered to be the simplest "reasonable" EOM). This plot shows that the CPU overhead associated with the various levels of modeling is relatively constant until the history force is included. This is a reason why it is typically neglected in many engineering computations. However, the window-model in seen to add only 27% to the CPU-time for FS-2. This is in contrast to the other history force models which can increase the CPU-time by more than 400% for FS-5-DL (which involves floating-point exponentiation) and roughly 250% for FS-5-MA. Thus, the penalty for including the history force is largely eliminated in by using the window model. The present study used an SGI Octane 2 with R12000 processors with a clock speed of 360MHz. Typical run time of an FS-2 case was approximately 46 hours when using the distributed force equation of motion.

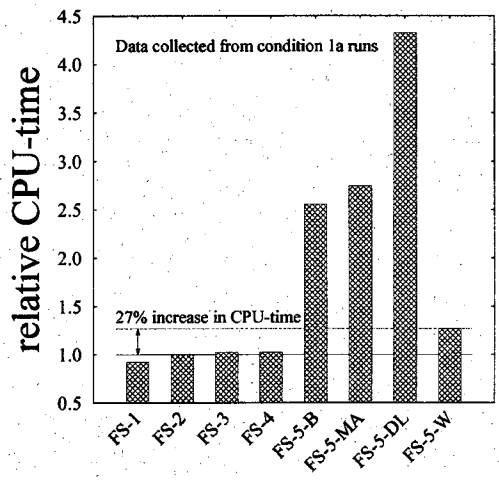

Figure 5.21: Comparison of CPU-time required for simulation of the various equations of motion (compared to FS-2).

5.2 Spatial interpolation and distributed force effects

The previous results were all generated using the distributed force formulation with a Lagrange basis for interpolating inter-cell fluid properties. This section considers the impact on several statistics of choosing less accurate formulations, such as using a tri-linear interpolant for fluid reconstruction or using the point-force approach. Additionally, the computational overhead associated with each approach is discussed. The results will show that depending on the desired level of fidelity, these simpler approximations can provide reasonable predictions at a lower cost. In all results presented below the FS-5-W EOM is employed.

Figure 5.22 shows the effect of spatial interpolant on the transverse distribution of particle for both the bubble and sand particles when using a point-force equation of motion. While the bubble condition shows negligible changes between the simple tri-linear interpolant and the higher-accuracy Lagrange interpolant (Figure 5.22a), the sand particle exhibits a small sensitivity (Figure 5.22b) where some minor differences in the predicted distribution can be seen. Note that since this comparison employs the point-force EOM no averaging over the finite particle size is done–the fluid conditions are simply interpolated to the particle center.

Figure 5.23 shows a similar comparison where the sensitivity of transverse distribution is considered for point vs. distributed-force equation of motion when the Lagrange interpolant is used. Interestingly, both particle conditions show negligible changes indicating that the bulk

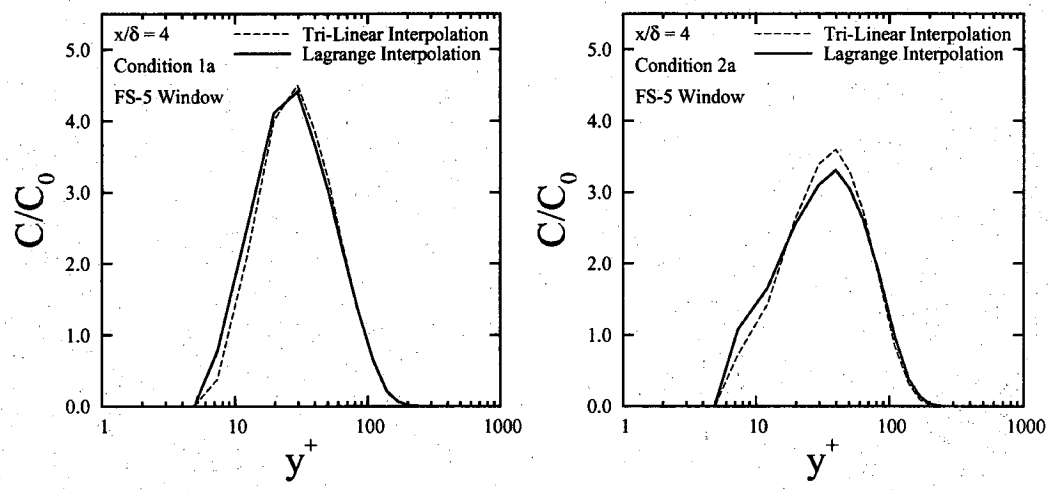

Figure 5.22: Effect of spatial interpolation scheme on particle concentration at $x/\delta = 4$ using point-force FS-5-W for (a) condition 1a and (b) condition 2a .

particle motion is equally well-predicted by the simpler point-force algorithm. This is a surprising result given the diameter of the particles ($d_p^+ = 9.8$) is sizable and presumed to be too large for reasonable point-force predictions.

Figure 5.24 considers the rms particle velocities predicted by the various methods using the surface forces of FS-5-W. In these plots, the predictions are normalized by the distributed force result presented in Section 5.1. In both condition 1a and condition 1b, the point-force algorithm combined with tri-linear interpolation under-predicts the rms motion of the particle. This is likely caused by the damping of the tri-linear interpolation which hides higher frequency modes that exist in the fluid solution. The Lagrange-point-force algorithm is seen to predict larger rms velocities owing to the added frequencies shown to the particle by the more accurate Lagrange basis. Comparing the point-force to the distributed-force results (where a Lagrange basis was used for both cases) shows a smaller effect than the differences observed due to interpolation method. For the case of the bubble (Figure 5.24a) a slightly larger particle velocity is predicted for the point-force approach. This is attributed to the smoothing effects of the distributed-force model which will tend to damp the motion induced by fluid fluctuations smaller than the particle diameter (which are directly experienced by the particle in the point-force approach). The sand particle (Figure 5.24b) shows a negligible influence of the distributed-force model. This may be due to the increased inertia (compared to condition 1a) which leads to larger Stokes numbers and thus less ability to respond to small-scale unsteadiness. Taken as a whole, a maximum deviation of

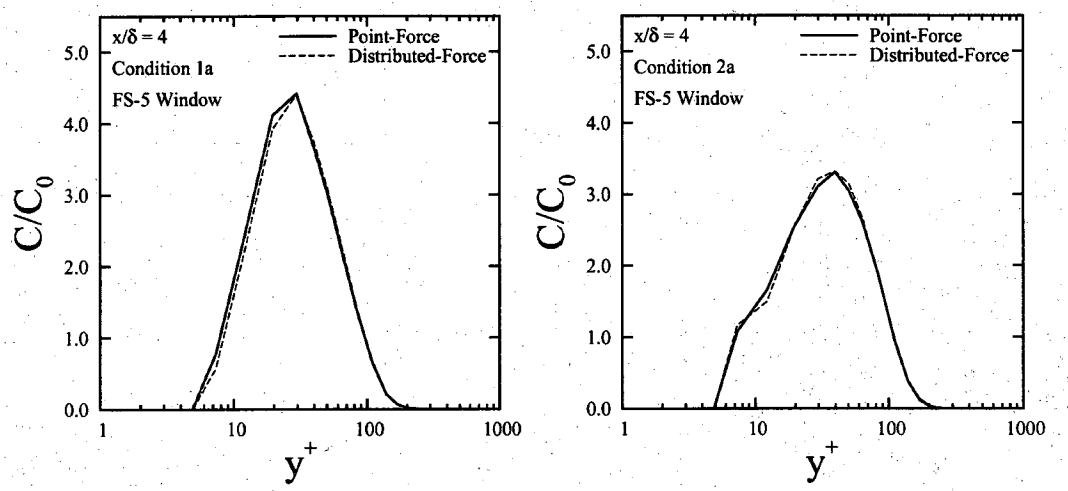

Figure 5.23: Effect of point vs. distributed-force EOM on particle concentration at $x/\delta = 4$ using a Lagrange basis and FS-5-W for (a) condition 1a and (b) condition 2a.

3.5% is seen due to choice of spatial discretization which is generally smaller than the differences seen from including/excluding the history force in Figure 5.17.

Figure 5.25 shows mean Reynolds numbers predictions for the bubble and sand particle. Similar to Figure 5.24, the point-force algorithm with tri-linear interpolation is seen to under-predict the particle Reynolds number compared to the higher-fidelity algorithms. Introducing the Lagrange interpolant into the point-force algorithm results in Reynolds number predictions that are larger than those predicted by the distributed-force algorithm for both conditions. As mentioned above, this is the result of the smoothing properties of the distributed-force algorithm which accounts for the particle's finite size. Figure 5.26 shows rms deviations of the Reynolds number from its Lagrangian mean for the same set of cases. The same general trend holds for as discussed for the mean Reynolds number.

Finally, the relative CPU-cost associated with the various methods discussed above are shown in Figure 5.27 where the results are normalized by the point-force algorithm with tri-linear interpolation. Not surprisingly, the tri-linear interpolant combined with the point-force algorithm provides the most efficient simulation approach. Introducing the Lagrange interpolant in the point-force algorithm results in a 33% increase in CPU-time. This is due to the increased number of floating-point operations required to construct and evaluate the higher-fidelity Lagrange interpolant. Finally, the Lagrange interpolant used in the distributed-force algorithm shows a 300% increase in CPU-time compared to the simplest algorithm. This increase is due to the

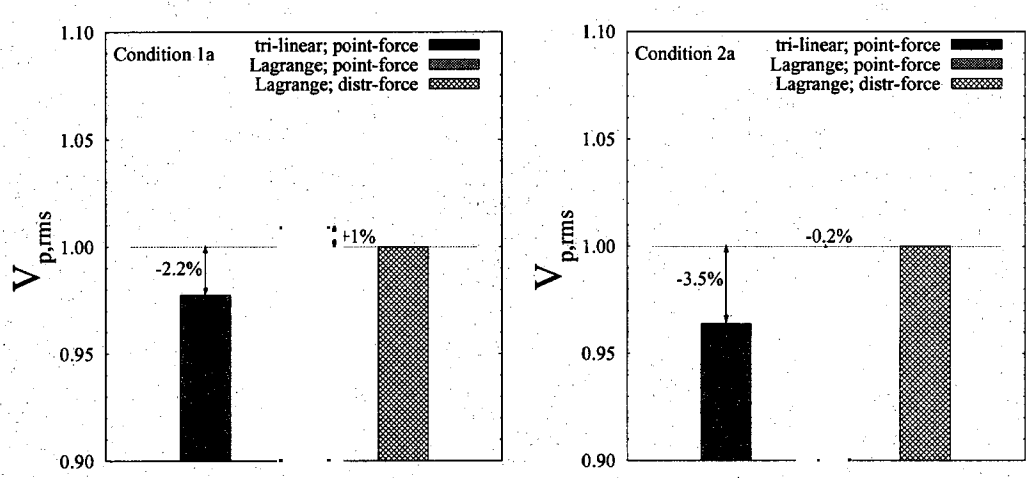

Figure 5.24: Effect of spatial interpolation scheme and surface force method on rms particle velocity using FS-5-W for (a) condition 1a and (b) condition 2a normalized by the Lagrange, distributed force result.

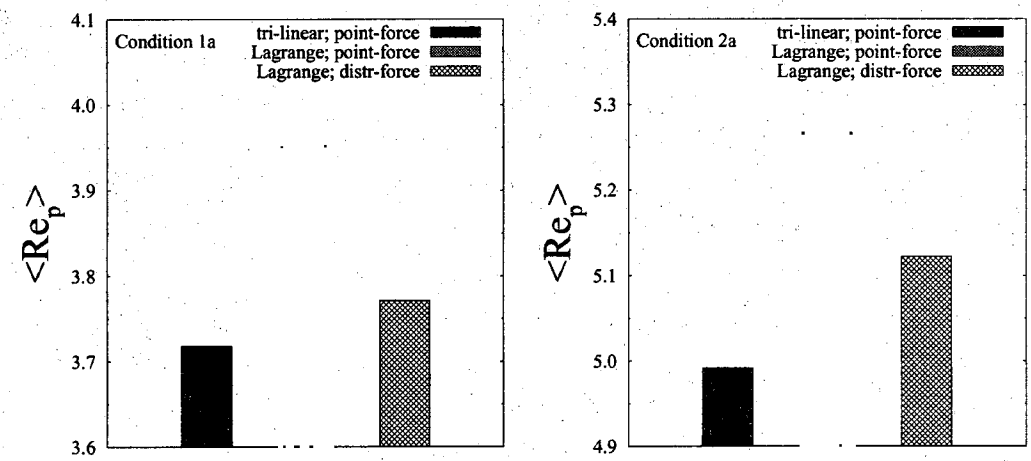

Figure 5.25: Effect of spatial interpolation scheme and surface force method on mean particle Reynolds numbers using FS-5-W for (a) condition 1a and (b) condition 2a.

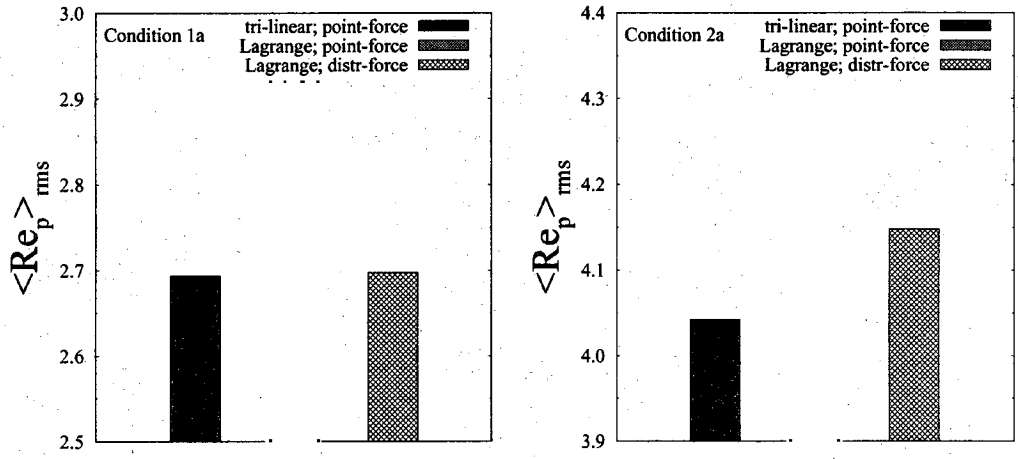

Figure 5.26: Effect of spatial interpolation scheme and surface force method on rms particle Reynolds numbers using FS-5-W for (a) condition 1a and (b) condition 2a.

distributed force algorithm requiring interpolated fluid data at six surface points in addition to the center point required for the point-force algorithm. In light of the above discussions, the simpler models may be sufficient for modeling the present conditions depending on the desired level of fidelity. Significant reduction in computational requirements can be realized in such cases.

5.3 Summary of EOM study

This first part of this study considered the effects of different surface forces (cast in a distributed-force formulation) on the prediction of low-density particle cloud evolution. Two particle conditions were considered: 1) an air bubble in a boundary layer of water and 2) a sand particle in a boundary layer of water. Both the air bubble and sand particle were injected near the wall and the evolution of wall-normal distribution was tracked for several boundary layer thicknesses downstream. Additionally, diffusion statistics as well as Lagrangian relative velocities were collected. It was found that the fluid acceleration terms are generally important for predicting wall-normal distribution of bubbles but other forces (such as lift and history force) were less important, especially at far downstream locations. The sand particle was found to be less sensitive to the fluid acceleration forces owing to its increased density. The lift force was seen to have only a small influence on the particle concentration when the terminal velocity was directed away from the wall. However, a study which also considered terminal velocity directed with, and

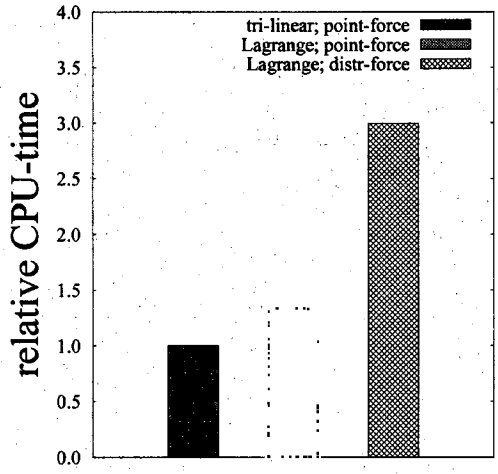

Figure 5.27: Comparison of the CPU-time required for the different algorithms (compared to the point-force model with tri-linear interpolation).

opposite to, the streamwise velocity shows that this is not a general result. For example, the case with terminal velocity directed parallel to the freestream velocity shows a dramatic increase in near-wall concentration compared to all other conditions.

Turbulent diffusion rates for the sand particle were generally insensitive to choice of EOM if the history force is neglected and only minor changes were observed for the sand particle with similar EOM's. In both particle cases, the history force is seen to reduce the diffusion rate, a result expected due to resistance to acceleration which that force provides. Lagrangian statistics taken along the particle trajectory are the most sensitive to choice of EOM. The mean and rms Reynolds number, as well as the rms particle velocity, all showed substantial variations and in some cases approaching 100% changes from EOM to EOM.

A second study considered the effect of fluid property spatial reconstruction on the particle statistics. The choice of spatial interpolation was found to have only small effects on predicting wall-normal sand particle distribution and was negligible for the bubble condition; however stronger effects were observed in the context of Lagrangian statistics. The study also considered the effect of using a point-force algorithm versus a distributed-force algorithm. The predictions of wall-normal distribution were found to be insensitive to this choice for both conditions. Thus, the point-force requirements commonly posed may be less restrictive for these types of flows (e.g. particles/bubbles injected near the wall in a turbulent boundary layer) if one wishes to predict particle concentration. The Lagrangian statistics again show some variation with the mean and

rms Reynolds numbers being the most sensitive.

Computational overhead for each of the techniques was considered and it was found that the distributed-force algorithm using the higher-order Lagrange interpolant cost roughly three times as much a simple point-force algorithm with tri-linear interpolation. The history force, which is neglected in many calculations due to the high CPU-cost, was shown to be efficiently calculated by using the window model developed in Section 3.2.2. This model allowed the inclusion of history force at an increased CPU-cost of 27% compared to 400% increases seen with other models.

In conclusion, the modeling of low-density particles can be accomplished using a variety of EOM's, interpolation schemes, and point or distributed-force algorithms. Depending on the outputs of interest (e.g. distribution profiles, Lagrangian statistics, etc.) and desired level of fidelity, simpler EOM's and algorithms can be used to obtain results at considerably lower costs. For example, distribution profiles were well-predicted using the point-force algorithm and tri-linear interpolation which could cut a factor of 3 from the simulation time compared to using the distributed-force algorithm with a Lagrange basis. Similarly, distribution profiles for bubbles were found to be only slightly sensitive to history force far downstream of injection. Thus, the history force could be neglected for an additional CPU-savings provided the quantity of interest was "far downstream distribution profiles". Lagrangian statistics were found to be the most sensitive and likely require the highest fidelity simulation to obtain accurate predictions. This was particularly true of the history force (which had only minor effects on particle concentration) and could have implications for future two and four-way coupling studies.

Chapter 6

Bubbles and sand particles: size study

This Chapter seeks to understand the effects of diameter on low-density particle distribution, Lagrangian statistics, and wall interactions. As mentioned in Chapter 5, modeling low-density particles typically requires additional surface-forces beyond the quasi-steady drag used in the heavy particle study of Chapter 4. Chapter 5 identified which of these forces was critical for different types of statistics and here we will apply the highest fidelity EOM to give robust and efficient predictions of Lagrangian statistics as well as wall-normal distributions (namely FS-5-W of Table 5.2) for several low-density particles.

This study considers low-density particles in dilute concentrations subjected to a low-Reynolds number, spatially-developing, turbulent boundary layer obtained through a DNS of the incompressible Navier-Stokes equations (see Chapter 2). This approach alleviates potential complications introduced through modeling the turbulence of the continuous-phase using other unresolved or semi-resolved approaches. The particles are injected near the wall with their terminal velocity directed away from the wall, consistent with the heavy-particle study of Chapter 4. The Lagrangian tracking technique described in Sections 3.4 and 3.5 is used to solve the particle equation of motion and advance individual particles through the boundary layer flowfield. The framework of the distributed-force equation of motion for finite-sized particles will be used along with the Lagrange interpolation method discussed in Section 3.5.2 for all cases.

Two density ratios are considered in this section and physically correspond to an air bubble and sand particle in a boundary layer of water ($\nu = 10^{-6}m^2/s$) with $Re_\tau = 270$, $\delta = 4.5$mm, and freestream velocity of $1m/s$. These flow conditions were chosen to match the non-dimensional parameters of the DNS flow and thus results in the thin boundary layer thickness. The baseline conditions were chosen such that the diameter of both the baseline bubble and baseline sand particle is $164\mu m$ and have nearly identical drift parameters of 0.19. Note that these are the same conditions considered in Chapter 5 to study different choices of surface forces and are denoted

Table 6.1: Summary of particle conditions for low-density particle size study.

Condition	ψ	d_p $[\mu m]$	r_p^+	St	St^+	γ	$Re_{p,term}$	y_{inj}^+	y_{bounce}^+
0a	1.0	0.0	0.0	0.0	0.0	0.0	0.0	9.8	4.9
0b	1.0	0.0	0.0	0.0	0.0	0.0	0.0	9.8	0.0
1a	0.00126	164	4.9	0.0081	2.18	0.197	1.94	9.8	4.9
1b	0.00126	100	3.0	0.0034	0.92	0.083	0.50	9.8	4.9
2a	2.0	164	4.9	0.0403	10.9	0.198	1.94	9.8	4.9
2b	2.0	73.5	2.21	0.0095	2.57	0.047	0.21	9.8	4.9
2c	2.0	44.8	1.34	0.0036	0.99	0.018	0.05	9.8	4.9

conditions 1a and 2a in Table 6.1. Several additional conditions (of smaller diameter) were generated to study the effect of varying bubble/particle size and density ratio on various statistics. These include one additional bubble case (1b) which has a diameter of $100\mu m$ and two additional sand particle cases (2b and 2c) with diameters of $73.5\mu m$ and $44.8\mu m$, respectively. Finally, a "tracer particle" with zero inertia and size (such that $\vec{V}_p = \vec{V}_f$) is considered for comparison with the finite inertia cases and is denoted particle condition "0". Two different bounce locations are considered for the the tracer condition where "0a" uses the same wall boundary condition as the finite inertia particle and "0b" uses the physically consistent condition where contact with the wall occurs at $y = 0$. The first condition (0a) is more appropriate for assessing the effect of inertia with the finite-sized particles while 0b is included to show the effect of the wall boundary condition on the tracer particle's distribution profile. Note that the non-dimensional parameters in Table 6.1 were computed using the finite Reynolds number drag expression (Eq. 3.20) at terminal velocity conditions in a quiescent flow.

The particles were released into the DNS flow at the position where the centroid of the baseline particle is one diameter away from the wall (i.e. at $y^+ = 9.8$) with a velocity equal to $\vec{V}_{term} + [\vec{V}_f]$, consistent with the heavy particle study presented in Chapter 4. An elastic collision was specified at $y^+ = 4.9$ (i.e. one r_p^+ of the baseline condition) such that the particle velocity was reflected when the particle centroid reached this y-location. Note that the choice to freeze the injection location and wall-collision location (as opposed to letting it change with the physical particle diameter) was made to alleviate confusion in interpreting the results (e.g. determining whether a change was the result of particle size or injection location).

6.1 Flow-visualization

Section 4.3.1 presented and discussed the particle-fluid interactions in the context of several instantaneous snapshots of the simulation. Here, a similar presentation is made where both horizontal and vertical cuts are examined. The horizontal plane shown in Figure 6.1 corresponds to a transverse location of $y^+ = 15$ where instantaneous streamwise velocity is indicated by color contours and the black dots correspond to particle locations in the vicinity of the plane ($12 \leq y_p^+ \leq 18$). While more coherent low-speed streaks are shown in the streamwise velocity by [90] at a lower location ($y^+ = 9.96$), evidence of these structures are still present in the current illustration which is taken at higher y-location due to the farther off-wall injection location required for these finite-sized particles. Note that these snapshots were taken at the same physical time during the simulation but Figure 6.1b shows a different fluid solution. Stability issues were encountered for this condition and a reduced time-step was required compared to the other conditions. Since the flowfield is turbulent, the fluid solution evolves along a different trajectory owing to the chaotic nature of the governing equations. It was verified that running this smaller time-step for the other conditions did not effect the statistical results such that the larger value was typically used to reduce computational requirements. While all conditions show a tendency of particle to be present in regions of low-speed fluid, we notice that some conditions form "clumps" of particles similar to those discussed in Section 5.1.1. This appears to be a phenomenon associated with inertial particles and the absence of these structures indicate that the particle behaves as a fluid tracer. Results presented in later Sections will show that condition 2c is near the tracer limit established by condition 0a. Here it is noted that there is an absence of particle clumps for this condition. These clumps pose a potential modeling issue for seemingly dilute conditions in which particle collisions may need to be accounted for in future work.

Figure 6.2 shows similar pictures for a vertical cut through the domain. In this case, the fluid solution corresponds to $z^* = 2.78$ (the center of the span) and the particles (shown as black dots) are located in a range surrounding the fluid plane from $2.60 \leq z^* \leq 2.95$. This limited spanwise range for particle positions was chosen to be large enough to include a significant number of particles for the visualization, but at the same time remain sufficiently small to insure that the selected fluid plane is a good representation of the fluid solution in the neighborhood of the actual particle location. This Figure shows that as γ decreases, movement of the particle cloud away from the wall also decrease due to a reduction in terminal velocity. The effect of reducing inertia can be

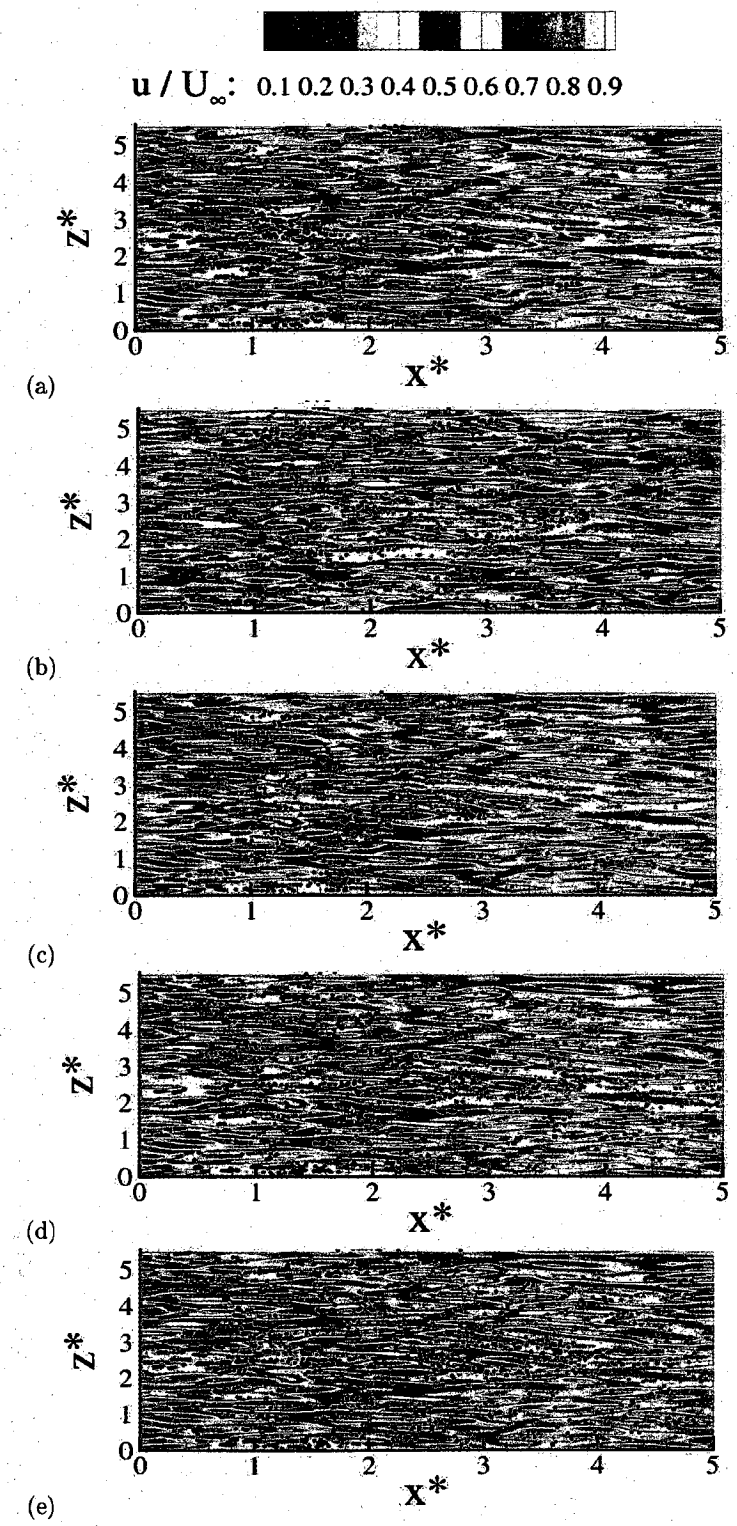

Figure 6.1: Horizontal plane at $y^+ = 15$ with instantaneous u-velocity contours and particle locations (shown as black dots) for conditions (a) 1a, (b) 1b, (c) 2a, (d) 2b, (e) 2c.

seen in comparing Figures 6.2c-d and focusing on the clump of particle near $x^* = 2.4$. In Figure 6.2c a strong clump is seen which tends to become less coherent in Figures 6.2d and 6.2e as Stokes has decreased for these conditions.

6.2 Particle concentration distribution

This section is concerned with the wall-normal particle concentration distribution of the conditions presented in Table 6.1. The present study collected distribution statistics (in the form of particle concentration) at streamwise locations corresponding to $x^* = \delta/2$, δ, 2δ, 4δ, 8δ, and 15δ. Herein, only the 2δ and 8δ will be presented as the other locations show similar trends. The particle concentration is defined in the same manner discussed in Section 5.1.2.

Before considering inertial particles, it is useful to first consider the motion of a tracer particle, i.e. a particle where $\vec{V}_p = \vec{V}_f$. Figure 6.3 shows concentration profiles for two tracers particles, namely conditions 0a and 0b of Table 6.1, which differ due to the choice of wall-reflection. Both conditions are injected at $y^+ = 9.8$ but condition 0a reflects at $y^+ = 4.9$ (just as the particles do) while condition 0b is allowed to diffuse all the way to $y^+ = 0$. Not surprisingly, the only differences are seen very near the wall where the 0a tracers stack-up against the reflection plane and are not allowed to diffuse close to the wall. Outside of $y^+ = 20$ the differences in the concentrations are negligible. Comparing Figures 6.3a and 6.3b, we see the expected trend where the particle cloud diffuses with increasing streamwise location. Also note that the peak concentration for both conditions at both locations remains near the injection location of $y^+ = 9.8$. The reason for the subtle shift of the peak towards the wall is the result of asymmetric diffusion imposed by the presence of the wall.

In the following figures, condition 0a will be compared to the concentration profiles of finite inertia particles. This condition is chosen in favor of 0b as it has the same reflection condition as the finite inertia particles. Thus, one is able to easily assess the effect of particle inertia on the concentration profile and determine if it is significant.

Figure 6.4 shows concentration comparisons for particles with constant density ratio (ψ) compared to the tracer condition 0a. First, focus is given to Figures 6.4a and 6.4b (the top row) which compare the several sand particles where $\psi = 2$. For this condition, only the largest particle (2a)

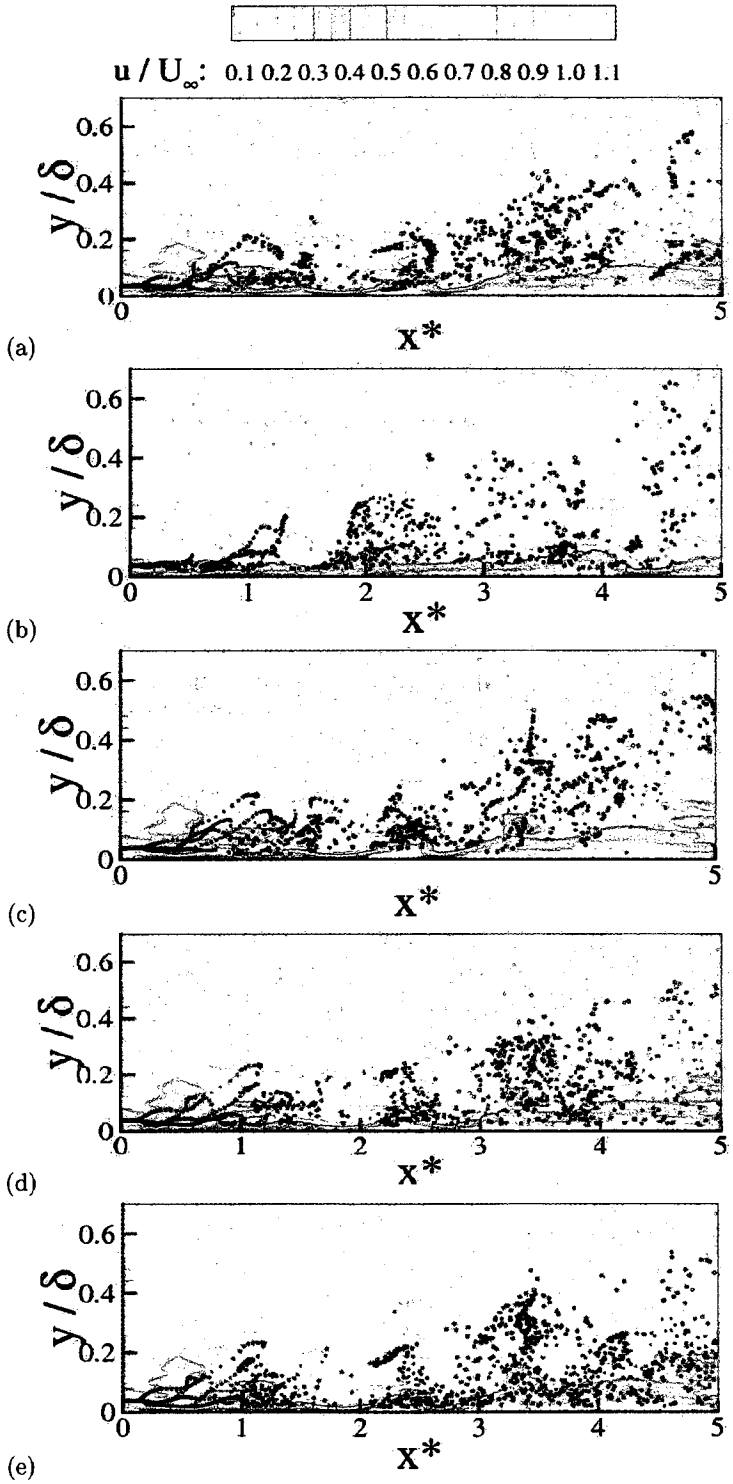

Figure 6.2: Vertical plane at $z^* = 2.78$ with instantaneous u-velocity contours and particle locations (shown as black dots) for conditions (a) 1a, (b) 1b, (c) 2a, (d) 2b, (e) 2c.

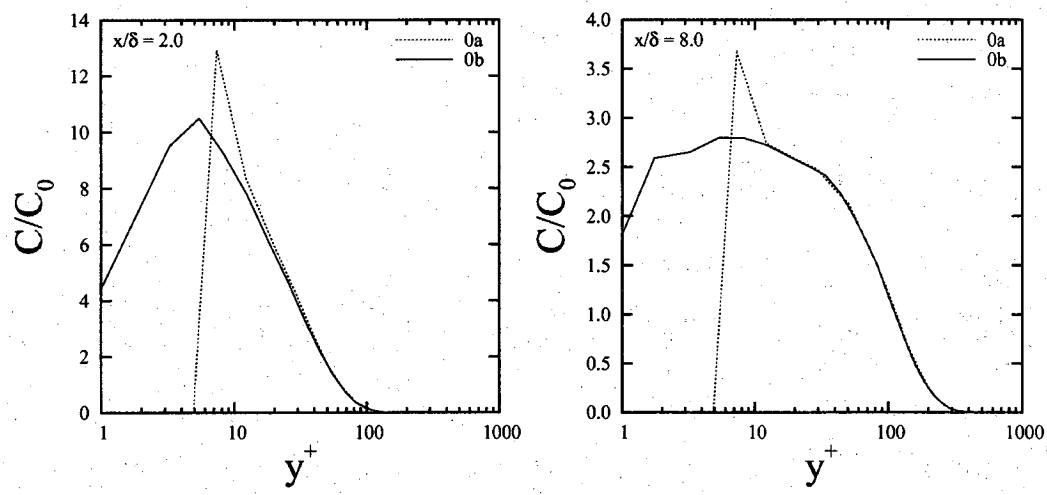

Figure 6.3: Distribution profiles at two streamwise locations for tracer particles with wall reflection at $y^+ = 4.9$ (condition 0a) and with wall reflection at $y^+ = 0$ (condition 0b).

shows strongly inertial behavior and the remaining cases (2b and 2c) approach the tracer limit. The smallest condition (2c) has an inner Stokes number of ≈ 1 and is seen to behave nearly as a tracer particle. Thus, for sand particles in a boundary layer it appears that a Stokes number smaller than $St^+ = 1$ behaves nearly as a tracer in terms of wall-normal distribution. Dorgan *et al* [36] show consistent results for heavy particles where a $St^+ = 2.7$ had slight inertial tendencies but smaller values (i.e $St^+ = 0.27$) were indistinguishable from tracers.

Similar comparisons are shown for the bubbles conditions ($\psi = 0.00126$) in Figures 6.4c and 6.4d. Immediately it is noticed that both bubble conditions possess significant inertia effects (as they behave differently than the tracer condition) despite the low Stokes number associated with condition 1b ($St^+ = 0.92$). This is an interesting result that is inconsistent with heavy-particle expectations and the present sand particle results. This effect is likely due to the fluid acceleration forces which are very important at low-density ratios. While we see inertial tendencies in both bubble conditions, note that condition 1b has moved towards the tracer limit consistent with a reduction in Stokes number. Further study of this behavior is warranted and should seek to quantify the limiting Stokes number for which smaller values are unimportant.

The peak bubble concentration is seen to move farther from the wall as inertia is increased. This trend is consistent with the heavy particle results shown in Figure 4.3b and can be explained as follows. Since the bubble conditions are at a constant Froude number, the increase in Stokes number is met with a comparable increase in γ. The increase in γ is associated with an increase in

V_{term} which acts to pull the particle away from the wall at a higher rate.

Figure 6.5 compares concentration predictions for conditions 1a and 2a which have the same diameter and drift parameter but different Stokes number and density ratios. Comparing the peak concentration location of the bubble and sand particle conditions, it is seen that both occur at roughly the same y-location. This is true at both streamwise locations and is attributed to the identical drift parameter of these two conditions. The sand particle shows an increased near-wall concentration compared to the bubble condition which is a result of the larger Stokes number associated with the former.

Finally, Figure 6.6 compares condition 1b with 2c. These conditions have approximately the same Stokes number but different density ratios and drift parameters. This figure highlights the very interesting result shown above where the bubble condition shows inertial behavior at Stokes numbers which are sufficiently small to be considered tracers by heavy-particle standards. The present study shows that assuming a bubble behaves as a fluid tracer based on heavy-particle expectations is incorrect.

6.3 Particle-wall interactions

Figure 6.7 shows predictions for the streamwise particle wall-collision velocity (u_{bounce}) normalized by the boundary layer friction velocity. These bounce velocities represent the average velocity of all particles contacting the wall between $x = 8\delta$ and $x = 15\delta$. This location was chosen (rather than a more upstream location) to avoid having the injection conditions potentially bias the results. Included in this figure for comparison are the heavy-particle results shown previously in Figure 4.7. Obviously the present results show the opposite trend with increasing γ as the heavy particles. This odd behavior is blamed on the choice of using a fixed wall-reflection plane at $y^+ = 4.9$ (which is only appropriate for the largest γ condition). The lower γ cases would, in reality, contact the wall at lower y^+ values (1.3 for the smallest particle, condition 2c) and would be expected to have lower velocities consistent with the fluid velocities in these regions. For example, consider condition 2c which is nearly a fluid tracer. This data point marks the left end of the sand particle curve in Figure 6.7 and has a bounce velocity of $\sim 6u_\tau$. The mean velocity at the wall-reflection plane is $4.9u_\tau$ (since $y^+ = 4.9$ is within the viscous sublayer where $u^+ = y^+$). The reason the bounce velocity is slightly larger than this value is a result of the mechanism which

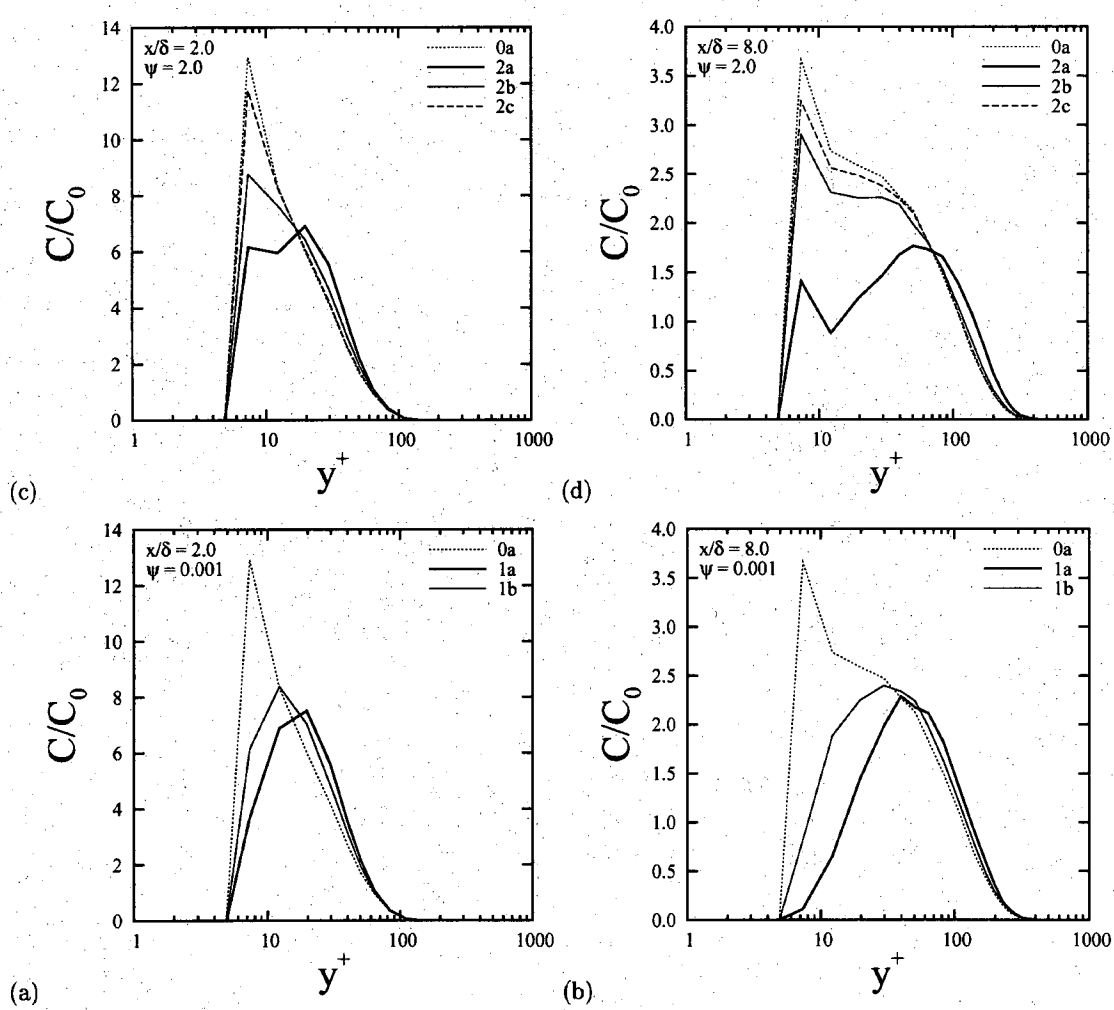

Figure 6.4: Distribution profiles at several streamwise locations for particles with different St and d_p^+ but constant density ratio compared to the tracer particle ((a) and (b) correspond to $\psi = 2.0$ while (c) and (d) correspond to $\psi = 0.00126$).

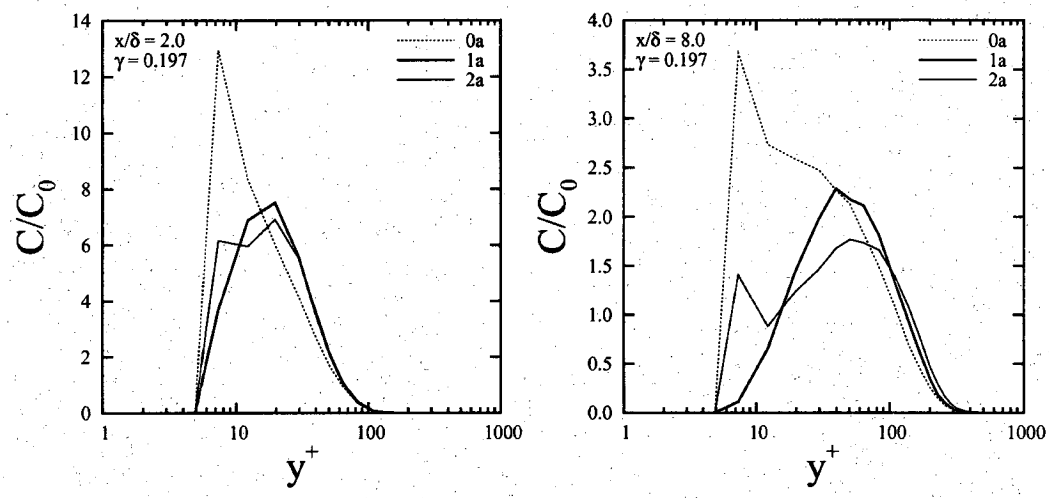

Figure 6.5: Distribution profiles at two streamwise locations for particles with constant d_p^+ and γ but varying St and ψ.

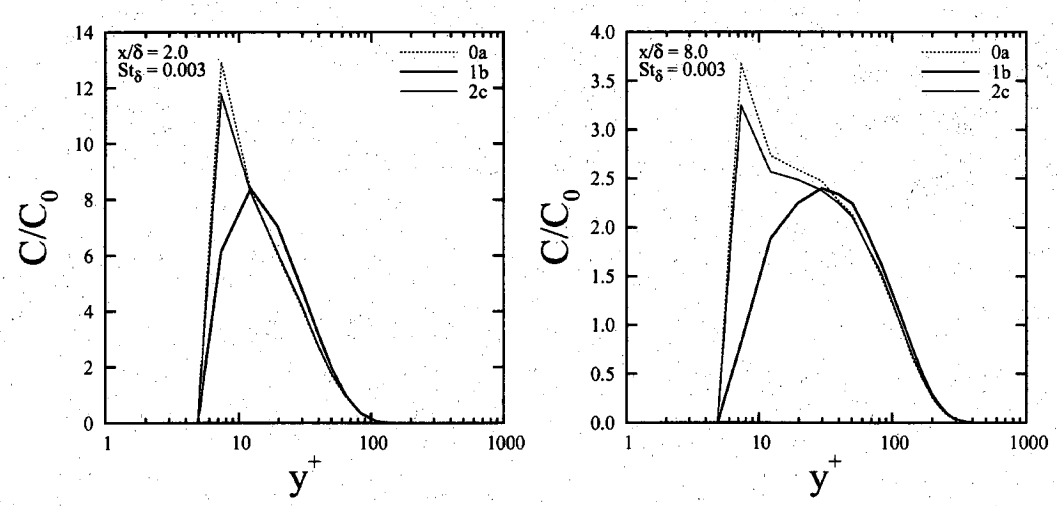

Figure 6.6: Distribution profiles at two streamwise locations for particles with constant St but with varying γ and d_p^+.

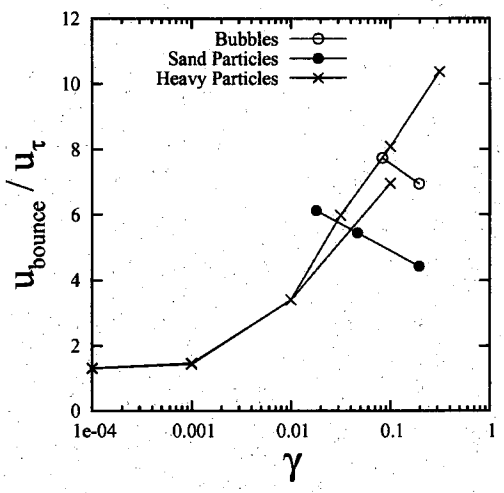

Figure 6.7: Streamwise bounce velocities for low-density particle at $Fr = 0.0815$ and heavy particles from the constant Froude number and constant Stokes number studies of Chapter 4.

forces particle to contact the bounce plane: higher velocity fluid moving towards the wall carries particles towards the bounce plane (consistent with $\overline{u'v'} < 0$ in the boundary layer) such that the impact velocity is higher than the mean fluid velocity in that region. Given the suspicion that the bounce statistics are contaminated for the lower γ values, this section proceeds considering only the baseline conditions for which the boundary condition is physically consistent.

Considering conditions 1a and 2a (the largest γ values) in the context of Figure 6.7 it is seen both these low-density particles have lower bounce velocities than the corresponding heavy particle. This is likely a cause of the difference in Stokes number between the conditions given that the heavy-particles were run at $Fr = 1.0$. As such, the heavy-particle at a similar γ has a Stokes number roughly 20 times greater than that of the bubble and 5 times greater than the sand particle. These lower Stokes number should allow the particle opportunity to adjust to the slower fluid velocity as the wall is approached. However, this is not the whole story as the bubble contacts the wall with higher velocity than the sand particle even though its Stokes number is 4 times smaller. This is most likely a result of the proximity of the bubble cloud to the wall compared to the sand particle cloud location. The former was shown to be further from the wall in Section 6.2 while the sand particles maintain a significant near-wall concentration in the vicinity of the bounce plane. Therefore, when bubbles contact the wall they have traveled from farther up in the boundary layer and are thus associated with higher velocities.

Figures 6.8a and 6.8b show predictions of non-dimensional bouncing frequency for the baseline

conditions. The non-dimensional bouncing frequency is defined as the fraction of particles which contact the wall in a discrete bin, e.g.

$$f_{bounce} = \frac{N_{bounce}}{\frac{\Delta x_{bin}}{\delta} N_p} \tag{6.1}$$

where N_{bounce} is the number of particles which contact the wall in a given bin, Δx_{bin} is the streamwise length of the bin, δ is the mean boundary layer thickness at $x^* = 0$, and N_p is the total number of particles in the simulation. This statistic is plotted as a function of x^* in Figure 6.8a where the x^*-value corresponds to the center of the bounce bin. Both conditions show an initial increase in bouncing frequency which tapers off after $x^* > 2$. The bubble condition (1a) continues this trend for the remaining streamwise locations while the sand particle (condition 2a) reaches a nearly constant bouncing frequency by $x^* = 3$. This behavior is consistent with the concentration results presented in Section 6.2 where it was shown that the bubble cloud continually diffuses away from the wall while the sand particle maintains a high near-wall concentration (attributed to it comparatively higher inertia).

Figure 6.8b focuses attention on the furthest downstream bounce bin and considers the results as a function of inner Stokes number. The results are compared with heavy-particles results given by [90] as well as the results shown in Section 4.3.4. These heavy-particle results all show an increasing bounce frequency with increasing Stokes number. A similar trend appears for the low-density particles but additional data points are needed to fully quantify the behavior. Interestingly, the low-density particles have similar bouncing frequencies despite the additional physics which become important when the density ratio is small.

Figure 6.8c shows a comparison of non-dimensional deposition velocities of the present low-density particles compared with the heavy-particle/boundary layer results of [90] combined with the data presented in Chapter 4, the heavy-particle/boundary layer simulation results of Kallio & Reeks [98], and the heavy-particle/pipe flow data of Liu & Agarwal [99]. Considering the different flow types (boundary layers & pipe flow) and the difference in density ratio the agreement among all the different studies is remarkable. The deposition model of Young & Leeming [16] is also included on the plot and is shown to give good predictions.

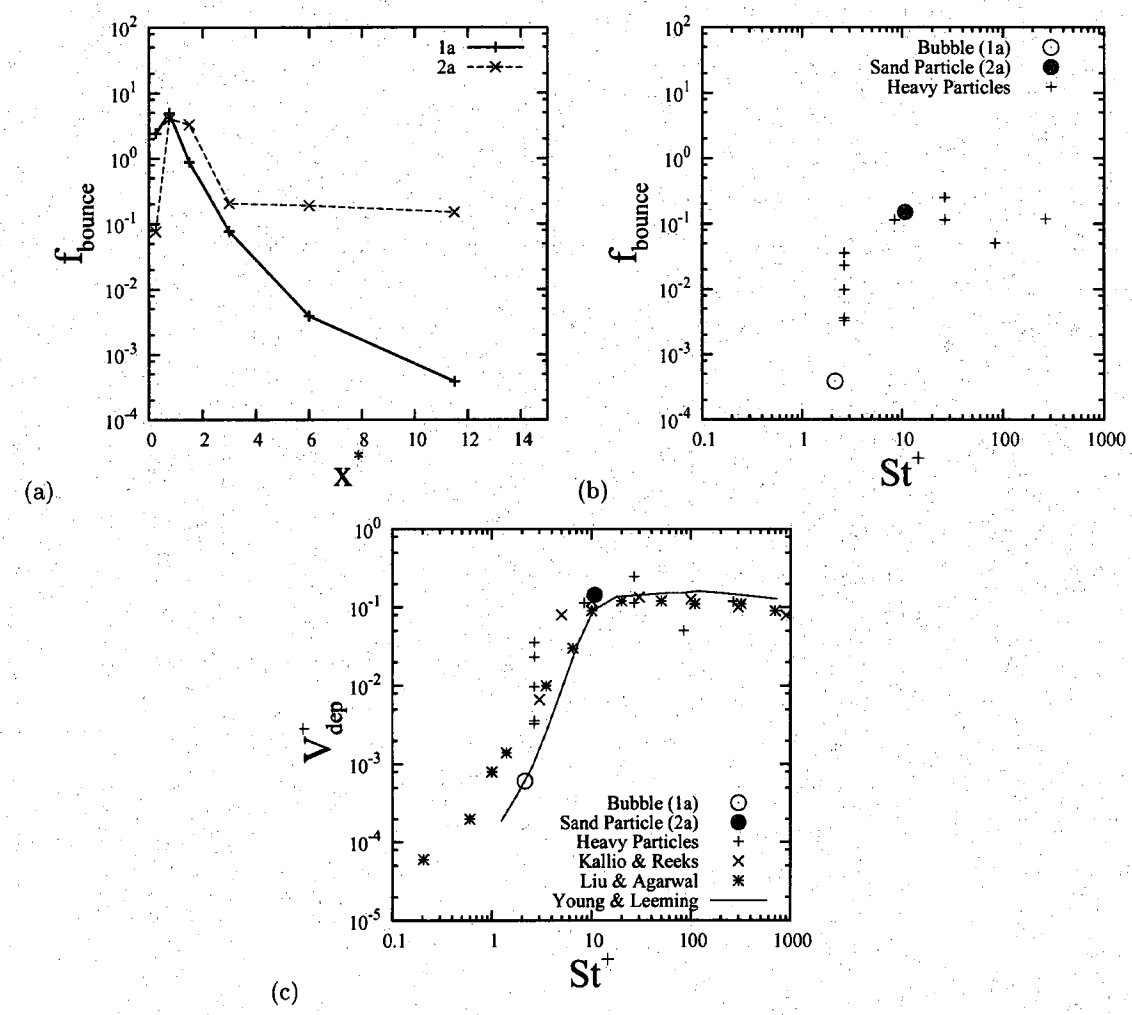

Figure 6.8: (a) and (b): Non-dimensional bouncing frequency for present low-density conditions compared with heavy particle results. (c) Non-dimensional deposition velocities for the present conditions compared with previous studies and the model of Young & Leeming [16]d.

6.4 Statistics along the particle trajectory

This section focuses on Lagrangian statistics collected along the particle trajectory. The first of these statistics is the wall-normal particle velocity shown in Figure 6.9a where the low-density results are compared with the previously discussed heavy-particle results of Figure 4.8a. In quiescent conditions, one would expect v_p to be equal to V_{term} (such that $< v_p > /V_{term} = 1$) given the choice of buoyancy direction for these cases. However, small γ particles in the presence of turbulence diffuse away from the wall faster than they would under terminal velocity alone. This effect seems to be an effect of γ alone as the heavy and low-density particles give similar results. One would also expect this effect to be a function of the turbulence intensity and distribution of the carrier phase (which was held constant between the heavy and low-density particle simulations for the present study).

Figure 6.9b shows the wall-normal relative velocity normalized by V_{term} for the present conditions compared to the heavy-particle results. If the particles are in equilibrium with a homogeneous, isotropic turbulence field, one would expect $< v_{rel} >= V_{term}$. Thus, deviations from unity represent inhomogeneous and non-equilibrium effects of the particle field. As discussed regarding Figure 4.8b and 4.8c, the heavy-particle deviations are related to transient effects and was explained with a theoretical model. The present low-density results are more complicated in that the equation of motion is non-linear and fluctuations from one direction alter the behavior in the other orthogonal directions. Thus, the expectation of $< v_{rel} >= V_{term}$ is only reasonable when the particles are in constant equilibrium with the fluid in the directions orthogonal to $\vec{V}_{term}$. Interestingly, the low-density particles appear to have the opposite trend with increasing γ compared to the heavy-particles. This could be a result of the different mechanisms causing the deviation from V_{term}: the heavy-particles are subject to transient effects while the low-density particles also suffer from complications of non-linear surface forces.

Figure 6.10 shows rms relative velocities about the Lagrangian mean, e.g.

$$\left\langle u'_{rel,rms} \right\rangle = \left\{ \langle u^2_{rel} \rangle - \langle u_{rel} \rangle^2 \right\}^{1/2} \tag{6.2}$$

and similarly for the wall-normal component, $v'_{rel,rms}$. The results shown in this Figure are normalized by the Eulerian turbulence level observed along the particle path, $\left\langle \left[u'_{f,rms} \right] \right\rangle$ and $\left\langle \left[v'_{f,rms} \right] \right\rangle$. To obtain these values, the DNS code was first run to generate mean field statistics,

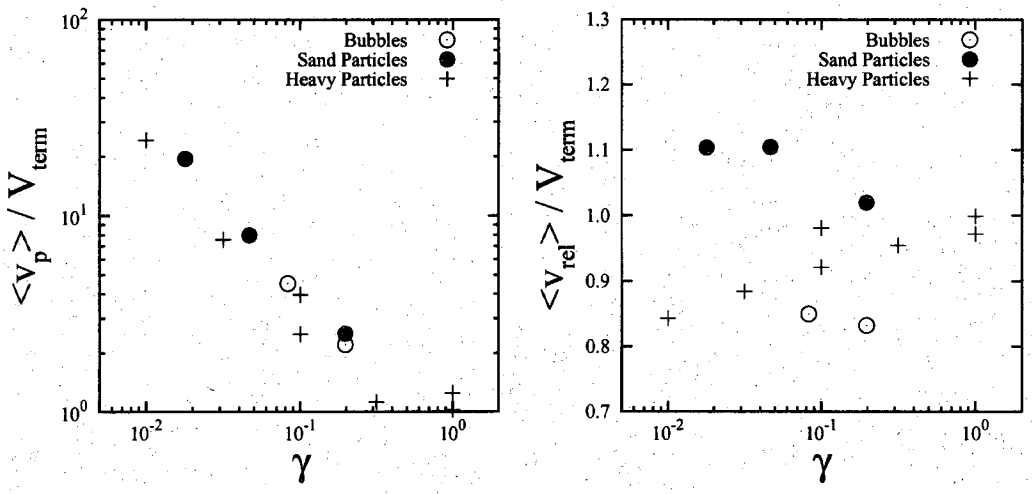

Figure 6.9: Particle velocity and relative velocity in the direction of V_{term} normalized by V_{term}.

e.g. $\left[u'_{f,rms}\right]$, which are shown in Figure 2.5. A look-up table was created from these mean values which was interrogated during subsequent particle simulations. Previous heavy-particle results have shown that for sufficiently large values of Stokes number the particle becomes a "moving-Eulerian" reference frame where the effects of turbulence are minimal and the rms relative velocities approach the Eulerian turbulence levels. The low-density conditions show similar increases with increasing γ which can be seen in Figures 6.10a and 6.10b. Note that the constant Stokes number heavy-particle results are reasonably flat while the constant Froude number results increase with increasing γ. This suggests that the statistic is largely controlled by the Stokes number. Since the present low-density study is at a much lower Froude number, we should expect a slower increase with γ. Indeed, this is the observed behavior.

Figure 6.10c is obtained if we choose to plot the rms statistic in terms of St_Λ which tends to collapse the predictions to a similar curve. Again, the results are compared with the heavy-particle results and the theoretical model of Eq. 4.5 is shown as well. The low-density particles are seen to have similar behavior as the heavy-particles and the DNS results are similar to the model predictions (but slightly larger).

Figure 6.11 shows the mean Reynolds number of the various particles as a function of γ. The heavy-particle results of Figure 4.10b ($Fr_\delta = 1.0$) are included for comparison along with $Re_{p,term}$ and the heavy-particle model based on Eq. 4.8. Interestingly, the low-density particles at a much lower Froude number (0.0815) show very similar behavior to the heavy-particles at a Froude

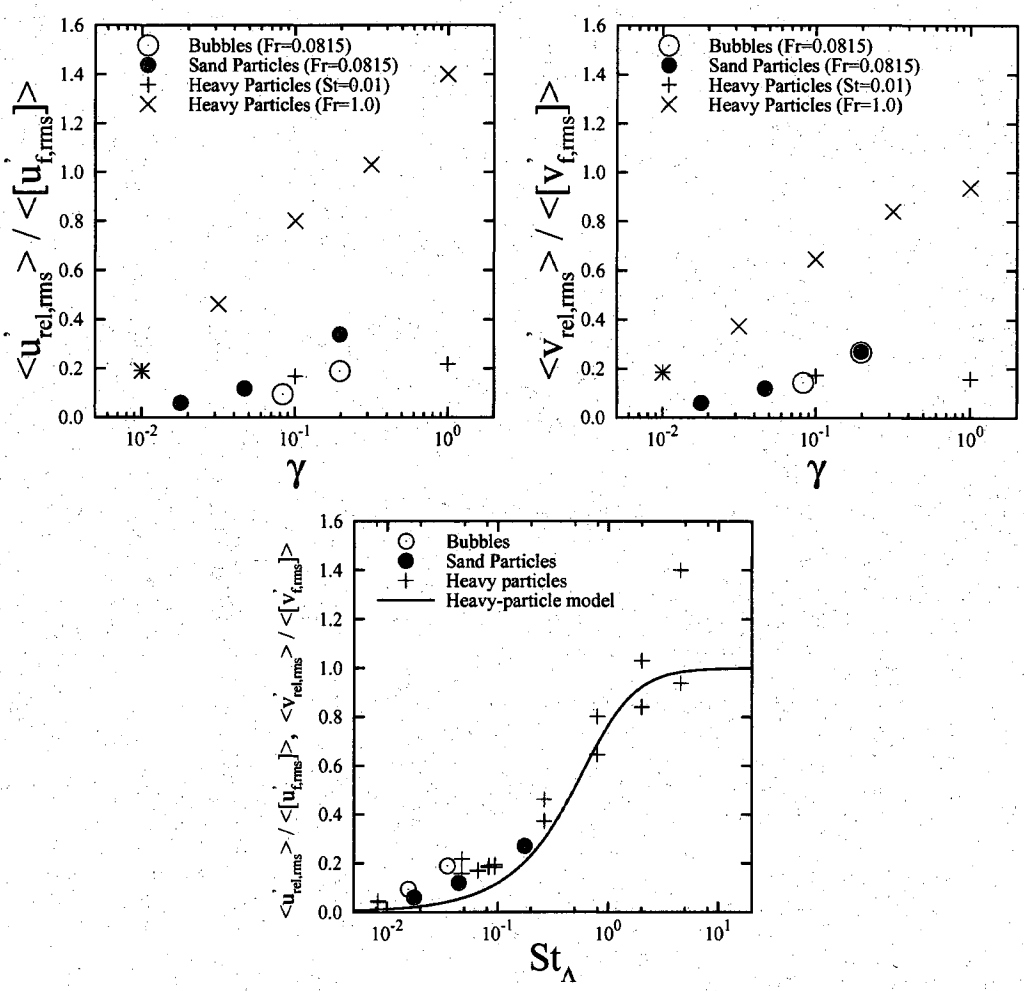

Figure 6.10: RMS relative velocities compared to heavy-particle results.

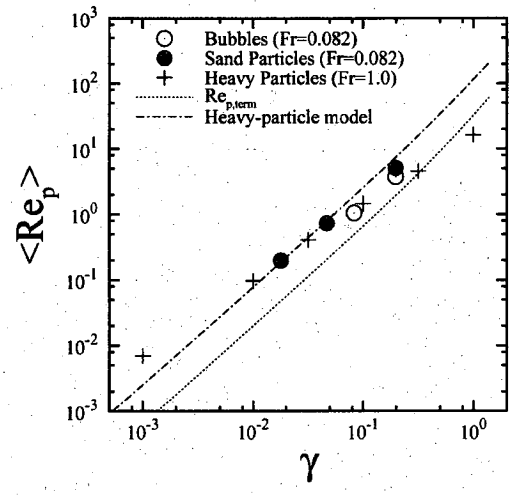

Figure 6.11: Mean Reynolds number predictions.

number of 1.0. This result is surprising given that heavy-particle simulations at a constant Stokes number show different behavior (Figure 4.10a) such that $\langle Re_p \rangle$ is more than just a function of γ. To obtain the model prediction curve, the "zero-turbulence" V_{rel} of Eq. 4.8 was replaced with V_{term} and the rms component was generated by the model in Eq. 4.5.

Figure 6.12 shows predictions for the ratio of mean particle kinetic energy to mean fluid kinetic energy,

$$\frac{k_p}{k_f} = \left(\frac{\left\langle V'_{p,rms} \right\rangle}{\left\langle V'_{f,rms} \right\rangle} \right)^2 \tag{6.3}$$

where

$$\left\langle V'_{p,rms} \right\rangle = \left\{ \left\langle \|\vec{V}_p\|^2 \right\rangle - \left\langle \|\vec{V}_p\| \right\rangle^2 \right\}^{1/2} \tag{6.4}$$

and the fluid kinetic energy is defined similarly. This statistic was deemed interesting for the present low-density conditions because the theory of Hinze [88] (which neglects the history force) predicts that the particle kinetic energy should approach nine times that of the fluid kinetic energy as St_Λ becomes arbitrarily large. This result can be seen by considering Eq. 3.92 in the limit of infinite τ_p and neglecting the history and lift forces:

$$\frac{d\vec{V}_p}{dt} = \frac{1 + C_M}{\psi + C_M} \frac{D\vec{V}_f}{Dt} \qquad \text{for } \tau_p \to \infty \tag{6.5}$$

This result shows that the coefficient of the fluid acceleration term approaches 3 in the bubble

limit ($\psi \to 0$) and thus the kinetic energy ratio should approach 9. This theoretical prediction is shown by the line with long dashes which quickly departs the upper boundary of Figure 6.12 and is given by

$$\left(\frac{k_p}{k_f}\right)_{Hinze,bubble} = \frac{1+9St_\Lambda}{1+St_\Lambda} \tag{6.6}$$

Clearly, the history force is important for accurate predictions of the particle kinetic energy as the current results lie very near $k_p/k_f = 1$ and do not show the Hinze behavior. This is confirmed by the experiments of Sun & Faeth [100] which show the ratio remains near unity even for large St_Λ.

Turning attention to the sand particles, it can be seen that the particle kinetic energy decreases with increasing Stokes number. This trend is also shown by the heavy-particle results as well as Hinze's theoretical prediction given by

$$\left(\frac{k_p}{k_f}\right)_{Hinze,heavy} = \frac{1}{1+St_\Lambda} \tag{6.7}$$

One would expect that the sand particle kinetic energy would decay slower than that of the heavy particles (tending towards the bubble result of $k_p = k_f$) but the present data set is too small to conclusively identify this behavior. Future studies should consider increased St_Λ values and other small-ψ particles to more completely categorize/correlate this effect. Note that the heavy-particle predictions of [17, 18, 19] are included here to show the success and accuracy of Hinze's model in the limit of large density ratios.

6.5 Summary of low-density particle study

This study conducted numerical experiments for air bubbles and sand particles of various sizes in a turbulent boundary layer of water at a constant Froude number. All bubbles/particles were injected near the wall at $y^+ = 9.8$ and were forced to reflect from the wall as their centroid crossed $y^+ = 4.9$, consistent with the physical radius of the baseline condition. After injection, the particles were tracked using a Lagrangian scheme for 15 boundary layer thicknesses downstream and their wall-normal distribution was monitored at several streamwise locations. Particle and fluid statistics were also gathered along the particle trajectory to formulate Lagrangian statistics.

The particle-fluid interaction was observed in the context of slices through the computational domain. Horizontal cuts showed correlations between low-speed fluid regions and particle presence

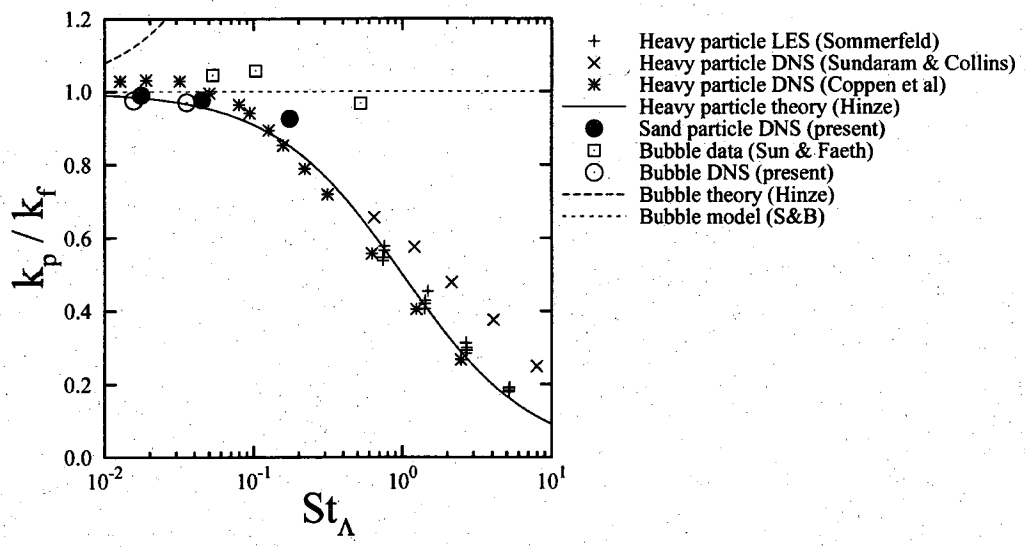

Figure 6.12: Particle to fluid kinetic energy ratio for the present conditions, the heavy-particle LES of Sommerfeld [17], the heavy-particle DNS of both Sundaram & Collins [18] and Coppen et al [19], and theoretical predictions from Hinze [19] and Spelt & Biesheuvel (S&B)[20].

for all conditions. Vertical cuts showed a correlation between drift parameter and proximity of the particle cloud to the wall. In both the horizontal and vertical pictures, particles were shown to form dense clumps in certain fluid structures so long as the particle has significant inertia. These clumps were seen to diffuse as the particles approached the tracer limit (i.e. Stokes number becoming negligible). Future studies may need to include collision modeling in light of these results even when the particle loading is assumed dilute as local, instantaneous concentrations can be large.

Wall-normal concentrations for both the bubble and sand particle condition were compared with results obtained for a fluid tracer. It was shown that while the sand particle behaves nearly like a fluid tracer for $St^+ \approx 1$, the bubble shows strong non-tracer effects at the same Stokes number. This result identifies a danger in using heavy-particle assumptions to predict the nature of low-density bubble motion. Bubbles and sand particles with identical drift parameters and diameters were shown to have similar peak concentration locations, though the sand particle generates higher near-wall concentrations due to its larger inertia (compared to the corresponding bubble).

Particle-wall interactions were also studied and it was theorized that the fixed reflection condition at $y^+ = 4.9$ caused inconsistently large streamwise bounce velocities. This argument was further supported by considering previous heavy particle data which showed that bounce velocity should

be an increasing function with drift parameter and the opposite trend was observed for the low-density particles. Thus, only the baseline conditions (for which the bounce plane location is physically consistent) were deemed meaningful. Non-dimensional deposition velocities for the two baseline conditions were compared to existing heavy-particle results (both numerical and experimental). It was found that the low-density particle deposition velocities agreed well with the heavy particle results and with the theory put forth by Young & Leeming [16]. This is perhaps a surprising result given the comparative complexity of low-density particle physics.

Several statistics were collected along the particle trajectory including the Lagrangian mean wall-normal particle velocity. This velocity was shown to be much larger than V_{term} for $\gamma < 1$ and is a result of turbulent diffusion migrating particles away from the wall at a rate much faster than terminal velocity would induce. Wall-normal relative velocities were shown to be of the same order, but not equal to, V_{term}. This was attributed to transient effects combined with non-linear effects associated with the finite Reynolds number surface-force description.

RMS relative velocities were shown to increase with increasing γ, consistent with the trends of the constant Froude number heavy-particles of Chapter 4, albeit at a slower rate. The slower increase was attributed to the significantly lower Froude number associated with the low-density test conditions. The rms velocities were shown to approximately collapse when plotted in terms of St_Λ. Surprisingly, both the heavy-particle and low-density particle predictions collapse to the same curve and were both equally well-predicted by the theoretical model set forth in Chapter 4.

Mean particle Reynolds numbers were also found to have similar behavior to previous heavy-particle results. The mean Reynolds numbers for the present low-density conditions with $Fr_\delta = 0.0815$ were found to fall on the same curve as heavy particles with $Fr_\delta = 1.0$ when plotted as a function of drift parameter. This is a surprising result given that heavy-particles with constant Stokes number were shown in Chapter 4 to have a very different behavior. Thus, the Reynolds number is not solely controlled by γ such that it is surprising that two different Froude numbers could lie on the same curve.

Finally, the ratio of particle kinetic energy to fluid kinetic energy was considered. The bubble results were consistent with experiments by Sun & Faeth [100] which showed the ratio to be near unity for a range of Stokes numbers. This is inconsistent with the theory proposed by Hinze [88] which neglects the history force and suggests the bubble kinetic energy should be 9 times that of the fluid for large Stokes numbers. The sand particle was found to exhibit the heavy-particle trend

whereby particle kinetic energy decreases with increasing Stokes number. Unfortunately, a larger range of conditions is needed to quantify the rate of decrease compared to heavy-particle expectations.

Chapter 7

Summary

This dissertation discussed research accomplishments in multiphase flow modeling and simulation. Four major objectives were set forth in Section 1.3 and are repeated here:

1. Review existing literature and construct an appropriate model for finite-Reynolds number and finite-sized particle dynamics. Discretize the model for implementation as part of a CFD solver.
2. Conduct heavy-particle simulations using a simplified equation of motion and interpret the results. This interpretation is more obvious in the context of the simplified equation of motion and will be a good place to start before considering the more complicated physics of low-density particle motion.
3. Determine, through simulation, the relative importance of the surface forces and discretization techniques for low-density particles.
4. Apply the new model to several low-density particle conditions and interpret and compare the results to the heavy-particle observations.

The objectives were addressed in the preceding pages. The below paragraphs summarize the findings.

7.1 Particle EOM

A thorough investigation of existing work regarding particle surface-force modeling lead to the creation of a finite Reynolds number equation of motion for particles subjected to weak spatial gradients (compared to the particle size) such that the conventional point-force approximation

remains valid. In addition to revisiting the conventional surface force expressions for quasi-steady drag, lift, added mass and fluid stress, an efficient expression for the history force is described along with a spin-equilibrium lift coefficient. These expressions are expected to be reasonable up to a particle Reynolds number of 50.

The proposed finite-Reynolds number equation of motion was extended to account for finite particle size and accommodate modeling of particles which are too large for the conventional point-force approximation. To this end, a spatially-averaged method consistent with known theoretical limits for the particle surface-force was developed to incorporate finite particle size effects. For a spherical particle with a no-slip surface, it results in a surface-average for the quasi-steady drag, history and lift forces and a volume-average for the fluid-stress and added-mass forces. The theoretical justification for these averages is discussed for both low Reynolds number and inviscid limits, and this is employed to put forth a generalized semi-empirical expression. It was shown that the surface-average can be obtained with simple six-point (front/back, top/bottom and left/right) discrete average while the volume-average can be constructed using a seven-point average based on the particle centroid and a spherical Simpson integration rule. These discrete averages correctly tend to the MR and AHP point–force expressions, including the Faxen corrections. Furthermore, they are fourth-order accurate for simple polynomial and sinusoidal shear flows and significantly more accurate than point-force analog. However, resolved-surface or experimental studies are needed to determine the robustness and limits of the proposed spatial-averaged approach in terms of both flow complexity and particle Reynolds number, especially for lift force where theoretical expressions are difficult to obtain even in the case of simple flowfields.

7.2 Heavy-particle simulations

Simulations were conducted for a range of particle drift parameters ($10^{-4} \leq \gamma \leq 10^{0}$) with a fixed inertia ($St_\delta = 10^{-2}$) and then with a variable inertia ($Fr_\delta = 1$). Flow-visualization revealed strong correlations between particle location and boundary layer ejections provided the terminal velocity was small. Increasing terminal velocity was seen to remove particles from the near-wall structures while large Stokes numbers were seen to reduce mean-spread of the particle cloud. Spanwise diffusion statistics revealed increased diffusion for increases in γ at constant Stokes number, but

decreased diffusion for increasing γ at constant Froude number. These results were attributed to turbophoresis, inertia, and wall interaction effects such that canonical homogeneous, long-time diffusion rates were never fully realized.

Lagrangian-average velocities showed a close coupling between transverse particle velocities and turbulent diffusion for small drift parameters, whereas the terminal velocity dominated the movement as the drift parameter approached unity. RMS relative velocities associated with high inertia particles were shown to approach the level of the Eulerian fluctuations but small inertia particles had comparatively lower fluctuations (as the trajectories were more coupled to the fluid unsteadiness). This behavior was described by a simple theoretical model. Similarly, mean particle Reynolds numbers indicated a transition from being dominated by turbulent diffusion at small drift parameters and small Stokes numbers, to being dominated by the particle's terminal velocity at large drift parameters. A model was also proposed to describe the mean Reynolds number behavior and was shown to give reasonable agreement with the DNS data.

7.3 Low-density EOM and discretization effects

A new equation of motion was proposed and the effect of each surface-force was considered as it related to the prediction of air bubble and sand particle motion in a turbulent boundary layer of water. Flow-visualization showed that particles tended to collect in certain fluid structures when the entire equation of motion was used. This effect was not as strong when drag-alone was considered. Wall-normal particle concentration was a primary metric in assessing the effect of each surface force. The added mass and stress gradient effects were found to be strong for bubble conditions, but were generally negligible for sand particles when considering wall-normal distribution. The lift force was shown to be very important when the particle's terminal velocity is directed with the freestream flow and leads to high near-wall particle concentrations. When terminal velocity was directed opposite to the freestream, the particles were forced away from the wall. The majority of the conditions considered a terminal velocity pointed away from the wall such that the influence of lift was comparatively small. Lagrangian statistics were shown to be the most sensitive to choice of equation of motion.

A study was also conducted that considered the choice fluid property interpolation and the effects of using a point vs. a distributed-force model. Both the tri-linear and Lagrange based

interpolation schemes gave nearly identical predictions of wall-normal concentration; however Lagrangian statistics showed some sensitivity. Similarly, the distributed-force algorithm was shown to have negligible effects on concentration with minimal impact on Lagrangian statistics. Thus, the point-force requirements commonly posed may be less restrictive for the present type of flow.

Computational overhead for each of the equations of motion and discretization techniques was also considered. While the standard finite Reynolds number history force models were shown to increase simulation time by as much as 400%, the efficient window model gave similar predictions with only a 27% increase. The distributed-force algorithm using the higher-order Lagrange interpolant was shown to cost roughly three times as much as a simple point-force algorithm with tri-linear interpolation. Thus, depending on what output is important for a given study (e.g. particle concentration), the simpler point-force model may be sufficient and is much cheaper to evaluate.

7.4 Low-density particle simulations for various diameters

The new equation of motion was also used to conduct numerical experiments for air bubbles and sand particles of various sizes in a turbulent boundary layer of water at a constant Froude number. Particle-fluid interactions were observed by flow-visualization where particles with appreciable inertia were shown to form dense clumps in certain fluid structures. These clumps were seen to diffuse as the particles approached the tracer limit, consistent with preferential concentration mechanisms. Future studies may wish to include collision modeling in light of these results even for globally dilute volume fractions as local concentration levels can be large.

Particle concentrations as a function of distance from the wall were computed for both the bubble and sand particle condition and were compared with results obtained for a fluid tracer. Consistent with heavy-particle results, the sand particle was shown to behave nearly as a fluid tracer when $St^+ \approx 1$. However, the bubble showed significant non-tracer behavior for a similar Stokes number. Bubbles and sand particles with identical drift parameters and diameters were shown to have similar peak concentration locations, though the sand particle generates higher near-wall concentrations due to its larger inertia (compared to the corresponding bubble).

Wall-deposition rates were considered and the present low-density results were compared to existing heavy-particle data. Remarkably, the data sets show similar results in spite of the vast differences

in density ratio. Written in terms of non-dimensional deposition velocity, the low-density results were shown to be well-predicted by the heavy-particle model of Young & Leeming.

Low-density particle Lagrangian statistics were compared to heavy-particle results. Vertical particle velocities were found to agree very well with previous heavy-particle simulations as were the rms relative velocity and mean Reynolds number. The latter two statistics were well-predicted by existing theoretical models which were developed in the context of heavy-particles. Particle kinetic energy was also considered and shown to be consistent with previous simulations and bubble experiments. Hinze's theoretical predictions of bubble kinetic energy were shown to be excessive, consistent with experimental data.

7.5 Recommendations and future work

The finite-size extensions proposed for the equation of motion need further study. As previously mentioned, the lift force could not be treated analytically for finite-size considerations. Thus, those extensions are based on physical arguments and the errors associated with the present treatment could not be assessed (though they should be smaller than those associated with conventional point-force approaches). Resolved-surface simulations of finite-sized particles would be very helpful in assessing the accuracy of the proposed extensions in fluid turbulence. Additionally, it is unclear if the finite-size and finite-Reynolds number effects should be combined as simply in the present study. There could possibly be modifications to the base surface-force description when making the extension to finite-size. While these would surely be of higher-order importance, future studies may wish to determine if such corrections exist.

In the context of multiphase physics, more simulations are needed to quantify the limiting Stokes number for which a bubble effectively behaves as a tracer particle. The present study shows that appreciable non-tracer effects are obtained at Stokes numbers where heavy-particles would nearly follow the fluid path. A study which changes the wall-reflection plane in a physically consistent manner would be helpful to further quantify the deposition behavior of bubbles and other wall-interaction statistics. Finally, a larger range of conditions is needed to quantify particle kinetic energy of low-density particles. While bubbles have been considered experimentally and shown to maintain a kinetic energy equal to the fluid kinetic energy, the sand particles represent an intermediate density ratio whose kinetic energy should decrease with increase Stokes number.

While this has been well-documented for heavy-particles, the decay of kinetic energy for these intermediate density ratios is not known. One would expect it to be less than that seen for truly heavy-particles, but the current data sets did not involve a sufficient range of Stokes number to make this determination.

References

[1] M. V. Dyke, *Album of Fluid Motion.* Parabolic Press, Inc., 10th ed., June 1982.

[2] K. V. Beard and H. R. Pruppacher, "A determination of the terminal velocity and drag of small water drops by means of a wind tunnel," *Journal of the Atmospheric Sciences*, vol. 26, no. 5, pp. 1066–1072, 1969.

[3] F. H. Garner and D. Hammerton, "Circulation inside gas bubbles," *Chem. Eng. Sci*, vol. 3, no. 1, pp. 1–11, 1954.

[4] G. Sridhar and J. Katz, "Drag and lift forces on microscopic bubbles entrained by a vortex," *Physics of Fluids*, vol. 7, p. 389, 1995.

[5] L. Schiller and A. Z. Naumann, "Über die grundlegenden Berechungen bei der Schwerkraftaufbereitung," *Ver. Deut. Ing*, vol. 77, pp. 318–320, 1933.

[6] N. Mordant and J. Pinton, "Velocity measurement of a settling sphere," *The European Physical Journal B - Condensed Matter and Complex Systems*, vol. 18, pp. 343–352, Nov. 2000.

[7] F. Odar, *Forces acting on a sphere accelerating in a viscous fluid.* PhD thesis, Northwestern University, 1962.

[8] P. Cherukat, J. B. McLaughlin, and A. L. Graham, "The inertial lift on a rigid sphere translating in a linear shear flow field," *Intl. J. Multiphase Flow*, vol. 20, pp. 339–353, 1994.

[9] B. D. Tri, B. Oesterle, and F. Deneu, "Premiers resultants sur la portance d'une sphere en rotation aux nombres de reynolds intermediaies," *C. R. Acad. Sci. Ser. II: Mec. Phys. Chim. Sci Terre Universe*, vol. 311, p. 27, 1990.

[10] Y. Tsuji, Y. Morikawa, and O. Mizuno, "Experimental measurements of the magnus force on a rotating sphere at low reynolds numbers," *J. Fluids Engr.*, vol. 107, pp. 484–488, 1985.

[11] H. M. Barkla and L. J. AuchterLonie, "The Magnus or Robins effect on rotating spheres," *J. Fluid Mech.*, vol. 47, pp. 437–448, 1971.

[12] P. Bagchi and S. Balachandar, "Effect of free rotation on motion of a solid sphere," *Phys Fluids*, vol. 14, pp. 2719–2737, 2002.

[13] D. Legendre and J. Magnaudet, "Lift force on a bubble in a viscous linear shear flow," *J. Fluid Mech.*, vol. 368, pp. 81–126, 1998.

[14] R. C. Jeffrey and J. R. A. Pearson, "Particle motion in a laminar vertical tube flow," *J. Fluid Mech.*, vol. 22, pp. 721–735, 1965.

[15] G. G. Poe and A. Acrivos, "Closed-streamline flows past rotating single cylinders and spheres: Inertia effects," *J. Fluid Mech.*, vol. 72, pp. 605–623, 1975.

[16] J. Young and A. Leeming, "A theory of particle deposition in a turbulent pipe flow," *J. Fluid Mech.*, vol. 340, pp. 129–159, 1997.

[17] M. Sommerfeld, "Validation of a stochastic lagrangian modelling approach for inter-particle collisions in homogeneous isotropic turbulence," *International Journal of Multiphase Flow*, vol. 27, pp. 1829–1858, Oct. 2001.

[18] S. Sundaram and L. R. Collins, "Collision statistics in an isotropic Particle-Laden turbulent suspension. part 1. direct numerical simulations," *Journal of Fluid Mechanics*, vol. 335, no. -1, pp. 75–109, 1997.

[19] S. W. Coppen, V. P. Manno, and C. B. Rogers, "Turbulence characteristics along the path of a heavy particle," *Computers & Fluids*, vol. 30, pp. 257–270, Mar. 2001.

[20] P. D. M. Spelt and A. Biesheuvel, "On the motion of gas bubbles in homogeneous isotropic turbulence," *J. Fluid Mech.*, vol. 336, pp. 221–224, 1997.

[21] M. R. Maxey and J. J. Riley, "Equation of motion for a small rigid sphere in a non-uniform flow," *Phys. Fluids*, vol. 26, pp. 883–889, 1983.

[22] T. R. Auton, J. C. R. Hunt, and M. Prud'Homme, "The force exerted on a body in inviscid unsteady non-uniform rotational flow," *J. Fluid Mech.*, vol. 197, pp. 241–257, 1988.

[23] P. Bagchi and S. Balachandar, "Effect of turbulence on the drag and lift of a particle," *Phys Fluids*, vol. 15, no. 11, pp. 3496–3513, 2003.

[24] L. Zeng, S. Balachandar, and F. Najjar, "Interactions of a stationary finite-sized particle with wall turbulence," *J. Fluid Mech.*, vol. 594, pp. 271–305, 2008.

[25] A. Merle, D. Legendre, and J. Magnaudet, "Forces on a high-reynolds-number spherical bubble in a turbulent flow," *J. Fluid Mech.*, vol. 532, pp. 53–62, 2005.

[26] D. E. Stock, "Particle dispersion in flowing gases–1994 freeman scholar lecture," *J. Fluids Eng.*, vol. 118, pp. 4–17, 1996.

[27] E. Loth, "Numerical approaches to dilute two-phase flow," *Prog. Energy Combust. Sci.*, vol. 26, pp. 161–223, 2000.

[28] L.-P. Wang and M. R. Maxey, "Settling velocity and concentration distribution of heavy particles in homogeneous isotropic turbulence," *J. Fluid Mech.*, vol. 256, pp. 27–68, 1993.

[29] D. Kaftori, G. Hetsroni, and S. Banerjee, "Particle behavoir in the turbulent boundary layer. I Velocity and distribution profiles," *Phys. Fluids*, vol. 7, pp. 1095–1106, 1995.

[30] D. Kaftori, G. Hetsroni, and S. Banerjee, "Particle behavoir in the turbulent boundary layer. II Velocity and distribution profiles," *Phys. Fluids*, vol. 7, pp. 1107–1121, 1995.

[31] J. B. McLaughlin, "Aerosol particle deposition in numerically simulated channel flow," *Physics of Fluids A: Fluid Dynamics*, vol. 1, p. 1211, 1989.

[32] J. B. McLaughlin, "Inertial migration of a small sphere in linear shear flows," *J. Fluid Mech.*, vol. 224, pp. 261–274, 1991.

[33] J. W. Brooke, K. Kontomaris, T. J. Hanratty, and J. B. McLaughlin, "Turbulent deposition and trapping of aerosols at a wall," *Phys. Fluids A*, vol. 4, pp. 825–834, 1992.

[34] S. K. Friedlander and H. F. Johnstone, "Deposition of suspended particles from turbulent gas streams," *Ind. Eng. Chem.*, vol. 49, pp. 1151–1156, 1957.

[35] C. Marchioli and A. Soldati, "Mechanisms for particle transfer and segregation in a turbulent boundary layer," *J. Fluid Mech.*, vol. 468, pp. 283–315, 2002.

[36] A. J. Dorgan, E. Loth, T. L. Bocksell, and P. K. Yeung, "Boundary layer dispersion of near-wall injected particles of various inertias," *AIAA J.*, vol. 43, pp. 1537–1548, 2005.

[37] M. R. Wells and D. E. Stock, "The effects of crossing trajectories on the dispersion of particles in a turbulent flow," *J. Fluid Mech.*, vol. 136, pp. 31–62, 1983.

[38] J. Xu, M. R. Maxey, and G. E. Karniadakis, "Numerical simulation of turbulent drag reduction using Micro-Bubbles," *Journal of Fluid Mechanics*, vol. 468, no. -1, pp. 271–281, 2002.

[39] M. R. Maxey, B. K. Patel, E. J. Chang, and L. P. Wang, "Simulations of dispersed turbulent multiphase flow," *Fluid dynamics research*, vol. 20, no. 1-6, pp. 143–156, 1997.

[40] A. Ferrante and S. Elghobashi, "On the physical mechanisms of drag reduction in a spatially developing turbulent boundary layer laden with microbubbles," *Journal of Fluid Mechanics*, vol. 503, pp. 345–355, 2004.

[41] A. Ferrante and S. Elghobashi, "Reynolds number effect on drag reduction in a microbubble-laden spatially developing turbulent boundary layer," *Journal of Fluid Mechanics*, vol. 543, pp. 93–106, 2005.

[42] A. Giusti, F. Lucci, and A. Soldati, "Influence of the lift force in direct numerical simulation of upward/downward turbulent channel flow laden with surfactant contaminated microbubbles," *Chemical Engineering Science*, vol. 60, pp. 6176–6187, Nov. 2005.

[43] V. Armenio and V. Fiorotto, "The importance of the forces acting on particles in turbulent flows," *Physics of Fluids*, vol. 13, p. 2437, 2001.

[44] E. Loth, "Lift of a spherical particle subject to vorticity and/or spin," *AIAA J.*, vol. 46, pp. 801–809, 2008.

[45] P. R. Spalart, R. D. Moser, and M. M. Rogers, "Spectral methods for the Navier-Stokes Equations with one infinite and two-periodic directions," *J. Comput. Physics*, vol. 96, pp. 297–324, 1991.

[46] P. R. Spalart and J. H. Watmuff, "Experimental and numerical study of a turbulent boundary layer with pressure gradients," *J. Fluid Mech.*, vol. 249, pp. 337–371, 1993.

[47] S. A. Orszag and G. S. Patterson, "Numerical simulation of Three-Dimensional homogeneous isotropic turbulence," *Physical Review Letters*, vol. 28, no. 2, p. 76, 1972.

[48] R. S. Rogallo, "Numerical experiments in homogeneous turbulence," NASA TM 81315, Ames Research Center, 1981.

[49] P. R. Spalart, "Direct simulation of a turbulent boundary layer up to $Re_\theta = 1410$," *J. Fluid Mech.*, vol. 187, pp. 61–98, 1988.

[50] T. Bocksell, *Numerical simulation of turbulent particle diffusion.* PhD thesis, University of Illinois at Urbana-Champaign, 2003.

[51] C. T. Crowe, M. Sommerfeld, and Y. Tsuji, *Multiphase Flows with Droplets and Particles.* Boca Raton, FL, 1998.

[52] G. G. Stokes, "On the effect of the inertial friction of fluids on the motion of pendulums," *Trans. Cambr. Phil. Soc.*, vol. 9, pp. 8–106, 1851.

[53] M. R. Maxey, "Equation of motion for a small rigid sphere in a non-uniform or unsteady flow," *ASME/FED Gas-Solid Flows*, vol. 166, pp. 57–62, 1993.

[54] H. Faxen, "The resistance against the movement of a rigour sphere in viscous fluids, which is embedded between two parallel layered barriers," *Annalen Der Physik*, vol. 68, pp. 89–119, 1922.

[55] T. R. Auton, "The lift force on a spherical body in a rotational flow," *J. Fluid Mech.*, vol. 183, pp. 199–218, 1987.

[56] J. Bataille, M. Lance, and J. L. Marie, "Some aspects of the modeling of bubbly flows," in *Phase-Interface Phenomena in Multiphase Flow* (G. F. Hewitt, F. Mayinger, and J. R. Riznic, eds.), Hemisphere Publishing Corporation, 1991.

[57] I. Kim, S. Elghobashi, and W. B. Sirignano, "On the equation for spherical- particle motion: effect of reynolds and acceleration numbers," *J. Fluid Mech.*, vol. 367, pp. 221–253, 1998.

[58] R. Mei and J. F. Klausner, "Unsteady force on a spherical bubble with finite reynolds number with small fluctuations in the free-stream velocity," *Phys. Fluids A*, vol. 4, pp. 63–70, 1992.

[59] R. Mei and J. F. Klausner, "Shear lift force on spherical bubbles," *Int. J. Heat and Fluid Flow*, vol. 15, pp. 62–65, 1994.

[60] R. Mei, C. J. Lawrence, and R. J. Adrian, "Unsteady drag on a sphere at finite reynolds number with small fluctuations in the free-stream velocity," *J. Fluid Mech.*, vol. 233, pp. 613–631, 1991.

[61] L. V. Wakaba and S. Balachandar, "History force on a sphere in a weak linear shear flow," *Int. J. Heat and Fluid Flow*, vol. 31, pp. 996–1014, 2007.

[62] F. Odar and W. S. Hamilton, "Forces on a sphere accelerating in a viscous fluid," *J. Fluid Mech.*, vol. 18, pp. 302–314, 1964.

[63] A. B. Basset, "On the motion of a sphere in a viscous liquid," *Phil. Trans. R. Soc. London*, vol. 179A, pp. 43–63, 1888.

[64] R. Mei and R. J. Adrian, "Flow past a sphere with an oscillation in the free-stream and unsteady drag at finite reynolds number," *J. Fluid Mech.*, vol. 237, pp. 323–341, 1992.

[65] P. M. Lovalenti and J. F. Brady, "The force on a sphere in a uniform flow with small-amplitude oscillations at finite reynolds number," *J. Fluid Mech.*, vol. 256, pp. 607–614, 1993.

[66] R. Mei, "Flow due to an oscillating sphere and an expression for unsteady drag on the sphere at finite reynolds number," *Journal of Fluid Mechanics Digital Archive*, vol. 270, no. -1, pp. 133–174, 1994.

[67] C. J. Lawrence and R. Mei, "Long-Time behaviour of the drag on a body in impulsive motion," *Journal of Fluid Mechanics Digital Archive*, vol. 283, no. -1, pp. 307–327, 1995.

[68] E. J. Chang and M. R. Maxey, "Unsteady flow about a sphere at low to moderate reynolds number. part 1. oscillatory motion," *Journal of Fluid Mechanics Digital Archive*, vol. 277, pp. 347–379, 2006.

[69] E. J. Chang and M. R. Maxey, "Unsteady flow about a sphere at low to moderate reynolds number. part 2. accelerated motion," *Journal of Fluid Mechanics Digital Archive*, vol. 303, pp. 133–153, 2006.

[70] R. W. Moorman, *Motion of a Spherical Particle in the Accelerated Portion of Free-fall.* PhD thesis, University of Iowa, 1955.

[71] P. G. Saffman, "The lift on a sphere in slow shear flow," *J. Fluid Mech.*, vol. 22, pp. 385–400, 1965. Corrigendum, 1968. 31, 624.

[72] I. Heron, S. Davis, and F. Bretherton, "On the sedimentation of a sphere in a centrifuge," *J. Fluid Mech.*, vol. 68, pp. 209–234, 1975.

[73] R. Mei, "An approximate expression for shear lift force on a spherical particle at a finite reynolds number," *Intl. J. Multiphase Flow*, vol. 18, pp. 145–147, 1992.

[74] S. I. Rubinov and J. B. Keller, "The transverse force on spinning spheres moving in a viscous liquid," *J. Fluid Mech.*, vol. 11, pp. 3447–3459, 1961.

[75] T. Tanaka, S. Yonemura, and Y. Tsuji, "Experiments of fluid forces on a rotating sphere and spheroid," in *Proc. 2nd KSME-JSME Fluids Engr. Conf.*, 1990.

[76] J. Happel and H. Brenner, *Low Reynolds Number Hydrodynamics.* Noordhoff, 1973.

[77] C. J. Lin, J. H. Perry, and W. R. Scholwater, "Simple shear flow round a rigid sphere: Inertial effects and suspension rheology," *J. Fluid Mech.*, vol. 44, pp. 1–17, 1970.

[78] S. Elghobashi, "On predicting particle-laden turbulent flows," *Applied Scientific Research*, vol. 52, pp. 309–329, 1994.

[79] H. Brenner, "The Stokes resistasnce of an arbitrary particle–IV arbitrary fields of flow," *Chemical Engineering Science*, vol. 19, pp. 703–727, 1964.

[80] E. W. Hobson, *The Theory of Spherical and Ellipsoidal Harmonics.* Cambridge Univ. Press, republished 1955 by Chelsea Publishing Comp., New York, 1931.

[81] E. Michaelides, "Hydrodynamic force and heat/mass transfer from particles, bubbles and drops–The Freeman Scholar Lecture," *J. Fluids Eng.*, vol. 125, pp. 209–238, 2003.

[82] T. M. Burton and J. K. Eaton, "Fully resolved simulations of particle-turbulence interaction," *J. Fluid Mech.*, vol. 545, pp. 67–111, 2005.

[83] P. Bagchi and S. Balachandar, "Steady planar straining flow past a rigid sphere at moderate reynolds number," *J. Fluid Mech.*, vol. 466, pp. 365–407, 2002.

[84] I. E. Barton, "Exponential-Lagrangian tracking schemes applied to stokes law," *Journal of Fluids Engineering*, vol. 118, p. 85, 1996.

[85] K. D. Squires and J. K. Eaton, "Particle response and turbulence modification in isotropic turbulence," *Physics of Fluids A: Fluid Dynamics*, vol. 2, p. 1191, 1990.

[86] C. Marchioli, V. Armenio, and A. Soldati, "Simple and accurate scheme for fluid velocity interpolation for eulerian-lagrangian computation of dispersed flows in 3d curvilinear grids," *Computers & Fluids*, vol. 36, pp. 1187–1198, 2007.

[87] A. J. Dorgan and E. Loth, "Simulation of particles released near the upper wall in a turbulent boundary layer," Tech. Rep. AE 03-05, UILU ENG 03-0505, University of Illinois at Urbana-Champaign, 2003.

[88] J. O. Hinze, *Turbulence.* McGraw-Hill Book Company, 1959.

[89] W. S. J. Uijttewaal and R. V. A. Oliemans, "Particle dispersion and deposition in direct numerical and large eddy simulations of vertical pipe flows," *Phys. Fluids*, vol. 8, pp. 2590–2604, 1996.

[90] A. J. Dorgan, "Boundary layer dispersion of near-wall injected particles of various inertias," Master's thesis, University of Illinois at Urbana-Champaign, 2003.

[91] B. van Haarlem, B. J. Boersma, and F. T. M. Nieuwstadt, "Direct numerical simulation of particle deposition onto a free-slip and no-slip surface," *Phys. Fluids*, vol. 10, pp. 2590–2604, 1998.

[92] C. Narayanan, D. Lakehal, L. Botto, and A. Soldati, "Mechanisms of particle deposition in a fully developed turbulent open channel flow," *Phys. Fluids*, vol. 15, pp. 763–775, 2003.

[93] A. J. Dorgan and E. Loth, "Efficient calculation of the history force at finite reynolds numbers," *Intl. J. Multiphase Flow*, vol. 33, pp. 833–848, 2007.

[94] S. L. Rani, C. Winkler, and S. Vanka, "A new algorithm for computing binary collisions in dispersed two-phase flows," *Numerical Heat Transfer Part B: Fundamentals*, vol. 45, pp. 99–109, 2004.

[95] E. Loth and J. Stedl, "Taylor nad lagrangian correlations in a turbulent free shear layer," *Experiments in Fluids*, vol. 26, pp. 1–6, 1999.

[96] K. Felton and E. Loth, "Spherical bubble motion in a turbulent boundary layer," *Physics of Fluids*, vol. 13, no. 9, pp. 2564–2577, 2001.

[97] K. Felton and E. Loth, "Diffusion of spherical bubbles in a turbulent boundary layer," *International Journal of Multiphase Flow*, vol. 28, no. 1, pp. 69–92, 2002.

[98] G. A. Kallio and M. W. Reeks, "A numerical simulation of particle deposition in turbulent boundary layers," *International journal of multiphase flow*, vol. 15, no. 3, pp. 433–446, 1989.

[99] B. Y. Liu and J. K. Agarwal, "Experimental observation of aerosol deposition in turbulent flow," *Journal of Aerosol Science*, vol. 5, pp. 145–148, Mar. 1974.

[100] T. Sun and G. M. Faeth, "Structure of turbulent bubbly jets. II: phase property profiles," *International journal of multiphase flow*, vol. 12, no. 1, pp. 115–126, 1986.

Appendix A

Window model validation

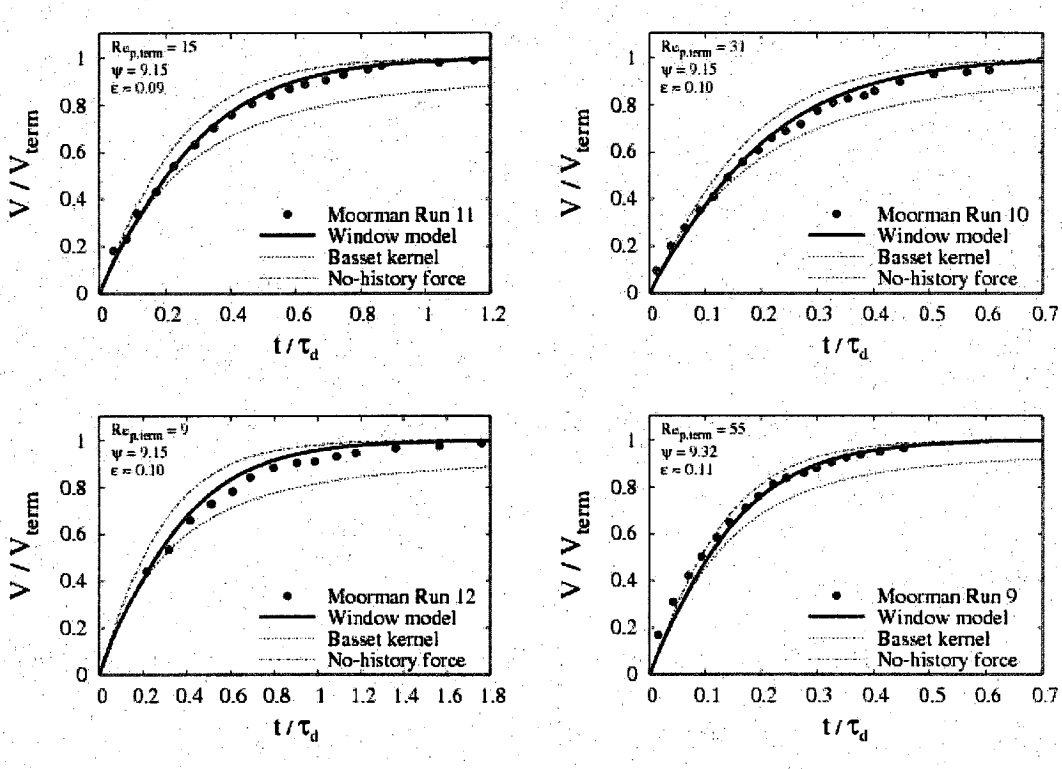

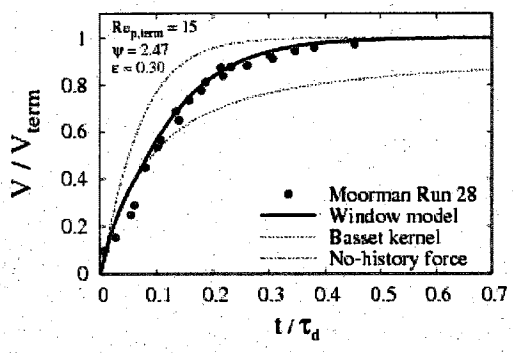

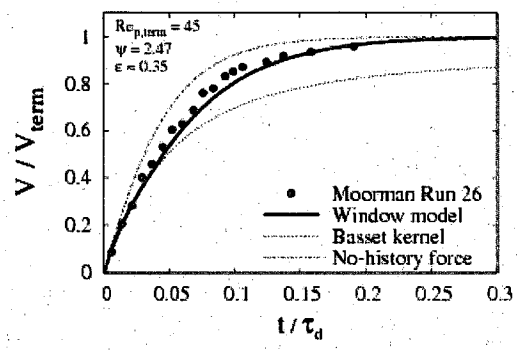

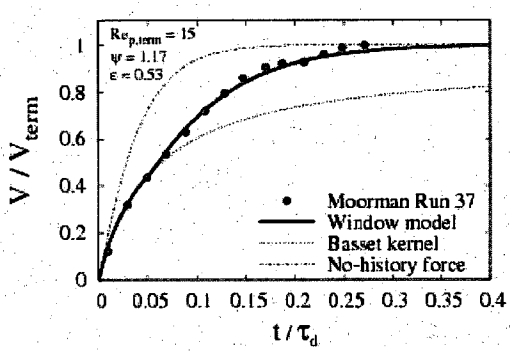

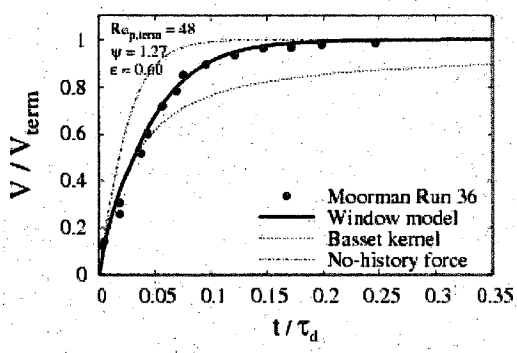

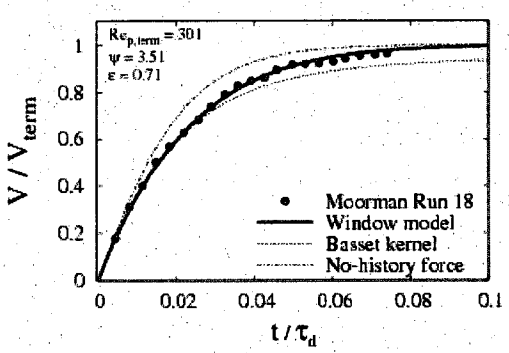

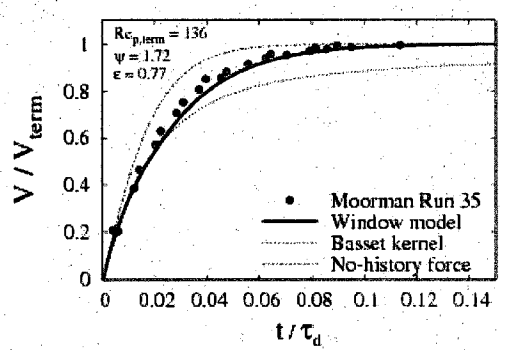

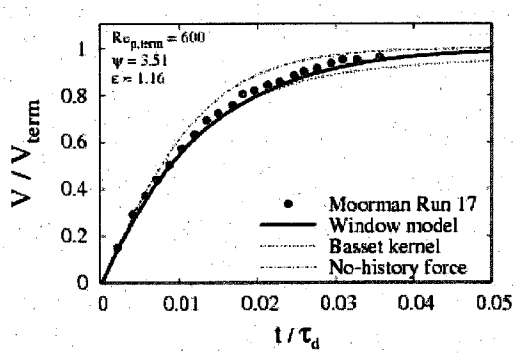

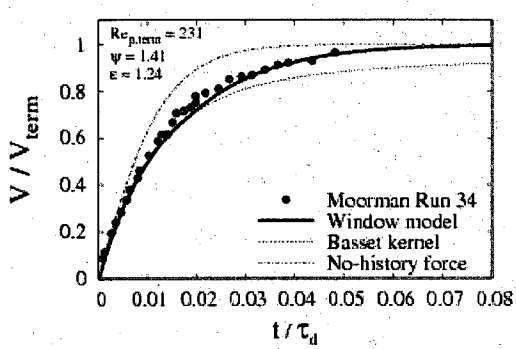

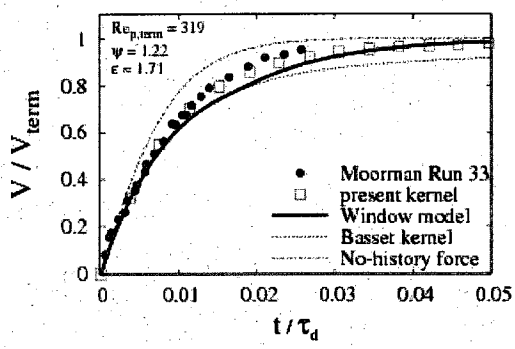

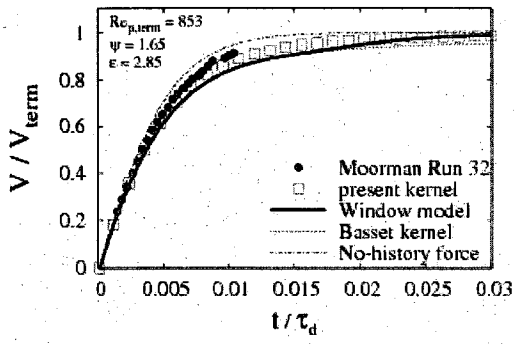

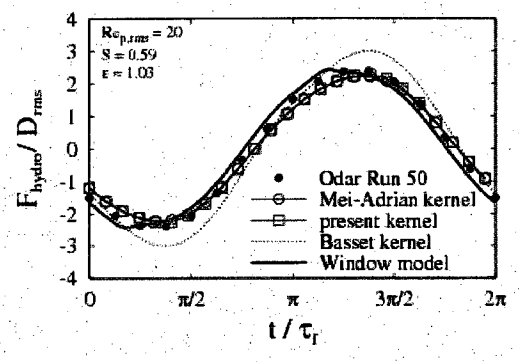

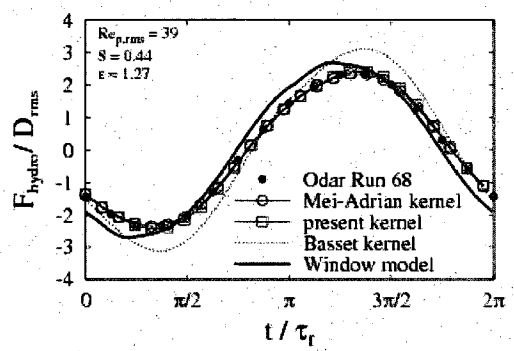

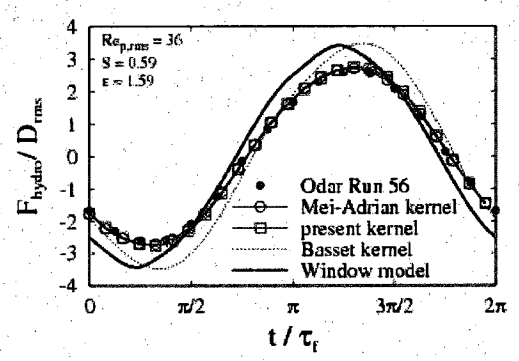

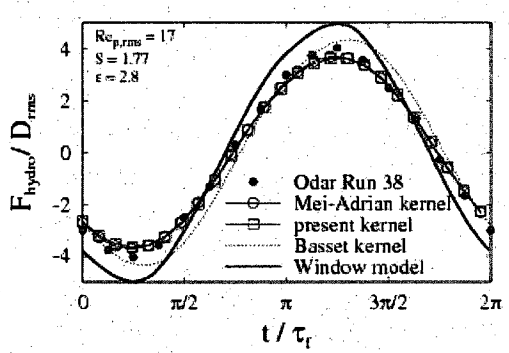

Curriculum Vitae

ANDREW J. DORGAN

1223 Lindenwood Avenue
Edwardsville, IL 62025
(217) 737-0002
andrew.j.dorgan@boeing.com

Education

The University of Illinois at Urbana-Champaign — Urbana, IL
Ph.D. Aerospace Engineering, Expected May 2009.
Dissertation topic: Modeling and Simulation of Bubbles and Particles
Advisor: Professor Eric Loth
GPA: 3.95/4.0

The University of Illinois at Urbana-Champaign — Urbana, IL
M.S. Aerospace Engineering, December 2003.
Thesis topic: Boundary layer dispersion of near-wall injected particles of various inertias
Advisor: Professor Eric Loth
GPA: 3.93/4.0

The University of Illinois at Urbana-Champaign — Urbana, IL
B.S. Aeronautical and Astronautical Engineering, December 2001, with Highest Honors
GPA: 3.91/4.0

Springfield College in Illinois — Springfield, IL
Associate of Arts, May 1999
GPA: 4.0/4.0

Industry Positions

The Boeing Company — St. Louis, MO
April 2006 – present
Specialist Engineer, Computational Fluid Dynamics

- Computational fluid dyamic tool development, with particular emphasis placed on efficiently, accurately, and robustly solving the governing equations on unstructured meshes.
- Support the application staff in use of CFD tool set.

The Boeing Company — St. Louis, MO
January 2004 – March 2006
Senior Engineer, Computational Fluid Dynamics

Academic Positions

The University of Illinois at Urbana-Champaign — Urbana, IL
May 2001 – present
Research Assistant to Professor Eric Loth

Significant Accomplishments:

- Conducted study of multiphase interaction between particles and bubbles in a direct numerical simulation of fluid turbulence.
- Performed analytical work regarding the proper form of the particle equation of motion for finite-sized particles.
- Constructed an efficient algorithm for the calculation of the unsteady drag (history) force which can lead to orders-of-magnitude reduction in CPU-time for simulations of finite-Reynolds number particles and bubbles.

The University of Illinois at Urbana-Champaign — Urbana, IL
August 2003 – December 2003
Teaching Assistant to Professor Mike Bragg.

Course description:

- Introductory course on incompressible flow covering the derivation and application of the Navier-Stokes equations
- Discussion of the idealizations which lead to the potential flow equations and their application to wing theory and classical low-speed aerodynamics.

Responsibilities:

- Designed and graded homework problems
- Taught problem sessions and held office hours to help students understand material

Teaching Interests

- All theoretical fluid mechanics including: incompressible and compressible flow, multiphase flow.
- Computational fluid dynamics and basic numerical analysis.

Research Interests

- Interactions of particles/bubbles with fluid turbulence.
- Computational fluid dynamics, numerical algorithms.

Honors and Awards

- AIAA Young Professional Award, St. Louis Section, Spring 2007.
- Aerospace Illinois Fellowship, Spring 2002.

- AIAA Academic Excellence Award for highest GPA in graduating class, Fall 2001.
- F. Paul LaFata Academic Scholarship, Spring 1998.

Professional Affliations

- Tau Beta Pi Engineering Honorary
- Sigma Gamma Tau Aerospace Honorary
- Order of the Engineer
- American Institute of Aeronautics and Astronautics
- Phi Theta Kappa
- Golden Key

Selected Publications

E. Loth & A.J. Dorgan, 2009. An equation of motion for particles of finite Reynolds number and size. Environmental Fluid Mechanics, to appear.

A.J. Dorgan & E. Loth, 2007. Efficient calculation of the history force at finite Reynolds numbers. International Journal of Multiphase Flow, Vol. 33, p. 833-848.

A.J. Dorgan, E. Loth, T.L. Bocksell, P.K. Yeung, 2005. Boundary-Layer dispersion of near-wall injected particles of various inertias. AIAA Journal, Vol. 43, p. 1537-1548.

A.J. Dorgan, E. Loth, E. Frazzoli, 2005. Autonomous control of micro-aircraft vehicles falling through an atmospheric boundary layer. AIAA Journal, Vol. 43, p. 768-775.

A.J. Dorgan, E. Loth, 2004. Simulation of particles released near the wall in a turbulent boundary layer. International Journal of Multiphase Flow, Vol. 30, p. 649-673.